GENERATION OF HETEROGENEOUS CELLULAR STRUCTURES BY SONICATION

María del Carmen Torres Sánchez

Submitted for the Degree of Doctor of Philosophy (Ph.D.) on completion of research in the School of Engineering and Physical Sciences,

Heriot-Watt University

February 2008

ABSTRACT

Many materials require functionally graded cellular microstructures whose porosity (i.e. ratio of the void volume to the total volume of a material) is engineered to meet specific requirements and for an optimal performance in diverse applications. Numerous applications have demonstrated the potential of porous materials in areas ranging from biomaterial science through to structural engineering. Polymeric foams are an example of a cellular material whose microstructure can be considered as a blend of material and non-material zones.

While a huge variety of foams can be manufactured with *homogenous* porosity, for *heterogeneous* foams there are no generic processes for controlling the distribution of porosity throughout the resulting matrix. Motivated by the desire to create a flexible process for engineering heterogeneous foams, this work has investigated how ultrasound, applied during some of the foaming stages of a polyurethane melt, affects both the cellular structure and distribution of the pore size.

After reviewing the literature concerning foam chemistry, ultrasound and sonochemistry, series of experiments were performed that used an ultrasonic field created by a sonotrode irradiating in a water bath containing a strategically placed vessel filled with foaming reactants. Prior to this, the acoustic field in the bath had been accurately mapped so that the acoustic pressure conditions within the foam container were known.

During the foam polymerisation reaction, the acoustic pressure in the water bath varied causing the bubbles to pulsate in a state of ‘stable cavitation’ (i.e. rectified diffusion). This pulsation of the bubbles pumped gas from the liquid to the gas phase inducing them to increase in volume. The eventual solidification resulted in a porous material with a cellular structure that reflected the acoustic field imposed upon it.

The experimental results revealed how the parameters of ultrasound exposure (i.e. frequency and acoustic pressure) influenced the volume and distribution of pores within the final polyurethane matrix: it was found that porosity varies in direct proportion to both the acoustic pressure and the frequency of the ultrasound signal.

The effects of ultrasound on porosity demonstrated by this work offer the prospect of a manufacturing process that can control and adjust the cellular geometry of foam and hence ensure that the resulting characteristics of the heterogeneous material match the functional requirements.

To my grandmother, Mamaría, because she is the beginning

A mi Mamaría, porque con ella comenzó todo

ACKNOWLEDGEMENTS

I would like to thank Professor Jonathan Corney for his supervision during my PhD. His outstanding intuition, creativity and imagination have guided this work, like a lighthouse to a ship, through many moments of darkness and confusion. He believed in me when no one else did, not even myself, and I am deeply grateful to him for that.

I am indebted to Dr Doug Clark for being my second supervisor and, once retired, for giving up so much of his spare time to read, correct and guide me to the completion of this PhD thesis.

Both my Spanish and French families have been source of love and inspiration right from the beginning of this journey.

I gratefully acknowledge the financial support of the Engineering and Physical Sciences Research Council (EPSRC) and the Neilson Endowment Fund, in the Department of Mechanical Engineering.

There are many people who have my sincere thanks because they have, sometimes unknowingly, helped, contributed and encouraged this work. They are too many to name and I fear to accidentally forget someone important. However, I truly acknowledge the contribution of the following key characters: Dr T. Lim, for his help in my settling at Heriot-Watt; and Dr J. Yang, for allowing me to use the image processing facilities in the General Western Hospital, for his assistance during endless hours in the lab and his friendship; Dr P. Tatum, from AWE plc, for the μ-CT scanning of the foam samples.

Professor I. Steel, former head of the department, for offering me a job, and Professor A. Moore, present head, for extending my contract, so I could be self-financed and, consequently, complete the writing up of this thesis.
Mr A. Buchan and his team of technicians, for ensuring a healthy and safe working environment, in both the lab and the office, during my research work.

My last piece of gratitude must go to my friend, my love, Steve Earl. He appeared in my life when many battles had lost their name and gave me a reason to face them again. Because certain issues in life are worth fighting for until the end.

ACADEMIC REGISTRY
Research Thesis Submission

Name*:*	María del Carmen Torres-Sánchez		
School/PGI:	School of Engineering and Physical Sciences		
Version: *(i.e. First, Resubmission, Final)*	Final	Degree Sought:	PhD

Declaration

In accordance with the appropriate regulations I hereby submit my thesis and I declare that:

1) the thesis embodies the results of my own work and has been composed by myself
2) where appropriate, I have made acknowledgement of the work of others and have made reference to work carried out in collaboration with other persons
3) the thesis is the correct version of the thesis for submission and is the same version as any electronic versions submitted*.
4) my thesis for the award referred to, deposited in the Heriot-Watt University Library, should be made available for loan or photocopying and be available via the Institutional Repository, subject to such conditions as the Librarian may require
5) I understand that as a student of the University I am required to abide by the Regulations of the University and to conform to its discipline.

* *Please note that it is the responsibility of the candidate to ensure that the correct version of the thesis is submitted.*

Signature of Candidate*:*		Date:	28th March 2008

Submission

Submitted By *(name in capitals):*	MARÍA DEL CARMEN TORRES-SÁNCHEZ
Signature of Individual Submitting:	
Date Submitted:	28th March 2008

For Completion in Academic Registry

Received in the Academic Registry by *(name in capitals):*			
Method of Submission *(Handed in to Academic Registry; posted through internal/external mail):*			
E-thesis Submitted			
Signature:		Date:	

TABLE OF CONTENTS

LIST OF FIGURES

LIST OF TABLES

NOMENCLATURE AND SYMBOLS

A	surface area, m^2; amplitude of the wave, m
a	factor in equation type '*y=a lnx+b*'
a_1, a_2, a_3	constants in quadratic equation
B	mass of blowing agent in the gas phase per unit polymer mass
b	factor in equation type '*y=a lnx+b*'
C	molar concentration, $kmol/m^3$
c	speed of sound, m/s
c_B	Specific heat of the blowing agent, averaged between liquid and vapour, J/kg.K
c_p	Specific heat at constant pressure, J/kg.K
c_{rest}	specific heat of the remaining components (acetone, water, etc), J/kg.K
D_B	binary mass diffusion coefficient, m^2/s
d_b	diameter of the bubble, m
d_{SE}	bubble shell thickness at rest, m
dB/dt	rate of formation of blowing agent + vaporisation rate of solvent, s^{-1}
dX/dt	reaction rate, rate of increase of reaction extent, s^{-1}
E	energy, J
f	frequency, s^{-1}
f_r	Bjerkness force, N
G	gain factor (by amplifier)
G_S	elastic shell parameter (bubble); shear modulus, Pa
ΔH_r	total heat reaction per unit of polymer mass, J/kg
h_v	latent formation (vaporisation) heat of blowing agent (solvent) per unit mass, J/kg
h_m	convection mass transfer coefficient, m/s
I	intensity, W/m^2
K	thermal conductivity, W/m.K
K_H	Henry's constant
K_m	mass transfer coefficient (diffusional), m/s
k	wave number
L	length between measuring probes, m
L_p	Sound pressure level, dB
N_B	molar transfer rate of specie B, kmol/s
$\dot{N}_B$	molar rate of increase of specie B per unit volume due to convection, $kmol/s.m^3$
n_b	number of bubbles per unit mass
P	pressure, Pa
P_m	nominal power, W
P_{RMS}	acoustic pressure in averaged terms, Pa
p(t)	instantaneous acoustic pressure, Pa
Q	reference electrical resistance, Ω
Q_x	electrical resistance offered by the foam in the vessel, Ω
R	bubble radius, m
R_a	acoustic intensity reflection coefficient
r	radius of a sphere, m
T	temperature, K
T_a	acoustic intensity transmission coefficient
t	time, s
u_x, u_y, u_z	velocity components in the x, y, z system of coordinates, m/s
V	volume, m^3
V_{BS}	base electrical voltage, applied excitation voltage, volts
V_i	measured electrical potential difference, volts
V_m	volume of material, m^3
V_O	Amplified measured electrical potential difference, output, volts
V_p	volume of pore, m^3
X	conversion rate
x_B	mole fraction of specie B, C_B/C
x, y, z	cartesian coordinates, m
Z	acoustic impedance, $kg/s.m^2$ or Rayl or Pa.s/m

∇	Laplacian operator

Subscripts

$( )_{x,y,z}$	conditions at x, y, z
$( )_w$	conditions at the vessel wall
$( )_0$	initial conditions; in equilibrium; at rest
$( )_B$	referred to the blowing agent
$( )_{B,S}$	referred to blowing agent on the membrane surface
$( )_{B,\infty}$	referred to blowing agent under free stream conditions
$( )_p$	referred to polymer
$( )_A$	referred to incident, applied, acoustic wave
$( )_x$	referred to point x
$( )_m$	nominal
$( )_b$	referred to bubble
$( )_l$	referred to liquid
$( )_v$	referred to vapour
$( )_g$	referred to gas
$( )_S$	referred to a surface
$( )_s$	referred to the bubble shell

Greek symbols

α	convection coefficient, W/K.m^2; acoustic absorption coefficient, m^{-1}
δ	dielectric constant, Ω m
γ	polytrophic exponent of the gas
ϕ	angle phase
λ	wavelength, m
μ	viscosity, N.s/m^2
μ_L	liquid viscosity, N.s/m^2
μ_S	viscous shell parameter (bubble), N.s/m^2
Θ	volume fraction of a foam
ρ	density, kg/m^3
σ	surface tension, N/m
ω	angular frequency, s^{-1}
ω_{Bo}	initial fraction of blowing agent

Overbar	averaged values in time; time mean
*	referred to the foam

LIST OF PUBLICATIONS AND RELATED COMMUNICATIONS DERIVED FROM THIS RESEARCH WORK

Torres-Sánchez C. and Corney J.R, *Porosity engineering of polymeric foams by localised sonication*, in Proceedings of the 19th International Congress on Acoustics (ICA 2007), p.384, ISBN: 84-87985-12-2

Torres-Sánchez C. and Corney J.R, *Effects of ultrasound on polymeric foam porosity*, Ultrasonics Sonochemistry, 2008. 15(4), p.408-415, ISSN: 1350-4177

Torres-Sánchez C, Corney J.R. and Clark, D.E.R, *CAD representations and CAM methods for porous ceramic materials*, in Proceedings of the International Conference on Porous Ceramic Materials (PCM 2005), p.25-33, ISBN: 90-5857-006-1

Torres-Sánchez C, Corney J.R and Lim T, *Manufacture of Heterogeneous materials with variable porosity: an application of sonochemistry in porous ceramic materials*, in Proceedings of the International Conference on Porous Ceramic Materials (PCM 2005), p.50, ISBN: 90-5857-006-1

Torres-Sánchez C, Corney J.R, Lim T, and Clark, D.E.R, *A survey of CAD representations and CAM methods for heterogeneous materials*, for the MC7 Conference: Functional Materials for the 21st Century, by the Royal Society of Chemistry, Edinburgh, 5-8 July 2005, UK

Torres-Sánchez C, Corney J.R and Clark, D.E.R, (Invited) *Generation of controlled porous structures by sonication*, in the workshop Proceedings of the International Workshops on Interfaces: Interfaces by Design, organised by the Lawrence Berkeley National Laboratory, CA, p.76

Lim T, Medellin H, Torres-Sánchez C, Corney J.R, Ritchie J.M. and Davies J.B.C, *Edge-based identification of DP-features on Free-Form solids* (Object Modelling), IEEE Transactions on Pattern Analysis and Machine Intelligence, 2005, 27 (6), p. 851-860. ISSN: 0162-8828

Torres-Sánchez C. and Corney J.R, *Characterisation of porosity distribution in polymeric foams*, (in preparation)

Torres-Sánchez C. and Corney J.R, *Manufacture of graded porosity foams: simulation of local ultrasonic pressure and comparison with experimental results*, (in preparation)

CHAPTER 1. INTRODUCTION

1.1 Background

Nature provides good examples of heterogeneous materials: e.g. wood, a composite of fibrous cellulose in a matrix of lignin; bone, calcium phosphate mineral of a functionally graded porosity reinforced by collagen fibrils; silk, chains of entangled monomers. Since the earliest times, humans too have devised manufacturing processes that allow the advantages of mixing materials to be exploited. Bricks (made of mud and reinforced with straw for construction purposes), paper (a matrix of cellulose microfibres) or pottery (ceramic utensils for cooking whose porous structure permits thermal insulation) are illustrations of the pre-industrial uses of heterogeneous materials.

More recently, engineers have also recognised [1] that the performance of materials can be dramatically improved if their composition and structure are varied to match precisely their functional requirements. Such heterogeneous materials have engineered gradients of composition, or structure, which offer superior performance over traditional homogeneous materials. Indeed, heterogeneous materials frequently demonstrate dramatic synergy, with their overall performance being far greater than a straightforward sum of the individual constituents. These types of materials offer great promise in fields where a high performance technology or active functionality is required (e.g. biomaterials, aerospace) because their nature offer the possibility of a composition where different substances can be blended, mixed, shaped or assembled to form components for optimal performance.

Today '*heterogeneous material*' is an umbrella concept that includes functionally graded materials (FGMs), composites and objects with engineered microstructure (Figure 1).

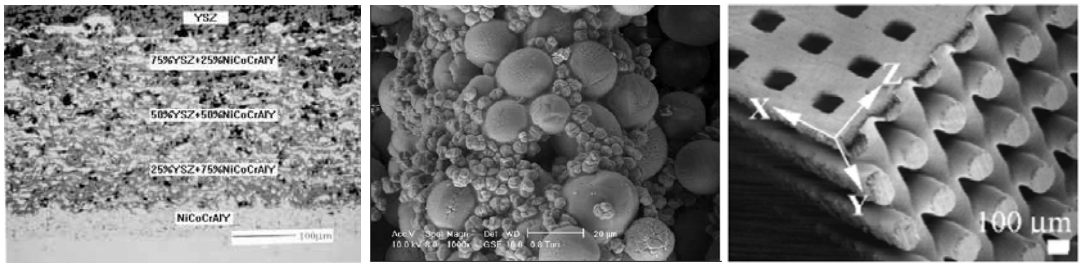

(a) Functionally Graded Material (Courtesy Nanyang Tech Uni, Singap.) (b) Composite [2] (c) Microstructure [3]

Figure 1: Three types of heterogeneous materials

Perhaps the best known examples of heterogeneous materials are the advanced composites (e.g. glass-fibre or carbon-fibre reinforced polymers, dental composites, aramid-fibre

reinforced concrete, etc) [4]. However, increasingly engineers are seeking to imitate natural materials with artificial cellular structures whose structure and internal architecture has a direct impact on their mechanical and biological behaviour [5].

But the enormous difficulties of designing and forming such complex materials using traditional manufacturing methods has so far prevented their widespread use in engineering applications. Indeed, despite the need for heterogeneous materials (in fields such as thermal and microelectronic technology, filtration, drug release, tissue engineering, and biomaterial fabrication of scaffolds and orthopaedic implants), the digital technologies that support the design and manufacture of these components are only nascent.

While the advances of 3D modelling and manufacturing technologies (CAD/CAM) have been remarkable [6], there are few viable methods for translating digital representations of heterogeneous materials into physical objects with gradients of composition, structure and resulting physical properties. The challenges for bridging the gap between heterogeneous materials modelling and manufacturing involve the following:

1. The manufacturing technology should enable broad digital specifications of the material properties (e.g. porosity) in order to generate materials automatically, without the need for exhaustive specifications of every detail of the geometry or composition involved.
2. Most of the manufacturing processes reported in Chapter 2 involve phase change (i.e. solid to liquid or vice versa, powder to solid, etc). Yet the digital representations describe only the end result; models are clearly required to also support temporal modelling of manufacturing processes.
3. Details of fabrication processes for heterogeneous materials require better modelling to account for physical processing phenomena such as shrinkage, pore geometry deformation, misalignment, cracks, etc.
4. A myriad of features and differing dimensional scales have to be considered when modelling a heterogeneous material. Physically-based material representations (i.e. defining material compositions and distributions within an object) and physically-based property representations (i.e. defining the distributions of physical and mechanical properties within a shape) are pillars for the definition of a geometric complexity. The amount of data required to support many of the heterogeneous material representations present challenges for PC based systems.

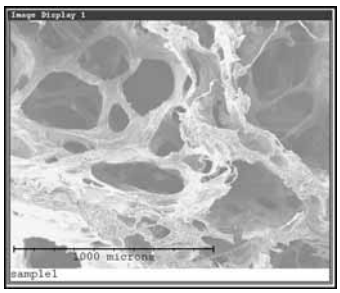

(a) Natural sponge [7]

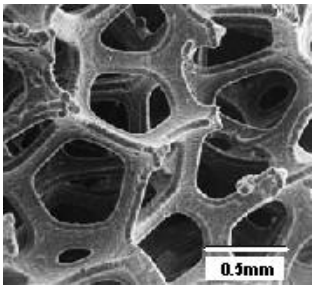

(b) Metallic Foam, (Courtesy ERG Aerospace, USA)

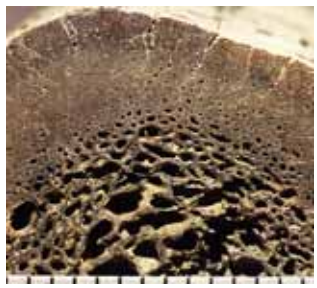

(c) Cross-section of a dinosaur bone (Courtesy Dr A.MacRae, Univ of Calgary, Canada)

Figure 2: Examples of cellular materials

This thesis is primarily concerned with the first of the above problems in the context of cellular structures, although its solution impacts on the other three. More specifically, how a cellular solid can be manufactured in such a way that its final form is digitally controllable for an '*ad-hoc*' application. Such materials could have a variable porosity (Figure 2), where the local properties can be calculated or systematically measured (i.e. instead of using averaged values).

Among the possible methods for manufacturing cellular materials, there are:

1. Growth and mineralisation, processing routes similar to those mineralised tissues found in nature, e.g. bones, teeth, shells, sponges, reef corals, etc.
2. Layered manufacturing: where successive 2D layers of the same or different material are spread on top of each other after a binder or heat has been applied to the binding or curing path. A 3D object is then built layer by layer from the bottom to top.
3. Mould and gel casting: an '*in-situ*' polymerization of monomers that are the setting mechanism for forming a green body or mould that will be used as solidifying pattern for another material. As reported in Chapter 2, this technique is broadly used in the production of bone scaffolds and tissue engineering.
4. Low-pressure injection moulding and extrusion: this manufacturing process originates discontinuities in the bulk of the material due to the provoked sudden decays of pressure. It is of wide use in the fabrication of parts of the automotive industry and also in food technology. Variants to this method are emulsification and phase separation.
5. Particulate leaching: when porogen particles (e.g. salt, granules, etc) are blended with the material and the mixture sintered. Once dissolved and washed out, they leave interconnected pores or channels in the composite structure.

6. Foaming: a reactant liquid can be injected with high pressurised gas during its solidification. When the viscous mixture is depressurised, the gas molecules abandon the viscous polymer, resulting in a sponge like structure. The majority of solid foams are fabricated with this process. Alternatively, for a solid, the reactant can be subjected to a high pressure (inside a chamber) which is gradually restored to atmospheric levels. During this procedure, pores are formed in the solid by the gas filtration into the solid.

Most of these methods have only been used for small-scale production of materials with graded density and have not been put into practice at industrial scale. Of these possible methods, foaming appears to offer the best prospect for a fast, flexible (i.e. generic) approach to manufacture of variable porosity materials. Among the different types of foams and after careful review of the alternatives, polymeric foams were chosen for this research.

1.2 Polymeric foam, a heterogeneous material

A polymeric foam is a particular example of a heterogeneous material, since it is composed of at least two phases, one (or more) solid, plus voids whose size and distribution can be varied.

Polymeric foam materials have demonstrated great application potential in a myriad of fields (biomaterials, tissue engineering, structural mechanics, etc) because of their lightness, low density, chemical inertness, high wear resistance, thermal and acoustic insulation [8]. They can be used to seal, cushion, filter, wick, insulate, absorb impacts or support loads. Playing the role of high-performance structural materials, they can perform and withstand severe environmental conditions, high acceleration and vibration loads, operate under high pressure and have high axial stiffness. This kind of versatility makes foam exceptional as a design material.

Moreover, they have compositional similarities with natural bone and, some of them, a certain level of bioresorbability[1]. Foam core materials offer weight minimisation, potentially improving the patient's tolerance to an orthopaedic implant, which is no longer a heavy piece of solid metal. This foam core implant can be designed with functionally graded porosity to suit the mechanical requirements and tailored to optimally match the

[1] A bioresorbable material is one easily disposable after use, as they are designed to decompose after a certain period of time, when exposed to light, to aerobic or anaerobic processes. In surgery, these materials remove the need for secondary operations after fulfilling their intended purpose, as happens with metal temporary implants.

patient's characteristics. On the other hand, polymeric foams offer the possibility of being blended with ceramic or metal to form polymer-ceramic/metal composites that overcome the disadvantages of a pure polymeric foam artefact (e.g. poor mechanical strength, short-lived nature, rapid degradability, etc).

Graded porosity artefacts would represent a major advance on the multilayer panels or composite structures shown in Figure 3. Figure 3a shows the cross-section of a series of panels containing sound absorbing materials that are often used for vibration and noise control of mechanical and architectural structures [9]. Sandwich-structured composites used in impacts and absorption of vibration also contain one part of foamed core in between two parts of denser material. For these applications, different types of absorbing materials have to be stacked (i.e. glued) in different types of multilayer configurations in order to reach performance specifications. To date, controlled graded porosity (Figure 3b) has been achieved only by the adhesion of different architecture scaffolds that present discontinuities that should be avoided for an optimum functionality when used in tissue engineering.

(a) 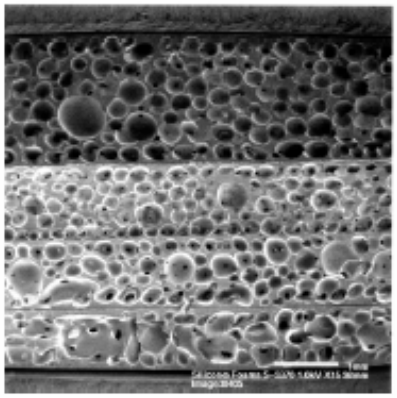 (b) 

Figure 3: Heterogeneous materials with discontinuous boundaries (a) Multilayer panel [10]; (b) Graded porosity prototype [11]

To the author's knowledge, no existing production process enables the additive-free manufacture of foams with continuous porosity gradation. The use of surfactants as well as the presence of boundaries is not acceptable in certain applications of structural materials (e.g. high temperature/pressure vessels) or bio-materials (e.g. *in-vivo* scaffolds, orthopaedic implants). It appears that no suitable porosity tailoring agent that can fulfil the hygienic, chemical and thermal conditions for functionally grading a biomaterial and shape its micro and macro structure at the users' request is available at present. A significant breakthrough innovation would be one that allows the control of density in the final structure without the use of any surfactant or solvent.

1.3 Ultrasound as porosity tailoring agent

Properties of foamed plastics are determined by the properties of the polymer base and the gases filling its cells and by the morphology of its cellular structure. Properties of plastic foams are considerably affected by the polydispersity and inhomogeneity of their structure in the bulk. All these properties greatly depend on the process parameters and the intermediate stages in the fabrication process of foam plastics.

The established ways of altering porosity in polymeric foams, some of which are surveyed in more detail in Chapter 2, are:

1. Heat treatments, when condensation of trapped gas can be controlled.
2. Pressure changes, evacuating gas from the mixture in order to increase density.
3. Chemical additives (i.e. surfactants and catalysts).
4. Physical blowing agents (i.e. pressurised gas).
5. Ultrasound, so far used to degas liquid mixtures.

After review of the options, the porosity-tailoring agent investigated in this study was ultrasound, because other techniques were less successful, convenient and/or practical for experimental purposes.

The advantages of ultrasound versus other potential methods (e.g. layered manufacturing based or lab synthesis with porogen agents) are:

- unlike foaming agents, the apparatus producing ultrasonic irradiation does not need to be in direct contact with the product to be foamed (hygienic and sterilised environments; ideal for the fabrication of implants), being, in principle, a ‘treatment without touching’.
- it is not chemically invasive (there are no coatings or chemical stabilisers to be added in the post-processing) and is also solvent-free.
- biomaterials manufactured using this technology are not likely to encounter legislative difficulties (e.g. toxicity, etc).
- any foam whose forming process involves gas dissolved in a liquid at the initial stage can undergo cavitation due to the ultrasound applied while the nucleation, growth and stabilisation of bubbles in the mixture.
- the working temperature of the foam production process is dictated by the material to be foamed, not by the fabrication process (e.g. manufacturing process).

In conclusion, control of the pore size distribution in the final product is one of the most important aspects in the manufacture of heterogeneous materials. Ultrasound and its interaction with the foaming process of a melted polymer provides a promising starting point for the manufacture of heterogeneous polymeric foams, with controlled porosity and structure customisation by means of ultrasonic irradiation at pre-determined stages of the reaction (Figure 4).

(a) 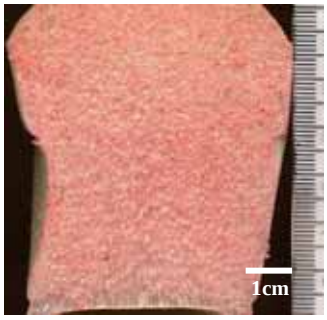

(b) 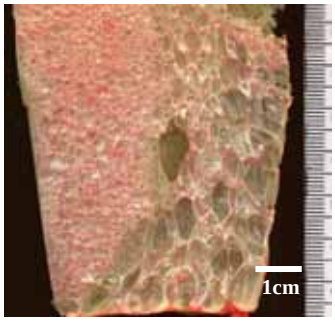

Figure 4: Polymeric foams generated (a) without and (b) with ultrasonic irradiation

1.4 Aims and Objectives

The thesis for this research work states that "**measured application of ultrasound to polymeric melts undergoing foaming can be used to tailor the porosity of the resulting polymeric matrix, and so customising the gradation of porosity**".

In other words, the motivation of this research was to explore a novel technology that could offer the opportunity to fabricate artefacts of a material that contains intrinsic properties tailored for function. This new manufacturing method for heterogeneous cellular materials would allow the design of functionally graded porosity through measured and localised application of ultrasound during the formation process of the material.

The following aims are inherent in this thesis:

1. Establish the relevant theoretical mechanisms (i.e. underlying physics and chemistry) of foamed materials.
2. Establish the feasibility as a manufacture process by setting the boundaries, in particular, for the operating range of the process variables.

A wide range of polymeric materials are suitable for foaming and available in the market. However, polyurethane has been the foam mainly used in this study[2] due to its broad application in both structural and bioengineering fields and its availability from stockists. In particular, polyurethane foam is used in blood-contacting applications (e.g. catheters, heart assistant pumps, etc) due to its stability over long periods of time, tolerability, and good physical and mechanical properties. Polyurethane foams have been proposed for use as a potentially useful matrix for bone-substitute compounds [12], but the porosity-customisation issue (necessary for living cell seeding and attachment, from the biological point of view, and the ability to withstanding external applied loads) is still unresolved.

Therefore, the objectives that this research work pursued are:

1. Verify experimentally the proposed mechanisms of ultrasound as porosity tailoring agent for polyurethane.
2. Establish the feasibility of tailoring the porosity of polyurethane foams through the application of structured acoustic fields.

1.5 Contribution to knowledge

The aim of this work is twofold: to contribute to the knowledge of the basic mechanisms involved in an acoustically influenced foaming process in a polymeric mixture, and to interpret the impact of ultrasound on the structural characteristics of the solidified porous matrix and the different ways in which the ultrasound can interact with the polymeric mixture undergoing foaming.

The suitable manipulation of the position of the foaming polymeric matrix within a controlled sonicated field (i.e. with known acoustic pressure amplitude) permits the tailoring of the bubbles (i.e. cells) to a desired size. In the experiments, polymeric melts were irradiated with ultrasound of variable intensity at critical points during the foaming process. These bubbles solidified, leading to a porous material with an engineered cellular structure. This was achieved through a precisely measured and localised application of ultrasound. The porosity distribution was also studied using a specially written MatLab™ application for assessing the graded porosity of these heterogeneous materials.

[2] Other foams, such as PDMSs, are examples for application of porosity gradation in Chapter 5, where results on porosity tailoring are presented and discussed in Chapter 6. These examples have been extracted from the report that summarises the most relevant findings for the feasibility study produced in 2006 for AWE plc.

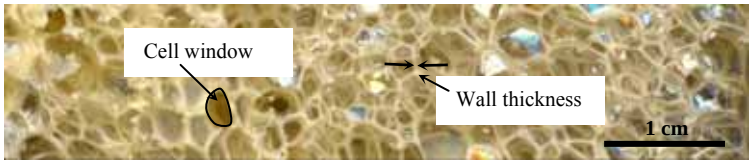

Figure 5: Polymeric foam irradiated from right hand-side

The structure of a foam is characterised by the size and wall thickness of cells in the bulk material (Figure 5, note the variation in wall thickness from right to left). These features are the result of many factors (e.g. temperature, pressure, reactants concentrations, etc) several of which can be affected by ultrasonic irradiation. The preparation procedures of these foams are presented in Chapter 4, and Chapter 5 presents the results, where direct correlations between porosity and sonication conditions can be seen.

It was found that bubble enlargement only occurred when melts undergoing foaming were irradiated within a distinct range of acoustic pressures. Lower magnitudes of sound applied to the liquid mixture had no visible effect on the cellular structure, and values above the operational range provoked degassing of the melt and, to a large extent, collapsed the growing foam (i.e. side effects of 'transient cavitation' effects, when bubbles grew rapidly to a non-equilibrium size and then imploded, provoking polymeric cellular collapse through the breaking of polymer chains). For this work, *selective* foam growth was the goal, so experimental conditions were controlled in such a way that the acoustic intensity fell between the lower and the upper threshold.

Within a range of acoustic pressures that favoured stable pulsation for the bubbles in the polymeric matrix, and for a fixed value of frequency, the porosity of the samples was found to increase with the amplitude of the signal. It was also observed that pore size increased with frequency and the average amount of gas contained in the bubble during the reaction increased proportionally to the frequency of the ultrasonic signal applied: a higher pulsation rate resulted in more rectified mass transfer per ultrasonic cycle.

However, there were also matrix homogenization effects observed near the transition from 'stable' to 'transient cavitation' where the magnitude of the acoustic field was sufficient to make changes to bubble size but not to cause coalescence.

The high values for porosity, when stable cavitation was established, were caused by the formation of larger pores when the mixture was still a *quasi*-liquid. Under normal (i.e. non irradiating) conditions, during the cross-linking of the monomers, a 'diffusion controlled

growth' mechanism (i.e. exchange of gas/vapour from bubble to bubble) evolved with the increase of viscosity into a 'stress controlled growth' until large viscosity values limited further enlargement. It is believed that, when the irradiation took place during the 'sensitive' phases of the reaction, acoustic pulsation enhanced the diffusion of gas and/or vapour into the bubbles from the matrix. Furthermore, it maintained lower values of viscosity for longer periods of time, hence delaying the viscoelastic stresses that could suppress the stretching motion in the latter stages of foam formation. In this way, ultrasonic irradiation is thought to sustain the flexibility of the cavities' walls and so decreased the probability of collapsing events within the neighbourhood of bubbles. During the final stages of the reaction, growth was halted by the rigidity of the cavities' walls and ultrasound shown no effect if applied at these latter stages.

The conclusion of the research is that there is a strong correlation between acoustic power and pore size distribution in the final solidified foam. Consequently, this study has allowed an understanding of the interaction between ultrasound and a foaming process to be developed. Therefore, the consequences of a particular pattern and strength of irradiation can be assessed by the measurement of the porosity. This information, when fed-back to the system, results in a more accurate tailoring for porosity gradation.

Foam irradiation in an ultrasonic field has proved itself to be an effective means to modify and control the pore size distribution in a final porous foam. This new polymer manufacturing technology would be particularly useful in biomimetics applications where biological micro-structures require inhomogeneous cross-sections to achieve particular functional, or structural, properties. The ability to control porosity would enable a variety of biomedical applications, ranging from the development of cell scaffolds to improved filtration, and drug release devices.

1.6 Thesis structure

This thesis is presented in eight chapters, the contents of which are briefly described below:

Chapter 1 is a brief introduction to the concept of heterogeneous materials. The objectives of the work are identified and a description of the claimed contribution to knowledge resulting from this research is given. In Chapter 2, the literature review assesses the 'state-of-the-art' in the manufacturing of heterogeneous materials, introduces some aspects of sonication as porosity-tailoring agent for polymeric foams along with a brief description of the cavitation phenomenon. Chapter 3 introduces the experimental hypothesis and outlines

chemical and ultrasonic principles underlying the sonicating process described. The methodology used is presented in Chapter 4, which details the experimental procedure, its success and limitations, before Chapter 5 presents the results. Chapter 6 discusses the wider significance of the findings before some conclusions are drawn. Chapter 7 summarises the main results of the research work with reference to the objectives presented in Chapter 1. Finally, in Chapter 8 some comments and suggestions for future work are made.

CHAPTER 2. LITERATURE REVIEW

Researchers across a wide spectrum of applications (e.g. biology, biomaterial and material science, rapid prototyping, chemical and mechanical engineering, etc) have reported various methods for the manufacture of a group of advanced materials that can be broadly classified as 'heterogeneous materials'. This chapter provides an overview of the diverse origins of these materials and the manufacturing methods used to create them. The survey identifies cellular materials as having particular promise but draws attention to the fact that they currently lack the flexible manufacturing processes. In support of the thesis identified in Chapter 1, the later sections of this chapter also review cellular polymeric foams and ultrasound effects and applications.

This review is divided into two main subjects: 1. manufacturing of heterogeneous materials, purposely including polymeric foams, and 2. sonication effects of ultrasound. As the motivation for this work is the manufacturing of polymeric cellular structures with engineered porosity by sonication, this review considers in more detail the emerging field of fabrication of heterogeneous materials. After the assessment of the 'state-of-the-art' in heterogeneous materials and the manufacturing routes that have been reported recently, the potential porosity-tailoring agent, ultrasound, is also reviewed along with other applications for which it is used, in order to set the context. The survey continues with ultrasonically induced processing of polymeric foams and the effects that ultrasound has been shown to have on the bubble dynamics. Scientific study would not be possible without an adequate method to measure, analyse, assess and compare porosity and porosity distribution within the cellular structure of the sonicated polymeric foams produced in this work. The methods appearing in the literature for determining porosity in cellular architectures are surveyed in the final section of this chapter. The navigation chart offered in Figure 6 illustrates the structure of chapter 2. At the end, a brief discussion pulls together all the topics covered and refocuses the argument on porosity tailoring of polymeric foams with ultrasound.

2.1 Heterogeneous materials

Heterogeneous components can be made of a single material with varying structure (e.g. porosity) or multiple materials whose proportions change throughout the body. Frequently, these mixtures demonstrate dramatic synergy, with the overall performance of components being far greater than a straightforward mix of the individual constituents. Such types of materials offer great promise in fields where a high mechanical performance or active functionality (i.e. functional materials) is required (e.g. bio-engineering, aerospace) and

they offer the possibility of substances that can be blended, mixed, shaped or assembled to form optimum components.

The motivation for the production of these distinct classes of heterogeneous materials arises from differing applications:

- Functionally Graded Materials (FGM) [13] are commonly used to join two different materials without stress concentration at their interface. Designers aim to define such gradations in properties from one portion to another by determining an appropriate material composition at every point in the body. For example, [14] describes a 'two graded' FGM formed from a copper-nickel mix that was to be fabricated to optimize properties that neither metal could offer individually.

- Composite Materials consist of one, or more, discontinuous phases, distributed throughout one continuous phase. The continuous phase, the matrix, is in many cases resin, ceramic or metal. The discontinuous phase, called reinforcement or inclusion, may be fibres, particles or voids. Reinforcement is used to improve certain properties of matrices, such as stiffness, behaviour with temperature and resistance to abrasion. [15] cites the example of a two-constituent metal/ceramic composite which is engineered to cope with different extremes of temperature at either end (hot and cold).

- Engineered Microstructures are small in comparison with the overall dimensions of the component (e.g. foams or other cellular structures). The effective properties of these materials are determined by the topology of their cells and the properties of the constituents. An important group of these are the so-called periodic microstructures, which are described by their base cells, which are the smallest repetitive unit of material and generally comprises of a material phase and a void phase [16].

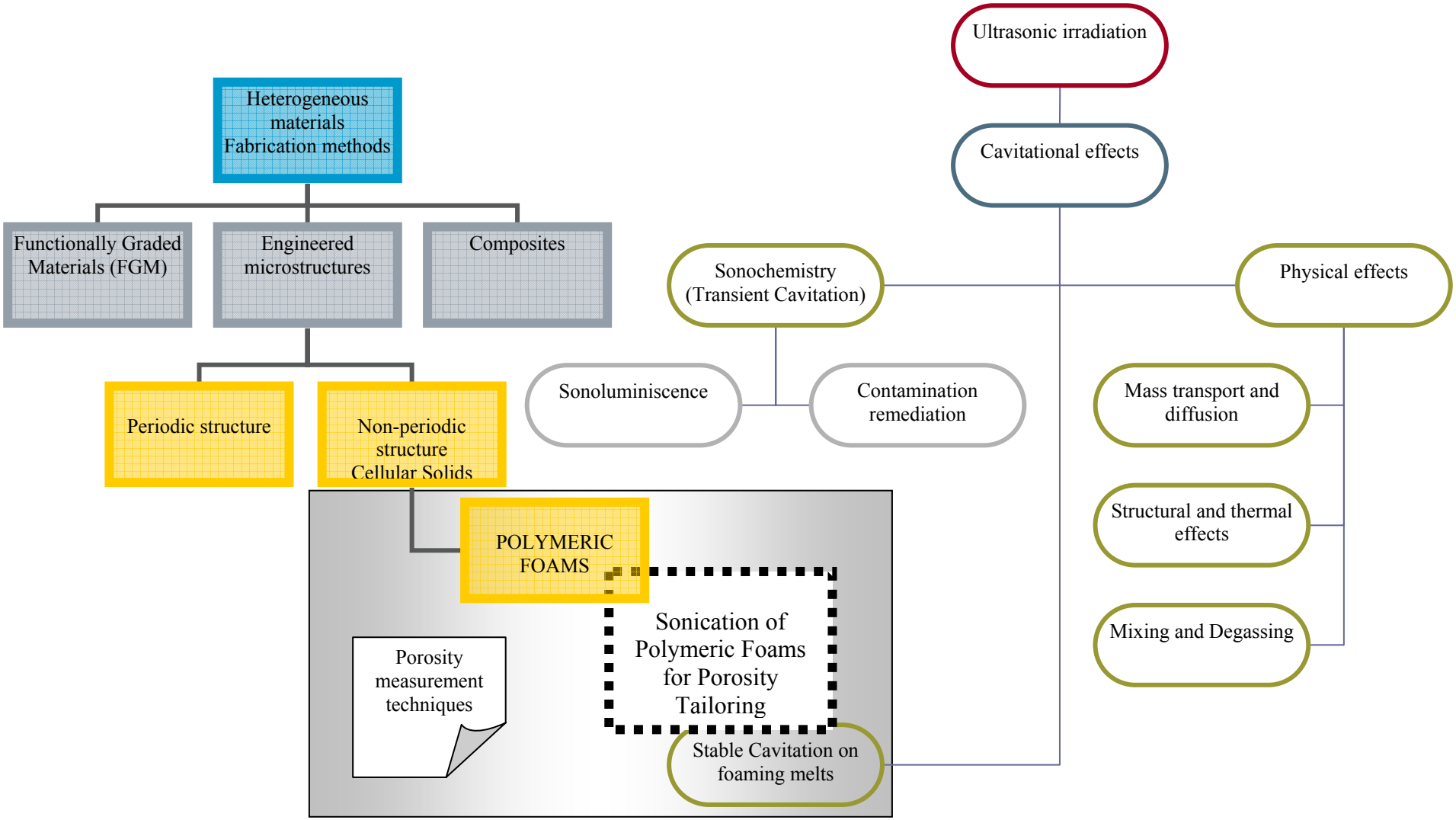

Figure 6: Literature survey navigation chart

2.2 Manufacturing Methods for Heterogeneous Materials

This section reviews manufacturing processes for heterogeneous materials. In order to provide a broad overview of these technologies, both automated and manual, manufacturing processes are reported across a wide variety of disciplines and application domains. The following sections group these methods by the class of material they are able to generate (i.e. FGMs, Composites, Microstructures).

2.2.1 Methods for fabrication of FGMs

Of all the heterogeneous materials proposed, FGMs have the largest range of viable manufacturing technologies already established or demonstrated. Nearly all of these arise from powder-based **Layered Manufacturing (LM)** systems developed to support Rapid Prototyping techniques (RP). Heterogeneous solid modelling has been increasingly gaining the attention of researchers in the last five years, but it is important to point out that the heterogeneous object fabrication capability is not widespread in current LM systems [17]. Here, the methods for fabrication of FGMs are classified into three groups, depending on the mechanism used for the powder to become a solid:

1. Solidification. Raw material (i.e. powder or resin) is spread and then fused through melting or chemical reaction
2. Deposition. Powder or plastic is melted as/during its deposition.
3. Binding. Powder is glued

Solidification and deposition are suitable for metals, ceramics and polymers. Binding is only used, so far, for ceramic and polymers, although research is ongoing in this area.

Essential LM systems are used to fabricate FGMs and other multi-material objects by selectively depositing various materials in a point-wise fashion under computer control [17]. The common feature for all of them is that the manufacturing process requires a nozzle (i.e. "tool") path and a specification of deposition mix at every point. These systems allow *direct fabrication*, without tooling, fixturing and other peripheral activities so making it possible to go from a computer-aided design (CAD) model to the physical object in a short time. The part geometry is typically decomposed into an intermediate representation (e.g. layers) prior to fabrication. Then, the information is fed to a computer which drives the tool that will manufacture the object after successively stacking up all the layers.

2.2.1.1 *Solidification*

Selective Laser Sintering (SLS) is a layer-by-layer manufacturing technique. The basic material consists of powder with particle sizes of the order of magnitude of 0.1-100 μm. Successive powder layers are deposited on top of each other. After deposition, a computer controlled CO_2 laser beam scans the surface and selectively binds together the powder particles of the corresponding cross section of the product. During laser exposure, the powder temperature rises above the glass transition point after which adjacent particles melt together. This process is called 'Sintering', and polymers, ceramic, metals and composites are all susceptible to sintering [18]. The representation method that precedes the fabrication is based on gradients and the information is stored in functions that can be evaluated when necessary during the fabrication process. Using this approach, Steidle et al. [19] demonstrated the fabrication of bioceramic-polymer composite implants, consisting of hydroxyapatite particles bonded together by a calcium phosphate glass phase. In principle, SLS machines should be able to form heterogeneous material by laying down mixes of powders. However, the difficulty of doing this in systems that are designed to 'roll-out' uniform layers of material means that, in practice, this is rarely done [20]. It is difficult to vary the composition of the powdered working layer, but it is relatively easy to vary the beam power applied during the sintering process. Consequently, SLS-based processes generally create components whose microstructure is varied by selective heat treatment [21].

Direct Light Projection (DLP) is a variant of stereolithography **(SLA)**. Starting from a 3D image, a part is built slice-by-slice from bottom to top, in a vessel of liquid resin/ceramic slurries that hardens when exposed to a laser beam. In particular, DLP uses a dynamic mask and visible light to expose photosensitive resins and provoke photopolymerisation [22]. Woesz et al.[23] have fabricated polymeric multiscale structures using a commercial system ('Perfactory®' from Envisiontec®). These structures can be used as casting moulds in a myriad of applications. With a resolution of 32μm, they achieved wall thicknesses down to 50 μm with vertical build speed of 15-20mm/h, which is slower than the build time of an SLS process for the same sample (4h in DLP vs 2.5h in SLS). The main advantages of the DLP machine are its significantly better feature resolution than SLS and its cheaper price. Water soluble photocurable moulds can be shaped with this technique and it is more suitable for moulding temperature sensitive materials (e.g. composites), in contrast to conventional moulds, which need to be removed by thermal decomposition. However, the limited dimensions of the build volume and slower speed are still the main drawbacks when compared to SLS.

Not every solidification-based approach to heterogeneous material manufacture involves lasers. Pompe et al. [24] presented an example of manufacturing FGM-biomaterials through **compression moulding** (essentially as a non-laser based sintering application). Artificial biomaterials were developed by building a graded structure consisting of ultra-high molecular weight polyethylene with a gradient in molecular weight. The manufacturing of this graded polyethylene composite material was executed in a cylindrical mould by a cycle of compression/decompression and temperatures variation. The flexibility of this manufacturing process provides freedom for the designer in terms of the optimisation of pressure and temperature cycle for each component configuration. The resulting cylindrical billet of material could be subjected to further manufacturing operations (e.g. milling or turning) to generate the final component.

2.2.1.2 *Deposition*

Although controlling the mix of powder within layers is difficult, precisely varying the composition of drops of molten material being deposited to form a solid is relatively easy. Consequently, several variations on the basic deposition process have been invented specifically for heterogeneous materials. For example, **Direct Metal Deposition** is versatile, but only feasible in low volume manufacturing case studies because the parts produced have no visible material resolution (i.e. no stratification or layers are only visible in the micro-structure). This is essentially a laser cladding process which consists of metal powder melted and deposited in a layer (approx. 0.025 cm thick) using a laser beam on a substrate. The fabrication of metal alloys, functionally graded material Cu-Ni, manufactured by DMD is also referred by Shin et al.[14].

Solidscape® Inc [25] has created a T6*x* Benchtop® model maker whose so called 'drop-by-drop' technology permits accuracy of 10^{-3} of an inch per inch in three dimensions. There are two nozzles depositing material, one is the molten material, the other is the sacrificial support material for the model and can be dissolved away after the model is finished. The feature resolution is better than in SLS, but slightly inferior compared to DLP. The main drawback of these model makers is the slow build speed (0.5-2.5mm/h vertical build speed) and the high risk of "sink marks" or holes in the final product if build parameters are not chosen accurately [23].

Laser Engineering Net Shaping (LENS®) [26] is a laser-based LM process commercialised under the trademark DMDS™ (Direct Metal Deposition System) and it is perhaps the most advanced form of commercial additive layer technique used to fabricate

fully dense metal parts directly from three-dimensional CAD data. Instead of bonding material in a bed of powder, as SLS does, the powder is delivered in a gas jet through nozzles that instantaneously melts it by the simultaneous application of the laser beam. The solid surface formed by solidification promotes layer to layer adhesion for the next step of the building up process. The LENS® approach to near-net-shape component fabrication is derived from the approach used by Rapid Prototyping processes to create plastic prototypes and casting patterns from STL files. The critical feature that distinguishes LENS® from any other RP processes is that it can make components out of structural metals directly, and thus can be used not only as a RP fabrication process for near-net-shaped prototypes but also as a manufacturing process for production of quality metal parts and injection mould tooling.

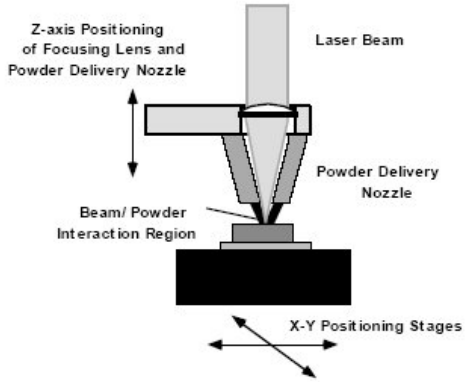

Figure 7: LENS® device, as appeared in [26]

Fused Deposition (FD) process (also known as **SDM, Shape Deposition Manufacturing**) can create FGM artefacts, (e.g. an injection-moulding tool, composed of three different materials to withstand mechanical, thermal and chemical requirements [27]) combining additive and removal processes.

Another illustrative example of FGM fabrication by SDM is the metal-ceramic alloy, referred in Shin et al.[14], which is the constituent material of the walls of a pressure vessel. The motivation for developing this material arises from the conditions pressure vessels endure during their life; high temperature/pressure conditions on the inside, while the outer surface is under ambient conditions. The solution developed is the fabrication of a ceramic-metal FGM: ceramic layer on the inner surface of the pressure vessel due to its high temperature properties, and a metal away from the inner surface owing to its good mechanical properties. If these two materials were joined abruptly a high stress would occur at the interface, provoking brittle facture of the hard metal (or ductile facture of the soft material). In practice the proportion of the metal needs to be gradually increased in a controlled manner starting from zero at the inner surface to unity at the outer. The authors demonstrate that the SDM process allows the manufacturing of such a metal-ceramic piece.

Fessler et al. [27, 28] also worked on SDM focusing on laser deposition systems in order to fabricate functionally graded metals using powder mixing. The main improvement of SDM versus other SFF techniques is that parts are decomposed into 3D layers -2.5D typically for SFF- with an arbitrary thickness and need not be planar. However, the problem still remains in the subtraction step, which causes 'stepping' in the final object.

More recently, SDM has been taken into the biomimetic field with the fabrication of artificial bone [29] where osteo-induction (i.e. cell growth in implanted scaffold) was overcome with the inclusion of interconnective micropores that favour bioactivity and broaden the artefact functionality.

Multi-nozzle Deposition Manufacturing (MDM) is a variant of SDM recently developed by Yan et al.[30]. The system consists of a four-nozzle arrangement designed to carry out a layer-by-layer process. By juggling with single-nozzle, bi-nozzle and tri-nozzle deposition processes, ceramic scaffolds with different properties can be created (an improvement on the previous SDM system). Yan et al.'s discussion reveals that the bone scaffolds made by the single-nozzle deposition process in the MDM system are the most suitable type for implantation to repair bone segment defects. The authors report that parts created by single nozzle systems appeared to have the slowest degradation/re-absorption rates and offered good compatibility and conductive properties. These results again reveal the difficulty of coordinating several nozzles to effectively deposit and fuse materials correctly.

Polymers are also suitable for FD techniques. Rodriguez et al. [31] optimized the design of acrylonitrile-butadiene-styrene components for anisotropic stiffness and strength through an FD method where unidirectional extrusion provoked an aligned functional graded configuration with directional mechanical properties.

Precision extruding deposition (PED) is presented in [32] as an improvement on previously reported Fused Deposition Manufacture (FDM) schemes that are used for metals and composites. The major difference with conventional FDM is related to the direct deposition of material without the need of pre-preparation in a filament form prior to deposition, as this is directly done in pellets of material to build the scaffold architecture. This allows higher manufacture precision, so mechanical properties can be studied in direct correlation to the degree of anisotropy, deposition and orientation layout pattern, and overall porosity for further structure optimisation.

Even though all the powder-based methods are “repeatable” (i.e. given the same powder mix and heating they will produce the same material), the material properties of the resulting component are not necessary predictable. Designing a particular FGM is still essentially a trial-and-error process.

2.2.1.3 *Binding- 3D Printing (3DP)*

3DP can also create graded artefacts using a technique in which mixtures of materials with diverse characteristics (polymers, ceramic, metals and polymer/ceramic powders) are, in principle, controllable. Among the LM processes, 3DP is particularly well-suited to the fabrication of parts with **Local Composition Control (LCC)** [33]. Commercial 3D printers create parts by spreading powder, and then use an ink-jet printer head to deposit a binder material into the powder bed and so define the component in a similar process to a 2D colour ink-jet printing. The resolution of the composition control is of the order 50-100μm. Such local composition control has demonstrated the printing of ceramic parts with local toughening. The information flow for LCC with 3DP is composed of Geometric Design, Material Design, Post-Processing and Fabrication.

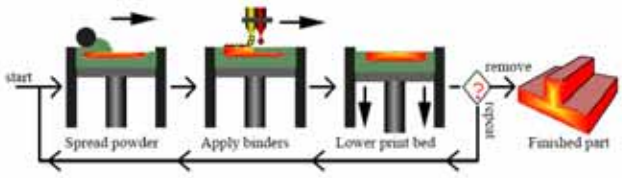

Figure 8: 3DP scheme process, by Jackson et al. [33]

Jackson et al. [33] employed a 3D printer for fabricating heterogeneous objects in a ‘Drop-by-drop’ (DoD) manner. However, Jackson [34] observed, in a deeper analysis of the system, the limitations of this technique, which applied an ‘on/off’ mode, as well as the partial mixing of materials in the cartridge prior to printing. With these methods for varying the output, it was possible to fabricate an item with high precision where heterogeneous objects are represented as blurred material distributions varying from point to point like a printing bitmap. Consequently, the link between CAD system and LM machines becomes weak and limits this technique. In addition, the lack of speed in the overhead cartridge (1.2m/s and 40kHz frequency of the available droplets leads to a minimum distance between droplets of 30μm) and the difficulty of controlling very small quantities of applied binder (binder droplets are of the scale ≈100μm) prevent this technique to be used at micro or nano level.

Closely related to Jackson's work, an improvement in digital half-toning was proposed by Wu et al [35] in an attempt to address a possible solution to partitioning a continuous material. Modifications to a standard half-toning algorithm were defined in order to consider the anisotropic voxels and uncertainties in droplet placement. This can optimally minimise the occurrence of blurred, out of focus textures and execute minimum run-lengths, so the blur effect in the Z-direction will be eliminated. But one of the main contributions to solve the material-to-material transition in DoD printing technology has been offered by Siu and Tan [36] with their definition of the "grading source", which gathers the type of grading, the position of grading, and the materials grading function in order to control and represent material transitions, as well as defines the transition between different grading sources. The definition of the material grading function inside every point is important, so an algorithm that subdivides each slice of a heterogeneous object into a list of multi-material contours according to the grading functions of different grading sources is defined. Three grading regions are defined to generate contours as the sum of the contours generated, and each contour has its own defining material composition array. The structure is generated to extract the material composition of the contours in each slice. Applying this at intersections and overlapping regions, a new contour is generated and three new regions are defined. In addition, three new sub-contours are regenerated, and so on. This makes it possible to identify different regions in the designed object and slice the item to be prototyped, improving in this way texture, surface finishing and avoiding abrupt transitions of materials, prone to mechanical failure.

The impact of surface finish of heterogeneous parts is an intrinsic limitation of powder-based processing. Lanzetta and Sachs [2] noticed that surface finish in 3D printed parts can be greatly improved by using very fine powders (1-50 μm). Spreading particles in the range of 1-10μm is complex due to their tiny size. These powders cannot be spread dry. A way of overcoming the problem was to adapt a wet pre-treatment of the raw material. They used commercial 3D DoD printers to produce their artefacts and demonstrated the enhancement in surface finishing. Other authors [37] have already tested potential biocompatible materials (e.g. natural polymers and water-based binders) as deposition materials with the intention to fabricate scaffolds suitable for implantation. Although 3D printing appears to be a feasible manufacturing technique, post-processing is still a crucial requirement for the manufactured object in order to provide better mechanical properties (i.e. printed powers are intrinsically of a brittle nature) and reduce the water uptake tendency. Porosity distribution is not controllable because the DoD deposition of material leaves voids causing the overall artefact to shrinkage in later stages.

Although powder based LM appears to be an extremely flexible technique, in practice the number of polymeric materials that can be used as raw materials is limited by the manufacturing processes. For example, in Fused Deposition Manufacturing and Selective Laser Sintering, only thermoplastics and a limited range of metals and ceramics can be used; 3D Printing techniques require solvents and binders. Powder based LM also requires explicit multifaceted manufacturing instructions to be generated that contain implicit corrections for anisotropic shrinkage during fabrication. The use of machines with multiple degrees of freedom (e.g. deposit non-planar slices) [38] and layer orientation [39] are aspects likely to make the LM process a more attractive alternative in the future because of the limited surface accuracy and the long build times that are required at present, in many cases due to the deposition of a sacrificial support structure.

2.2.1.4 *Hybrid methods for heterogeneous objects manufacture*

Some researchers have combined LM with other methods in order to overcome the above limitations and produce more accurate techniques and/or improve the characteristics of the resulting item. In conventional LM fabrication techniques, when a 2D object is manufactured, the only way of varying the density is by altering the thickness of layers. However, 3D heterogeneous objects can be enabled by the combination of different manufacturing techniques. For example, traditional Stereolithography (SLA) can be mixed with other manufacturing processes in the creation of structural components with complex composite microstructures [40]. A component with an inner skeleton –or microstructure– is arranged to maximise the stiffness-to-weight ratio. The process consists of ceramic processing around an SLA pattern, pattern removal and metal casting. At present, this process is limited because only one constitutive material is employed, but the long-term goal is a heterogeneous fabrication with two materials (either, two solids or one solid plus void) to create a functional gradient within the microstructure and so allow a single property to be optimised with respect to weight.

Another example of a hybrid manufacturing method is the indirect LM manufacturing approach, where the part is used as a mould to cast the final product. Examples of 3D Printing used along with conventional methods can be found in [41] and [42]. Through LM, the 3D part is produced and then post-processed (e.g. cleaning, curing, finishing) to yield the final mould. This mould will cast the definitive part. 3D Printing is a versatile technique and can be also used together with solvent casting. Using this technique a polymeric-ceramic composite [41] can be created to get graded mechanical stiffness. Polymer provides toughness and plasticity; the ceramic phase adds high strength. This type of composite is

suitable for use as a bio-component. These are applications where the variables are stricter than in non-medical environment. The main advantage is that the technique also provides tools to enhance control over cell differentiation which allows researchers to develop the reconstruction of multi-tissue organs, tissue interfaces, bone, cartilage, tendon, ligament and muscle.

Stereolithography has also been paired to a low-pressure injection moulding process which has shown to be a successful solution for ceramic microcomponents, non-necessarily porous. Knitter et al. [43] cite advantages as low cost, flexibility for design modifications and a rapid processing with the high precision required in microengineering and electronics. On the other hand, it has evident problems with the scale-up, since bigger parts or large series cannot be sintered under the same advantageous conditions.

2.2.2 Methods for fabrication of Composites

The main characteristic of a composite is the existence of a continuous phase and a discontinuous one, which can be a single material or several. Polymer composites formed by polymer-polymer and polymer-ceramic mixtures are widely used for industrial purposes. In particular, biocomposites (i.e. ceramic-polymer) are acquiring more importance in biomedical applications. Bioceramics are widely known in the field of bone repair and are preferred materials for bone grafts because of their low density, chemical inertness, high wear resistance, excellent tissue adherence and compositional similarities with natural bone. However, ceramics are inherently brittle and exhibit poor mechanical strength, so a blending with a plastic can mitigate the disadvantages and become a material perfectly suitable for human implantation.

The most common process for fabrication of composites is **polymer reinforced by polymer**. The continuous phase, the matrix, which is normally a resin, a ceramic or a metal, is reinforced by a discontinuous phase in the form of inclusions, fibres, particles, or even voids. Heterogeneous composites can also be ones that are manufactured with a special control over crystallization and internal structure control. One particular interesting approach to composite manufacture is described by Loos et al. [44], who reported an investigation of polyethylene-fibre reinforcing polyethylene, where polyethylene fibres act as nucleation centres for the high density polyethylene matrix. This provides the sample with directional mechanical properties and controlled behaviour along different axes. Reinforcing a common polyethylene with polyethylene fibres by hot pressing leads to a strong and stiff single polymer composite. It has the intriguing property that it is a

homogeneous material in the number of constituents, but heterogeneous in its physical characteristics.

Mikos et al. [45, 46] have reported a **solvent casting aided by particulate leaching** techniques with the objective of manufacturing porous biodegradable polymer conduits and malleable substrates for guided tissue regeneration, particularly interesting in those cases where a tubular conformation is required. The extruded tubular polymer/salt composite is manufactured by solvent casting, compression and a salt leaching process. For these polymer composites, the pore morphology is affected by the weight percent of salt crystals in the solution. Nevertheless, a drawback of this method is the difficulty of automation, because it requires hand finishing.

Hot pressing [47] has been used to sinter a ceramic-polymer composite material prepared from poly-L-lactic acid acting as a matrix reinforced by hydroxyapatite fibres. Mechanical and in-vivo analysis demonstrated successful application of these materials as temporary bone fixation. This simple but efficient solution enables the preparation of specimens with specific mechanic and chemical conditions.

It is interesting to note that manual manufacture processes are common in composite production, and further research is needed to achieve the same level of automation, accuracy and control that are available for FGMs or engineered micro-structured materials.

2.2.3 Methods for fabrication of heterogeneous materials with Engineered Structures

This section reviews the available technologies for manufacturing materials with internal microstructures. These substances contain internal frameworks whose mechanical properties can be characterised and controlled by a wide range of variables. The applications are widely researched in aerospace, where components with outstanding mechanical and chemical properties are needed, automotive manufacturing and medical devices. This is down to the material's potential to produce lightweight structures, with an optimum weight-to-load ratio, inert nature and diversity in materials to use in the manufacture of final objects. Engineered structures are frequently required in biomaterials manufacturing, e.g. drug delivery, tissue engineering, permanent orthopaedic implants.

The approaches presented here to the fabrication of heterogeneous materials with engineered structures can be broadly categorised into two groups: Derivative Layered Manufacturing and Foaming processes.

2.2.3.1 *Derivative Layered Manufacturing*

Several LM fabrication methods have been developed or adapted to support the generation of heterogeneous materials with engineered microstructure. For instance, fused deposition processing has been reported that produce 3D interconnected composite scaffolds with controlled porosity [11]. The researchers' goal was to develop biocompatible polymer-ceramic composites by homogeneous mixing of tricalcium phosphate (TCP) in Polypropylene (PP), and then to fabricate and characterise porous TCP-PP composite scaffolds for bone graft applications. These were fabricated by a single screw extruder followed by fused deposition. 3D interconnected porous TCP-PP composite scaffolds were fabricated for physical, mechanical and biological property evaluation. The prototype is a "3D honeycomb"-shape with a complex internal architecture where the pore geometry varied from centre to the periphery (Figure 3b). The resulting structure was spiral because rods in each successive layer were made to rotate by a 15° angle (keeping other parameters constant for all the layers). This technique offers many advantages because of its high flexibility in synthesizing strong, biocompatible, bio-resorbable components, depending on the choice of materials. Pore size and pore volume can be varied in an '*ad-hoc*' manner, which has definitive repercussions on the mechanical aspects of the item. The drawback comes with the impossibility to create a one-unit continuous scaffold with graded porosity throughout. The way porosity was varied in this case was by connection of disk-shape struts with different porosity with abrupt discontinuities between disks.

For biomaterials production, even living cells or other bioactive components (e.g. dispersed in hydrogel) can be built up into 3D scaffolds. The so called 'Bioplotter', by EnvisionTec™ [22], dispenses a plotting material into a medium to cause solidification and to compensate gravity force through buoyancy. When handling tissues, conditions become more demanding in terms of environmental conditions and the milli-micro scale used. Moisturising, hygiene and temperature are restrictive variables.

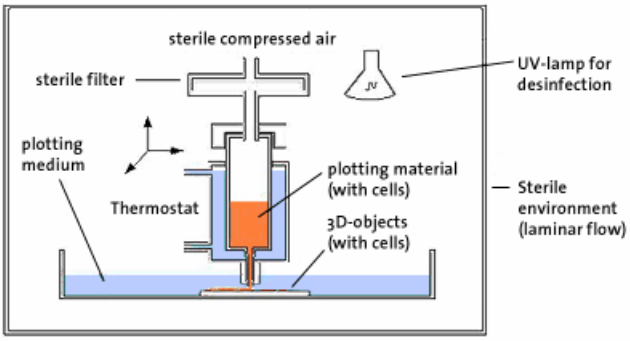

Figure 9: Bioplotter™ principle, as explained in [22]

The advantage of this approach is that sacrificial structures are not needed to be built in because collapsing is prevented by the plotting medium. Solidification of the material during plotting is only caused by the expected mechanism (i.e. precipitation, phase transition or chemical reaction).

Also for biomaterials production, a hybrid LM process has been created for casting objects with internal scaffolds that formed porous architectures. This technique combines LM and a traditional fabrication method (i.e. sponge scaffold) to create a material suitable for use as bone replacement [48]. Taboas [41] developed methods for casting scaffolds which demonstrated control over global (i.e. bulk) and local pore size and 2D orientation. It was also shown that control over global pore architecture requires automation. LM scaffold manufacturing methods offer excellent control over external shape and internal pore interconnectivity and geometry. However, the authors state that it offers limited micro-scale resolution.

Likewise, gelcasting is a 'near-net-shape' forming method that, used in combination with LM techniques has also been proved to be a viable process for production of engineered microstructures [23]. From a liquid or plastic state, shaping happens after reaching the gelation point. Ceramic or polymeric powders are dispersed within a precursor that hardens in a mould that has been created using any of the LM techniques already presented for engineered microstructures. This technique offers a possible fabrication method for porous ceramics, or ceramic foams at a low price and high accuracy in porous size and location of the channels without the large shrinkage level typically suffered in the pieces fabricated without supportive mould. However, one foreseeable drawback comes from processing time, which is very high.

2.2.3.2 *Foaming processes*

Foams constitute a good example of a heterogeneous material with a microstructure that could be engineered '*ad-hoc*', since almost any material (e.g. metals, pure polymer and polymer-based ceramic) can, under suitable conditions, be foamed. Reticulated materials have been increasingly used in many applications and for structural purposes such as: metal foams in automotive industry and aerospace; ceramic foams, in processes where fluid transportation in the microstructure is required (e.g. molten metal filtration, hot gas filtration, catalysis supports, etc); polymeric foams, in thermal, acoustic insulation, filtration, cushioning, packaging, absorbing the kinetic energy from impacts, etc. Their uses

exploit the unique combination of properties derived from the purposely controlled distribution of voids in the material.

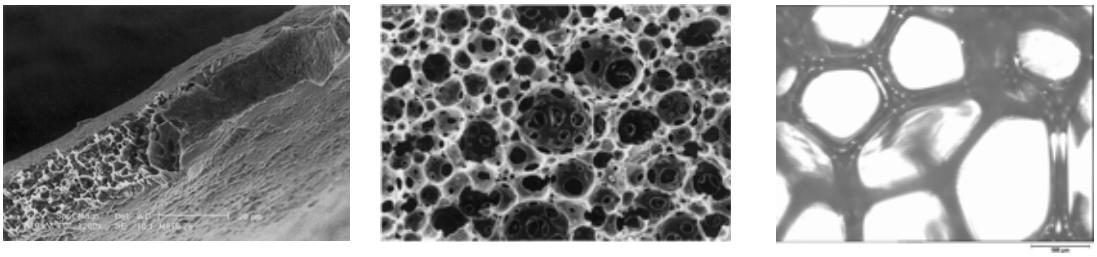

(a) (b) (c)

Figure 10: SEM images of: (a) Metallic foam, in [49]; (b) Ceramic foam, in [50]; (c) Polymeric foam, by the author

The process routes used to create metallic, ceramic and polymeric foams are similar to a certain extent. For the ceramic materials, foam production processes are traditionally classified into three main types. The most frequently used method for engineering structural foams is the patented 'Schwartzwalder and Somers' [51], **'Replica Processing'** method. This technique uses a foamed polymer as a pre-form for the ceramic porous material. The polymeric foam is dipped into slurry containing an appropriate binder and ceramic phases. The soaked polymer is then sintered without increasing pressure conditions at elevated temperatures. When the polymer decomposes, a ceramic green body is obtained with similar porous structure to the pre-form polymer. The 'replica process' produces ceramic foam with open-cells, which is ideal for biomedical applications due to the open channels where flow can be induced, but has the drawback that pyrolysis of the polymer skeleton in many cases produces flaws or leaves residues in the cellular ceramic. In addition, because of the need for a pre-form, some dimensional shrinkage will occur during fabrication. This problem was addressed by Nangrejo and Edirisinghe [52] who prepared silicon carbide foams using polyurethane foam as the pre-ceramic mould, and studied the effect of varying the concentration of pre-form solution content in order to reduce the shrinkage effect observed after decomposition of the polymer. Another example of this technique for the preparation of ceramic TiO_2 foams can be found in [53].

The **'placeholder technique'** shares the principle of the replica method, but does not need a sacrificial framework. Rather, it consists of co-dispersing a ceramic powder with an easily burnable second phase, forming a green body, burning out the second phase and sintering the body. Van Tienen et al. [54] present an example of the fabrication of porous ceramic using the 'placeholder' approach. They developed a matrix of a polyurethane/salt composite by foaming the polymer at different salt concentrations in order to achieve the proper

porosity. The preparation of the foam consists of obtaining a ceramic based on the polymer phase. Ceramic powder is added to both the resin and the isocyanate component, stirred and left to complete reaction and cross-linking. The resulting foams have different mechanical features (e.g compression moduli and porosities) depending on the concentration of added salt. Peng and Fan [55] described the preparation of ceramic foams by expansion of a ceramic suspension based on a polyurethane system. Foamed ceramics possess open cells in a nearly equiaxed shape but the cell size is much finer. In this case, the aim was to get a foam with homogeneous pores.

A highly developed expertise in the extrusion foams industry, the **'bubble-forming' technique,** is also employed for production of ceramic foams. They are based on producing and stabilising bubbles within the mass that have been created by chemical (e.g. chemical reactions resulting in gaseous components) or physical agents (e.g. blowing gas or by turbulent mixing). When the polymer is initially mixed with a ceramic component, ceramic foams can be formed. Garrn et al.[56] and Sepulveda et al. [50] are both examples of the 'bubble technique' to obtain ceramic foams. The ceramic suspension is obtained from powder mixed with additives and then mechanically stirred until foams are obtained. Further treatment (polymerization, de-binding, drying, sintering, etc) leads to the porous ceramic structure.

The techniques for metallic foam processing can be classified into two main groups [57]: those manufacturing processes that sinter loose metal powders with [58] or without [59] space-holders, similarly to the 'placeholder' and 'replica processing' in ceramic foams, respectively; and those methods where the melted aerated [60] matrix is compacted. Prior to the hot densification, the inert gas would have been mixed in the molten metal and would be set to expand following the same procedure that the 'bubble forming' technique.

The literature reports many fabrication methods for foams whose composition is purely polymeric. The most common techniques are the thermally induced phase separation methods (derived from the 'bubble forming' technique), where the gas component is separated due to changes in pressure and temperature from the mixture and acts as the blowing agent, and the use of chemical and/or physical foaming agents (e.g. surfactants and others, similar to the bread-baking process).

In both cases, at initial stages of the reaction, foam is the dispersion of a gas in a polymeric liquid, which creates a characteristic structure when the matrix solidifies. Once cured, the

foam consists of individual cells, or pores, the walls of which have completely polymerised and solidified to form a skeletal structure. The cells can be open with interconnected cells having a thin membrane between the skeletal ribs, or closed with separate cells which are non permeable and resistant to moisture and oil, insulating against heat and cold and absorbent of impacts or vibrations. A typical foaming [61] involves four stages:

1. Bubble generation (nucleation) and growth (often involving a blowing agent)
2. Packing of the bubble network and cell window stabilization
3. Polymer stiffening and cell opening
4. Final curing (solidification)

The resulting foam structures are affected by the both their chemical composition (e.g. blowing agents, surfactants, catalysts) and processing conditions, such as pressure, viscosity, temperature, cure time, humidity, impurities, surface tension of reactants, etc.

There are too many variations to the polymeric foaming processes to cover in detail here (further details may be found in [62] and [63] for an overview of this large topic). Instead, the focus will remain on the manufacture of polymeric foams by using chemical blowing agents.

2.3 Effects of ultrasonic irradiation

The effects of ultrasonic irradiation on chemical processes have been widely covered since Richards and Loomis [64] first reported to the international scientific community the effects of ultrasound in the acceleration of a convectional reaction using a piezo-electric ultrasonic source in 1927. The applications of ultrasound have spread out to a broad range of fields, from Medicine (e.g. imaging) to Materials Science (e.g. acoustic emission testing) and chemical/physical applications.

Ultrasound has many effects on chemical and physical phenomena, but given the context of this work, ‘cavitation’ phenomenon should be introduced first. The term ‘acoustic cavitation’ was first standardised by Apfel [65] who gave a broad description of the phenomenon that could embrace all the definitions used at that time. Acoustic cavitation was characterised as any observable activity of bubble(s) moving due to acoustic field stimulation. Although Crum [66] later specified a more accurate classification where the differences between *transient* and *stable* cavitation were stated. Essentially, the effect is this: when a gas is dissolved in a liquid, changes in pressure and temperature can cause the

liquid to become supersaturated and so bubbles are formed. When these bubbles, of initial small radii, are irradiated, they experience alternate expansion/contraction due to the sinusoidal nature of the soundwave field. Under conditions of *stable cavitation*, this process is positive, and expansions are bigger than contractions, so the bubble growth is in resonance with the soundwave. However, if the bubble size, the ultrasound power and/or frequency go above a certain threshold, *cavitation becomes transient.* The bubble is no longer in resonance and the pressure produced during the next compression cycle causes the bubble to implode. The nature of the acoustic cavitation will be given by the predominant behaviour of bubbles in the liquid.

The review here sketches the boundaries of ultrasonic applications in the context of effects caused by soundwaves on chemical reactions or physical processes that relate to the research work covered by this thesis. Due to the amount of work carried out by scientists across the world in the past 20 years, it seems unfeasible to cover with accuracy and perspective such a vast research field with branches many of which now stand by themselves as fully developed fields of knowledge.

Therefore, this section contains two main parts. The first one aims to present some interesting examples of the chemical effects produced by ultrasound (so called, sonochemistry). This will be followed by a revision of the physical effects caused by ultrasonic irradiation. A dividing line between pure chemical and physical effect is difficult to establish due to the lack of a full understanding of the mechanisms of sonication. Later, a section where applications based on a combination of physical and chemical phenomena completes this review on effects of ultrasonic irradiation. Finally, this section finishes by highlighting some of the published work on ultrasonically induced polymeric foaming and the ultrasound influence on the bubble dynamics.

2.3.1 Sonochemistry: chemical effects produced by ultrasound

Sonochemistry is the effect of ultrasound on chemical reactions. From the early 80's, researchers such as Suslick and Mason have been doing outstanding work on sonochemistry and its consequences. The majority of these applications exploit ultrasonically stimulated transient cavitation effects (i.e. the rapid growth and explosive collapse of microscopic bubbles as the alternate compression and rarefaction phases of a sound wave passes through the liquid). Since their pioneering work, the field has grown deeper and wider, with researchers now working on a myriad of aspects of the interactions between ultrasound and chemistry. Suslick's research line derived towards the chemical exploitation of the

sonication effect, and culminated in a publication in Science [67] that brought the concept to the broader non-specialist scientific audience. From his initial work on organic chemistry and non-aqueous liquids, through organichemistry synthesis, then inorganic solids and catalysis, and more recently protein micro-encapsulation for drug delivery, the boundaries of sonochemistry have been stretched enormously. One of the best reviews of his -and his collaborators'- work over 20 years was published in 1999 [68] and it provides an excellent overview of sonochemistry principles. His work constitutes a breakthrough and has been the starting point for many researchers to look into chemical effects provoked by the application of high-intensity ultrasound. The two most important fields of application have been in polymerisation reaction and sonoluminiscence.

The impact of ultrasound on reactions for polymerisation is two-fold, and the involvement of different lab techniques and many diverse researchers' motivations have developed a deeper insight of the twin performance. Sonochemistry and its consequences derived from the formation and violent implosion of bubbles, which provoke 'hot-spots' (i.e. mini-reactors with extreme conditions of temperature and pressure) that have been demonstrated to enhance the reaction rate of polymerisations and increase molecular weight (even without the presence of any catalyst), of styrene [69], polyester and polyurethane [70] and, more recently, methyl methacrylate [71]. On the other hand, ultrasound can also be directed towards the molecules cleavage (i.e. atoms bonding bridge) and provoke their breakage aided by those 'hot spots': polysterene in alkane solution [72], unfilled silicone [73], poly(dimethyl siloxane) PDMS [74], etc. This feature of ultrasonic sonochemistry has been exploited by some authors to induce polymeric degradation and devulcanisation [75, 76], which offers the advantages of a clean polymeric recycling process avoiding poisoning incinerations [77].

One of the most remarkable effects of sonochemistry that have fascinated researchers for years is the emission of light from a sonicated bubbly liquid, called sonoluminescence. Under some circumstances, especially if the solution is a hydrocarbon mixture or a noble-gas is dissolved, the implosion of bubbles will ionise the gases inside them, and they will emit light [78-82]. Still at the lab scale, this branch of sonochemistry is being used to assess the mechanisms of reaction inside a bubble during transient cavitation provoked by sonochemistry.

At the same time that the chemical applications of sonication have developed, Mason et al. [83], among others, have expanded the field and nowadays ultrasonic sonochemistry is

widely used in water/soil remediation [84-86] and textile cleaning [87]. These are based on the hydrodynamic cavitation principle [88] that couples microjets and hydrolysis via transient cavitation to transform hydrocarbon waste into carbon dioxide and water in a short period of time. This effect is provoked by the ultrasonic cavitation in thin liquid layers, where a large amplification of the acoustic pressure promotes the violent implosion of bubbles [89], and the released energy erodes dirt and degrades molecules.

2.3.2 Physical effects produced by ultrasound

The effects of ultrasound are not exclusively of a chemical nature. A myriad of physical effects have been observed and reported in the scientific literature.

Enhancement of mass transport and diffusion aided by ultrasound have been proved [90, 91] due to the membrane distorsion caused by acoustic streaming (i.e. ultrasound shock wave deforms the cell membrane) and stable cavitation (i.e. bubbles cyclic expansion/contraction introducing stress in the cell boundaries that makes them more flexible). This ability of the ultrasound to modify diffusivity and membrane permeability has been known for decades and it is now an established technology for food dehydration [92] and drug delivery [93].

Controlled microstreaming and shockwave energy can decrease particle size and even its distribution (i.e. more particles of similar size) and are employed to produce rupture of polymeric particles (e.g. polyethylene, polypropylene, etc) [94], in the preparation of nanocomposites [95] and desorption mechanisms [96], in sonocrystallisation [97], in food processing [98] and grain refinement during metal casting solidification [99] due to the vibrational effect of ultrasonic waves.

The pressure difference caused by stable cavitation acts as a nucleation (‘seeding’) agents that lead to agglomeration of finely suspended and/or nanoparticles of ice [100] and pollutants [101]. This last application has been investigated and scaled-up for industrial exploitation [102].

Mechanical stirring produced by ultrasound has been exploited as a mixing mechanism for creating a better blend in polymeric alloys [103], and also as an instrument for creating superior dispersion of fillers in the polymeric composite by reducing viscosity during aggregation of fillers to the plastic composites [104]. As a homogenisation instrument, it is now a fully developed technique in industry. Extruded polymeric mixtures with the aid of

high-frequency (in the order of MHz) ultrasonic irradiation [105-107] (where more bubbles of a smaller size were produced, generating in this way a more homogeneous matrix) is one of the best known applications of this technology. Ultrasound has also been used as a degassing agent during metal casting [108].

Frequently, researchers cannot distinguish if the sonication effects are chemically-driven or the dominant effect is purely of a physical nature. For example, cold gelation of proteins [68, 109] and catalysts [110] along with fabrication of microcapsules [111] are only some of the examples of acoustic irradiation where researchers claim that both physical and chemical effects take place. Emulsification and thorough mixture would be the physical outcome and acoustic cavitation that enables cross-linking enhancement, i.e. the chemical contribution that keeps the content (i.e. drug) encapsulated. Therefore, these two effects of ultrasound can be coupled towards production of smarter devices that can slowly release its content to assist drug delivery. Turbulence, transient cavitation (i.e. implosion of bubbles) and/or acoustic streaming (i.e. micro-jets) might all team up to produce bubble coarsening which accelerates drainage and subsequent foam breakdown in liquid foams and froths [112]. This strategy has already been commercialised via high-power acoustic power radiated from plates in reaction/fermentation vessels [113].

2.3.3 Effects of ultrasound on foaming polymeric melts

To date, as far as the author is aware, the conditions for the mechanical growth in a steady, sustainable way, (i.e. stable cavitation, for bubbles in a polymeric matrix) have not been described. Nucleation of bubbles has only been reported to be substantially enhanced by ultrasonic excitation as a means of mechanical activation via ultrasonic excitation, which is employed as a means of locally introducing sufficient energy to overcome the energy barrier for bubble nucleation [114].

Although theoretical studies of the behaviour of a single bubble in liquid, commonly water, exposed to ultrasound have been extensively published [115-119], the behaviour of an ultrasonically-induced bubble in a polymeric or viscoelastic melt, or whole matrixes of growing bubbles (i.e. a foam) do not appear to have been explicitly modelled until recently [120],[121-123], with the exception of [124] in the mid 90's, where the problem was first stated. The non-linear bubble oscillations at high ultrasonic intensities and the complexity of modelling viscosity behaviour (whose role is crucial in the foaming processing) in terms of non-proportionality with the changing melt rigidity, are major difficulties in attempting a general solution. Since Church et al.'s work [124], various viscoelastic models have been

proposed, but these all require more research effort for their verification and final standardisation.

Bubble dynamics play an important role in the foaming process of polymeric melts, and ultrasound applied to the system could influence the dynamics of the process. These sonication effects should influence both bubble growth and nucleation rates in foams since both are strongly influenced by the concentration of dissolved gas in the resin (in other words, the saturation level determines the gas pressure and hence the driving force for bubble growth).

Particularly important in the context of foams and other high viscosity fluids is the ability of ultrasound to produce an increase in mass transport due to diffusion variation [125], facilitating in this way diffusion and mixing of constituents. Essentially, sound affects the viscosity of fluids significantly (usually decreases their viscosity) [126, 127], so acoustic radiation reduces the diffusion boundary layer, increases the concentration gradient and may increase the diffusion coefficient. Since viscosity is inversely proportional to the diffusion coefficient, the latter will increase in sound fields. Convection also decreases the thickness of the mass transfer boundary layer, i.e. the wall of the pore. An increase in the membrane transport is due to reduced wall thickness. In addition, ultrasound creates stresses that disrupt the normal configuration (shape, wall thickness) of pores, and thus increases the membrane permeability towards gas/vapour (the blowing agent). However, if the intensity (i.e. pressure amplitude) is too high, ultrasound can go above the threshold and become transient, provoking shockwaves that can rupture cell walls.

Once initiated, ultrasound could affect the process of bubble growth in a number of ways [75], individually or in a combination of these:

1. **Heating and mixing**. Increase in temperature due to absorption of sound waves can provoke convections and turbulences that stir the mixture.
2. **Structural effects.** Dynamic agitation and shear stresses produced can affect structural properties (e.g. viscosity) and provoke mechanical rupture.
3. **Compression and rarefaction** (‘sponge effect’). The rate depends on the frequency of the ultrasonic wave. A dense material will crack if these cycles are too rapid but, if a system is viscoelastic in nature, compression/rarefaction can also affect the size of bubbles.

4. **Cavitation** (when compression occurs to a greater extent than expansion, bubbles implode). Side effects occur in the chemical reactions: ultrasound can enhance polymerisation or depolymerisation, thereby breaking the bonds of the mixture.

When the bubble growth is controlled by irradiation, which is applied at certain locations of the bulk of the foam and at sensitive stages of the physical-chemical reaction (see 'bubble-forming technique' under *Foaming processes* in this chapter), it can be modified (accelerated or retarded with acoustic power, frequency, etc) in order to control the size of the pores, their wall thickness or their orientation. These phenomena will be manifested in the final cellular structure when the foam has solidified.

2.4 Porosity measurement techniques

To assess the effects of the ultrasound exposure on the foam's cellular structure, an effective method of characterising the porosity distribution within the material is essential. The fact that the polymeric foams manufactured in this research work were closed-cell cellular structures restricted the measurement options. A brief review on methods used across many disciplines (e.g. Biomaterials, Volcanology, Medicine, etc) is presented below.

In open-cell structures (e.g. flexible foams, rocks), porosity can be measured using established methods such as the liquid displacement techniques (e.g. Arquimedes', toluene infiltration displacement, mercury-porosimetry, etc). These methods provide an average density value for the bulk material (e.g. measurement of permeability and tortuosity in a sample) and yield an average pore size distribution, but give no information about where the pores actually are, and how they are connected. However, the aim of this work is the manufacture of heterogeneous foams with functionally graded porosity, therefore bulk or averaging methods are not applicable.

The distribution of porosity can be recorded using internal scanning techniques (e.g. X-ray or SEM) and some attempts have been made to convert digitalised 2D images of porous material microstructure into finite element meshes [55, 128, 129], so 2D microstructural features (e.g. pore size and shape) can model the global mechanical response. Although some authors [130, 131] have defended this method stating that, in some cases, there is a good correlation between three-dimensional distributions and the two-dimensional data, it appears to the author that quantification of the results is not simple in heterogeneous materials, because the multiple 2D "slices" (i.e. images) generated by these methods have to be interpolated to allow the 3D heterogeneous geometry to be rendered. In addition, since

this technique will use PC simulations from a limited number of 2D-micrographs, the accuracy will be reduced proportionally to the heterogeneity of the porous solid. Therefore, for heterogeneous structures with a non-regular distribution of pore size, position of intersections, etc, will not be successfully represented using this strategy.

Sound has been used as an assessing tool to evaluate skeletal status. Soundwave propagation parameters (very high frequency, of the order of 1MHz) have been also used [132] to characterise cellular structures (e.g. cancellous bone). However, the relationship between a measurement of density of a porous structure (i.e. porosity) and the sound attenuation is not a simple linear function and the technique requires further research.

Three dimensional micro-computed tomography (3D μ-CT) appears to be the most sophisticated of the porosity measurement techniques nowadays and it is becoming widely used among researchers. However, the high prices for beam time still appear to be the major drawback, especially for those investigations where a large number of samples need to be examined. Explicit structures in smaller regions allow the qualification of foams. Spatial distribution of pores, surface area per unit volume, density distribution and degree of interconnectivity are among the main features that this technique can measure in solid cellular materials. μ-CT is used for measuring non-destructively the degree of bone regeneration [133], bone structure [134] and porosity of scaffolds [41, 135], aiding in this way computer modelling design. The data obtained from μ-CT scanning can be used to create virtual models whose internal geometry matches the specific internal geometry of the original porous solid (Figure 11). However, ensuring reproducibility in the results (when compared to the real cellular solid data) of the image processing technique, further increases the cost [136].

Figure 11: Triangular mesh, voxelisation and porosity distribution within the model generated from sandstone data, in [137]

2.5 Fabrication methods for polymeric foams with an engineered porous structure: Discussion

This section contains a discussion of the fabrication methods described above, with special attention paid to foam porosity tailoring and methods to control their porous structure.

The development of a manufacturing process that allows the fabrication of tailored parts of heterogeneous materials will be successful only if the following two aspects are fully understood by researchers:

1. The macro and micro-structure of the object to be produced. These are directly linked to the mechanical, physical-chemical, biological (or a combination of these) functions required of the artefact.

2. How the fabrication process develops (e.g. mechanical processing, post-treatment, coating, etc) and which stages are critical.

Layered manufacturing techniques have shown highly flexible fabrication capability and demonstrated that graded compositions can be designed along with the geometry of the part, tailoring its physical properties for a specific purpose or function. From the bio-engineering point of view, these manufacturing processes limit the choice of biomaterials available to fabricate bone scaffolds and implants (e.g. teeth, prostheses, etc).

Several critical issues arise when dealing with the design and manufacture of implants from biocompatible materials. One of such is the porosity gradation, which must reproduce the equivalent functionality of the original part (e.g. equivalent mechanical strength and also help proliferation of seeded living cells). Geometry must also be considered, since the prosthesis has to fit into the surrounding bone structure and, finally, the artefact must be designed taking into account the patient's condition (e.g. age gender, lifestyle, medical history, etc) and the physical dimensions extracted from medical images (e.g. computer tomography (CT) and magnetic resonance imaging (MRI)).

One of the main challenges that heterogeneous materials manufacturing processes face for the future is undoubtedly the possibility of manufacture at the micro scale. Although, theoretically, representation models can be developed at any size, when they are downloading the information for the fabrication process, the limitations of the actual machinery clearly cannot be neglected. Engineers and material scientists have succeeded in 'thinking micro', now they have to create supporting technologies to 'make micro'. Challenges in this area lie on the need for re-scaling the available manufacturing processes without compromising quality and reliability in the final product. In other words, could the tolerance of a rapid prototyping machine reach the accuracy of a CT or MRI image?

As far as manufacture is concerned, the trend that can be foreseen is the integration of different natures of manufacturing processing. Many of the methods discussed here will

have to adapt their strategies to a more demanding production process where highly job specific materials (e.g. biocompatible, bio absorbable materials) can be dealt with successfully in many domains (e.g. a 3D printing process able to form objects at the micro scale). Details of processes (e.g. FDM) still require better adjustment to avoid some undesirable physical process phenomena, such as phase change, shrinkage or pore geometry deformation.

Many traditional techniques will have to be modified to match mechanical, chemical and biological requirements. These traditional methods are manual processes, which make them difficult to be fully incorporated in industrial processes. They are common at the lab scale for heterogeneous materials production, and further research must be undertaken in order to achieve industrial levels of automation, accuracy and control. This is necessary for composites and engineered micro-structured materials in order to create these artefacts in engineering and biomaterials fields, because at present the technology has difficulties in high-quality production of fine micro-patterned components.

In biomaterials, the control of porosity is crucial. The digital fabrication of structures that act as a template to guide, help and enhance proliferation, growth and development of living cells in a three dimensional space, is largely a blue-sky research field at the moment. The most demanding applications arise in biomaterials, where the porous structure of a scaffold is not an end in itself, because of the difficulty of placing living cells inside the intricate architecture of interior regions. A possible solution comes from the development of a fabrication method which allowed the creation of materials with functionally graded porosity, that can be tailored to enable seeding and cellular attachment and also withstand functional loading (e.g. mechanical forces). This fabrication method must also be hygienic; the process itself should not involve the use of toxic chemicals nor high temperatures (e.g. sintering) because this would induce the cells to die if subjected to a thermal shock.

Among the main advantages that the ultrasonic irradiation as porosity-tailoring agent offers is its ability to create unique, high-energy intermediates at mild ambient temperatures. Therefore, thermally sensitive reactants are protected and the reactions take place at controlled locations (i.e. the ‘hot-spots’). The enhanced mixing and transport properties that the ultrasonically enhanced *cavitation* can lead to are also remarkable. It is difficult to make a porous structure via a typical polymer melt foaming process with only the help of blowing agents, because of the intractability of the polymer (i.e. high molecular weight –long monomer chains-, and high viscosity of the melt). However, the process might be controlled

by influencing, enhancing and boosting the physical and chemical process via localised ultrasonic irradiation. This research seeks to investigate if *stable cavitation* established in the polymeric foaming could facilitate a manufacturing process based on ultrasound that can be manipulated in a way that builds rather than destroys.

It is seen that the work surveyed on porosity representation has almost exclusively addressed the problems of porosity measurement in close-pore foams. The only truly reliable method for analysis of micro/macro-porosity requires costly scanning, and even then, there is no established convention on how the new data (e.g. clouds of points in a 3D space) should be analysed for a final description of the foam or solid cellular architecture, or information on nature of those material(s) that constitute it.

One of the most interesting issues in heterogeneous materials, as far as porosity is concerned, is the interconnection among pores in the bulk material. The quality, functionality and suitability of a foam to a certain application will depend not only on the pore size distribution of foam but also on the dimensions of the narrower necks connecting larger pores, and how pores are interconnected. The methods surveyed here fail to offer a consistent strategy porosity representation and analysis. This restriction comes from the inability of image analysis software to convey this information from the scanned cellular material. The output that is offered by those scanning strategies is a histogram of population of dots which carry no explicit information on cell size or its topology.

This is the reason why the extrapolation of data from 2D to 3D that some authors have proposed is only valid for highly-regular cellular distributions. Here, the porosity gradient is not taken into consideration, and this is vital in the definition of heterogeneous materials. Bulk characteristics define mechanical properties, but only in those homogeneous structures with a small degree of anisotropy. In heterogeneous materials (e.g. cellular solids), the forces will not be distributed in the same way within a volume, as some parts might be loaded more than others, performing balancing effects that can lead to erroneous mechanical characterisation.

Although this approach (from 2D to 3D) allows researchers to view and interactively assess/measure the cellular structure of a material, the calculation of porosity from 3D models is still a significant research issue. To date, μ-CT data is still processed by using *linear* cell densities to assess cell density [136].

Even when restricted to a two dimensional work, this research work has tried to address the problem of measuring and quantifying graded porosity in heterogeneous materials and details of this strategy are presented in Chapter 4, along with the results of this approach, in Chapter 5.

CHAPTER 3. THEORETICAL FOUNDATION

This chapter introduces the scientific principles that have influenced the design of the experimental work described in Chapter 4. A theoretical understanding underpinning the following four phenomena is presented to support the research hypotheses stated later in this chapter:

1. Conductivity can be used to monitor the reaction phases (i.e. progression through pre-gelation, gelation and post-gelation stages)
2. Ultrasound can have a physical and sonochemical effect on the polymerisation reaction
3. Ultrasound can affect the dynamics of the foaming process by affecting the mass and heat transfer
4. Sound field pattern can be used to tailor porosity within the bulk of the foam by subjecting the bubbles to stable cavitation and pulsations that allows bubble size adjustment before solidification

The next sections will provide background on the theoretical principles underlying the chemical reaction, the electrical resistivity and the properties of ultrasound, the boundaries of what is known; the answers that this research work intends to provide, and those issues that remain still unsolved.

In Chapter 1, the author conjectured that it should be possible to modify the behaviour of foaming processes with careful application of ultrasound and, as a direct consequence, alter the cellular structure (i.e. porosity and cell size distribution) of the resulting material. And this chapter is dedicated to explaining the rationale of the experimental work carried out to investigate the hypotheses and establishes the relative importance of the different mechanisms acting on the irradiated polymeric system.

3.1 Polymerisation reaction

Like many of the polymers in widespread use today, polyurethane was first synthesised in 1937 by Otto Bayer at the Farben Laboratories in Leverkusen, Germany [138]. At that time there was little scientific understanding, but a highly practical and economically-driven motivation.

The use of polyurethane in industry has grown rapidly but the theoretical modelling of the chemical reaction has not developed at the same pace. The following sections give an overview of the process of polyurethane formation.

3.1.1 Chemical reaction

Polyurethane (PU) is made by the polymerisation of a monomer mixture (polyol –Figure 12a– and isocyanate –Figure 12b–) after the addition of a catalyst [138]. The urethane group formed (Figure 12c) has robust mechanical and chemical properties that have made this polymer one of the most widely used in industry over the past seventy years.

PU has a firmly established market with countless applications. However, the frothing process involved in this chemical reaction is a group of sophisticated chemical-physical reactions that are still not completely understood.

Reactants		Products	
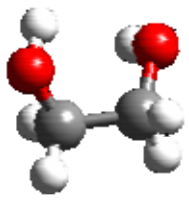	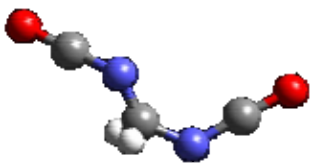	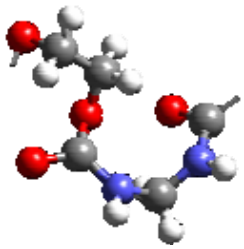	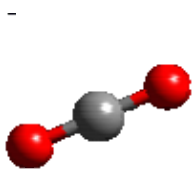
a) Polyol	b) Isocyanate	c) Urethane group	d) Carbon dioxide

Figure 12: 3D models of reactants and products of polymerisation reaction

In order to understand how the foaming process is affected when an external "agent" (such as ultrasonic irradiation) is introduced into the foaming system, it is necessary to understand how the process variables react to it throughout the whole process.

The foam used in this study is created by a chemical reaction between the polyols and the diisocyanate group to produce polyurethane. Distilled water is used as a blowing agent.

$$\text{R-N=C=O (}\mathbf{liq}\text{) + d}H_2O\text{ (}\mathbf{liq}\text{) } \leftrightarrow \text{ R-}NH_2\text{ (}\mathbf{liq}\text{) + }CO_2\text{ (}\mathbf{gas}\text{)}$$

$$\text{HO-R-OH (}\mathbf{polyol}\text{) + O=C=N-R'-N=C=O (}\mathbf{diisocyanate\ group}\text{) } \rightarrow \text{ -O-R-O-CO-NH-R'-NH-CO- (}\mathbf{PU}\text{) + }CO_2\text{ (}\mathbf{g}\text{)}$$

The water diffuses across the holes formed between the chains of polyurethane reacting simultaneously with the isocyanate groups at the end of the chains, causing the reticulation (or cross-linking) of the polymer, and forming a semi-rigid solid. The gas product, carbon

dioxide, acts as a blowing agent and fills up the cavities forming a polymeric foam once the matrix has fully solidified.

A qualitative description of the foaming process using a chemical blowing agent can be described in terms of the following three characteristic stages:

1. Cream stage: After nucleation, the polymeric mass begins to expand in volume when the boiling point of the blowing agent is reached. This happens when the temperature increases (due to the exothermic reaction) and the blowing agent's[3] boiling temperature is reached (becoming active). In the case of water, the reaction produces carbon dioxide, CO_2, which acts as the blowing agent. As it can be seen from the reaction equations, the amount of water added to initial mixture is directly related to the amount of CO_2 formed (and this represented an important factor in the designing of the experiments).

2. Rise stage: Foaming occurs at constant pressure but with variable volume (i.e. free expansion in an open vessel). A physical and/or chemical blowing agent raises the polymeric melt until a maximum height is reached. Foaming occurs simultaneously with the reaction which is a result of the vaporisation of a low boiling agent (if a physical blowing agent is employed) or a result of the formation of the blowing agent (CO_2) if a chemical agent has been used, due to the exothermic heat of reaction. Then, there is a liquid foam, a metastable system that evolves dynamically due to two processes: foam drainage (liquid flows through the intersticial volume between bubbles) and foam coarsening (gas exchange between bubbles. Coarsening accelerates drainage and consequently foam breakdown).

Once the foam has reached its maximum height, the exothermic energy of the reaction is used for the creation of links between monomers, cross-linking, creating long chains that form the polymer, entangled units that will form cells. In the case of open-pore foams, the process develops further and the pressure inside each bubble is sufficient to provoke rupture of cell walls that separate bubbles, creating open channels.

3. Gelation: at this point, the final structure of the foam is reached. The rigidity of the fluid is high enough to consider the bubbles as cells. Bubble size becomes fixed and there is no possibility for the bubbles to expand or collapse, as the increasing viscosity of the plastic makes the walls stiff and strong against shear forces. The gel point is typically obtained experimentally by periodically moving a thermocouple during the reaction and noting the temperature and time at which the mixture seems solid. Conversion rate (the ratio of products to reactants) at that point is considered by some authors [139, 140] to be approximately 0.5. Finally, when all the polymeric mass has gelled, the final structure is

[3] The blowing agent added can be chemical (i.e. water, as used in this study) or physical (e.g. CFC, R-11 gases, etc) which is pressurised, mixed and supplied simultaneously to the catalyst addition.

obtained. The end of the reaction happens when the conversion rate reaches unity. Cross-linking finishes and foam starts a curing period where cells become fully solidified.

The procedure used here varied slightly from the above description. For example, no physical blowing agent was added to the mixture and a water bath was used to minimise the temperature gradient. The most outstanding change is the application of ultrasound that was performed in the experimental stage. In order to study possible interaction mechanisms between the ultrasound and the foaming reaction, both energy and mass balances need to be considered to characterise the polymerisation reaction.

3.1.2 Energy and Mass Balances

The mathematical modelling of polymerisation requires of the definition of reaction kinetics, reaction energetics and an expression to describe the variation of the viscosity value with time during each reaction stage. Although researchers have demonstrated [141] that kinetics of polyurethane formation are enhanced by mechanical stirring (e.g. shear rate is increased), it is not within the scope of this research work to investigate ultrasound's impact on the reaction kinetics. However, both energy and mass balance (i.e. reaction energetics) along with the viscosity variation were considered.

A complete energy balance for the PU formation was first developed in the 1980's [140, 142] and later authors [143, 144] improved and extended the original work for a myriad of foaming conditions (e.g. close mould, adiabatic conditions, etc). However, this energy balance failed to consider either density gradient or temperature gradient in axial and vertical directions.

In the case of closed moulds [106, 114] the energy balance includes an expression for the variation of pressure with time, once the mass has filled the whole mould. The authors in Table 1 developed their work for, mainly, closed moulds (e.g. reaction injection moulding – RIM– processes)

The extensively reported work on the energy balance for PU formation is summarised in the following table. Using the equations proposed by these authors, an integrated definition for each of the stages that the melted polymer goes through during the foaming process will be developed.

Authors	Energy Balance	Mass Balance	Main contribution	Limitations
Lipshitz et al. (1977) [139]	Contribution only by chemical reaction	Not defined	First author to define the energy balance in PU polymerisation in adiabatic conditions	Simplicity of the model
Rojas et al. (1982) [140]	Contributions from the reaction and the vaporisation of the blowing agent	Not defined	First author who defines density as a function of the amount of blowing agent in the mixture, cream and rise time	Considers mass transfer to the bubble as an instantaneous phenomena vs heat transfer
Marciano et al.(1986) [142]	Contributions from the reaction, the vaporisation of the blowing agent and heat conduction	Not defined	Considers conduction as a heat transfer term and defines temperature gradient as main generator of skin (higher density outer layer)	Gradients of temperature are only considered on the z-direction, perpendicular to the close mould base.
Niyogi et al. (1992) [145]	Contributions from the reaction and the vaporisation of the blowing agent	Surface-resistance controlled mass transfer and diffusion controlled mass transfer (for both diffusion coefficient constant and variable) considered	Intensive analysis of the mass transfer phenomenon, nucleation rate, bubble population balance, bubble-size distribution, etc	Convection is considered negligible and mass transfer is purely diffusional controlled by the liquid resistance. Assumed instantaneous gelation for the entire polymeric mass
Baser et al. (1994) [146]	Same as Rojas et al.	Mass transfer considered as a diffusion process	Heat loss to the surroundings by radiation once the reaction has ended. Mass transfer resistance to foaming is also incorporated.	Neglects competition among neighbouring bubbles and convection in the mass balance. Requires input of number of bubbles for accuracy vs experimental results
Gupta et al. (1999) [143]	Contributions from the reaction, the vaporisation of the blowing agent and heat conduction	Reaction rate depends on the decrement of concentration with time. Mass transfer is considered instantaneous	Uses the fact that the blowing agent can be added in both liquid and gas phase. Intensive study on variables affecting the skin thickness	Neglects diffusion in the mass transfer
Modesti et al. (2000) [144]	Contributions from the reaction, the vaporisation of the blowing agent, heat conduction and convection	None formulated	Considers heat dissipation through the mould. Performs a density assessment when different chemical and physical blowing agents are used in the reacting mixture	For the model development, adiabatic conditions in closed moulds are considered. Convections effects are ignored when applying to his special scenario.

Table 1: Various authors' contribution to energy and mass balances for PU polymerisation

In contrast to the studies reported in Table 1, the experimental conditions of the experiments detailed in Chapter 4 are:

- Polymer is prepared in an open vessel, dP/dt = 0. Atmospheric pressure is the only external force over the mixture at all times.
- The reported energy balance for PU foaming does not include a convection term but only heat transfer due to conduction.
- The reported energy balance does not include a gradient of temperature or density in the x- and y-direction, only in the z-direction. Consequently, the equations developed here will contain the Laplace operator:

$$\nabla = \left(\frac{\partial}{\partial x} + \frac{\partial}{\partial y} + \frac{\partial}{\partial z} \right) \quad (1)$$

- Foaming takes place under non adiabatic conditions that are convenient for reaction kinetics investigation, (especially when reaction is fast and exothermic). The aim is to investigate possible mechanisms of interaction between ultrasound and heat transfer, so non adiabatic conditions must be modelled.

3.1.2.1 *General Energy Balance Equation*

The balance presented here has been developed for the purpose of this study. The energy balance (units: J/s.m^3) lists the contribution of generated/consumed heat during the foaming process as well as the transmitted heat to and from a unit volume of foam. In it, a differential control volume of thickness dx, width dy and height dz, is defined. The temperature gradient in this system is considered orthogonal to the mould walls.

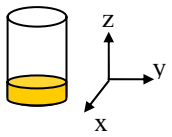

Figure 13: Coordinate axis for the energy and mass balances

Before the reaction takes place, the liquid foam fills approximately one quarter of the container. The growth is presented as a variation on the z-axis.

For the control volume (of sizes dx, dy and dz), the First Law of Thermodynamics is applied:

The rate of energy accumulation in the control volume added up to the net transfer of energy by fluid flow must be equal to the sum of: the rate of internal heat generation due to the chemical reaction subtracting the net heat of transfer by convection, the net heat

transferred by conduction and the net rate of heat transfer from the control volume to its environment due to formation of the blowing agent (CO_2 from water) and/or vaporisation of the solvents (e.g. acetone).

$$\bar{\rho}\cdot\bar{c}_p\cdot\left(\frac{\partial T}{\partial t}+u_x\frac{\partial T}{\partial x}+u_y\frac{\partial T}{\partial y}+u_z\frac{\partial T}{\partial z}\right)=(1-\omega_{Bo})\cdot\Delta H_r\cdot\bar{\rho}\cdot\frac{dX}{dt}-\bar{\alpha}\cdot A\cdot\nabla(T_x-T_w)-K\cdot\nabla^2T-\bar{\rho}\cdot h_v\cdot\frac{dB}{dt} \quad (2)$$

Net transfer of Energy

Rate Energy accumulation

Heat produced due to the exothermic reaction

Convection

Conduction

Formation of blowing agent

Equation (2): General Energy Balance equation, adapted from [147] and [148]

In this expression, the averaged values of the foamed polymer in time, density, ρ, and specific heat, c_p, are considered at each interval. In fact, the density of each element, ρ, changes with the formation/vaporisation of the blowing agent and mass expansion. The value for the specific heat, c_p, has been defined by [139], and it is a function of the temperature, the specific heat of the blowing agent (i.e. average between liquid and vapour states), c_B, and the specific heat of remaining components, c_{rest}.

$$c_p=\omega_{B_0}\cdot c_B+(1-\omega_{B_0})\cdot c_{rest} \quad (3)$$

Other variables also present are: Initial fraction of blowing agent, ω_{Bo}; conversion rate, X, therefore, dX/dt is the reaction rate, i.e. rate of increase of reaction extent; thermal conductivity, K; and ratio of liquid blowing agent, B, where dB/dt is the "umbrella term" where both the rate of vaporisation of solvent and the rate of formation of blowing agent from the reaction with water, are represented in the following.

The thermal conductivity, K, has been shown to be [142, 143] a function of the instantaneous density,

$$K(\rho)=a_1\cdot\rho^2+a_2\cdot\rho+a_3 \quad (4)$$

The heat of reaction (i.e. the total reaction heat per unit of polymer mass), ΔH_r, the average convection coefficient for the surface (bulk), α, which is a constant, and the latent vaporisation heat of blowing agent per unit mass, h_v, are constant values during the reaction. The viscous dissipation has been considered as negligible in this analysis.

3.1.2.2 *General Mass Balance Equation*

Regarding mass transfer for this particular case, gross fluid motion (convection) combines with diffusion (ruled by Fick's Law) to promote the transport of the blowing agent formed by the reaction, for which there exists a concentration gradient, driving force for the flux of mass within the polymeric matrix.

The transfer rate through the polymeric wall (from bubble to bubble or from cavity to cavity) has been tackled by studying the concentration boundary layer [147, 148]. The boundary layer plays an important role in the foaming of the polymeric melt process because this manifests via three phenomena: surface friction (i.e. gas/vapour on bubble shell layer), convection heat transfer and convection mass transfer across the bubble shell layer (both from liquid to bubble, or vice versa).

For compressible fluids (e.g. CO_2 and vapour) being transferred from a liquid and liquid-to-viscous media to/from the bubble, the mass balance needs to be done on a molar concentration basis, as density varies within the polymeric bulk:

$$\underbrace{\nabla^2\left(C \cdot D_B \cdot x_B\right)}_{\text{Diffusion}} + \underbrace{\dot{N}_B}_{\text{Convection}} = \underbrace{\frac{\partial C_B}{\partial t}}_{\text{Concentration rate of blowing agent in the mixture}} \tag{5}$$

Equation (5): General Mass Balance equation, adapted from [147] and [148]

This general expression indicates that there are two contributions to the absolute flux of species (i.e. how the concentration of blowing agent changes in the mixture from the start of the reaction): a contribution due to diffusion (i.e. motion of gas/vapour relative to the motion of mixture) and a contribution due to convection (i.e. motion of gas within the mixture). No further simplifications can be made, as the blowing agent and vapour from solvents are incompressible fluids and neither the blowing agent/solvent diffusion coefficient nor molar concentration are kept constant throughout the process and within the polymeric solution or, at a later stage, solid matrix.

3.1.2.3 *Energy and mass balances to the polymeric foaming proces*

The different stages of foam growth presented earlier in this chapter have been considered and the corresponding expression for the mass and energy balance are presented below. Table 2 presents a summary of when these equations are applied to the different stages of the reaction of this research.

Event	Stage[4]	Chemical reaction	Formation of blowing agent	Evaporation of blowing agent or solvent	Heat Transfer			Mass transfer	
					Convection	Conduction	Radiation	Convective	Diffusive
Before catalyst	A								
Cream time and Rising time	B	✓	✓	✓	✓ . But only considered by [144]			✓	
Pre-gelation	C	✓	✓	✓	✓	✓		✓	✓
Post-gelation	D	✓	✓	✓	✓ . Minimum over conduction	✓	✓ . Only some authors [146]	✓ . But minimum	✓
After end of reaction	E					✓			✓ . Minimum

Table 2: Summary of energy and mass balance phenomena at different stages[5]

[4] As referred in this research work

[5] tick indicates phenomenon active during the stage

Stage A	Stage B	Stage C	Stage D	Stage E
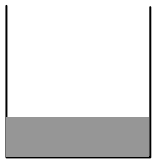	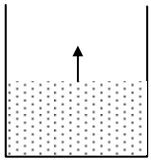	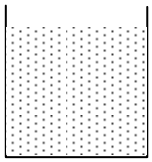	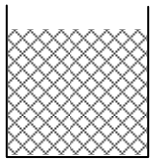	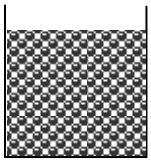
X=0 Liquid foam in the container at t=0 Tx, Ty, Tz=Twalls	X>0 Foam growing T>Twall	0<X< X_{gel} Foam reaches stable height and start cross-linking	X_{gel}<X<1 Gelation point is reached. After that point, bubbles do not grow or collapse. Final size is reached.	X=1 and after Solid foam in the container, t = t_{final} Tx, Ty, Tz=Twalls

Table 3: Summary of stages during foam formation

- **Stage A: X=0**

Before the start of the foaming reaction, the reactants are placed in the container and tempered at the environmental conditions (i.e. $T_{x,y,z} = T_{wall}$). There is no heat or mass transfer. The liquid is assumed to be a homogeneous mixture. There are no gradients of temperature or density; the mixture is of a liquid nature.

- **Stage B: X>0**

The catalyst, water, has been added and the reaction starts. As the liquid is considered to be supersaturated, the initial increment of temperature due to the exothermic reaction makes bubbles start appearing and the foam grows rapidly from then onwards. This is the "cream time". Once nucleated, the bubbles grow as the macromolecules of dissolved gas move within the bulk of the viscous mixture in a convective way, a process that couples mass and energy flux. This is the so called "rising time".

Due to the exothermic nature of the polymeric reaction, the temperature inside the container is greater than the temperature at its walls. A gradient of temperature is established.

As the mixture is still a liquid, convection will be the main heat transfer agent within. Recalling the general energy equation and applying it to this specific stage, the contributions to the energy balance are: the heat generated due to the reaction, convection and formation of blowing agent (CO_2 gas)/ vaporisation of acetone, which for simplicity are expressed by an "umbrella term".

$$\bar{\rho}\cdot\bar{\bar{c}_p}\cdot\left(\frac{\partial T}{\partial t}+u_x\frac{\partial T}{\partial x}+u_y\frac{\partial T}{\partial y}+u_z\frac{\partial T}{\partial z}\right)=(1-\omega_{Bo})\cdot\Delta H_r\cdot\bar{\rho}\cdot\frac{dX}{dt}-\bar{\alpha}\cdot A\cdot\nabla(T_x-T_w)-\bar{\rho}\cdot h_v\cdot\frac{dB}{dt} \quad (6)$$

Assumptions at the stage B are the following:

- Velocities u_x and u_y can be considered of equal value due to the small dimensions of the container. In addition, a plane front is moving faster in the z-direction due to the rapid growth of the foam.
- Likewise, the gradient of temperature in the x- and y-direction is small compared to the one in the z-direction because the rising of the foam is only in the z-direction. Temperature at the wall (T_w) stays below the temperature in the vessel (reaction temperature, $T_{x,y}$) so:

$$\frac{\partial(T_x-T_w)}{\partial x}=\frac{\partial(T_y-T_w)}{\partial y}=0 \quad (7)$$

Therefore, the general equation can be simplified as follows:

$$\bar{\rho}\cdot\bar{\bar{c}_p}\cdot\left(\frac{\partial T}{\partial t}+u_x\frac{\partial T}{\partial x}+u_y\frac{\partial T}{\partial y}+u_z\frac{\partial T}{\partial z}\right)=(1-\omega_{Bo})\cdot\Delta H_r\cdot\bar{\rho}\cdot\frac{dX}{dt}-\bar{\alpha}\cdot A\cdot\frac{\partial(T_z-T_w)}{\partial z}-\bar{\rho}\cdot h_v\cdot\frac{dB}{dt} \quad (8)$$

Equation (8): Stage B Energy Balance

Similarly, at this stage, the mass flux is, predominantly, by convective mass transfer. Consequently, the general equation for the mass balance can be written as,

$$\frac{\partial C_B}{\partial t}\approx\dot{N}_B \quad (9)$$

$$\frac{\partial C_B}{\partial t}\approx\frac{d}{dt}\left(\overline{h_m}\cdot A_s\cdot\left(C_{B,S}-C_{B,\infty}\right)\right) \quad (10)$$

Equation (10): Stage B Mass Balance

As explained in [149], a volume cell, chosen as a reference of motion, moves to the central region of the container, catches up with the flow front and experiences the “fountain flow” at the upper region of the container, near the interface with the open air. The volume cell then moves to regions near the wall and then slowly moves towards the central region again. This process continues during the rise time until the maximum height in the foam is reached.

After that, in stage C, convective mass transfer is paired with another mass transfer event, diffusion.

- **Stage C: $0<X<X_{gel}$**

At the end of stage B ("rising time"), the maximum height of the foam is achieved. The formed cells have trapped CO_2 gas (the blowing agent that is formed during the reaction) inside. This gas diffuses through the polymer melt into the bubbles and moves from cell to cell, these might coalescence and/or implode, and this can provoke events of partial collapse of the foam. This stage is the one at which more phenomena contribute in terms of energy transfer: chemical reaction, formation of CO_2/evaporation of acetone, convection and conduction, due to the viscoelastic characteristics of the mixture. The assumption at this stage is:

- Except at localised areas where events of collapse might happen during a short period of time, velocity on the z-coordinate can be considered zero, as the foam does not grow (u_z=0).

This assumption is introduced into the general energy balance and the resultant energy balance equation for this stage C is the following:

$$\overline{\rho}\cdot\overline{c_p}\cdot\left(\frac{\partial T}{\partial t}+u_x\frac{\partial T}{\partial x}+u_y\frac{\partial T}{\partial y}\right)=(1-\omega_{Bo})\cdot\Delta H_r\cdot\overline{\rho}\cdot\frac{dX}{dt}-\overline{\alpha}\cdot A\cdot\nabla(T_x-T_w)-K\cdot\nabla^2T-\overline{\rho}\cdot h_v\cdot\frac{dB}{dt} \quad (11)$$

Equation (11): Stage C Energy Balance

Along with the energy balance, a mass balance needs to be considered for the reaction from the start of stage C to the instant at which gelation point takes place. This mass balance is of a two fold nature: diffusive and convective, and both elements have to be considered when recalling the general equation for mass transfer and expanding its terms, as shown below. It also needs to be noticed that the assumptions taken in order to simplify equation (5) into equation (12) are that the gradient in the three coordinates (x, y and z) of specie B, i.e. blowing agent, ∇x_B, is much greater than the gradient of the concentration, ∇C, as the viscoelastic mixture is of homogeneous nature, i.e. same chemical composition at any point of the mass, and than any gradient of diffusion coefficient, ∇D, this considered negligible.

$$\nabla^2\left(C\cdot D_B\cdot x_B\right)+\dot{N}_B=\frac{\partial C_B}{\partial t} \quad (5)$$

$$\frac{\partial}{\partial x}\left(C\cdot D_B\cdot\frac{\partial x_B}{\partial x}\right)+\frac{\partial}{\partial y}\left(C\cdot D_B\cdot\frac{\partial x_B}{\partial y}\right)+\frac{\partial}{\partial z}\left(C\cdot D_B\cdot\frac{\partial x_B}{\partial z}\right)+\frac{\partial}{\partial t}\left(\overline{h_m}\cdot A_s\cdot\left(C_{B,S}-C_{B,\infty}\right)\right)=\frac{\partial C_B}{\partial t} \quad (12)$$

Equation (12): Stage C Mass Balance

From this equation, it can be seen that there is a direct relationship between the variation of the blowing agent concentration with time and the diffusivity coefficient, therefore the mass

balance contains a diffusive component. Other authors have also shown a similar relationship [146]. When the non-instantaneous mass transfer from liquid to bubble is incorporated in the mass balance formulation, and concurrently considering that the maximum resistance will be related to the formation of blowing agent, the following relationship was defined (for *quasi*-spherical bubbles with a diffusional component):

$$\frac{dB}{dt} = K_m \cdot (B - B_0) \cdot n_b \cdot \rho_p \tag{13}$$

In this equation, $(B\text{-}B_0)$ is the increment of mass of blowing agent (CO_2/vapour) up to that instant, n_b the number of bubbles per unit mass which will evolve into cavities and K_m is the mass transfer coefficient with a diffusional component [145, 146], defined for this particular case as,

$$K_m = 2 \cdot D_B \cdot \pi \cdot d_b \tag{14}$$

This relationship shows that the diffusivity coefficient is directly linked to the formation of the blowing agent. Higher rates of diffusion will be associated with high rates of blowing agent formation.

- **Stage D: $X_{gel}<X<1$**

At the end of stage C, the gelation point is achieved. This commences a new stage, which is considered to start at gelation point ($X\approx0.5$) and finish at the end of the reaction, when the conversion factor is (theoretically) 1. After the gelation point, when it is considered that no more cavities (i.e. cells) are created and/or the formed ones in previous stages do not collapse, it is widely reported [143-145] that all the blowing agent (CO_2 gas) is already produced. Effectively, for the general energy equation, this results in: $dB/dt = 0$.

At the start of this stage, bubbles have reached their maximum expansion by trapping the CO_2 gas. When a material element reaches the reaction extent of gelation, it is assumed that its density will remain constant. Bubbles can neither grow nor collapse. Gelled elements keep pressure uniform, but not constant, throughout the matrix. The final structure is obtained when the whole polymer matrix has gelled. In ideal circumstances, the gelation point happens simultaneously for the whole foam. Although not really true, this is assumed by many authors. Experimentation [142, 144, 150] shows that the foamed material that gels first is the one located near the container walls, because it remains at a lower temperature during the foaming process.

The contributions to the energy balance in stage D are: heat generated by the reaction, conduction and convection. Although convection is still considered here (due to the presence of large pores), conduction is a dominant phenomenon over convection, which will decrease in value until becoming negligible at the start of stage E.

The assumptions at this stage are:

- Vapour/Gas molecules velocities are considered small and decreasing at this stage (u_x, u_y, u_z =0).
- The gradient of temperature along the z-axis (variation of temperature of the foam with height, dT/dz=0) is considered negligible, since the heat transfer from the foam surface to the surrounding air is insignificant (air is a poor conductor of heat and there is no variation of velocity or foam height in the z-direction.
- Dissipated air by convection is also considered negligible due to the lack of turbulent air above the free surface of the solidifying foam)

Introducing these assumptions into the expression for the general energy balance, the following equation is obtained:

$$\overline{\rho}\cdot\overline{c_p}\cdot\left(\frac{dT}{dt}\right)=(1-\omega_{Bo})\cdot\Delta H_r\cdot\overline{\rho}\cdot\frac{dX}{dt}-\overline{\alpha}\cdot A\cdot\left(\frac{\partial(T_x-T_w)}{\partial x}+\frac{\partial(T_y-T_w)}{\partial y}\right)-k\cdot\left(\frac{\partial^2 T}{\partial x^2}+\frac{\partial^2 T}{\partial y^2}\right) \qquad (15)$$

Equation (15): Stage D Energy Balance

The mass balance also contains a term which represents the diffusion (by Fick's Law in the gradient at the boundary layer) and, in a smaller contribution, the convection term. Any gradient in the z-coordinate is considered negligible here too.

$$\frac{\partial C_B}{\partial t}=\frac{\partial}{\partial x}\left(C\cdot D_B\cdot\frac{\partial x_B}{\partial x}\right)+\frac{\partial}{\partial y}\left(C\cdot D_B\cdot\frac{\partial x_B}{\partial y}\right)+\frac{\partial}{\partial t}\left(\overline{h_m}\cdot A_s\cdot\left(C_{B,S}-C_{B,\infty}\right)\right) \qquad (16)$$

Equation (16): Stage D Mass Balance

After the gelation point, the viscosity increases drastically in detriment of diffusion, and consequently the mass diffusion coefficient (D_B) decreases making the transfer of the blowing agent slower through the boundary layer, among wall cavities. The stiffness of the cavities' walls promotes heat transfer mainly by conduction. As a consequence, it can be concluded that the soft elastic gel nature created after gelation does not promote growth of bubbles.

- **Stage E: X=1**

At this stage, the reaction finishes. The only event at this stage is that the temperature decreases until it matches the water bath temperature. Once that temperature is reached, the conditions in the reaction vessel are adiabatic, as there is no exchange of heat.

As the foam is rigid and the polymeric cells are fully formed, the convection contribution to the energy balance can be assumed to be zero since the velocity at which vapour/gas molecules moves (from cavity to cavity or inside each cavity) is too small to be significant. This velocity decreases rapidly from the gelation point due to the introduction of a rigidity term in the polymeric matrix. It is also assumed that the gaseous fluid adheres to the wall of the cavities, and therefore the heat flow at the wall will be by conduction, not by convection [144]. For this reason, heat will be transmitted mainly by conduction (which causes the drying of the foam) until there is no temperature gradient in the foam (dT/dt = 0).

$$\overline{\rho} \cdot \overline{c_p} \cdot \left(\frac{dT}{dt} \right) = k \cdot \left(\frac{\partial^2 T}{\partial x^2} + \frac{\partial^2 T}{\partial y^2} + \frac{\partial^2 T}{\partial z^2} \right) \tag{17}$$

Equation (17): Stage E Energy Balance

Similarly the mass transfer equation for this stage does not include a convective term. The only process related to the mass flux during this stage is the diffusion of any remaining solvent and vapour from the foam volume to the outer environment. The content of the blowing agent here is mainly vaporous resulting from the drying of the foam.

$$\nabla^2 \left(C \cdot D_B \cdot x_B \right) = \frac{\partial C_B}{\partial t} \tag{18}$$

$$\frac{\partial}{\partial x}\left(C \cdot D_B \cdot \frac{\partial x_B}{\partial x} \right) + \frac{\partial}{\partial y}\left(C \cdot D_B \cdot \frac{\partial x_B}{\partial y} \right) + \frac{\partial}{\partial z}\left(C \cdot D_B \cdot \frac{\partial x_B}{\partial z} \right) = \frac{\partial C_B}{\partial t} \tag{19}$$

Equation (19): Stage E Mass Balance

3.2 Monitoring the reaction: Temperature and Conductivity

Because only some phases of the foaming process may be sensitive to sonication, it is desirable to monitor the progress of the reaction so the start and end points of each stage can be identified. However, any intrusive input in this fast growing system could provoke instability and, to a greater extent, collapse of the system. Furthermore, as soon as the polymeric melt sample is taken out from the reactor, it changes because the reaction cannot be instantly frozen. Hence, it was impossible to monitor the reaction by periodic samples extracted from the container where the foam was reacting. Therefore, only a non-invasive indirect measurement could be used for the experimental rig.

Because the urethane polymerisation reaction is exothermic by nature (i.e. it produces heat into the surroundings and increases the temperature in the sample), the reaction temperature was employed to measure the conversion rate and identify the moment at which the reaction ends. Once the maximum temperature had been reached, the reaction finished [139], and the bulk temperature reduced until the ambient temperature (i.e. water bath temperature) was reached.

Electrical conductivity also offers the possibility of monitoring the events inside the vessel containing the foam. This technique is particularly valuable in processes where foams cannot easily be visualised [151] (e.g. continuous monitoring of draining rates and stability of foams [152]). This variable will be exploited in Chapter 5 for analysis of the different foaming stages and comparison against the theoretical stages referenced in the literature and described in section 3.1.2.3 of this chapter.

3.2.1 Conductivity. Hypothesis

Electrical conductivity is the inverse of electrical resistivity. Electrical resistivity of a foam indicates its ability to impede the flow of electrical current through the substance. The hypothesis made here is that its variation during the reaction reflects the state of the process (e.g. liquid, rising, cross-linking, solid, etc). In the liquid state, resistivity will be very low (i.e. high electrical conductivity due to the dissolved species). However, during cross-linking, the electrical resistivity will increase due to pore formation, producing cavities that will dry up by the end of the reaction. This situation will produce a very high value of electrical resistivity readings. The greater the porosity, the higher the resistivity is registered.

Mathematical relationships between electrical properties and mechanical properties have been widely reported in the literature where researchers have been motivated by the desire to create non-destructive testing methods [153].

Electrical resistivity of a foam can be measured by applying a voltage between two probes which are in intimate contact with the material and measuring the response voltage, by the following relationship:

$$Q_x = \delta \cdot \frac{L}{A} \tag{20}$$

Where Q_x represents the resistivity, δ the dielectric constant of the material, L, the fixed distance between the measuring probes, and A area of exposed surface.

The dielectric constant can only be considered as a constant value if the material is homogeneous and does not contain impurities. The tabulated values for dielectric constants widely found in the literature have been calculated after testing solid pieces of material which have not suffered deformities during testing. However, if the material undergoes a distinguishable variation, causing its chemical (i.e. nature) or mechanical (i.e. viscosity) or structural (i.e. porosity) characteristics to vary, its dielectric value will also change. In this case, the dielectric property was measured in the foam simultaneously with its chemical reaction which also provoked mechanical and structural changes. Therefore, a constant value for δ, dielectric constant, cannot be assumed.

During the foaming of the polymeric melt, the wetted surface on the measuring probes varied with time. In a first stage, the wetted area on the probes corresponded to the liquid mixture volume held in the container, and the resistivity value of the solution (i.e. monomers, acetone and water). When the foam was growing, the wetted surface increased with the foam's height in the vessel. In later stages, once the final height was reached, the effective path length between the probes changed due to the cavity formation during the chemical reaction. The surface decreased due to cross-linking (i.e. the material formed cavities that are interconnected among them by 'necks'. The surface area in intimate contact with the probes decreased). This area is related to cell walls and their thickness. Therefore, it can be considered that resistivity of a foam depends on:

- Resistivity of the foam liquid components (i.e. acetone, water) and their amounts.
- Pore architecture –varies depending on the stage of the reaction.

Electric current can only pass through a polymeric foam because of the conductive solution that it contains. When the foam dries up, it becomes a good electrical insulator. In the system studied, the hypothesis stated is that resistivity will exhibit an exponential decay (from liquid, high conductivity, wetting the probes) to a solid with voids that make it very insulating (very low conductivity).

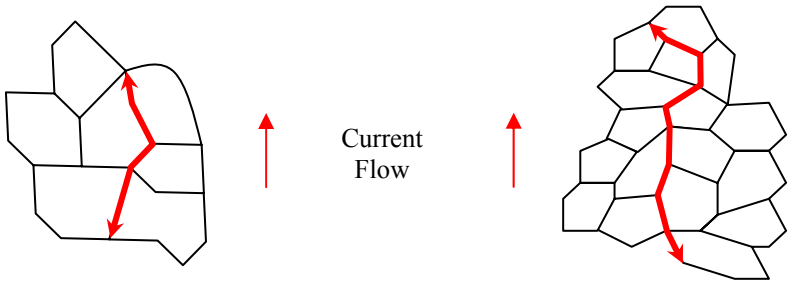

(a) Initial stages of polymer foaming (b) Later stages: reticulated foam

Figure 14: Cross-linking process monitored by resistivity

Therefore, an estimation of the stages at which the reaction is could be established as a function of the electrical resistivity measured in the foaming system:

Stage 1: (melted monomers + C_3H_6O) + H_2O :: Liquid = Resistivity 1

Stage 2: Closing pores towards a closed-cell structure :: Gelatine = Resistivity 2

Stage 3: Cross-linking process finished :: Solid PU foam; resistivity in network ≈ very high, Resistivity 3

Resistivity 1 < Resistivity 2 < Resistivity 3

Consequently, it appears likely that if the resistivity is plotted against time, the progress of the cross-linking process can be monitored.

As can be seen in Figure 14, in the latter stages of the foaming process, the electric current path is longer when polymer is cross-linked, which increases electrical resistivity.

To summarise: One of the hypotheses for this work is that electrical resistivity measurement provides information on foam progress with time, and thus making it possible to identify specific stages in the reaction (section 3.1.2.3). Furthermore, it will enable investigation on how ultrasound affects the length of the reaction stages.

3.3 Theoretical principles of Ultrasound

Sound, as a form of energy, has been chosen to interact with the foaming polymeric melt and, when irradiated in a controlled way, has become a porosity tailoring agent. The upper human audible threshold is 18 kHz (varying with age and gender). Accordingly, frequencies beyond 20 kHz are termed ‘ultrasound’. Ultrasound, as any other wave transmitting through a material medium, causes the particles of the irradiated medium to be set into vibrational motion and gain kinetic energy [154]. The defining equation for a pulsating incident field of sound is:

$$p(t) = P_0 + P_A \cdot \cos(\omega \cdot t + kx) \tag{21}$$

Where P_0 represents the initial sound pressure in a undisturbed medium (i.e. hydrostatic pressure); P_A, applied acoustic pressure; ω, angular frequency which depends on the frequency of irradiation (ω =2πf); k, wave number; x distance from the source, so the term 'kx' represents the phase angle of the signal.

For the purpose of this work, a wave was continuously emitted (standing wave within rigid boundaries, i.e. walls in between which it was transmitting) from the source. Therefore, the defining equation is expressed as [118, 154, 155]:

$$p(t) = P_0 + P_A \cdot \cos(kx) \cdot \sin(2\pi f \cdot t) \tag{22}$$

An ultrasonic standing wave is characterised by its frequency and amplitude. Frequency is related to period and wavelength. If the medium where the waves are transmitted is known, the wavelength, λ, can be calculated by using the relationship:

$$\lambda = \frac{c}{f} \tag{23}$$

Where c is the speed of sound in the medium (e.g. 1480m/s in water at normal conditions of temperature and pressure. The speed of sound in water only varies significantly from its value in extreme conditions, e.g. the deep ocean [156]); and f, the transducer irradiating frequency. Therefore, the spatial position of nodes and antinodes can be localised at one half-wavelength (λ/2) apart.

As the ultrasound travels by sinusoidal waves in the medium, during the positive half of the stress cycle, energy is absorbed and during the negative half, energy is given up.

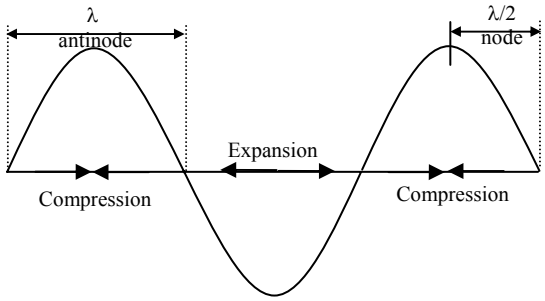

Figure 15: Energy cycle for an irradiated bubble

This will have a pulsating effect in the polymeric liquid and viscoelastic foam medium, where bubbles will bounce when irradiated. The ultrasonic gassing/degassing of the bubbles

in the liquid has been defined as [115, 117-119, 124, 157-159], where p(t) is the instantaneous acoustic pressure suffered by the bubble:

$$p(t) = P_0 \pm P_A \cdot \sin(2\pi f \cdot t) \tag{24}$$

3.3.1 Ultrasound attenuation

Ultrasound attenuates as it progresses through a medium. Assuming no major reflections (i.e. ideally avoided by covering all rigid walls in the experimental environment with sound absorbent material) the three major causes of attenuation are scattering, absorption and diffraction.

3.3.1.1 *Scattering:*

Since clean water is used for the water bath, there are no particles that could produce scattering effects, so it is assumed that attenuation of ultrasound due to scattering is negligible.

3.3.1.2 *Absorption:*

The same displacement, amplitude (A, m) around the neutral position will happen at any distance, x, from the source of energy if attenuation is not considered. However, in real cases, attenuation takes place, producing a decrease in amplitude as the distance x increases from the source. Attenuation due to absorption is intrinsic by the decay in energy of any sound wave travelling through a material medium. On the same plane of irradiation [154], the decrement of energy is inversely proportional to the distance from the source and the absorption coefficient, α, (5.10^{-4} cm^{-1}, for water at 50ºC, 1 atm – working conditions in this case):

$$\frac{dE}{E} = -2 \cdot \alpha \cdot dx; \quad \text{as } E \propto I \; ; \frac{dI}{I} = -2 \cdot \alpha \cdot dx \tag{25}$$

If the latter expression is solved by applying the boundary conditions, ($I=I_0$ when x=0), the intensity integral becomes:

$$I_x = I_0 \cdot \exp(-2 \cdot \alpha \cdot x) \tag{26}$$

And this expression gives the following, since intensity is proportional to the square of the amplitude [154, 155]:

$$A_x = A_0 \cdot \exp(-\alpha \cdot x) \tag{27}$$

In the last two expressions, the subscript ‘x’ represents the magnitude (intensity, amplitude) at any point, distance x from the source, and the subscript ‘0’ is the initial value for intensity or amplitude.

When the irradiation source is localised at a point, the maximum acoustic pressure (P) depends on the intensity provided by the ultrasonic device (I), the density of the medium (ρ), and speed of sound in that medium (c). For practical purposes, the acoustic pressure is expressed in averaged terms (i.e. RMS) and it is usually measured with the aid of a hydrophone.

$$I = \frac{P_{RMS}^{\ 2}}{\rho \cdot c} \tag{28}$$

3.3.1.3 *Diffraction:*

A travelling soundwave that encounters different materials will diffract (as happens with light) and, in its extreme, reflect. The boundary between two materials of different acoustic impedances is an acoustic interface, similar to light travelling from continuous medium 1 to continuous medium 2. For this research work, the sound waves travelling through water that encounter a polystyrene wall and, after that, a viscoelastic foamy medium to propagate, will suffer diffraction.

Acoustic impedance (Z) is the most important acoustic property of a material and it defines how it transmits, deflects or refracts sound. Essentially, Z, (units Kg/s.m^2 or Rayl) is the resistance to displacement of the medium particles by sound.

$$Z = \rho \cdot c \tag{29}$$

For plastics and rubbers, Z falls in the interval 1 to 5 MRayls; in particular, polypropylene's impedance is 2.47 MRayls. Impedance of water and air are, respectively, 1.48 MRayls and 400 Rayls.

As with light, when sound strikes an acoustic interface, the amount of sound energy that is reflected, diffracted and transmitted across the boundary depends on the incidence angle. The intensity transmission coefficient (T_a) between a medium with impedance Z_1 to another medium with impedance Z_2, is defined via the relationship [154, 155]:

$$T_a = \frac{4 \cdot Z_1 \cdot Z_2}{(Z_1 + Z_2)^2} \tag{30}$$

Also well established as a factor to measure the quality of coupling agents (e.g. for ultrasonic irradiation in medical applications) is the intensity reflection coefficient (R_a),

$$R_a = \frac{(Z_2 - Z_1)^2}{(Z_1 + Z_2)^2} \tag{31}$$

Consequently, it can be shown that the greater the difference between the acoustic impedances, the higher the reflectivity.

In this case of study, the ultrasound was produced by a piezoelectric (PZT) crystal [154, 156] mounted on a ultrasonic probe that emitted inside an ultrasonic bath. In free-field conditions, the transducer horn-tip used in this study moves as a circular piston. This probe emitted ultrasound in spherical waves: it propagated sound in all directions in a uniform absorbent isotropic medium by a point source having a nominal power, P_m. The intensity of the sound is related to the radius by the inverse square law. When an infinitely non-absorbent medium is used, intensity, I, at any point at a distance, r, from the source is obtained by dividing the rate of flow of energy (i.e. power of source) by the total surface area of a sphere of radius, r, having the source at its centre:

$$I = \frac{P_m}{4 \cdot \pi \cdot r^2} \tag{32}$$

3.3.2 Single Bubble behaviour in an acoustic field

By subjecting a liquid (with a dissolved gas in equilibrium following Henry's Law, $C(t)=K_H.p(t)$) to a sinusoidal irradiation (i.e. sound field with a given pressure, amplitude and frequency), cavitation bubbles can be formed and the initially dissolved gas acts as nucleation sites for these bubbles [65, 66]. As illustrated in Figure 16, if the subsequent expansions/contractions of the bubbles are not too sudden, the cavitation can be maintained in a stable regime (i.e. also termed as rectified diffusion). However, if these are not constructive, transient cavitation will take place and bubbles implode.

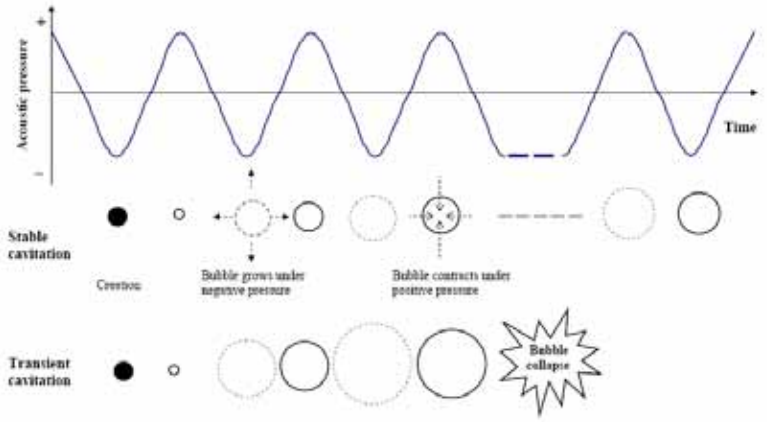

Figure 16: Types of cavitation by an irradiated bubble, based on [98]

This happens due to two effects [115, 117, 157, 160]: A bubble pumping the gas, initially dissolved in the fluid, into its cavity by using the energy of the sound field, will be subjected to the phenomena described below when considering Henry's law conditions (i.e. pressure inside of the bubble decreases with concentration):

1. ‘Area effect’: during bubble pulsation, the surface of the expanding bubble exposed to the irradiating wave is greater than that of the bubble in the compression cycle. The amount of gas that enters the bubble during expansion is higher than the amount of gas leaving when compressing, so the increment in volume for the bubble is positive. The bubble gains a considerable amount of gas over many cycles.
2. ‘Shell effect’: gas diffusion is controlled by the thickness of the ‘shell’ around the bubble (i.e. the diffusion layer). When the bubble expands, the shell becomes thinner and the concentration gradient increases. Flow rate increases. When the bubble is compressed, the shell is then thicker, and the concentration gradient decreases. Flow rate decreases.

$$P_b - P_l = \frac{2 \cdot \sigma}{R} \tag{33}$$

Equation (33): Laplace’s equation

Where P_b is the pressure inside of the bubble, P_l, the pressure in the liquid, σ, the surface tension and R, is the bubble instantaneous radius.
For a smaller value of radius, values of ΔP are bigger, and involve more flow rate in order to keep the energy equation consistent.

For a particular frequency of the sound field, there is a threshold of acoustic amplitude above which a bubble with a given radius will grow, and below which it will tend to dissolve. This threshold is established by a balance of forces, where the most distinctive term is the Bjerknes force, which is the force originated from the pressure difference across the bubble [117, 161], this is, the pressure gradient generated in a unit volume, averaged in time:

$$f_r = -\langle V(t) \cdot \nabla p(t) \rangle \tag{34}$$

As p represents the pressure field in a standing wave, the most common expression for the Bjerknes force is:

$$f_r = k \cdot P_A \cdot \sin(kx) \cdot \langle V \cdot \sin(\omega \cdot t) \rangle \tag{35}$$

Equation (35): Bjerknes force for a bubble in a standing wave

Crum et al. [66, 115, 162] and Apfel [65], among others, have attempted the numerical calculation of this threshold or its determination from experimental data [161]. It has been demonstrated by both theoretical and experimental studies that these equations adequately

predict the threshold of an acoustic pressure value for a gas bubble pulsating in a gassy liquid. However, these relationships have been established for single, isolated bubbles in water. Therefore, these cannot be immediately applied to a community of bubbles evolving dynamically in a viscoelastic medium. When considering polymeric solutions, these defined equations have limited applicability and need further research to develop equations that cover a variety of conditions (e.g. varying viscosity, damping effect, progressive sound attenuation, etc). Section 3.3.3 details the few reported results for such complex systems.

A dynamic threshold is a better approach versus a minimum value of acoustic pressure stated initially and maintained during the process. When a community of bubbles pulsating in a polymeric matrix is considered, it seems more appropriate to suppose that a different and incremental minimum acoustic pressure will be needed as the rigidity of the bubbles shell, then cavities walls, increases with the extension of the polymerization reaction.

3.3.3 Multi-Bubble behaviour in an acoustic field

The cell size and distribution within a foam largely determines its mechanical and physical properties, as its internal architecture will influence the way the whole artefact will react to any loading (e.g. impact, continuously applied pressure, etc). Several factors (e.g. temperature, pressure, viscosity range, solubility of blowing agent and nucleating agents, etc) can affect the final cell size distribution of a foam [163]. These can influence the polymeric matrix of bubbles in many different ways ranging from deforming and shaping cells through to coalescence and bursting of bubbles. Once the bubbles solidify, they will create cavities and pores. Therefore, any event affecting the initial bubbly mass will eventually have an impact onto the final foam architecture.

Much has been written about motion of a gas bubble in liquid when it is irradiated. Translational motion due to buoyancy and drag forces are not significant here since they have been defined for bubbles in aqueous solutions and in this case bubbles are pulsating a polymeric matrix that constrains their positions in the matrix from an early stage due to a "packing effect" (i.e. bubbles grow competing for space).

In particular, bubble growth rate has been generally predicted and represented by the Rayleigh-Plesset equation and its several approximations (e.g. Safar's, Eller's, Crum's, etc) [115, 162]. Many researchers have attempted to obtain simplified solutions to this hard-to-compute equation of motion for the particle surface and generated the following expression [116-118, 160]:

$$R\cdot\frac{d^2R}{dt^2}+\frac{3}{2}\cdot\left(\frac{dR}{dt}\right)^2+\frac{4\mu}{\rho_l\cdot R}\cdot\frac{dR}{dt}=\frac{1}{\rho_l}\cdot\left(P_g-p(t)+P_v-\frac{2\cdot\sigma}{R}\right) \tag{36}$$

Equation (36): Rayleigh-Plesset equation for bubble growth in a standing wave

Where P_g and P_v represent, respectively, gas and partial vapour pressures, the latter assumed to be constant during the process.

However, this expression was developed for 'free' bubbles, those which are suspended in a Newtonian liquid (i.e. water). On the contrary, the bubbles considered in this study are so called 'shelled' bubbles, bubbles pulsating in a viscoelastic matrix that offers resistance to the bubble's expansion/contraction induced by ultrasonic irradiation.

In the context of this work, the expression for encapsulated bubble growth rate (i.e. bubbles in a polymeric or starch matrix) by Church [124] and then simplified by Hoff [120], where the only variable is the bubble radius, is particularly important.

$$\begin{aligned}\rho_L\cdot\left(\frac{d^2R}{dt^2}\cdot R+\frac{3}{2}\cdot\left(\frac{dR}{dt}\right)^2\right)&=P_0\cdot\left(\left(\frac{R_0}{R}\right)^{3\gamma}-1\right)-p(t)\\&-\frac{4\mu_L}{R}\cdot\frac{dR}{dt}-\frac{12\mu_S d_{S0}R_0^{\,2}}{R^4}\cdot\frac{dR}{dt}-\frac{12G_S d_{S0}R_0^{\,2}}{R^3}\cdot\left(1-\frac{R_0}{R}\right)\end{aligned} \tag{37}$$

Equation (37): Growth rate for encapsulated bubbles in a standing wave

In this expression, γ is the polytrophic exponent of the gas, μ_L the liquid viscosity, $d_{S,0}$, represents the shell thickness at rest and G_S and μ_S are the elastic and viscous shell parameters.

After linearization to second order, Church [124] gave a possible analytical solution, that models the variation of the bubbles' radius with time, of the form:

$$R(t)=R_0+R_1\cdot\sin(\omega\cdot t+\phi_1)+R_2\cdot\cos(2\cdot\omega\cdot t+\phi_2) \tag{38}$$

In that same year, Leighton [157] published a similar approach, whose solution also shows the harmonic behaviour of the bubble size, which bounces, expanding and shrinking, while immersed in an acoustic field.

$$R(t)=R_0-\left[R_1\cdot\sin(kx)\right]\cdot\cos(\omega\cdot t-\phi) \tag{39}$$

Where R_0 represents the changes in the time-averaged radius due to the non-linear response of the bubble (i.e. the equilibrium radius that the bubble under study oscillates about); R_1 and R_2 represent the amplitude of the linear first harmonic and second harmonic pulsation,

respectively. R_1 is also the radius of a bubble subject to acoustic pressure at the first antinode, which is a maximum. ϕ_1, ϕ_2 and ϕ are angle phases taken relative to the phase of the incident acoustic wave. The positive signs in Church's expression and the negative sign in Leighton's represent the same aspect, but with a different sign convection: in both cases, the expressions describe the increment in bubble volume caused by acoustic pressure irradiation.

3.4 Research hypotheses

Now that the essential theoretical principles related to this research work have been presented, the hypotheses driving this investigation can be stated. These will be presented in the same order that the theoretical background and state-of-the-art have been introduced. The hypotheses proposed here can be summarised in the following statements:

1. Ultrasound has a sonochemical effect on the reaction, enhancing the reaction rate and aiding a faster production of intermediate species to generate the products.
2. Ultrasound affects convective mass transfer during foaming, especially during rise and pre-gelation stage, and enhances diffusion of the blowing agent (i.e. CO_2 gas) from bubble to bubble in the pre-gelation and post-gelation stages.
3. Electrical resistivity can be used to monitor the different stages of the foaming process with significant variations in measurements produced during the polymerisation and drying of the final solid foam.
4. Ultrasound has a physical effect in the foaming: the (Bjerknes) forces and shear stresses applied allow mechanical stirring that decreases viscosity, increases flexibility of the cavity walls and aids permeability. This makes the foaming polymer less prone to collapse while the mass of gas transfer into the bubbles can be sustained for longer time.
5. Ultrasound influences dissipation of heat by conduction, as this is directly linked to the instantaneous density of the foam. A direct consequence of this is the ability that ultrasonic irradiation has to reduced "skin" formation in foam billets.
6. The spatial position of nodes and antinodes are located at one half-wavelength ($\lambda/2$) apart (Figure 15). Sound travels in a medium at a speed, given by the expression: $c = f \bullet \lambda$, where value for c in water is 1480m/s (a value which remains constant at standard conditions of temperature and pressure). Considering that different media transmit sound at different velocity, there is a mismatch expected between the theoretical locations of maxima/minima, and the experimental ones, due to the

change in the value for λ. per acoustic interface (i.e. the boundary between two materials of different acoustic impedances, Z_1 and Z_2).

7. Acoustic pressure by ultrasound can be tuned in such so that bubbles can pulsate in a stable cavitation (i.e. rectified diffusion) state. These bubbles are predisposed to pump gas from liquid, so they grow due to positive displacements. The size of the bubbles will, under certain conditions, reflect the position of nodes and antinodes in the acoustic field and the variation in the acoustic pressure.
8. When conditions of stable cavitation are established, ultrasound can create porosity gradation by producing bubbles of different sizes depending on the acoustic pressure that they are subjected to within the standing wave. This allows porosity to be engineered.
9. Under conditions of transient cavitation, the foam will nucleate, grow, coalescence and collapse due to the implosion of bubbles. The proposed mechanisms are both physical (i.e. extended shear stresses and mechanical stirring that have a degassing effect) and sonochemical (i.e. 'hot spots' in the matrix that produce undesirable chemical reactions that burn the foam).

These statements are further discussed in the following sections.

3.4.1 Effects of ultrasound during foaming. Proposed mechanisms

3.4.1.1 *Diffusion and Convection*

The following discussion recalls the equations that define the energy and mass balances for each of the stages of the polymeric foaming process.

Stage B is characterised by convection due to a rapid increase of volume at constant pressure. The contributions to the energy balance at this stage are the heat produced due to the exothermic reaction and the umbrella term that includes the vaporisation heat of solvents and the formation of CO_2 from the water. This can be assumed to remain constant when fixed quantities of water and acetone are used. It is unlikely that ultrasound plays an important role at this stage, since the foam growth is too fast to interact with the ultrasonic irradiation in a significant way that could produce a long term effect. If it did, it would aid a macroscopic convection of the blowing agent produced and its homogeneous distribution into the polymeric meta-stable bulk.

Stage C is the one where the largest number of variables contribute in terms of both energy and mass transfer, and, therefore, it is when the ultrasonic irradiation might have its biggest effect. At this stage, the melted polymer fills the container uniformly, and the cross-linking reaction takes place in order to turn bubbles into pores, strengthening the neck of the cavities. The opportunity to create a gradient of pore density arises at this stage. The density of each element (dx, dy, dz) changes accordingly to the formation of $CO_2(g)$ – blowing agent- and there is mass exchange (vapour, not liquid) with the neighbouring elements. A convective transport of mass and energy is intensified when ultrasound is applied to the sample.

Consideration of the energy balance for this stage shows that the conduction term is the one that can be affected and enhanced by ultrasonic radiation. Reported in the literature [142] and successively referenced in [143] is the fact that the thermal conductivity, K, is a function of instant foam density, $\rho(t)$. In other words, the dissipation of energy can be accelerated by the ultrasonic radiation, by both conduction and convection. This will decrease the difference in temperature (ΔT) at inner locations in the vessel and on the perimeter of the sample. A forced dissipation of heat assisted by ultrasound decreases the gradient of temperature at the container walls and in turn leads to a minimisation of skin formation during processing. This is an important aspect in terms of manufacture since skin formation (i.e. a high density layer of the same material) is undesirable in foams for structural applications, as the skin has very different mechanical properties from the core foam.

In addition to the convective event, mass-transfer resistance can be decreased with the application of ultrasound, as the mass diffusion coefficient (D) will increase. If D can be increased, then the formation of the blowing agent can be enhanced [146], by equations (13) and (14), $dB/dt=f(D)$. Conversely, the formation of blowing agent/vaporisation of solvents suggests D is the variable affected by ultrasound. Therefore, if ultrasound can influence the diffusivity, it can also accelerate the formation of CO_2, and vice versa, resulting in a reaction that is brought to “gelation point” in a shorter time.

The mechanical work put into the system by ultrasound assists the diffusion by increasing the rate of mass flux. Bubbles are subjected to stretching, shearing and compression-expansion (Bjerknes) forces.

Due to the difficulty in testing the viscosity of a polymeric material near the liquid-solid transition, many authors have been defending opposing viewpoints during the past 20 years. However, recent technological advances are permitting more accurate measurements, and the latest published results [141, 164] indicate that viscosity of the polyurethane viscoelastic melt is dependent on the shear rate and so a shear-thinning effect (i.e. viscosity decreases when shear rate is applied, independently with time) is created. Subsequently, one of the underpinning mechanisms in this work is that ultrasound provokes stirring and so the viscosity of the PU melt decreases due to its viscoelastic nature and shear-thinning type of viscosity.

At Stage D, ultrasound improves the permeability of the gas through the cavities walls. Although its impact on the polymer density is less pronounced than the effect produced in Stage C. Convection, even if small compared to conduction, is enhanced too, and both contribute to a larger permeability.

Ultrasound will have no effect on the foam's porous architecture if irradiated during Stage E, because the porous architecture is fully set, the walls rigid and the cavities defined.

3.4.1.2 *Sonochemistry*

The description of the foaming process presented in the previous section suggests that kinetics of polyurethane formation is likely to be enhanced as the shear rate is increased [141]. However, it is also possible that ultrasound will enhance the chemical activity during the polymerisation, extending the influence of ultrasound further than purely mechanical and physical effects.

The hypothesis presented here is that ultrasonic irradiation can enhance the formation of radicals (especially OH^-) and speed up the reaction via acoustic cavitation which leads to the formation of reactive species described in the reactions in the section 3.1.1.

3.4.2 How ultrasound can tailor porosity. Proposed mechanisms

3.4.2.1 *Stable cavitation in a sonicated field*

It has been stated by many authors, (section 3.3.3), that air bubbles can grow when the ultrasonic pressure amplitude is more than a threshold acoustic pressure. The first step in this work aims to determine whether polyurethane foam has a similar threshold for acoustic pressure below which there is no distinguishable effect on the porous architecture by the

ultrasonic irradiation. However a second upper threshold should also exist above which implosion and coalescence of bubbles is promoted. Between these two thresholds there is a region where acoustic pressure influences bubble size (i.e. 'stable cavitation' activity, rectified diffusion, promoted) without coalescence (i.e. 'transient cavitation', destructive, effect).

The bubble size is strongly connected to the standing wave. Because of the Bjerknes forces, and the maximum, in absolute values, of the acoustic pressure defined by the half-wavelength, the bubbles will grow gradually in the antinode of the standing wave due to the enhanced gas diffusion. The vessels containing the reactants will be placed in a sonicated field, whose intensity must be mapped within the bath so that known magnitudes of acoustic intensity can be related to the resulting porosity.

The different regions in the standing wave of the sonicated field might produce a variation in the bubble size distribution due to differences in the hydrodynamic forces acting on the bubble in the wave. The vessels' location has to be chosen considering that different media transmit sound at different velocity, there is a change in the value for λ per acoustic interface (i.e. boundary between two materials of different acoustic impedances, Z_1 and Z_2).

In addition to acoustic magnitude influencing the porosity gradation, frequency will also be tested in order to see whether the rate of bubble growth and, by extension porosity distribution, can be modified and tailored.

3.5 Summary

As it has been seen from the literature review, there are some applications of stable cavitation that have not been investigated yet. One of them, potentially, is porosity tailoring in the manufacture of polymeric foams. When the ultrasound is radiated into the polymeric melt undergoing foaming, the interaction that takes place at the early stages of the bubble growth and the later setting of the matrix, could be used as a porosity modifying agent for the polymeric foam.

After the analysis of both energy and mass balances, it is plausible that ultrasound could play an important role in the stages after rise time (when foam grows to its maximum height) and before the 'gelation point' (Stage C), enhancing the creation of CO_2 and pulsating cell wall causing it to expand without rupture; and between the gel point and the

end of the reaction (Stage D) assisting bubble permeability, convection and assisting gas migration.

The mechanism of fluid friction against the cavities wall is ruled by the 'Thin boundary layer' theory which states that there is a direct relationship between the transfer of fluid momentum to the wall and the transfer of heat by convection. In other words, rates of heat transfer are proportional to the shear stress between a fluid and the adjacent cavity wall.

As viscosity is a function of the shear rate, and PU is a shear-thinning liquid, when the melt is stirred, its viscosity decreases, making its viscoelastic walls less prone to collapse. Ultrasonic irradiation should produce a lowering in viscosity due to the stirring and heating of micro-areas. This gives more flexibility, the internal pressure inside the bubbles decreases, and they can grow bigger as a direct outcome. The direct implication is a density (mass per unit volume) reduction of those irradiated areas.

Ultrasound could have an effect because it affects the convection rate and, as the conductivity is a function of the density, also the conduction rate. This might provide a tool to control the temperature gradient in the reacting vessels walls, permitting minimisation of skin thickness. By provoking the bouncing of the bubbles, ultrasound could accelerate the mass diffusion and convection effects that are created in stages C, D and, in a small scale, in stage B.

This chapter has detailed some of the types of behaviour which might be expected in bubbles pulsating in an acoustic field. Experimentation has been carried out with low acoustic power in order to determine whether these effects (i.e. stable cavitation) can be quantified in practise.

These expectations on how and when ultrasound can affect the foaming process will be discussed further in the experimental results chapter (Chapter 5).

CHAPTER 4. EXPERIMENTAL INVESTIGATION

This chapter describes the apparatus and procedures for the experiments conducted to investigate the theoretical phenomena identified in Chapter 3. Firstly, a description of the methodology for polyurethane foaming is given. Then, a summary of the variables that were taken into consideration in the design of a prototype experimental rig are listed and discussed, followed by the description of the final design for the experimental rig used in this work. The acoustic environment of the apparatus was studied in detail in order to determine the experimental characteristics of locations used for the reactant vessels inside of the water bath. Each of these locations provided different irradiation conditions for the samples, producing a different effect in porosity and cell distribution size. The chapter ends by discussing the issues of quantifying the porosity distribution in the foamed samples, and the different alternatives available for image processing of the sonicated foams in order to assess both porosity and cell distribution size.

4.1 Methodology

Although the formation of the foam has been described already in Chapter 3 in general terms, this section provides a detailed description of the procedure used. Figure 17 presents the different stages in the foaming process.

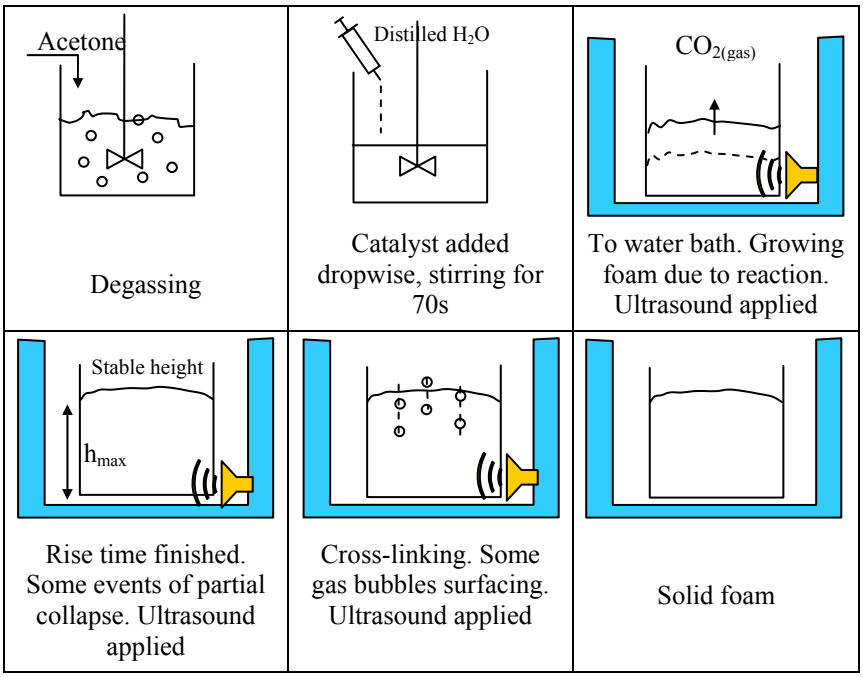

Figure 17: Foam formation in the lab

1. The polymers used in this study (Dow Pro Series polyurethane Foam, Dow Europe GmbH, Switzerland, RS 202-2636), were degassed from the blowing components (i.e.

methane, ether, isobutane) by dissolving in pure acetone. Acetone also assisted in removing moisture. It was important that these gases were removed from the mixture to allow control of the amount of initially dissolved gas. In this way, the amount of foam produced was only a result of the chemical reaction and the production of a known amount of blowing agent ($CO_{2(g)}$).

In the interval between preparation of the mixture and its foaming, the mixture was stirred (introduction of air in the fluid mass was minimum, i.e. without whisking, the bottle was rocked on a surface) in order to keep concentration homogeneity and temperature was controlled to minimise organic solvent evaporation. In all cases, the diisocyanate content in the mixture was rectified to have a fixed 40%. The relation PU-Acetone used was 50/50 %vol.

2. The caramel coloured liquid inside of the polypropylene container was placed inside the water bath and both thermocouple and conductivity probes inserted at this time (to obtain readings of conductivity and temperature when the water, catalyst for the reaction, is added). The water bath played a two-fold role in this application: it minimised any extreme gradient of temperature inside the container (from the foam to the surroundings and within the foam) during its formation to avoid the impact of temperature variation in the porosity gradient (sudden condensation of water or evaporation of solvents) and to buffer any build-up of the temperature due to ultrasonic irradiation.

3. The polyurethane forming reaction described in Chapter 3 was initialised by the addition of warm distilled water, which had the role of catalyst for the reaction and chemical blowing agent for the foaming process. This predetermined amount of distilled water (20%vol H_2O per ml of diisocyanate present in the mixture) was added drop-wise by syringe. The solution then turned into a milky brown colour due to the suspension of water/acetone droplets, which were perfectly miscible. The mixture was stirred for 70 seconds using a standard procedure for stirring and minimising air intake into the mixture. As described in Chapter 3, the addition of water simultaneously induced the generation of urethane and the formation of $CO_{2(gas)}$. Ultrasonic irradiation was commenced at this stage.

4. Instantaneously to the addition of water, the temperature of the mixture inside the container started to increase. The exothermic process kinetics in the acetone-polyurethane system is referred to in [165]. After a few seconds, the system reached the vaporisation temperature for the acetone (56.6^{o}C approx), which started to evaporate leaving more molecules of water free to react and so, increased the production of $CO_{2(gas)}$ (in the following referred to also as ‘blowing agent’).

5. Rapid cell expansion occurred at the beginning of the reaction due to the high rate of $CO_{2(gas)}$ production. The cream time (Stage B) started: the foam began to grow, filling homogeneously the volume of the container. Temperature continued to rise, causing super-saturation of the blowing agent in the reactive mixture, as indicated in Chapter 3 following Henry's Law. The diffusion of CO_2 from the liquid into the formed gas nuclei followed. Due to this diffusion into the bubbles, the cell growth produced a liquid mass expansion which occurred simultaneously with the polymerisation process.

6. During the initial stages of the process, the liquid foam was a *meta-stable* system (i.e. being an unstable and transitory but relatively long-lived state) that evolved dynamically: during expansion, cell wall thinning might have occurred, provoking temporary rupture of these (i.e. partial collapses). As the viscosity increased, cell walls became more rigid/less flexible, so the associated bubble pressure increased dramatically. This increment in the internal pressure gave rise to the existence of larger tensile stresses on the cell surface which may have resulted in cell rupture. During the rising time, bubbles were subjected to stretching, shearing and compression forces that could have provoked bubble implosion. If the shockwave affected the neighbourhood, it could make them implode also, provoking a partial collapse of the foam. Because this takes place at an early stage of the foam formation, the foam can recover and grow again, because CO_2 is still being formed. The diffusion of $CO_{2(gas)}$ among bubbles evolved towards an equilibrium. Gas permeated from smaller into larger bubbles because the internal pressure of smaller bubbles is higher than those of a bigger size. Cross-linking happened simultaneously to this process.

7. 5-6 minutes after the reaction started, the stable height of the foam was reached (rise time, Stage C). The termination of the foam rise was ascribed to a combination of depletion in the $CO_{2\ (gas)}$ concentration of the fluid matrix and the increased resistance of the bubble wall to expansion. The mixture was very viscous at this stage.

8. Once the stable height was reached, the production of $CO_{2\ (gas)}$ was considered to be finished. This happened at the, so called, 'gelation point' (end of Stage D). The final structure of the foam (cells walls bounding voids) was obtained. Bubbles could neither expand nor collapse. The overall reaction continued strengthening the walls: the polymerisation of urethane and its cross-linking. The bridges between cells hardened and, eventually, the bubbles formed rigid pores. Some bubbles could still float to surface due to the hydrodynamic buoyancy force. The foam was still sticky 'to-the-touch'.

9. After 10-12 minutes from the start, the foam became a solid and not sticky-to-the-touch. The temperatures dropped and followed any changes in the water bath. Ultrasonic

irradiation was stopped at this point. Samples were kept inside of the bath after the reaction finished for an extra 30minutes until the foam had a rigid complexion. This was done to avoid sudden changes of temperature that could provoke collapse of the pores due to the migration of trapped water vapour and $CO_{2(gas)}$.

10. Finally, samples were placed in a warm, humidity-controlled closet for 24 hours until they were fully cured.

4.2 Design of experiments

In this work, the sonication conditions for stable cavitation of polymeric foams have been explored. The design of the experimental rig and the experimental planning started with a 'trial-and-error' process to assess the then unknown effects of the ultrasonic irradiation when applied to different stages of the foam formation.

A summary of this has been compiled in Appendix I, where the most important variables that were taken into consideration during the design stage of the experimental rig, as well as the reaction conditions that had a major impact on the process, are detailed.

Figure 18 illustrates the iterative process by which the experimental conditions were optimised and the experimental rig developed.

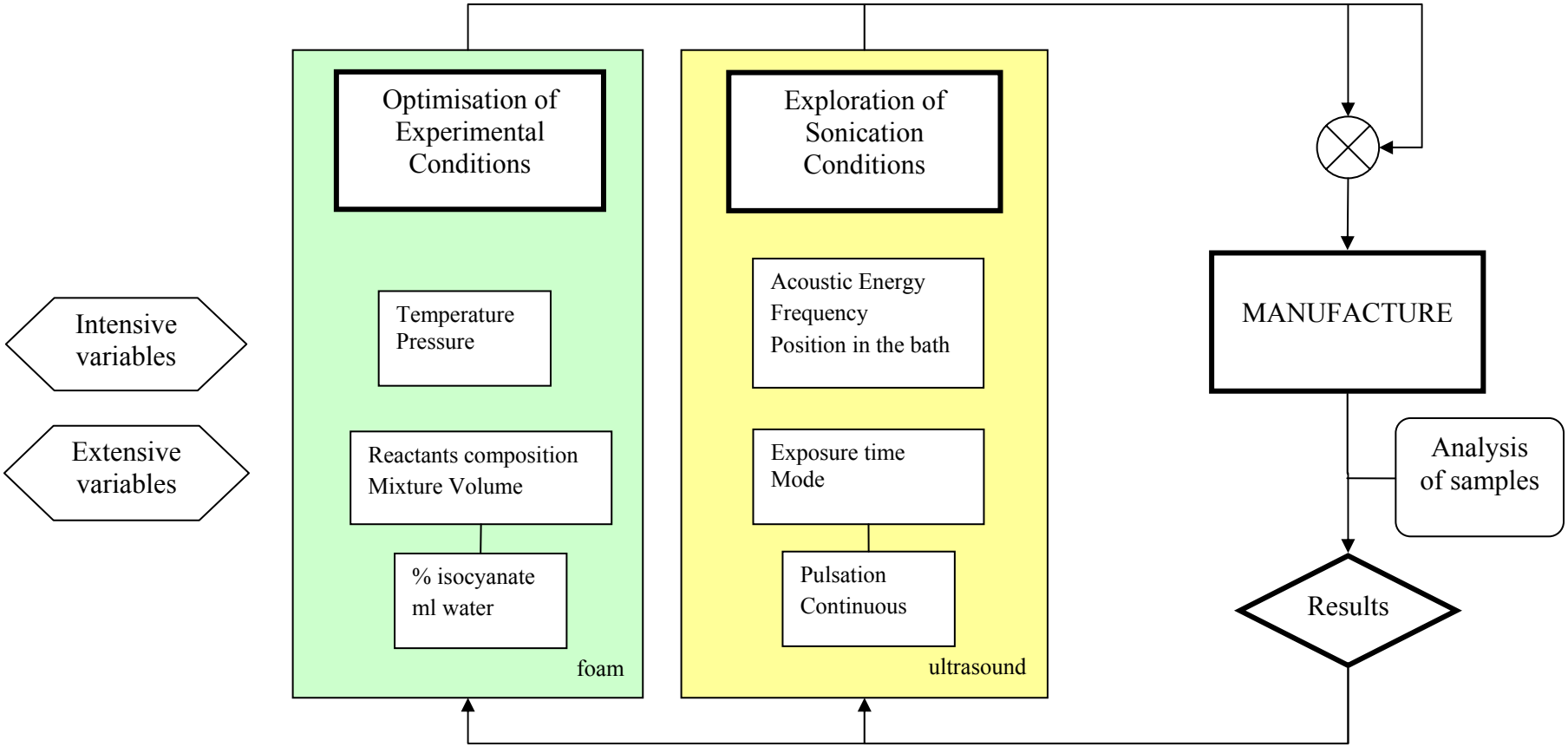

Figure 18: Flow chart for the design and manufacture process

4.3 Experimental rig

To enable a systematic investigation of the effect of ultrasound on the formation and final porosity of polyurethane foam, samples were irradiated in a temperature controlled water bath over a range of low frequencies and powers. The following sections detail the arrangement of ultrasonic sources/receivers for the experimental sessions and sensors within the water bath for the sound field mapping, and the chemical reactants used.

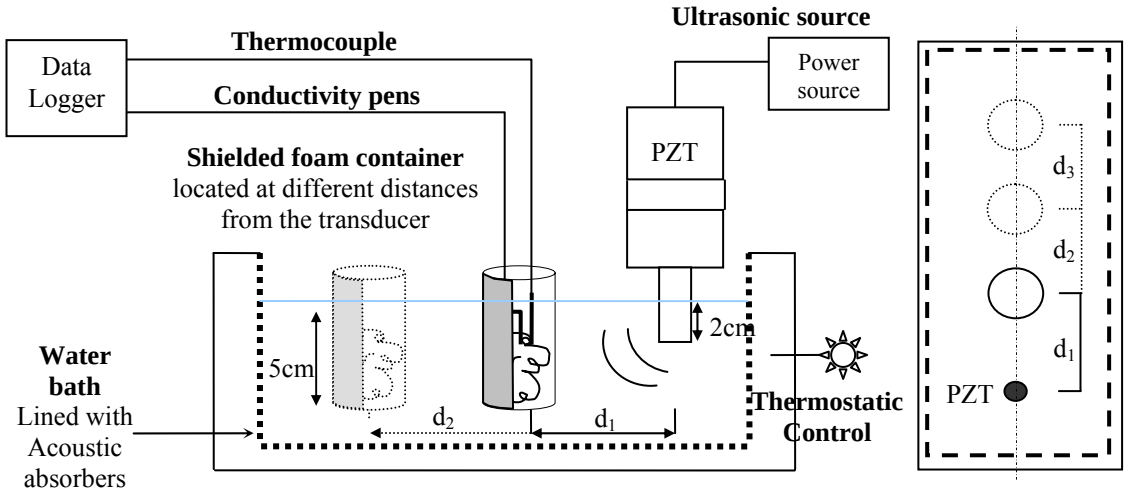

Figure 19: Schematic of the experimental rig, lateral and plan views

4.3.1 Apparatus

The schematic shown in Figure 19 illustrates the location of the ultrasonic source and the polypropylene container (a material chosen for its similar acoustic impedance to water) that holds the reactants (5cm diameter, 7cm height, 0.16mm thickness) within the 4 litres (30x15x15cm) water bath (all walls lined to minimise ultrasonic reflection). The container was firmly clamped with a lab stand and positioned along the longitudinal axis of the bath. The ultrasonic piezoelectric source used were a Bandelin Sonopuls horn, Germany, UW 3200, irradiated at 20 kHz; and a Coltène/Whaledent Biosonic US100, USA, irradiated at 25 kHz and 30 kHz. The applied power to these transducers varied depending on the experimental series detailed in Chapter 5, Results.

In order to have both transducer and receiver (i.e. the bubbling polymeric matrix) aligned, the sonotrode tip was immersed 2cm below the free surface, on the same plane as the central plane of the container, 5cm away from the right wall and in a central location (7.5cm from the long sidewalls). The use of the water bath ensured the temperature of the environment could be controlled independently of the effects of ultrasound. The bath temperature was set at 323K and controlled within +/-1K. Water was used as coupling agent

for ultrasound to transmit inside the bath (from the ultrasonic probe to the containers) because of its high specific heat.

Thermocouples were used to monitor the reaction and establish its completion (i.e. after peak temperature). They were held in the middle of the mixture foaming in an open-vessel.

The temperature variation with time was monitored and measured during the reaction with the aid of a K-type thermocouple (Farnell, 3mm x 150mm). It was recorded using a data acquisition system for each sample. Figure 20 illustrates the temperature record generated by an experiment.

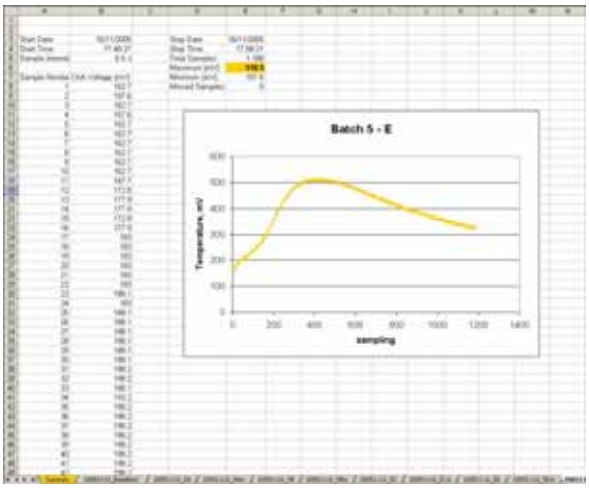

Figure 20: Screenshot from the data acquisition software for temperature

As already mentioned in Chapter 3, the maximum temperature recorded coincided with the end of the reaction [139]. This parameter (peak temperature) was used to compare the thermodynamics of the reaction for the different sonication conditions.

Electrical properties of the foams were evaluated in order to monitor the progress of foam formation through the different stages, as described earlier in this thesis (section 3.2). Electric resistivity of the foams was measured by using a two-probe resistivity measurement method. The circuit diagram is presented in Figure 21. In this method, the resistance offered by the foam (Q_x) to the excitation voltage applied (Base voltage, V_{BS}, 2.5volts DC) across the two measuring probes (terminals) immersed in the container where the reaction happens was measured. To do that, a potential drop produced by the foam resistance was measured after amplification of the signal at the instrumentation amplifier (Op-Amp). The output from the logic function in the Op-Amp was collected by the Data Acquisition Card (DAC) as shown in Figure 21b. The DAC is also a multi-functional instrument, datalogger and

oscilloscope (DS1M12 StingRay, USB Instruments™, EasySync Ltd., UK) and two channels could be collected at a time, one for the thermocouple readings and the other one for the resistivity.

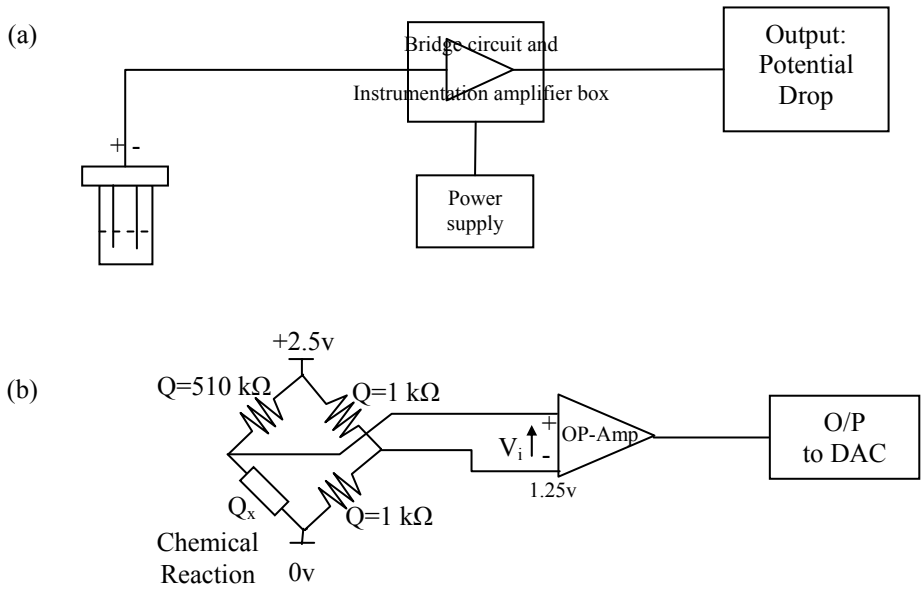

Figure 21: (a) Circuit Diagram of the apparatus used in two-probe resistivity measurement method; (b) Electronic diagram of the logic used

The size of the copper probes used to measure the electrical resistance were 2mm in diameter and 7cm in length, with a fix interval of 39mm between probes. Since the distance between these two surfaces was constant (fixed electrode spacing) and the applied excitation voltage (V_{BS}) is constant, the electrical resistance of this volume of foam was determined by measuring the output potential difference.

The measured potential difference is related to the applied voltage (V_{BS}) through the transference function, f(x), in this Wheatstone bridge by the relationship,

$$\frac{V_i}{V_{BS}} = f(x) \tag{40}$$

As the signal V_i is very small, an instrumentation amplifier is used. The block diagram for this system is as follows:

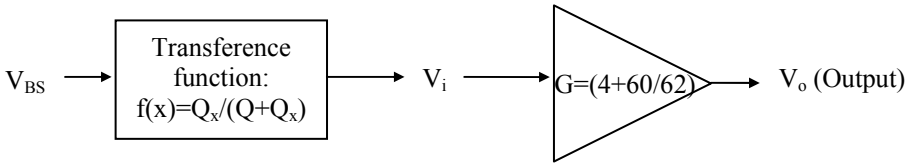

Figure 22: Block diagram for the electrical resistance measuring rig

And hence the relationship between the input voltage and the system parameters (e.g. resistors, voltage base) can be expressed as:

$$V_i = f(x) \cdot V_{BS} = \frac{Q_x}{Q + Q_x} \cdot V_{BS} \tag{41}$$

$$V_o = V_i \cdot G = \frac{Q_x}{Q + Q_x} \cdot V_{BS} \cdot G \tag{42}$$

Solving for R_x and including the numerical values for the gain, (G = 4 + 60/62), the supplied potential difference (V_{BS} = 2.5volts) and the reference resistance, (Q = 510 K-ohms), the value for Q_x , in kilo-ohms, is given by the equation:

$$Q_x = \frac{V_o \cdot Q}{G \cdot V_{BS} - V_o} = \frac{V_o \cdot 510k\Omega}{12.419 - V_o} \tag{43}$$

Equation (43): Relationship between foam resistance value and output voltage

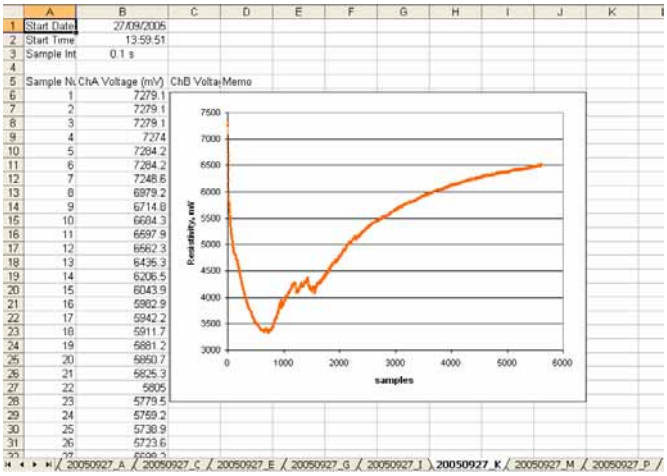

Figure 23: Screenshot from the data acquisition software for potential drop

All mixtures were sonicated in an open-vessel container to avoid the build up of the internal pressure due to the water vapour and gases generated by the reaction that could provoke unwanted implosion of bubbles. The container faced perpendicularly to the sonicating probe and had the opposite 180° of their surface shielded by an absorbent material to diminish reflections from the walls and enable investigation of the effects of “direct” sonication.

During the polymer foaming, the sonication conditions were of 'far field' (i.e. pressure waves are combined to form a more uniform front that the one in the 'near field' [155]). This is an area where the ultrasonic beam is more uniform and spreads out in a pattern originating from the centre of the transducer. A container located at shorter distances to the ultrasonic probe (i.e. 'near field'), is subjected to wave interference and extensive fluctuations in the sound intensity. The advantages of irradiating in the 'far field' (instead of the 'near field') of the sound waves coming from the transducer, is that interferences and fluctuations in the sound intensity are diminished. Essentially in 'far field' conditions, the foam 'sees' pressure waves that are combined to form a more uniform front that the one in the 'near field'[155].

Pairs of experiments were carried out to test the repeatability of the foaming process. The foams were irradiated for 20 minutes in a duty cycle of 2min on/1min off, starting after adding the distilled water. The level and frequency of this cyclic irradiation was established by initial experimentation (see Appendix I 'Design of experiments') and was sufficient to induce changes in the foam structure without causing collapse.

Recalling the basic experimental procedure, it is summarised as follows:

1. A measured amount of reactant was placed in the container located at a certain distance from the sonotrode
2. The process was initiated by addition of water, which is the chemical blowing agent and acted as a catalyst for the reaction
3. Ultrasound was applied
4. On completion of the reaction, the foam was left to cure for 48 hours
5. Once the sonicated foams were fully cured, they were de-moulded and cut in half with a coarse-tooth saw and trimmed
6. The cross-sections were scanned for further analysis.

4.3.2 Sonication field

The propagation pattern of the ultrasonic field at each of the frequencies and powers applied to the transducers was studied under constant values of ambient temperature and atmospheric pressure. This sonication field was also determined by the internal geometry of the water bath, the relative position container transducer, and by the attenuating properties of the transmitting medium –water–.

In order to obtain accurate values of the acoustic pressure required to acoustically excite a bubbly polymeric matrix at a specific position within the bath, it was necessary to know the spatial variation, layout of the stationary acoustic wave along the x-axis of the bath (Figure 25). This variation was measured with the use of a calibrated needle-type hydrophone (Brüel&Kjær, Denmark, type 8103) that was mounted on a lab stand moving on a rail. The hydrophone received the acoustic signal while immersed in the bath at each location and sent the electric signal to a data-logger digital oscilloscope (DS1M12 StingRay, USB Instruments™, EasySync Ltd., UK) connected to a computer (a Pentium II of 262MB RAM with a CPU 300MHz). This allowed assessment of attenuation and local signal strength during the irradiation process.

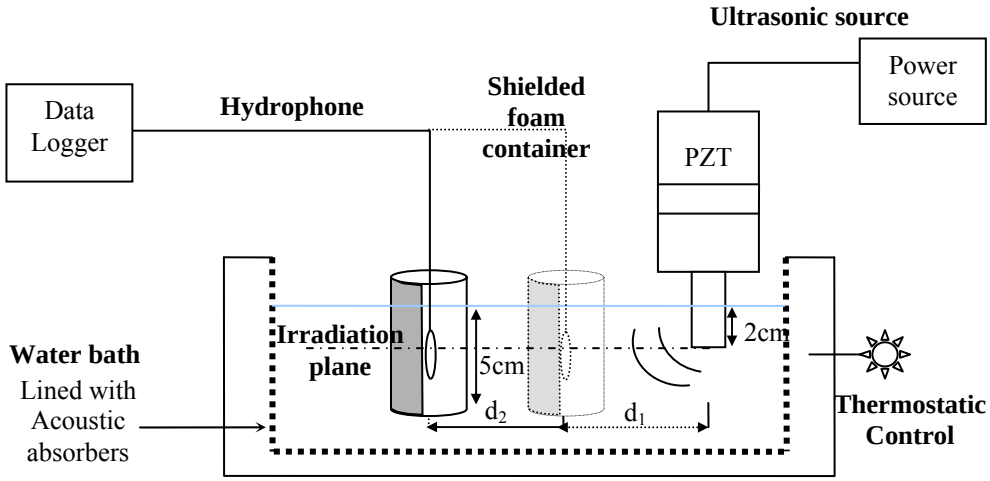

Figure 24: Strategy for signal strength mapping within the water bath (measured inside the vessel)

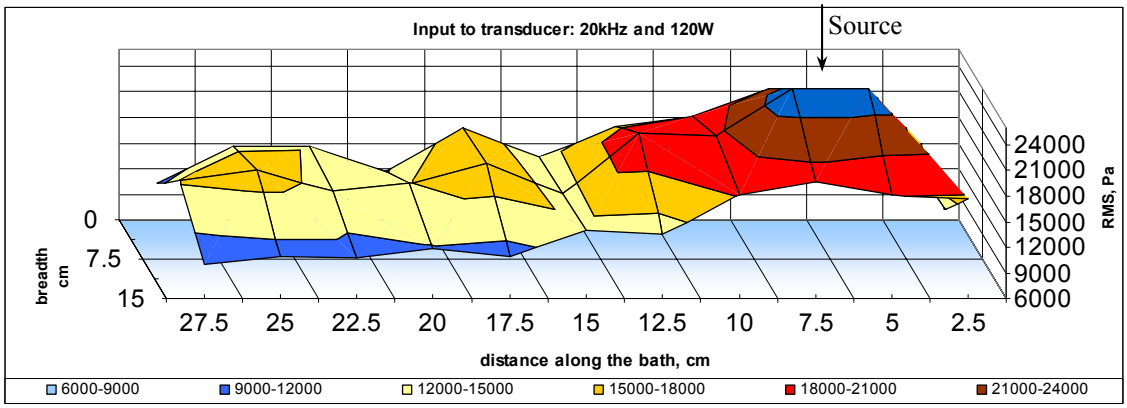

Figure 25: Mapping of water bath showing attenuation and partial maxima at half-wavelengths

Accurate measurement of this profile was necessary to establish the acoustic pressure amplitude at each position along the plane of study. This was determined from the voltage output, in root mean squared (RMS) mV, of the hydrophone, transformed to acoustic pressure, in Pa, using the calibration data on voltage sensitivity (27.8 μV/Pa) provided by the calibrating service/manufacturer.

To represent the acoustic field at which polymeric mass was subjected to, and to reduce effects of the hydrophone itself, the ultrasonic signal within the bath was mapped using a shielded hydrophone. The shield was a barrier made of the same material as the vessels that hold the chemical reaction. Measurements were taken with increasing distance from the horn-tip and on the same horizontal plane of irradiation where the central part of foam container was placed. The three working frequencies and every input power used to irradiate the foams were tested. Some of the resultant profiles can be seen below (Figure 26).

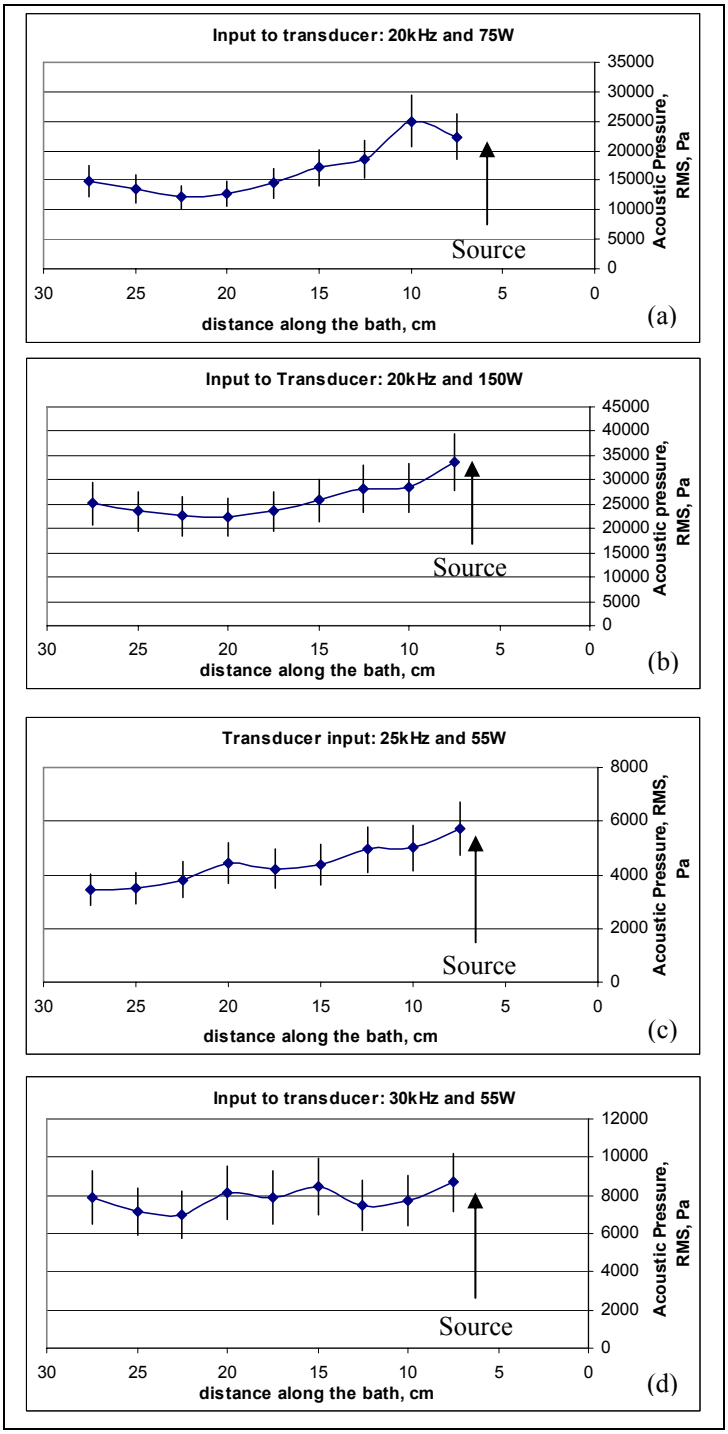

Figure 26: Acoustic activity in water bath for experimental conditions of frequency and applied power to transducer, measured with a hydrophone

A decreasing trend in the acoustic activity, i.e. signal intensity, was observed with an increase in the distance from the horn tip. These figures show that the stationary wave in each case has been distorted and a declining acoustic pressure profile existed due to the attenuation of the signal (i.e. absorption of energy by the transmitting medium acting as a coupling agent, scattering, reflections, etc [154]). The mapping and control of this pattern was of great relevance since, as demonstrated in Chapter 5, the acoustic pressure dramatically affected the porosity and cellular structure of the foaming system.

It can be also seen (Figure 26) that the acoustic activity and the resulting pressure field shows intermediate peaks (i.e. partial maxima in pressure at $\lambda/2$ distance, and odd multiples, from the source). This phenomenon has been reported in the literature [158, 166] and been exploited to check the type of cavitation involved in the sonochemical reactor [159, 167]. For the piezoelectric device irradiating at 20 kHz in an empty water bath, the half-wavelength ($\lambda/2$) is 3.7 cm; for 25kHz, $\lambda/2$ is 2.95 cm, and for 30kHz, $\lambda/2$ is 2.45 cm. However, the location of these partial maxima and minima were offset along the bath due to the diffraction and refraction events that the soundwave front experiences (i.e. liquid-solid-liquid interfaces, where the solid is the wall of the container where polymer reacted; bath walls and free surface of the bath).

4.3.2.1 *Simulation of the acoustic pressure distribution with COMSOL MULTIPHYSICS™*

The mapping of the water bath using the hydrophone illustrated the complex acoustic field within the water bath. In order to better understand the environment inside the bath, a numerical model was developed to simulate the propagation of the ultrasound signal within the bath.

The simulation was created using the finite element software package COMSOL Multiphysics™ 3.3 (Appendix II reports details of the numerical method used to calculate and carry out the simulation and a summary of the parameters chosen for the model). This application modelled the different conditions of wave profile type, boundary conditions, subdomain nature, locations of vessel, sonotrode intensity, etc.

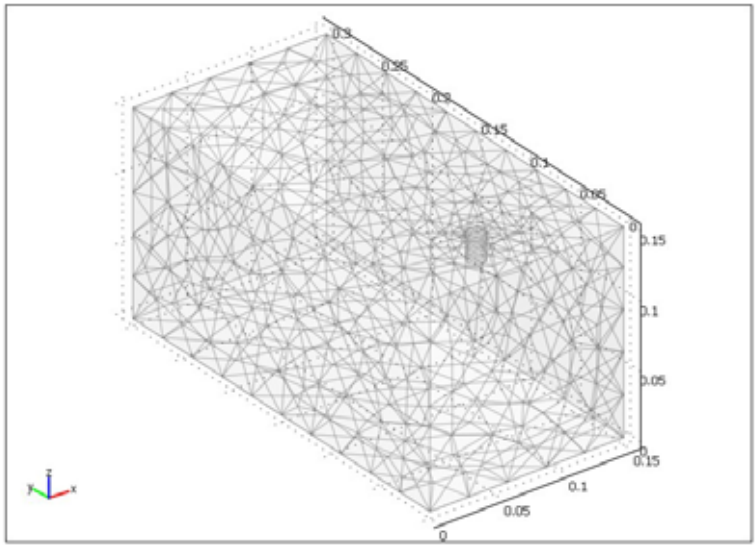

Figure 27: Mapped mesh of the bath in simulator

The water bath was modelled as a rectangular volume of length 30cm, width 15cm and height 15cm. The probe was represented as a cylinder of 13mm diameter and 2cm height (Figure 27).

One of the key parameters of the model was the nature of the boundaries surrounding the volume of the bath. To investigate the effect of wall conditions, plots of acoustic pressure along sections and lines through the volume were compared for different types of wall. Table 4 shows a comparison of modelled values for different simulation scenarios. The change from the “spherical wave” to the “cylindrical wave” condition did not significantly alter the pattern of the resulting acoustic pressure. Therefore, the model was simulated with an irradiated cylindrical wave, as detailed in the technical specifications for the ultrasonic probe. The power irradiated by the sonotrode into the bath was set to 150W, equivalent to 914476.8Pa, for a probe diameter of 13mm. The cross-sections were obtained in the middle of the water bath, and the plots along the x coordinate aligned to the sonotrode’s free face plane.

The mesh consisted of 6030 elements and the solver parameters used in this simulation for the time stepping were 0:0.5:10s with a relative tolerance of 0.01s. The average solving time was 72.6 seconds on a Pentium 4 with 512MB RAM with a CPU 2.40GHz.

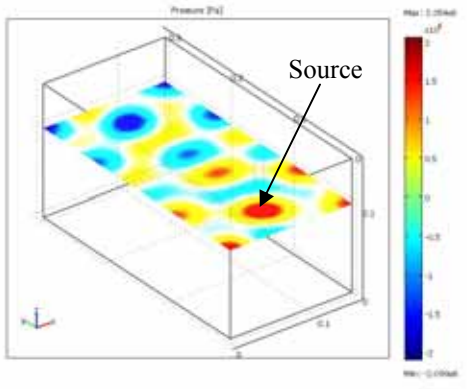

(a.1) ‘Hard’ walls. Plane

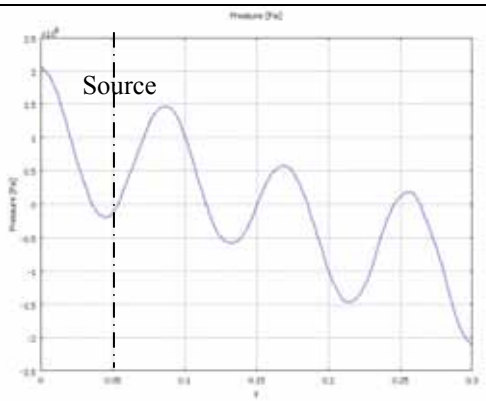

(a.2) ‘Hard’ walls. Plot across the bath

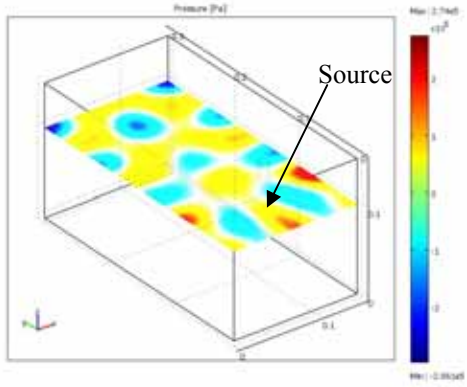

(b.1) Steel walls. Plane

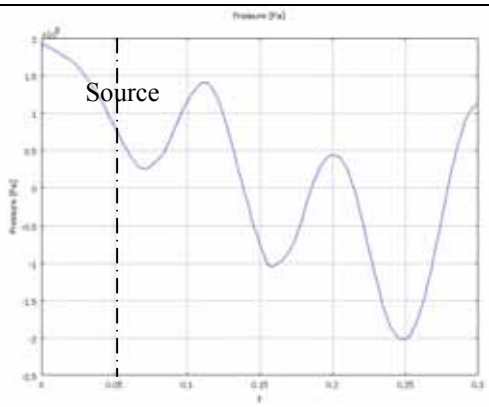

(b.2) Steel walls. Plot across the bath

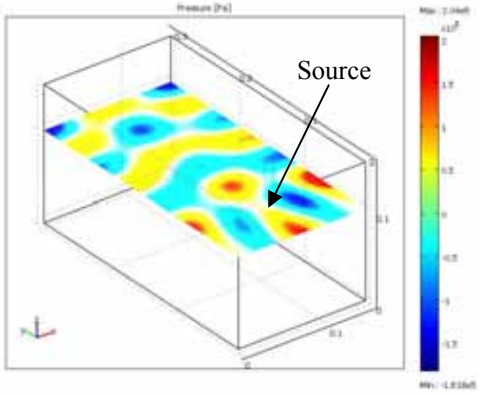

(c.1) Aluminium walls. Plane

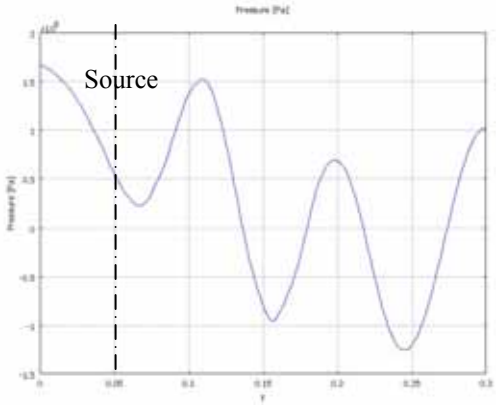

(c.2) Aluminium walls. Plot across the bath

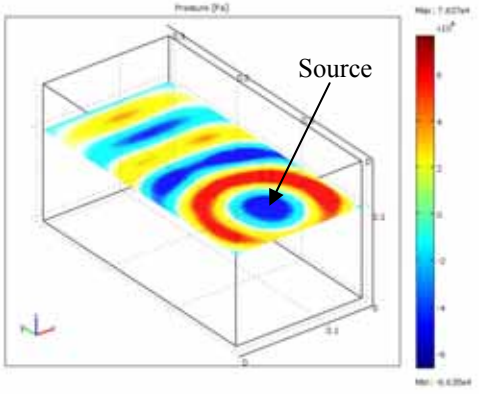

(d.1) ‘Semi-finite’ walls. Plane

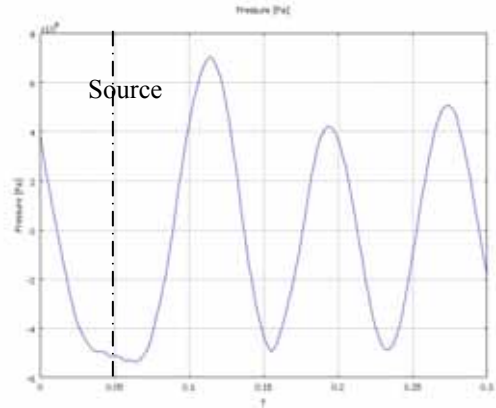

(d.2) ‘Semi-finite’ walls. Plot across the bath

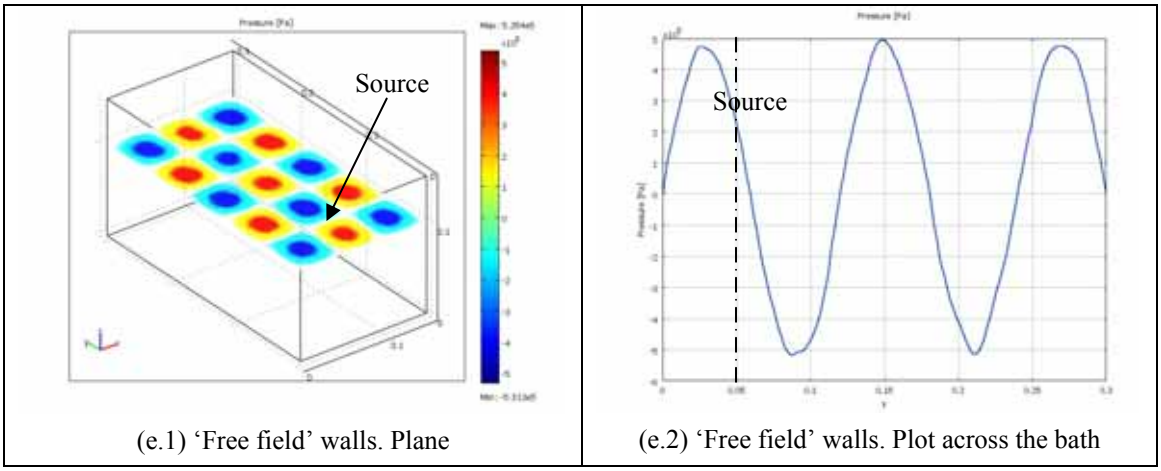

(e.1) 'Free field' walls. Plane

(e.2) 'Free field' walls. Plot across the bath

Table 4: Comparison of acoustic profiles in the modelled water bath

It can be seen that the shape of the acoustic field was strongly influenced by the boundary condition of the walls. In case (a), all walls were 'hard' walls (i.e. perfect reflectors) of very large acoustic impedance, Z value. In (b), all walls were considered to be made of steel, which has an impedance of 45.6×10^6 Pa.s/m, except the water|air interface (on the surface of the tank), which was modelled like a hard wall, due to the reflection coefficient being approximately equal to 1 (see Appendix I for explanation; $Z_{water} = 1.48 \times 10^6$ Pa.s/m, $Z_{air} = 429$ Pa.s/m). To obtain scenario (c), the walls impedance was changed to 20×10^6 Pa.s/m, the typical acoustic impedance of metals such as aluminium, tin, etc. For (d), the conditions established were of semi-finite boundaries, this is, *quasi*-total absorption of sound energy at the walls, but maintaining a hard-wall interface with the air. Finally, in (e), conditions were of 'free-field', those in which the soundwaves propagated without any restriction, like a sonotrode irradiating in the sea, without the proximity of the water|air interface. This is done by setting all the walls in to a 'radiation condition' mode.

The model values were compared against the experimental results in order to assess the model's suitability for the purpose of this work. Verification of the current model when many complex reflections were involved was obviously difficult. However, the extreme possibilities could be discarded at this point. The water bath did not behave like option (a), where all walls perfectly reflected the soundwaves, or like option (e), where all walls perfectly absorbed the sound energy. Both cases are mathematical illustrations of ideal cases which helped to validate the model. Real cases are represented by the remaining options, (b), (c) and (d). Case (d) of the model, with a semi-finite physical boundary, is relatively straightforward. The results can be seen to correlate closely with those reported on [158].

In order to verify the correlation between simulated results and those obtained from hydrophone-mapping measurements, similar variables must be compared. As the values presented in Figure 26b are in RMS, the model results have to be transformed into comparable expressions (i.e. averaged value in time for the acoustic pressure). The sound pressure level (in dB), as defined in equation (44), provides a tool for direct correlation between experimental and simulated results as it quantifies the change in amplitude level [154-156]. The pressure reference is $20x10^{-6}$ Pa this case.

$$L_p(dB) = 20 \cdot \log_{10}\left(\frac{P_{RMS}}{P_0}\right) \tag{44}$$

The three feasible scenarios presented in Table 4 (cases b, c and d) can be shortlisted into two (b and d), since (c) is a sub-case of (b). The sound pressure level (L_p) was extracted for planes across the bath when aligned to the sonotrode depth (Figure 28a and b).

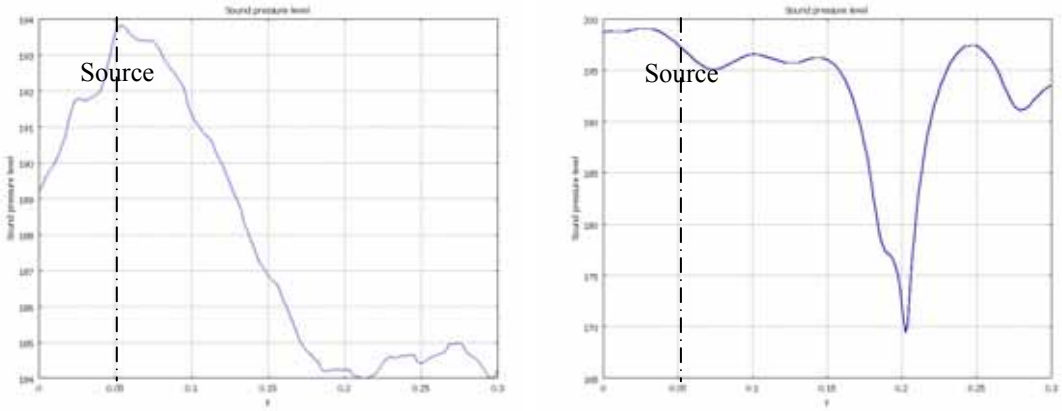

(a) Semi-finite boundaries (absorbent 'soft' walls) (b) Steel walls (partially 'hard' walls)

Figure 28: Acoustic pressure distributions for two modelled scenarios inside the water bath

In both cases, a minimum of sound pressure can be seen at 20cm along the bath (15cm distant from the probe tip). For the 'hard walls' simulation, the sound pressure level drops drastically from the probe to the other end of the bath, as the walls absorb the sound. However, for the bath modelled with steel walls, the sound pressure stays constant for half of the total length of the bath to drop at approximately 20cm and recover in the last 10cm of trajectory.

In order to gain confidence in the model, the acoustic pressure pattern was simulated and compared to the results obtained experimentally. As mentioned in section 4.3.2, the mapping of the water bath was carried out with the hydrophone shielded with a polypropylene barrier in order to extract realistic values of acoustics pressure at which the polymeric mixtures were subjected to while foaming. This situation was also modelled with

the simulator and values of the acoustic field were obtained. Figure 29 presents the comparison of the sound pressure values obtained by the hydrophone when the sonotrode irradiated at 150W input (acoustic pressure in RMS -Figure 26b- converted into L_p via equation 44) versus the values obtained by the simulator.

It can be seen in Figure 29 that the model produced credible results when compared with the data obtained from the hydrophone mapping. Both series of values present similar patterns across the bath. The results suggest that the real case had a hybrid behaviour somewhere between hard and soft boundaries (cases b and d). In other words, ideally the model would create an acoustic field in an environment with a strong water|air interface and reflective walls in the bath. In the proximity of the source (between 5cm and 15cm), the behaviour is well represented by 'hard' boundaries (Figure 28b), with a minimum value between 20 and 22.5cm. Further away from the probe (approx. 25cm along the bath), the behaviour of the bath followed that of a 'soft' wall model with an increase of the sound pressure values.

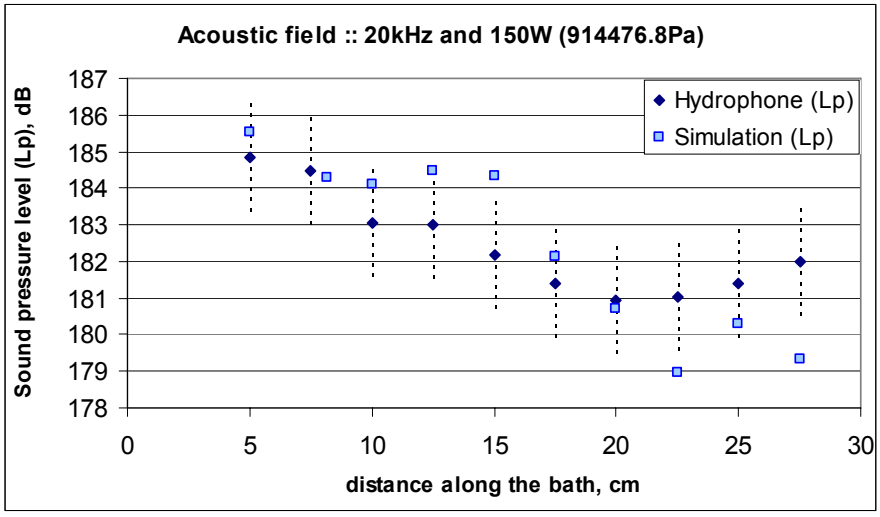

Figure 29: Sound pressure distribution in the yz plane for modelled scenario and experimental rig

The agreement, in general terms, between the simulated model and the hydrophone measurements permitted further investigation to optimise the relative location of the sonotrode and the reaction vessels, along with other features such as acoustic signal magnitude and boundary conditions for the containers. These results can be found in Chapter 5.

4.4 Verifying the sonochemistry effect by ultrasonic irradiation

The purpose of the experiment described in this section was to assess whether the ultrasound produced a sonochemical effect in the polymerisation cross-linking (i.e. a

measurable effect on the sonochemistry of the reaction) simultaneously with the physical interaction (i.e. thermo-mechanical effects, stirring).

The chemistry presented in Chapter 3 showed that water produced extra radicals OH^- that were available for reaction, along with the hydroxyl groups. The influence of OH^- concentration in the reaction is under study here by tracking the effect of those radicals on the foam (irradiated versus non-irradiated). When water is irradiated with ultrasound, acoustic cavitation might induce sonolysis of water and reactive species such as OH^- radicals could be formed due to thermolysis of water molecules [85, 88, 168].

This experiment was formulated so that the chemistry of the reaction itself assisted in the detection of any effect of ultrasound on the individual reactants involved in the reaction. A thorough investigation of the kinematics and thermodynamic features for each of the reactants and products involved is not part of the scope of this thesis. However, a closer look at the pathway of the polyurethane polymerisation indicates, as explained in Chapter 3, that the presence of water molecules in the reaction can initiate, catalyse and, to some extend, even control the reaction. If the presence of water molecules could be varied in a way that more or fewer of these molecules were available for reaction, a relationship could be established and show whether or not ultrasound can have any input in sonochemical terms. In order to carry out this investigation, two agents (salt, Sodium chloride, NaCl, BDH Chemical Ltd, Poole, UK, and Hydrogen peroxide 20 volumes, Fisher Scientific Ltd, Loughboroughshire, UK) were used in the reaction and results were compared to those obtained from a control sample.

a. ‘Salting-out’ effect for PU foam

With the addition of NaCl salt crystals to the distilled water that was used as a catalyst, fewer water molecules were available for the reaction between monomers to produce PU and also less water was available to dissolve the acetone molecules in the initial mixture. The mechanism was described in [85] as the preference of the water to form hydration spheres around the salt ions, instead of remaining available for the polymeric monomers to aid reaction and produce the cross-linking.

Solutions with a different salt-content (i.e. 10%, 16%, 18%) were prepared to be added as a catalyst to the polymeric mixture. The same procedure was repeated for those foams that had equal formulation and were sonicated under known conditions of sonication (controlled

bath temperature 330K ± 2K, 21W applied power to the transducer at a fixed distance (7.4cm) from the containers).

b. Peroxide effect for PU foam

In order to produce the opposite effect, that is, to offer more water molecules than are normally deployed with pure water, hydrogen peroxide (H_2O_2) was added to the distilled water to act as a catalyst [85]. The reaction benefited from the extra radicals OH^- formed on the H_2O_2 sonolysis in the liquid bulk.

In solution, the equilibrium is $H_2O_2 \leftrightarrow 2\ OH^-$. Therefore, along with the hydroxyl (alcohol) groups, more OH^- radicals are available to react with the isocyanate monomer and produce more urethane as well as CO_2 gas.

Aqueous solutions with a different content on H_2O_2 (10%, 13%, 20%, 30%, 40% v/v) and a few drops of pH controller (to maintain an alkaline pH in the solution and facilitate the dissociation of H_2O_2 into OH^-) were added to the foams. This experimental procedure was followed for both sonicated and non-sonicated foams under the same sonication conditions explained in the previous section, when the salt was added. Foam samples were produced in duplicate to monitor repeatability. Half of the total samples were sonicated under the same irradiation conditions as used in the previous section (i.e. controlled temperature 330K ± 2K, 21W input to the transducer, fixed distance, 7.4cm).

Chapter 5 presents the results and these are discussed in Chapter 6.

4.5 Quantifying porosity distribution in closed-cell polymeric foams: Image processing

As highlighted in section 2.2.4, an effective method of characterising the porosity distribution within a material is essential in order to assess the effects of the ultrasound irradiation on the cellular structure of the foam. For this work, close-pore foams were manufactured and so the methods mentioned in Chapter 2 were not applicable. Porosity measures, in the context of this work, should not just reflect an average bulk value, but also provide information on the local porosity, pore size distribution and dimensions of the necks connecting larger pores.

In the search for a reliable and automated method to perform porosity measurements, the following four different strategies were surveyed in order to find a suitable method to measure porosity and porosity gradient of irradiated foams.

4.5.1 Quantitative method: QWIN

The software Leica QWIN is an image analyser optimised for quantitative microscopy applications. It uses a statistical approach that computes local features at each pixel in an image and derives a set of statistics from the distributions of these features (i.e. mean of area, mean of perimeter, standard deviation of selected colour level, standard deviation of area). The simplest features to use would be the grey levels and the simplest statistics would be the moments of the grey-level histogram of an image or region [169]. For the study of polymeric foam cross-sections, this software allowed the use of RGB colour levels and the corresponding colour intensity/frequency histogram for finer tuning and more accurate results. This method's limitation is the fact that statistics carried no information regarding the relative position of pixels with respect to each other. This drawback had to be overcome with manual input from the user, who had to refine the edge-detection operator applied to the image.

The procedure explained next was followed to assess the functionality of QWIN.

4.5.1.1 *Sample preparation*

Once the sonicated foam was cured, it was de-moulded and samples were prepared for image analysis to measure porosity. In order to preserve the morphology of the pores, the structure needed to be reinforced (due to the brittle nature of the cell walls) prior to cutting. The pores had to be filled with a material that could preserve their size and morphology. Under this strategy, the foam could be sliced with six transverse cuts in the vertical plane (Figure 30) to obtain a minimum of three samples per foam which could be representative of its internal structure. The sample sizes were approx 65mm in length, 45mm in breadth, and 3mm in width.

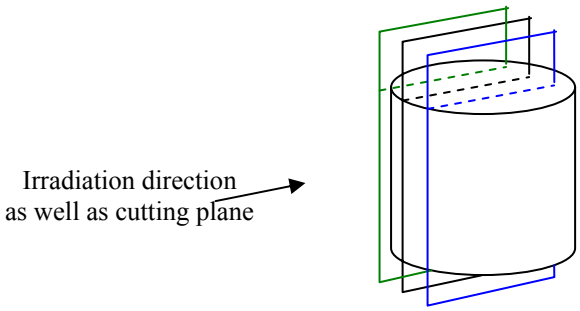

Figure 30: Foam slicing procedure

The filling material used was molten liquid paraffin wax. The foam was immersed in a wax bath at a temperature just above its melting point. The liquid filled the cavities of the pores evenly and the samples were left to cool. The whole process was automated and required approximately 24 hours to be completed. Once finished, foams embedded with paraffin were mounted onto the saw, sliced with a thickness of 3.0±0.1mm and transferred to a paraffin dissolving solution (a mixture of hexane and other solvents) where samples were simmered until the paraffin was completely removed and the slice allowed drying.

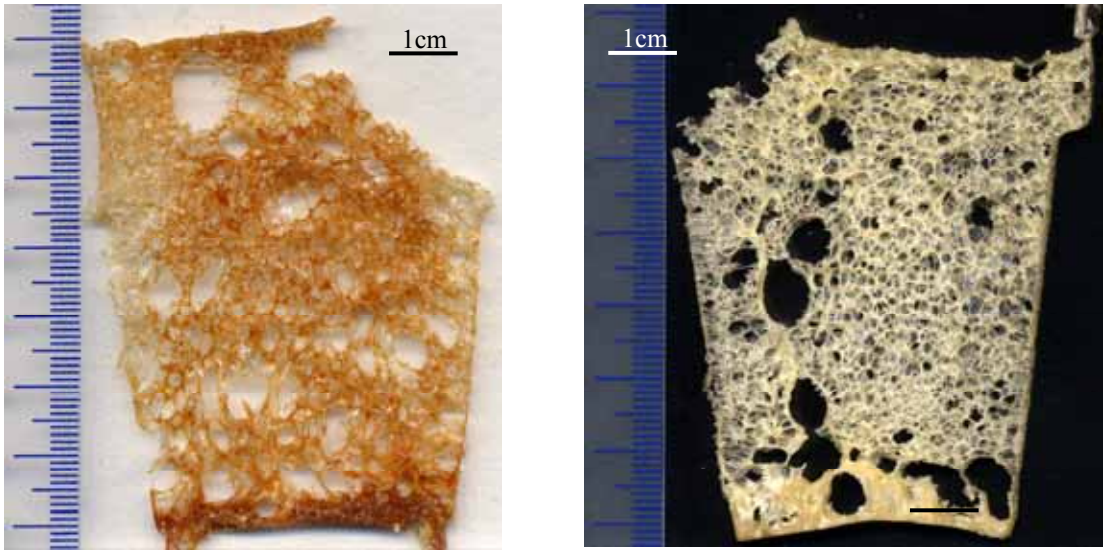

Figure 31: Samples after paraffin removal

4.5.1.2 *Analysis*

To undertake the image acquisition, a Leica MZ6 Stereo Colour Light microscope equipped with a JVC-3CC colour camera was used to acquire digital images of the foam samples. Digital images were obtained at a setting of 10 times magnification (object lens 0.63) at resolution of 768x603 pixels in JPEG format for image analysis. Since the entire sample could not be captured in a single frame, frames were acquired sequentially to cover the entire slice, beginning from the upper left to the bottom right in the fashion shown in Figure 32 [7]. A black sample holder was used under the foam to enhance colour contrast in the case of white/yellow foams, and a white sample holder was used when the foam was of a

darker colour (i.e. brown). Depending on the size of the sample, between 20 and 40 images were taken for each sample.

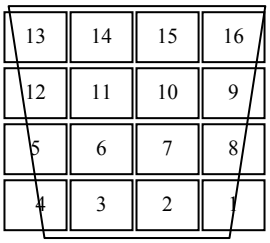

Figure 32: Image acquisition strategy

The digital images obtained were post-processed with QWIN (Figure 33) to estimate the quantities of cell wall and void proportions (%). The cell walls were white/yellow and the background black in some cases, and brown foam on white background in others. Each cell had to be interactively identified and its boundaries, in most of the cases, manually drawn by fitting a polygon via mouse input. The image analyser Leica QWIN Standard v.2.6 was adjusted to detect the colour of the voids and determine the proportion of foam to void for each of the images.

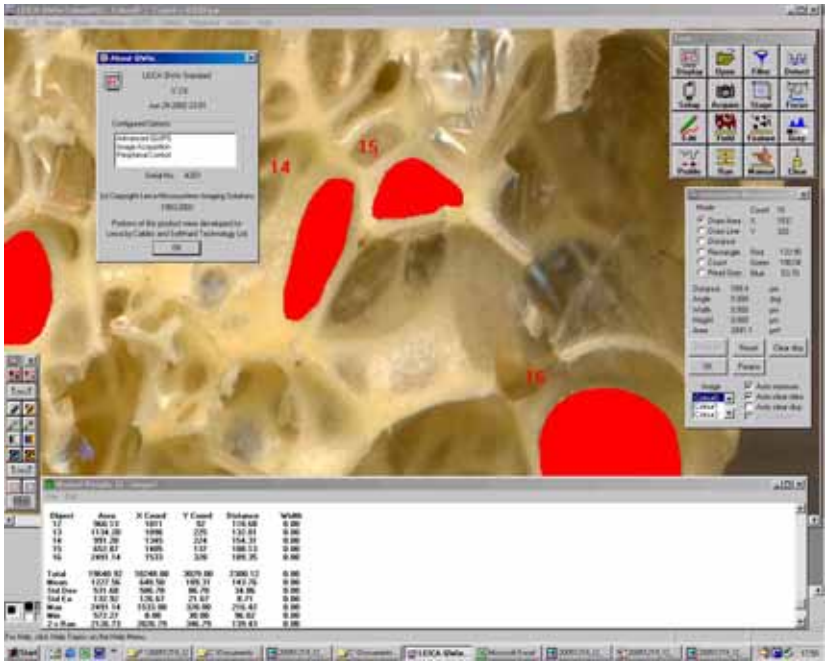

Figure 33: Image Analyser QWIN printscreen

Due to the high number of samples, a Leica QWIN module, the Leica QUIPS, was chosen to perform the image analysis because it provides with a means of macro programming. A QUIPS routine is a sequence of instructions that perform repetitive image analysis tasks. The observation was made that the void area of the cells are a different colour to the walls. This difference is sufficient to isolate the cells shown in Figure 33. A macro which

contained specific instructions for applying colour filters and a string of various calculations to apply to each image was programmed [7] to automate the procedure and final results were written in a spreadsheet. These could be used to represent the density (results in %) in a 3D graph. Figure 34b presents an example of a foam sample whose density distribution was analysed using this methodology.

Although effective, the method was too labour intensive to be viable for large number of samples. The image shown in Figure 34, for example, took 48 hours to create. Consequently, other methods for quantifying the distribution of porosity were sought.

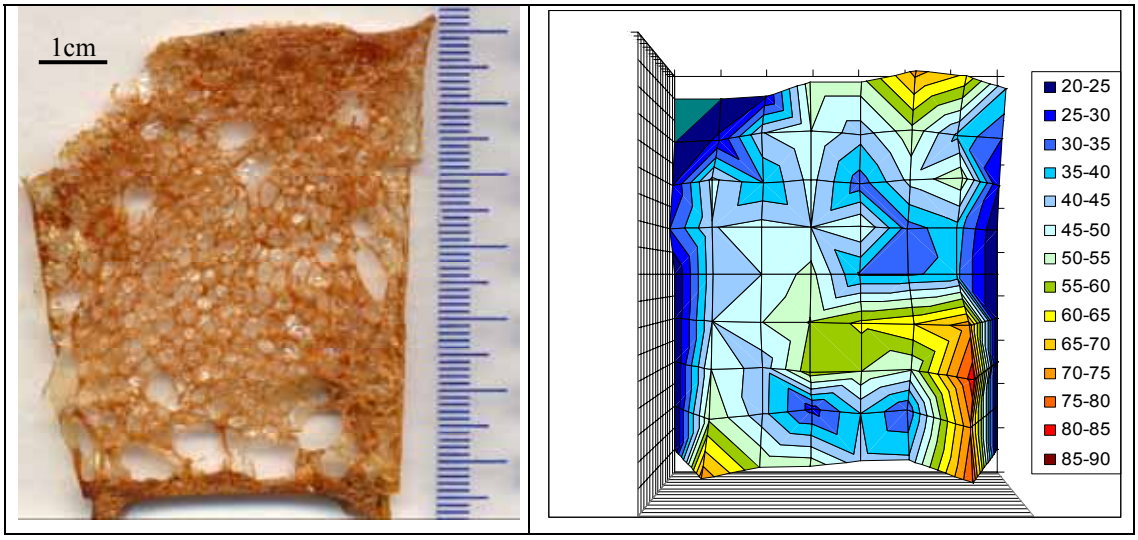

Figure 34: a) Original sample; b) Correspondent density profile (values in %), being 100% fully solid

4.5.2 Quantitative method: a4i Docu "Aquinto"

The bulk density (volume divided by mass) of a foam is indicative of a material's porosity. Therefore, porosity is defined as the fraction of the total volume which is empty, i.e. constructed by voids. To a good approximation, changes in foam bulk density are indicative of changes in porosity. Since the mass will be proportional to the volume of material, bulk density will be directly related to the volume fraction of a foam:

$$\theta = \frac{V_p}{V_m} \tag{45}$$

Where θ is porosity, V_p volume of pores and V_m volume of material. In the context of a 2D image, this relationship is equivalent to

$$\theta = \frac{A_p}{A_m} \tag{46}$$

Where A_p represents the area of pores and A_m, the area of the sample. This relationship equates the area fraction to porosity.

Within the sliced samples, the 3D network of the foam structure can be clearly observed (Figure 35) because of the differences in colour between the sectioned walls and the darker recesses of the cells. However, the image processing software used in preliminary studies, were not capable of isolating the cells in the images of the cross-sections due to the insufficient variation in colour between the sectioned walls and cavity (Figure 36a).

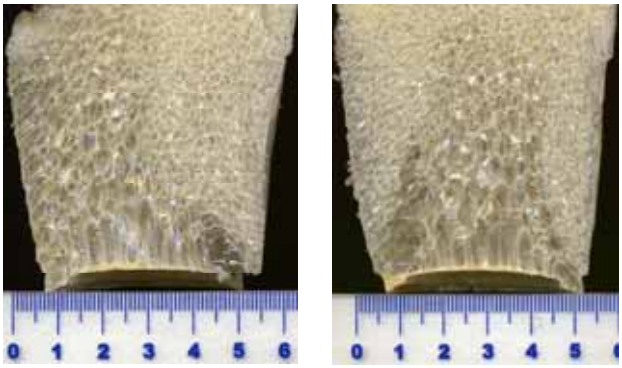

(a) (b)

Figure 35: (a) and (b) Sonicated polyurethane foams

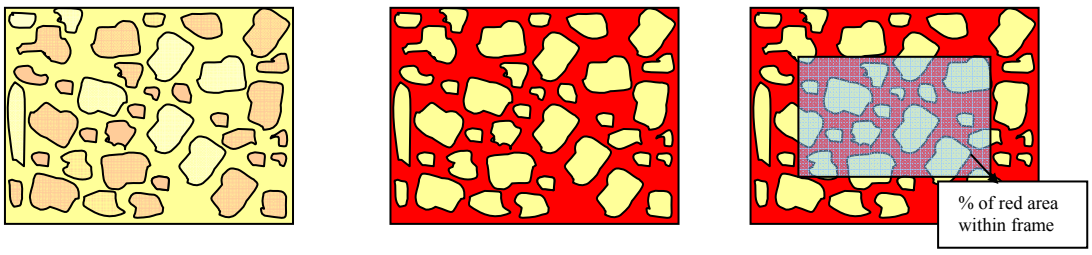

(a) Schematic of foam cross-section (b) Masking agent to enhance cells walls (c) Frame for calculation of area fraction

Figure 36: 'a4i Docu' Software-aided procedure for porosity calculation

To enhance the contrast between cell walls and cavities, a red masking agent was applied to the surface of the foam cross-section prior to scanning the samples (Figure 36b). This effectively isolated the cellular voids. The stained samples were scanned at a 1500dpi resolution on an EPSON Perfection Scanner 1640SU. These images were then analysed with the Aquinto ('a4i Docu' v.5.0.0 software) which calculated the area fraction, in percentage, of the pores by summing the number of red pixels within a region (Figure 36c).

The frames were centred on the horizontal irradiation plane of the source and encompassed the exposed volume of foam. Wall and base of the foam were excluded because in these areas local boundary effects influenced the porosity in a non-controlled manner. Similarly, the portion of foam that was produced above the water bath was also excluded. This was the value used to quantify density for each foam in section 5.4. Figure 37 shows a screenshot of the image analysis program's user interface.

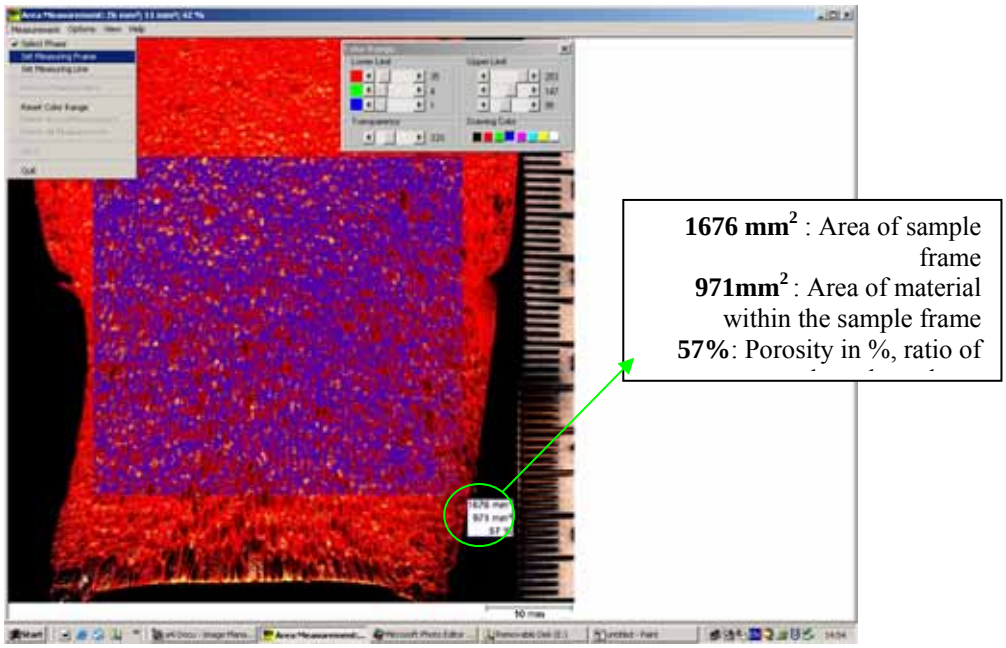

Figure 37: Screenshot of density measurement with 'a4i Docu' software for one of the samples

However, while this measured the overall porosity within the sample, it did not allow the variation of local porosity within the cross-section to be quantified. The following section describes how quantification of the porosity distribution was obtained.

4.5.3 Qualitative method: Topo-porosity mapping

To allow analysis of the density (or porosity) of the heterogeneous sonicated foams and delineation of the distribution of the porous formations, an imagine analysis application was developed using MatLab™, the "*Topo-porosity mapping*" tool. Noting that the density in % of the foam has been defined [8] as the ratio of the density of the foam to the density of the solid material (ρ^*/ρ_s). The density of a foam is indicative of its porosity, ($1-\rho^*/\rho_s$) in %. The purpose was to correlate the topographic distribution of density in each sample with its manufacturing features (e.g. sonication power, frequency, location and position in the sonicating field). In essence, the program calculates the amount of cell wall material in different areas of a cross section of the foam. Points with the same range of density will be connected by curves in the same way that contour lines in a topographic map connects continuous points of the same altitude. These topographic maps of density provide

information on the porosity distribution within a foam cross-section, indicating relative positions of areas with equivalent porosity. Unlike QWIN, where statistics of features from one pixel carry no information on its location, this application brings together both types of information, density (or porosity) ratio and location, considering not only the distribution of % of voids (porosity) but also the position of pixels with equal or nearly equal density.

Once the sonicated foams were fully cured, they were de-moulded and cut in half with a coarse-tooth saw and trimmed. The coarse-tooth saw guaranteed the preservation of the pore structure (pore size and wall thickness) so the extracted samples was representative of the bulk material. The program proved more effective at identifying cell walls and so did not require the elaborate sample preparation demanded by QWIN. The samples were scanned at a 1500dpi resolution on an EPSON Perfection Scanner 1640SU. These images were then analysed with the 'Topo-porosity mapping' program written at Heriot-Watt [170]. In order to isolate the surface plane, the RGB levels of the foam matrix colour picture were filtered from the image (Figure 38a). Colour power, colour threshold and intensity were also used for fine tuning. Using this filtered image, a grid was applied to the image, which counted the pixels and adapted (i.e. reduced or expanded) the size of squares in the grid until they matched a given value of intensity. This intensity was set via the mesh spacing initially chosen so it reflected the observed distribution of cellular density. The image was then pixelated so each grid contained a value which was the number of pixels contained in that area. Applying MatLab's "contour" function, a set of curves, isolines, was obtained (Figure 38b) which linked points of equal porosity.

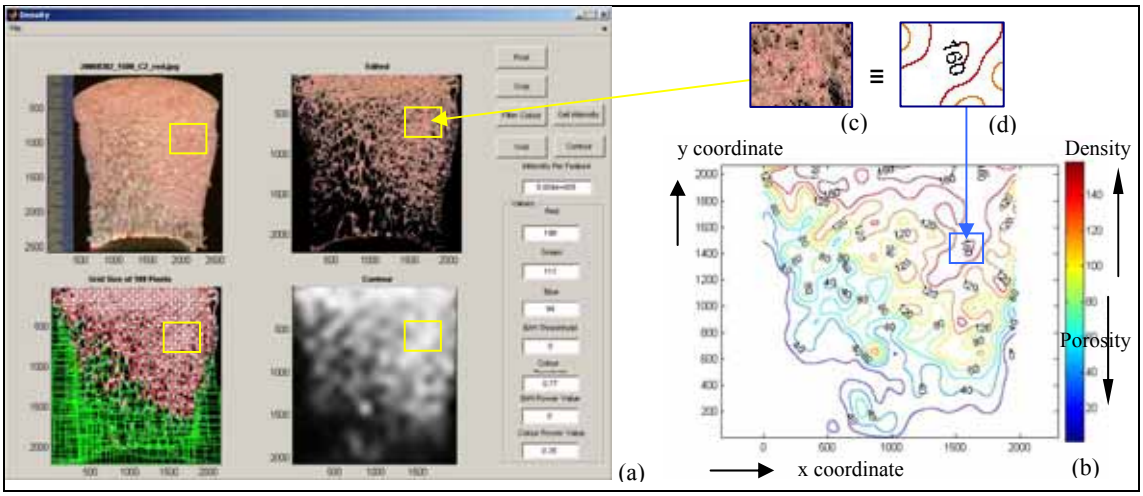

Figure 38: (a) Topo-porosity mapping interface; (b) isoporosity contour lines; (c and d) correspondent areas in image analysis and contour lines

The results were topographic pictures, where points of equal density were joined by contour lines. The relative position of these provided information about the rate of change within an

image. Based on the ratio ρ^*/ρ_s, the contours effectively mapped density distribution where a value of 200 was set to be equivalent to the density of solid polyurethane. For areas where the colour was red or intense red, the density was higher, so porosity low. For areas where colour was blue, porosity was higher. For areas with no lines, or spaces between lines, there was no variation of porosity in the samples (given the interval used to generate the plot). The following sub-section provides a detailed explanation on how the correlation is done between contour line and 'true' density. For example, when foam occupied 80% of the total volume, the value of the lines was 160, as shown in Figure 38c and Figure 38d. By using the same parameters for colour filters and threshold, a comparative study among samples could be made.

4.5.3.1 *Calibration of density contour lines*

In order to assess the accuracy in the representation of the density contour lines, a comparison between two different techniques for analysing the same sample image was performed.

Figure 34a, image of a foam cross-section, was processed with the 'Topo-porosity mapping' (Figure 39). The resulting contour map was compared against Figure 34b, porosity distribution illustration, as calculated from direct measurements on the sample.

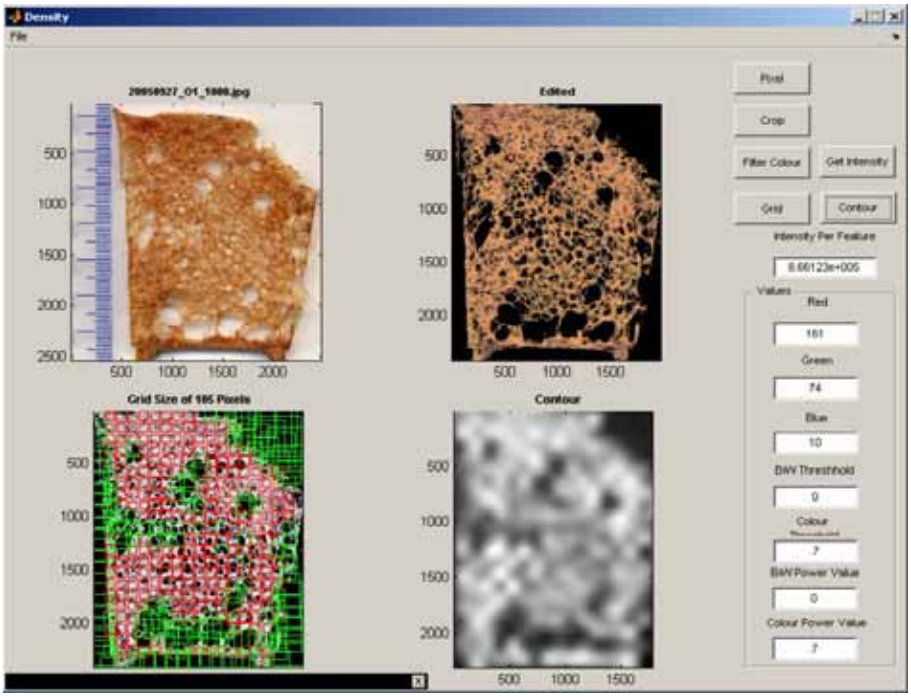

Figure 39: Interface for image analysing of foam slice

By comparison of the two processed images (Figure 40), a direct correlation between the contour line values and the measured density in the sample can be seen. It needs to be noted that the correlation is not linear. A value of 40 in the contour line map represents a 40% of density (i.e. 60% of porosity). A value of 100 represents a 55% of density. Likewise, a value 160 in the contour lines represents a 90% of density in the foam. In other words, the correspondence in areas of low density is very good, but as density increases, the clarity of the images and so the accuracy of the MatLab™ application is poor and results a non-linear mapping.

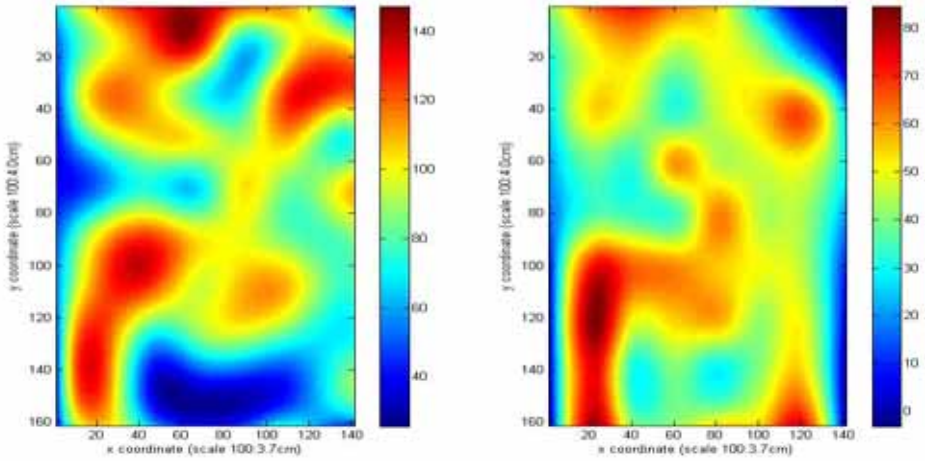

(a) (b)

Figure 40: Comparison of images obtained from different techniques: (a) Topo-porosity mapping and (b) direct measurement of density

4.5.3.2 *Porosity gradation comparison among samples*

The typical porosity distributions found when foams were irradiated can be characterised by these three illustrative examples (Figure 41a). A cross-section of the topographic profile was created by recording values parallel to a y-axis which was aligned to the irradiation plane of sonication (i.e. aligned with the horn tip) (Figure 41b). This allowed comparison of porosity gradient among different foams. The efforts focused on characterising the symmetry of those distributions. Taking a 'OX' plane to set apart the two halves of the curves, as shown in Figure 41b, it can be seen that for foams type 1 and 2 the asymmetry is qualitatively obvious to the naked eye. For type 3 foams, both halves of the curve are almost symmetrical. These curves were analysed using the trapezoidal rule for numeric integrals. The values for the numeric integral obtained from the left half of the foam was subtracted to the one on the right, giving a negative number for type 1 foams, a positive number for type 2 foams and zero for symmetrical foams (type 3). The degree of symmetry for type 3 foams is reported by the number's closeness to 'zero value' once this operation has been performed.

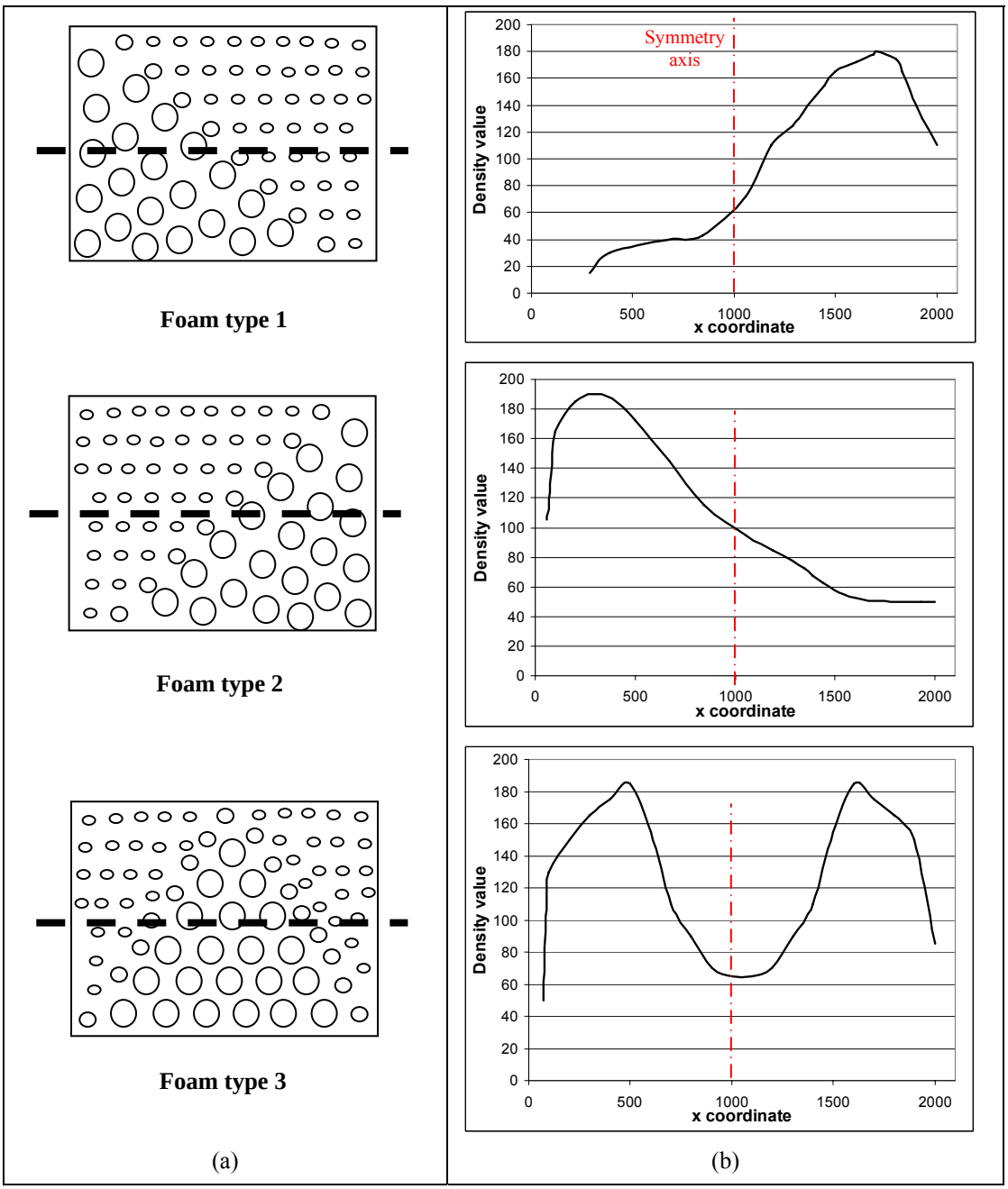

Figure 41: (a) Topographic profile of the foam types 1, 2 and 3; (b) Schematic of the pore distribution for each of the foams in (a). (Dashed line represents the irradiation plane, y-value at which this topographic profile corresponds)

In general terms, for foam distributions similar to the type 1 foam, the gradient of porosity is considered negative, as the porosity decreases from left to right of the picture. For distributions like foam 2, the porosity gradient is considered positive, as an increment in porosity is detected in the picture. For symmetrical distributions, the value resulting from the subtraction lies on the OX axis, as it can be seen in Figure 42. Type 3 foams have the characteristic that the foam has a graded distribution from the centre of the foam (large porosity) to the outer boundary (small porosity), it is referred to as 'bell-shape' porosity distributions.

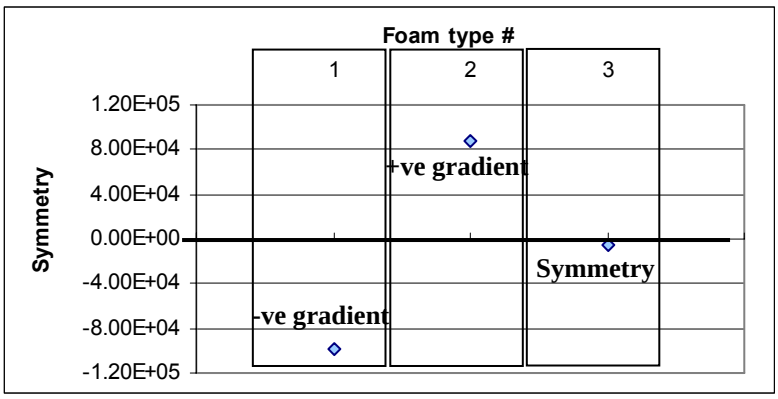

Figure 42: Illustrative values for quantification of the symmetry degree

Thus the analysis allowed porosity gradients to be classified into three broad types: foams with a positive gradient of porosity, from small size to large pore size; negative porosity gradient, from large to small pore size and symmetrical foams with a 'bell shape' in their porosity distributions.

4.5.4 Quantitative (possibly also Qualitative) method: micro CT (μ-CT)

Three-dimensional imaging of cellular materials (e.g. polymeric foams) by synchrotron radiation micro tomography (μ-CT) is the most detailed way of measuring a foam internal structure without the need for partial (at times, total) destruction of the sample or the introduction of a contrast material (as required for other alternative imaging methods, e.g. 'a4i Docu', SEM, etc). The computer tomography system generates a point cloud which is then processed by a reconstruction software used to convert the raw data into a volumetric image (Figure 43 a, b and c).

The scanning of the samples presented below was carried out in the microfocus tomography system (Skyscan m-CT) at AWE plc (Aldermaston, Reading, UK). The microfocus X-ray set was a 225kV X-ray head with a 225 watt target. The detector was a Perkin Elmer flat panel detector with 2000 x 2000 pixel array - 14 bit ADC (analogue to digital convertor) and a 200 micron pixel size. The foam was positioned on a turntable platform between the X-ray tube and the detector where it was rotated at 0.135290 degree increments. At each increment, a full field X-ray image of the sample was recorded (Figure 44). For creating the figure of the sample presented below, 2661 images were taken. Then, the data was analysed using CT Pro, a CT reconstruction software from X-Tek Systems Ltd, (X-Tek Group, Tring, Hertsforshire, UK), to produce the volumetric image.

Further details on the acquisition geometry, filter and reconstructed volume can be found in Appendix III.

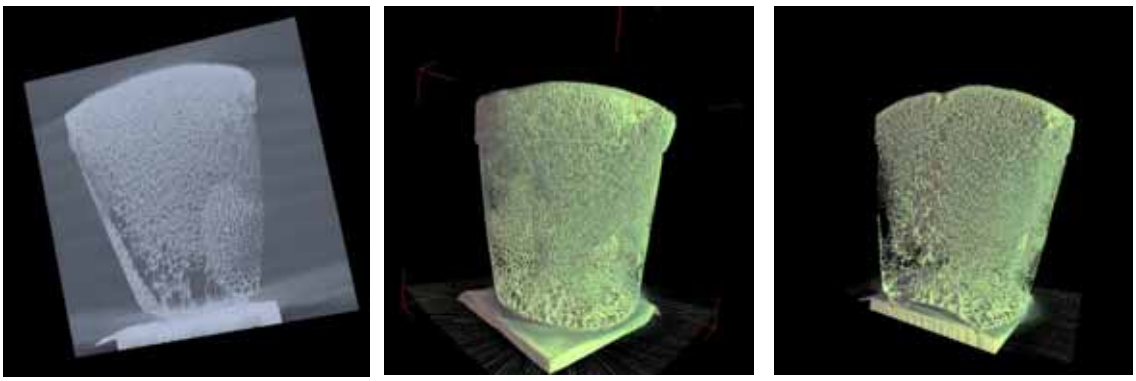

(a) Vertical cross-section of foam 1 (b) Volumetric image of sonicated foam 2 (c) Volumetric image of sonicated foam 3

Figure 43: Results from the micro tomography scanning to foam samples irradiated in the lab

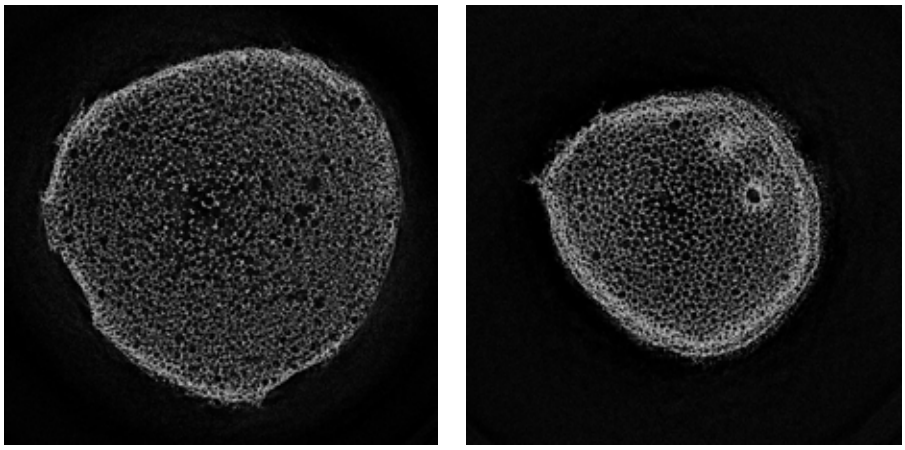

Figure 44: Cross-section images of polymeric foams, as obtained with the micro tomography system

Although the μ-CT images provide an unrivalled tool for examining the distribution of porosity in 3D, there is no software available for the quantification of porosity distribution.

4.5.5 Comparison of methods and selection

In the search for a method that could provide robust quantification of porosity, the previous sections have described four potential methods. Established methods (e.g. liquid or gas porosimetry) could not be used due to the close-cell nature of the polyurethane foam used here. Although these methods can yield an average pore size distribution, they could not generate information about where the pores are and how they are connected. The same could be said about two of the image analysis methods examined here: 'QWIN' and 'Aquinto a4i_Docu', where the user is highly involved in the process and the typical output is a histogram of population measures (i.e. cell size and/or cell wall density).

The choice of a suitable image processing method is argued in the following paragraphs by comparing the results given by all the presented methods, the time consumption and the

demand of user input (which intrinsically appears to be a source of errors). A cost-effective, automated, user-friendly and accurate image analysis method is required:

'QWIN' and 'μ-CT' were both discarded as options for this purpose. Although 'μ-CT' characterised the foam structure in great detail, no software was available for quantifying the 3D structures displayed, and for that reason, it had to be discarded. 'QWIN' was abandoned because the statistical procedures did not allow a digital input and the process could not be fully automated. Therefore, each cell of each sample had to be manually identified one at a time. The laborious work that the samples required made it impracticable.

In this particular case, due to the brittle nature of the foam, only a finite number of layers could be scanned, therefore the 'Topo-porosity mapping' tool was a *(2+1)*D method.

The compromised solution was to choose the quantitative method 'Aquinto a4i_Docu' for the assessment of power influence in porosity for foams. The 'Topo-porosity mapping' program was preferred for the measurement of tailored porosity in the heterogeneous cellular structures.

CHAPTER 5. RESULTS

This chapter presents the data obtained from the experimental rig following the procedure explained in Chapter 4. Using these data, values for polymeric matrix conductivity, reaction rate, sonochemistry effects, porosity values and their relationship to the irradiation intensity will be obtained. Analysis and discussion of these results are presented in Chapter 6.

In addition to the porosity and its distribution, the influence of sonication power on reaction time and conductivity has also been studied. The results are presented in sections 5.1 and 5.2 of this Chapter.

5.1 Electrical resistivity of the polymeric matrix

Electrical resistivity measurements, as described in Chapter 4, proved to be a useful tool in this work for monitoring the foaming reaction and obtaining more information about how the reaction developed from liquid to solid. Once the foam expansion commenced, electrical resistivity was found to increase logarithmically during the cross-linking reaction, drying and eventual solid foam formation. It was suggested that this logarithmic phase of the resistivity curve could be used to characterise the stages during the foam formation due to the direct relationship established to the electrical resistivity.

In section 4.3.1, the relationship between the potential difference and the electrical resistance by the foaming mixture was described. Using equation (43), the value for the electrical resistivity, Q_x, was obtained. An example of the raw data of foam potential difference collected by the data acquisition card (DAC) is shown in Figure 45a, and the corresponding values for the electrical resistance, in Figure 45b.

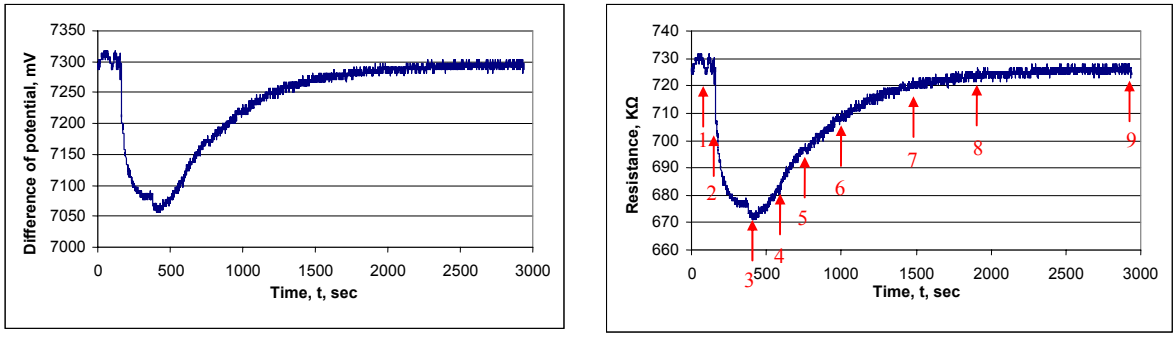

(a) (b)

Figure 45: Electrical resistivity: (a) Raw data collected by DAC, (b) Corresponding electrical resistance

The arrows on the curve (Figure 45b) locate the phenomena occurring to the polymer as it changes from a liquid mixture to a solid cellular structure. As described in section 4.1, the polyurethane-acetone mixture is mixed with the catalyst and stirred. The annotated points on Figure 45b can be associated with the events as read from the DAC:

(1). Represents the moment at which the electrical resistivity measuring probes, inserted in the vessel, started transmitting data

(2). At this point, the ultrasonic source was switched on at the frequency and power set for the experiment

(3). Foam had expanded to reach an average height of 5 cm

(4). Bubbles were rising to the surface of the foam and, on occasions, foam height may have oscillated around the final height

(5). Stable height was reached. Notice here the slight change in the slope for the curve, a quasi-inflexion point

(6). Foam surface was sticky to the touch

(7). Foam surface was non-sticky and had a springy surface

(8). Temperature did not show any variation and the bath temperature was read. Reaction was finished

(9). Logging was stopped

5.1.1 Electrical resistance monitors the foaming process

The resistance, Q_x (Ω), of the foaming material is related to the applied voltage, V_{BS} (mV) by equation (43), in Chapter 4. This resistance is also defined by equation (20), in Chapter3. In that expression, δ is the dielectric property of the material, measured in ohms per metre (Ωm), L the material-length distance between measuring probes, in metres (m), and A the cross-sectional area of the specimen, surface area of foam in between the measuring probes, in square metres (m^2).

As already mentioned in section 3.2.1, the dielectric *constant*, δ, is assumed to vary with the increment of viscosity. In the study of polymeric foam undergoing foaming, the initial value, δ_0, and variation with time for δ is unknown. Conversely, as the variation (Q_x/L) with time was measured, the variation of the ratio (δ/A) with time can be obtained from equation (47).

$$\left(\frac{Q_x}{L}\right)dt = \left(\frac{\delta}{A}\right)dt \tag{47}$$

Although at any given moment the exact values of δ, L and A are unknown, the variation of Q_x was monitored. And if the conductive path length (L) between the probes is regarded as approximately constant, then variations in Q_x can be explained in terms of δ and A. In other words, the variation of (Q_x/L) with time should equal the change in (δ/A) over the course of the reaction. Figure 46 shows a minimum value for (Q_x/L) when the foam texture was just a viscous mass of bubbles. From that instant, the cross-linking commenced and the bubbles started forming cells, which eventually formed pores. When the solid was formed, the maximum value for (Q_x/L) was at the asymptote. The dielectric property of the foam decreased due to the effect of cavity formation (i.e. porosity) on the cross-sectional area between the probes as follows:

(1). At initial time, t=0, the value for A (A_o) was known because the proportion of the amount of liquid prepared to react to its depth in the vessel.

(2). The value for A approached a maximum when the bubbly mixture in the vessel wetted up to the maximum height of the resistivity pens (copper pens).

(3). After the peak (at point (4) in Figure 45b), the wetted height of the conductivity pens was fixed, and therefore, the cross-sectional area of foam, A, decreased due to the cross-linking in the foam and cavity formation.

(4). Once the reaction had finished, the value for A (A_{final}) was unknown, but assumed to be a minimum value as the foam had its final porosity set.

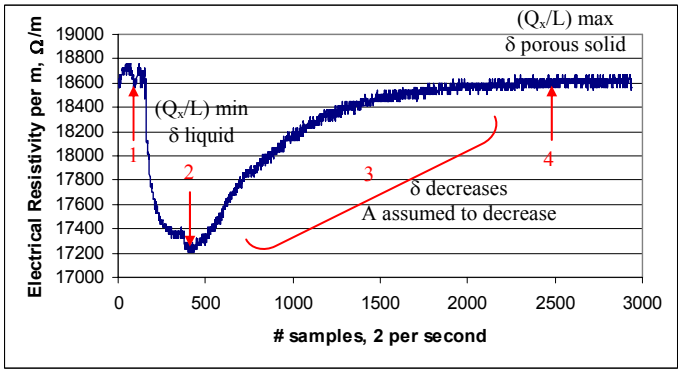

Figure 46: Time variation of electrical resistivity per m, (Q_x/L)

The conclusion that can be drawn is that the variation of electrical resistivity in the mixture reflects the foam formation stages: cream time, gelation time, rising time and end of reaction. The disadvantage of this method is the poor accuracy due to the delayed response that the system might have at initial times, when diffusion of the water was occurring at a

very fast rate and the foam was undergoing alternated stages of growing/micro-collapsing. Another disadvantage lies within the intrinsic structure of the foam. Foams might be anisotropic, i.e. the measured resistivity for the mass of foam between the resistivity pens could vary largely with location and orientation in the bulk of the foam.

5.2 Reaction rate

This section summarises the results from the experiments to assess the influence of acoustic pressure on the reaction rate for the polymeric samples. To do this, the electrical resistivity and the temperature were monitored simultaneously in the reaction.

Both electrical resistivity and temperature signals were logged and recorded using two different channels (see section 4.3.1) and the variation of these provided information about the time at which the reaction was completed (i.e. reaction time). The comparison of the two graphs for each foam sample tested the point at which the reaction ended (Figure 47).

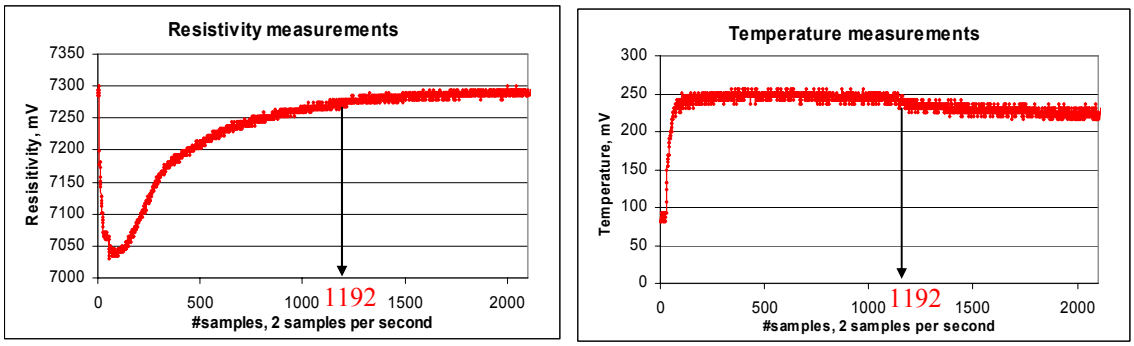

(a) (b)

Figure 47: Temperature and resistivity measurements to locate end of reaction

Both curves simultaneously changed at the point when the reaction was finished: temperature dropped and from that point onwards, it tended towards the bath temperature. Electrical resistivity became asymptotic at that point. The variations in temperature were difficult to assess due to the small range of values that were recorded (i.e. small difference between maximum value and bath temperature) and the large "inertia" that temperature readings had due to the high specific heat value of the water surrounding the reaction container in the bath. Resistivity readings varied in a broader range, therefore it was easier to identify any variations and so results could be interpreted with less ambiguity.

The total reaction time for the samples to become fully solid polyurethane foams was 10-14min, in average. Using the resistivity variation with time (already presented in section

5.1), these values could be fitted to a curve of the form 'y=a ln(x) +b'. Then, the 'a' coefficient of that function was used to compare different sets of experiments in order to study the influence of ultrasonic irradiation magnitude on the development of the reaction (Figure 48).

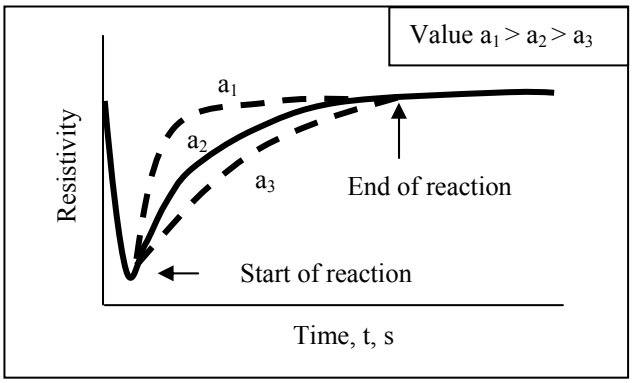

Figure 48: Logarithmic phase of the resistivity with different slope 'a'

For example, when the 'a' coefficient from the samples irradiated at 20 kHz was plotted against the acoustic pressure values (measured with the hydrophone) that they were subject to, a clear incremental trend can be observed (Figure 49).

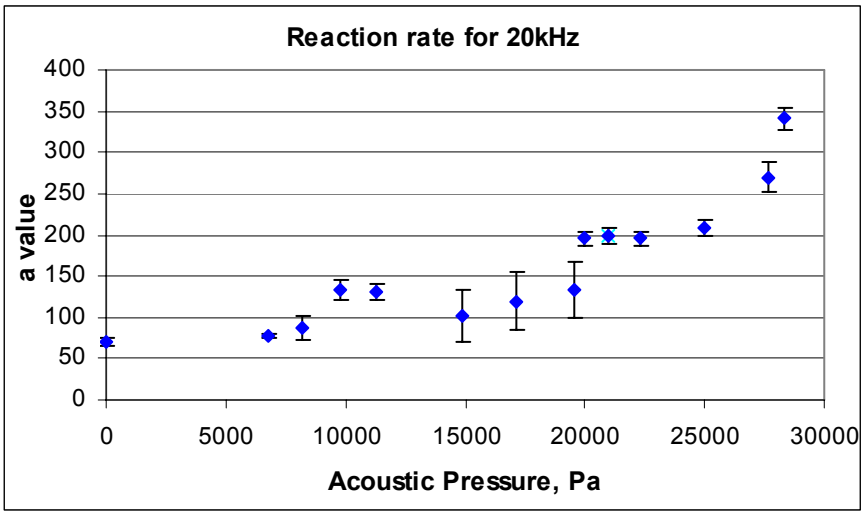

Figure 49: 'a' value for different samples irradiated at 20kHz

An example of how ultrasound affected the resistivity values during the drying stage is shown in Figure 50. When the 'resistivity vs time' plot is examined in detail (Figure 50b), it can be observed the small change in resistivity when irradiation is applied. As described in section 4.3, the ultrasound was applied in a 2min on/1 min off fashion. The curve sections with a steeper slope corresponded to those periods when the ultrasonic probe was switched on, and the less steep sections of the curve, to the 1min-off periods. This shows a direct influence of the ultrasonic irradiation on the drying (at the macroscopic scale) stage, where ultrasound (either by pure stirring of the CO_2 gas, inflation of the cavities, enhancement of

the cross-linking, or a combination of these) has a bulk effect on the mixture. Unfortunately, there was no data available to conclude on the relationship between frequency and reaction rate.

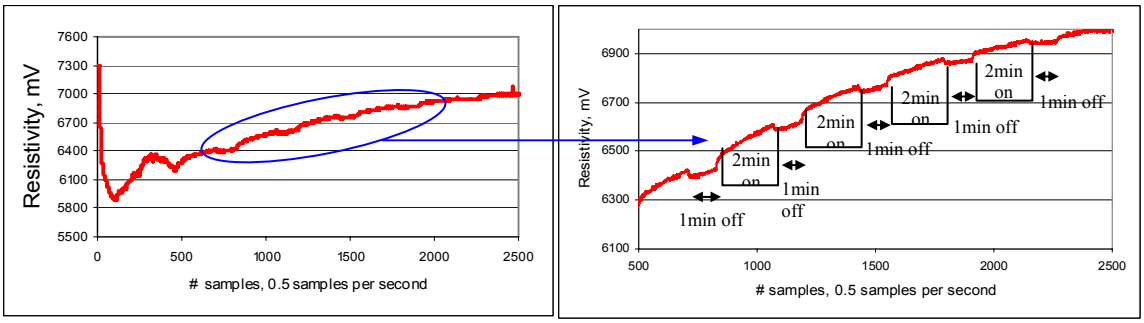

Figure 50: a) Ultrasound influence on reaction time; b) Detail

As a conclusion to this section, it can be said that the foaming stages (especially the drying phase) were accelerated when the acoustic pressure was applied to the sample. The value of the 'a' coefficient increased directly with the acoustic pressure applied. Consequently, for the same overall curing time for a foam, the 'gelation point' was reached sooner in those samples where a larger acoustic pressure was irradiated during the reaction.

5.3 Sonochemistry

The verification of the sonochemistry in the polyurethane reaction was done by comparing the values of the 'a' coefficient for the sonicated and non-sonicated batches. Figure 51 shows the values for the samples whose catalyst was either a salt solution, a perodixe enriched mixture or pure distilled water.

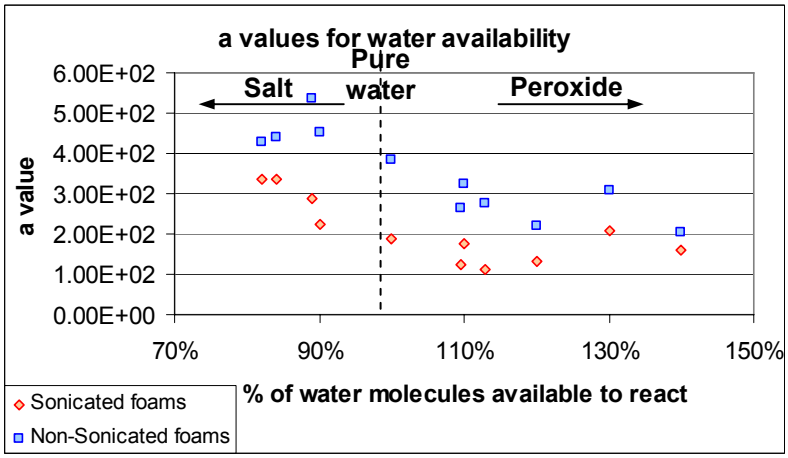

Figure 51: Sonochemistry effects for polymerisation reaction

The point on the x-axis labelled '100% of water molecules available to react' refers to the use of distilled water as a catalyst. For values lower than 100% of water molecules available to react, the catalyst added in each case was a solution of NaCl in water (the lesser the % of

molecules available indicate the more quantity of salt dissolved), as explained in section 4.4. On the contrary, for % of water molecules available higher than 100%, the solutions used were various % of hydrogen perodixe dissolved in water, as also explained in section 4.4. The hydrogen peroxide enhanced the production of hydroxyl groups to be used up in the reaction.

In general, for both batches (sonicated and non-sonicated), when the reaction was catalysed with the salt solution, the reaction ended faster than when there were more water molecules available to the reactants. This result was expected because, if the hypothesis presented in section 4.4 is true, a smaller amount of one of the reactants made the reaction finish in a shorter time.

Likewise, when the catalyst added was the peroxide, more molecules of water were available to react. Therefore, the reaction took a longer time to complete and fully consume all the reactants available in solution. When compared to samples whose catalyst had been pure water, or salt solutions, this reaction time was longer.

It also needs to be noted that, for higher % of salt (>18%) and peroxide (>40%v/v) content in the solution added as a catalyst, the polymeric mixtures did not foam properly due to the unbalance produced by an excess of salt (which provoked a 'leaching effect': i.e. axial channels were created in the foam instead of pores) and peroxide (an excess of which produced an extended reduction –pyrolisis- and samples had a "burnt" final appearance).

When the samples were irradiated with ultrasound under the conditions explained in section 4.4, a general 'slow down' effect was produced on all the samples. They reached their 'gelation point' later than non-sonicated specimens. Another observation that can be extracted from Figure 51 is the fact that sonicated 'salt' mixtures and non-sonicated 'peroxide' mixtures have equal 'a' coefficient values. This implies that 'peroxide' (i.e. water-enriched) samples took the same time to react as those sonicated 'salt' (i.e. water-depleted) samples. This phenomenon can be explained by the variation in water vapour for each of the mixtures. The alteration of the physicochemical properties of the aqueous reaction mixture by the addition of salt in the reaction mixture resulted in a reduction of vapour pressure and increased surface tension, promoting a faster rate for the reaction (reaction ended very quickly). The contrary effect occurred when the peroxide was added, when the vapour pressure was increased and this supported the reaction for longer periods of time.

In the ‘salting-out’ case, samples tended to have bigger pores in the areas directly exposed to the ultrasonic probe. It is thought that walls thinned when sonicated due to the stirring effect of ultrasound. The cellular structure was stiffer when compared with non-sonicated samples. In the ‘peroxide’ case, when irradiated, foams tended to form better cellular structures, more clearly defined walls. Those areas directly facing ultrasound had usually, on average, a bigger pore size.

Therefore, it can be concluded that the drainage rate (i.e. liquid flow through the interstitial volume between the bubbles) was faster for a salt-solution type of catalyst. This is because the available water molecules were consumed and there was none available for further stages of the reaction. The drainage rate value was slower for the case with pure water as a catalyst, and finally the smallest rate was for those samples when peroxide was used.

5.4 Effect of ultrasound on porosity

In this section, the influence of ultrasound intensity on the bulk cellular structure of the foams is described. To undertake this study, a series of frequencies and acoustic pressures (as measured by the hydrophone) were applied to polymeric melts undergoing foaming in a water bath.

The following describes the results of a series of experiments to investigate:

1. **Porosity as a function of applied acoustic pressure for a given frequency**: the acoustic pressure from each applied power ‘seen’ by the sample was varied by placing the vessel at different locations in the bath. The corresponding pressure was determined by the signal magnitude map at distances 7.4, 11.1, 12.95, 14.80, 16.65 and 20.35cm from the ultrasonic probe.

2. **Porosity as a function of frequency for equal acoustic pressure**: the selected frequencies were 20, 25 and 30 kHz. In order to study porosity as a function of frequency, the location of the vessel was fixed at the first half-wavelength distance external to the vessel’s axis, varying the applied power onto the sonotrode so that the same wave amplitude (i.e. acoustic pressure amplitude) was obtained.

The porosity was measured using the a4i Docu “Aquinto” method, described in section 4.5.2. In this way, the porosity was measured on the area of the irradiation plane (4cm

below free surface which was the depth of transducer's tip) and ±1.5cm around that axial plane of sonication.

5.4.1 Porosity as a function of applied acoustic pressure for a given frequency

The following table summarises the experimental parameters.

	Acoustic Pressure, Pa			
distance, cm	20 kHz, 75W	20 kHz, 150W	25 kHz, 67W	30 kHz, 55W
7.40	24971.22	33517.99	7654.68	8676.26
11.10	18575.54	28345.32	6302.16	7733.81
12.95	17143.88	28223.02	5035.97	7460.43
14.80	14568.35	25748.20	4273.38	8446.04
16.65	12748.20	23496.40	5402.88	7884.89
20.35	12064.75	22258.99	5107.91	-

Table 5: Experimental parameters for the series porosity vs acoustic pressure

5.4.1.1 *Porosity of foams irradiated at 20 kHz and applied horn power of 75W*

Figure 52 presents six photographs of the central region in sonicated foams, from left to right, then down, at the working distances.

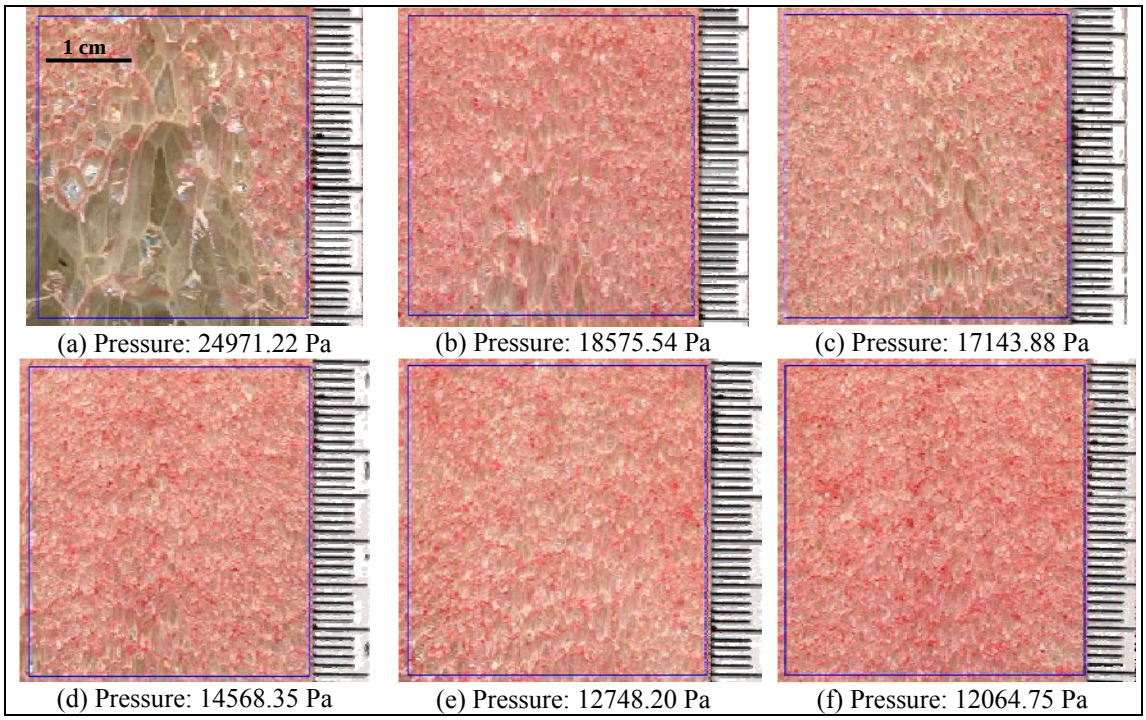

Figure 52: Selected frames of foams sonicated at 7.4, 11.1, 12.95, 14.80, 16.65 and 20.35cm from the probe radiating at a frequency of 20kHz and with horn power 75W

The area fraction of a region (i.e. ±1.5cm) around the axial plane of sonication (i.e. the depth of the transducer's tip) for foams sonicated at 7.4, 11.1, 12.95, 14.80, 16.65 and

20.35cm distant from the probe was used to characterise the porosity of each sample. Plotting these values against measured signal strength at each sample location (Figure 26a) a linear relationship can be observed (Figure 53).

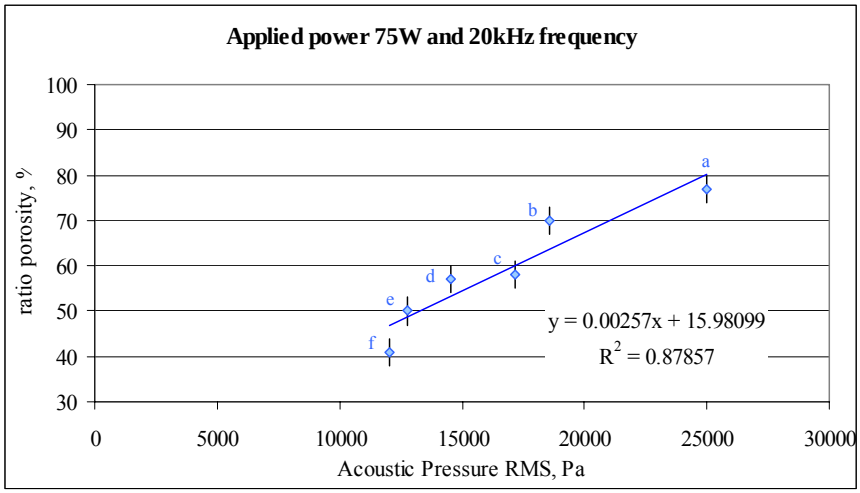

Figure 53: % porosity for samples irradiated at 20kHz and 75W

5.4.1.2 *Porosity of foams irradiated at 20 kHz and applied horn power of 150W*

The procedure was repeated using an applied power to the transducer of 150W for the same frequency. Again, the porosity values from the image analysis were correlated with the acoustic pressure measured at each location and plotted in Figure 55.

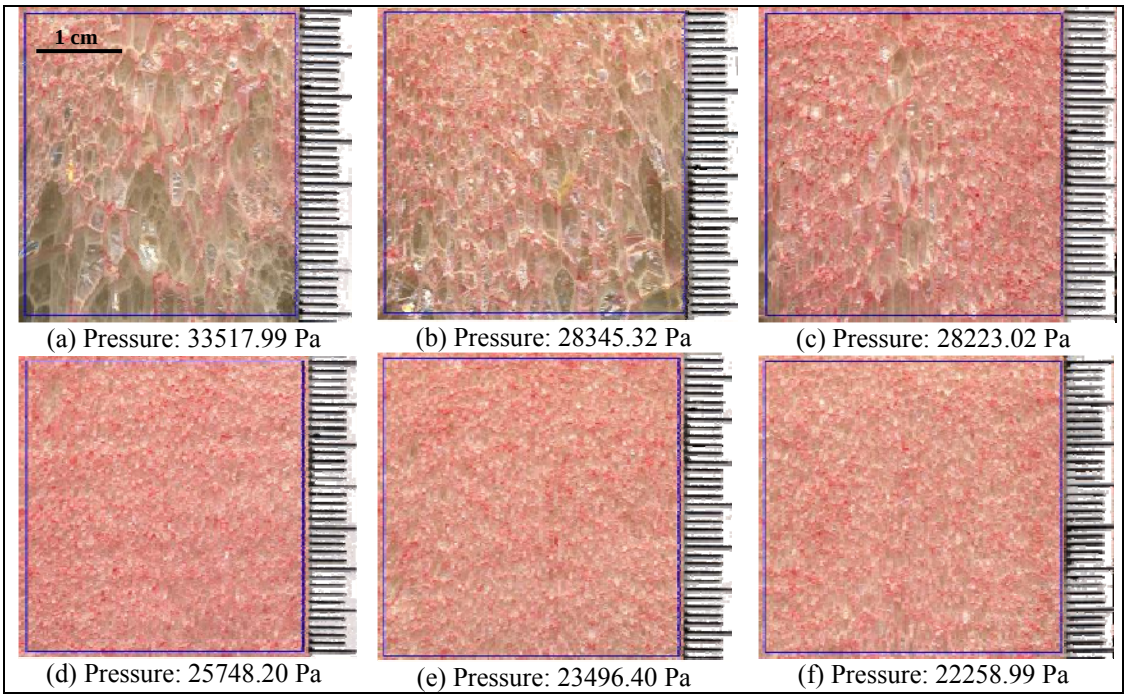

Figure 54: Foams sonicated at 7.4, 11.1, 12.95, 14.80, 16.65 and 20.35cm from the probe radiating at a frequency 20kHz and with horn power 150W

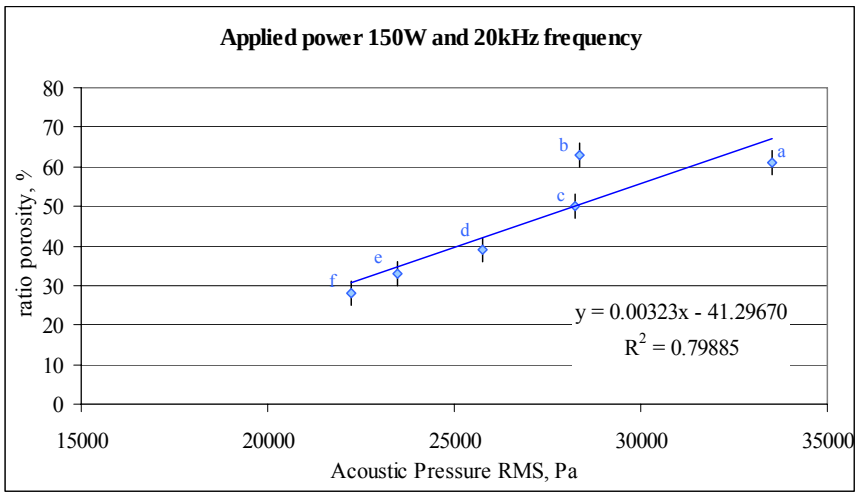

Figure 55: % porosity for samples irradiated at 20kHz and 150W

5.4.1.3 *Porosity of foams irradiated at 25 kHz and applied horn power of 67W*

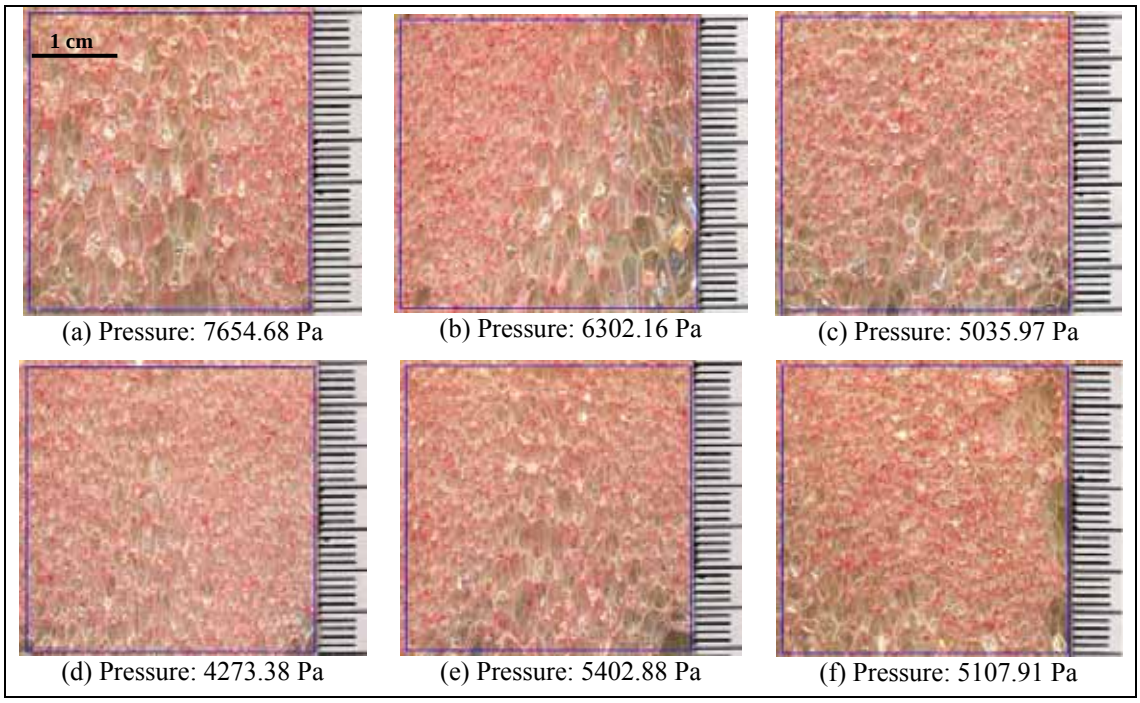

Figure 56: Foams sonicated at 7.4, 11.1, 12.95, 14.80, 16.65 and 20.35cm from the probe radiating at a frequency 25kHz and with horn power 67W

Likewise, the porosity values from the image analysis were plotted against acoustic pressure at each location along the bath for values of 25 kHz and applied power of 67W. Again, the results plotted in Figure 57 suggest a linear relationship between porosity and acoustic pressure.

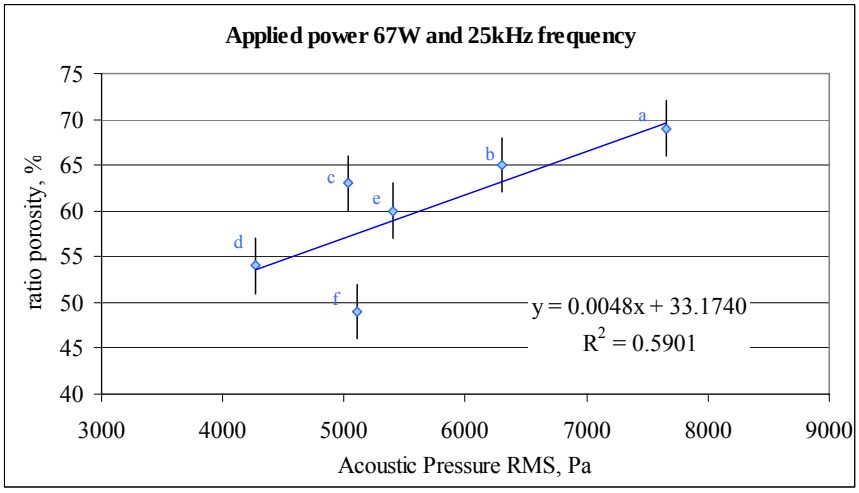

Figure 57: % porosity for samples irradiated at 25kHz and 67W

5.4.1.4 *Porosity of foams irradiated at 30 kHz and applied horn power of 55W*

The same process was used here to investigate the relationship between porosity values obtained via the image analysis and the measured power in the water bath for samples irradiated at a frequency of 30 kHz and an applied power to the transducer of 55W.

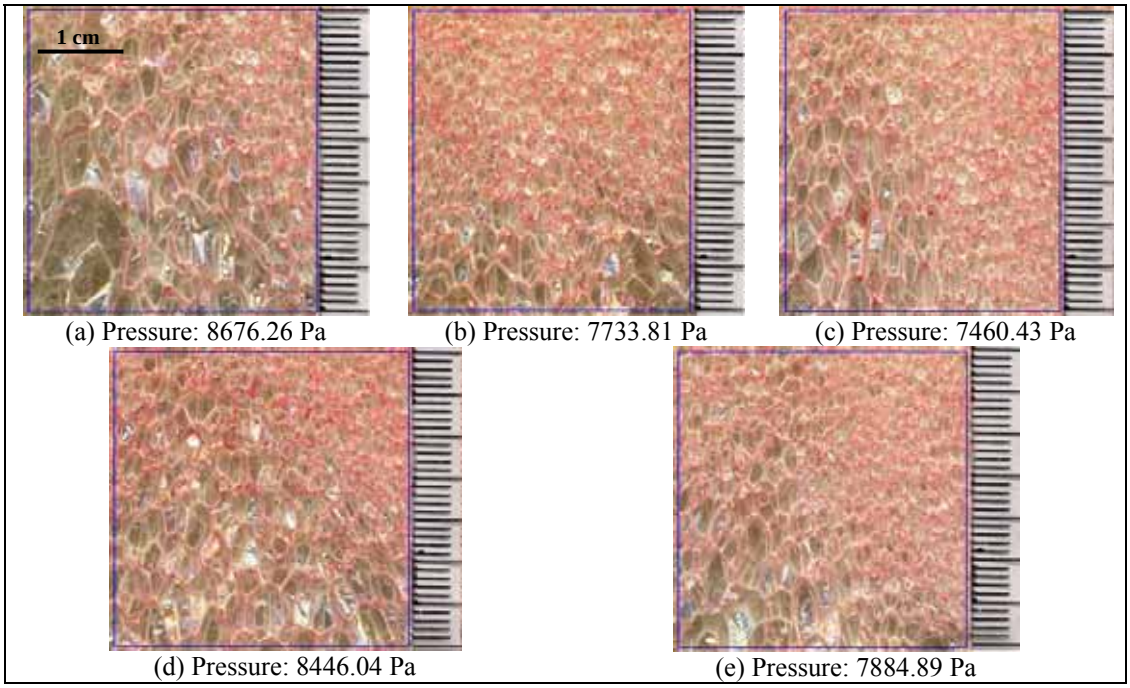

Figure 58: Foams sonicated at 7.4, 11.1, 12.95, 14.80 and 16.65cm from the probe radiating at a frequency 30kHz and with horn power of 55W

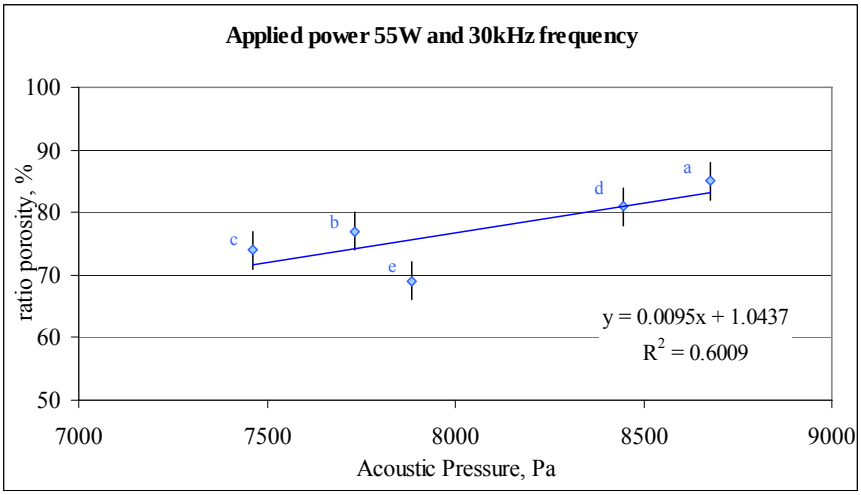

Figure 59: % porosity for samples irradiated at 30kHz and 55W

5.4.2 Porosity as a function of frequency for equal acoustic pressure

The selected power applied to the transducer for this series of experiments was adjusted in order to obtain an equal value of acoustic pressure (i.e. signal magnitude) when the distance was each frequency's first half-wavelength distance external to the vessel. The acoustic pressure was 8750 Pa (7% tolerance) for 20 kHz located at 11.1cm from the transducer; for 25 kHz, at 8.85cm; and for 30 kHz at 7.35cm. Values of porosity versus frequency are plotted in Figure 61.

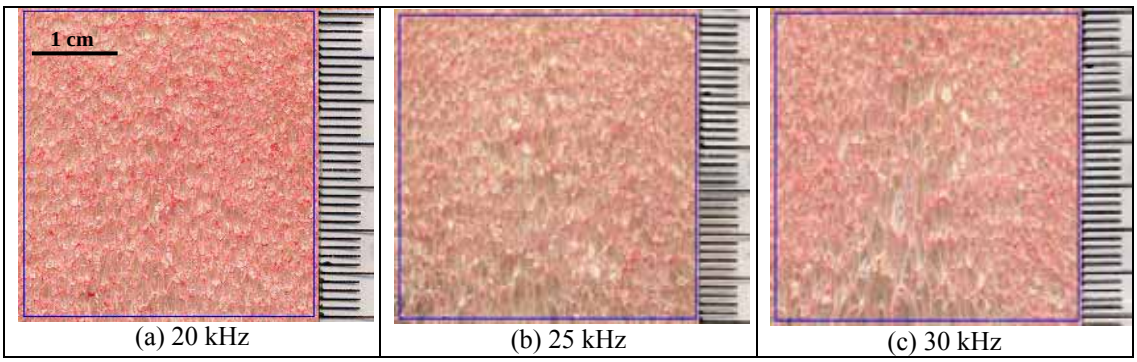

Figure 60: Sonicated foams at 55W and at first maximum and 20, 25, 30kHz, respectively

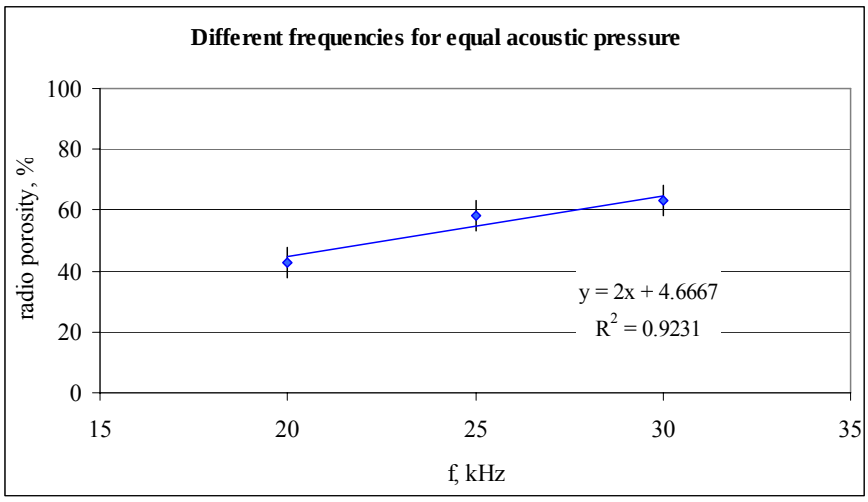

Figure 61: % porosity for samples irradiated at same acoustic pressure with different frequencies

Conclusion to sections 5.4.1 and 5.4.2: For constant frequency and decreasing irradiation power (e.g. increasing distance), the porosity in the bulk of the sample is reduced. This is related to the attenuation of the signal inside the water bath with increasing distance from the probe, and the fact that the sonicating field becomes "unfocused": direct irradiation is mixed with secondary (scattered, reflected) waves. In other words, the samples produced at a greater distance between source and sample show more attenuated effects of acoustic pressure and consequently the signs of stable cavitation are less evident.

When analysing the effect of frequency for a given power and distance, it can be seen that the 20kHz frequency presents lower porosity values than the foams sonicated at 25kHz, and these in turn are less than the ones sonicated at 30kHz. The penetration power for 30kHz is higher than for 25 and 20kHz. Therefore, when the frequency increases, the pore size also increases.

5.4.3 Effect of ultrasound on porosity: other example of foams

An investigation was also undertaken to assess the effects of high power ultrasound on a different formulation for the polyurethane and silicone foam. All the reactants were provided by an industrial collaborator, which supplied in-house formulations (per 100g of polyol: 135g of isocyanate (for an index of 115), 1g of surfactant and 0.4g of catalyst). The foams were irradiated at a fixed frequency of 20kHz, constant 150W input to the transducer and a fixed distance to the probe of 7.4cm, inside of the water bath, where temperature was kept constant and the acoustic pressure value read by the hydrophone was 35000Pa. Samples were produced in duplicate and those sonicated samples compared to non-sonicated ones produced under the same experimental conditions of temperature in the bath, room temperature, humidity, etc.

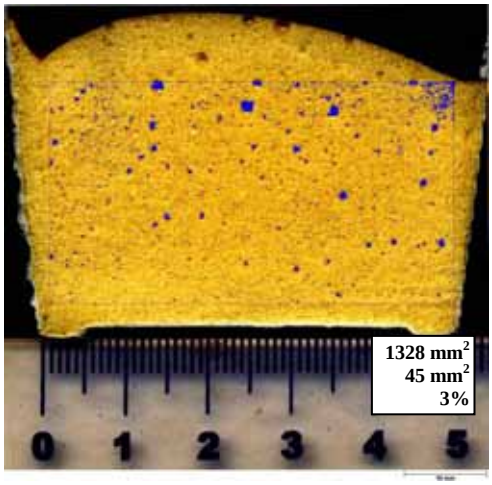

(a) Non sonicated PU sample. Ratio 3% porosity

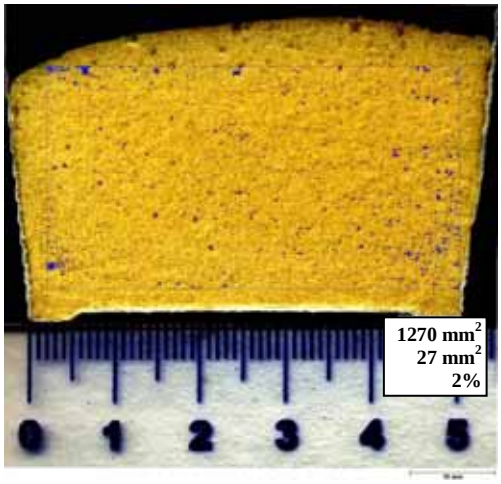

(b) Sonicated PU sample. Ratio 2% porosity

Figure 62: PU foams with degassing effect from ultrasonic irradiation

This system was also tested for foams of a different nature. Silicone foam reactants, in-house formulated by the industrial collaborator, were supplied for ultrasonic testing. The proportion was 20g resin to 1g catalyst. The irradiating conditions were equal to the previous ones (20kHz frequency, 35000Pa acoustic pressure), except the bath temperature, which was kept constant at 17ºC due to manufacturing reasons for this specific group of foams. The effect can be seen in Figure 63. More details on the effect of sonication on porosity for PDMS were compiled in [171].

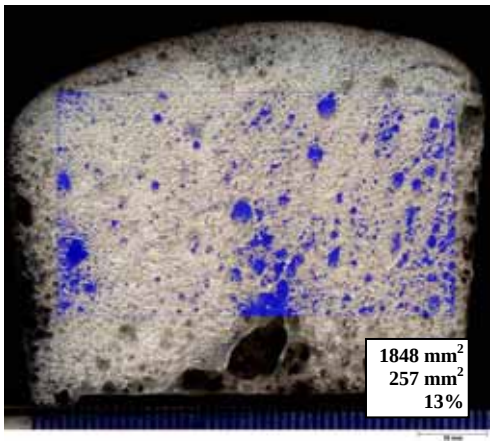

(a) Non sonicated PDMS sample. Ratio 13% porosity

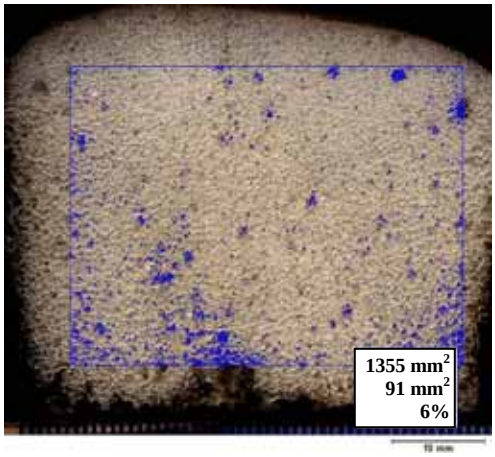

(b) Sonicated PDMS sample. Ratio 6% porosity

Figure 63: PDMS foams with degassing effect from ultrasonic irradiation

Conclusion: At higher values of applied acoustic pressure (i.e. high sonication power), the effect observed on the foams was a pronounced degassing. The ultrasound had a mechanical effect on the matrix and this homogenised the sample. It is thought that the outcome is related to the point at which cavitation becomes transient (i.e. bubbles implode), and below that level, the effect is of stable cavitation, as seen in previous sections.

5.5 Porosity engineering of polymeric foams by localised sonication. Tailoring heterogeneous cellular structures

The method used to quantify porosity distribution in polymeric foams was the one based on the MatLab™ based image processing software already presented in section 4.5.3, the 'Topo-porosity mapping' tool. This method allowed the measurement of the pore size distribution within the irradiated samples. Topographic maps were produced for each foam under analysis and the irradiation plane curves were intersected and isolated for further numerical study. The comparison of those lines, which connected points of same density for each polymeric foam, were performed through examination of their topographic profiles. In a later stage of this section, when tailoring porosity becomes the main focus, numerical analysis techniques were employed in order to quantify the topographic profiles in a way that both position and value could be linked.

5.5.1 Sonication threshold for heterogeneous foams

This section describes the results of the quantification of heterogeneity in foams produced in a controlled sound field. As explained in Chapter 4, the foams were located in the bath at positions where the acoustic pressure was known. Therefore, a direct relationship between porosity distribution and acoustic pressure could be established.

To begin with, the low threshold of sonication (i.e. the minimum acoustic pressure at which ultrasound has any distinguishable effect on the foam porosity distribution) was established. In other words, if a foam was sonicated at higher acoustic pressure than the threshold one, the internal structure which resulted was more heterogeneous.

The low acoustic pressure threshold was established for each of the working frequencies. Once the threshold had been established, the relationship between porosity gradient and the intensive variables of the system (i.e. frequency, intensity) could be studied and related to the porous structure for the sonicated polymeric foams.

5.5.1.1 *Foams irradiated at 20 kHz*

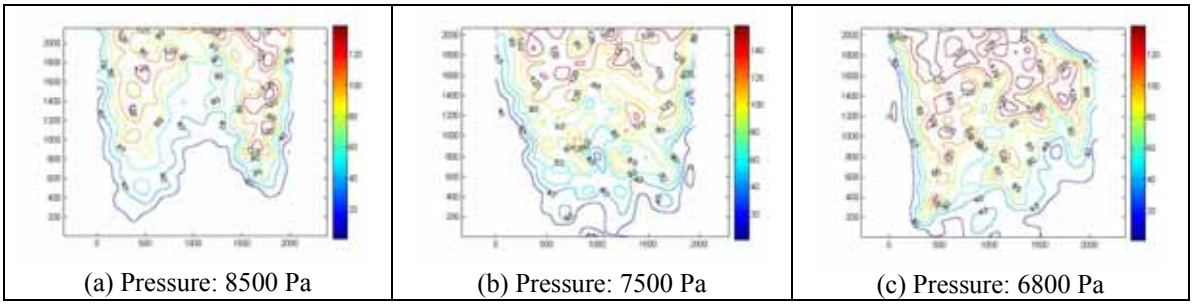

(a) Pressure: 8500 Pa | (b) Pressure: 7500 Pa | (c) Pressure: 6800 Pa

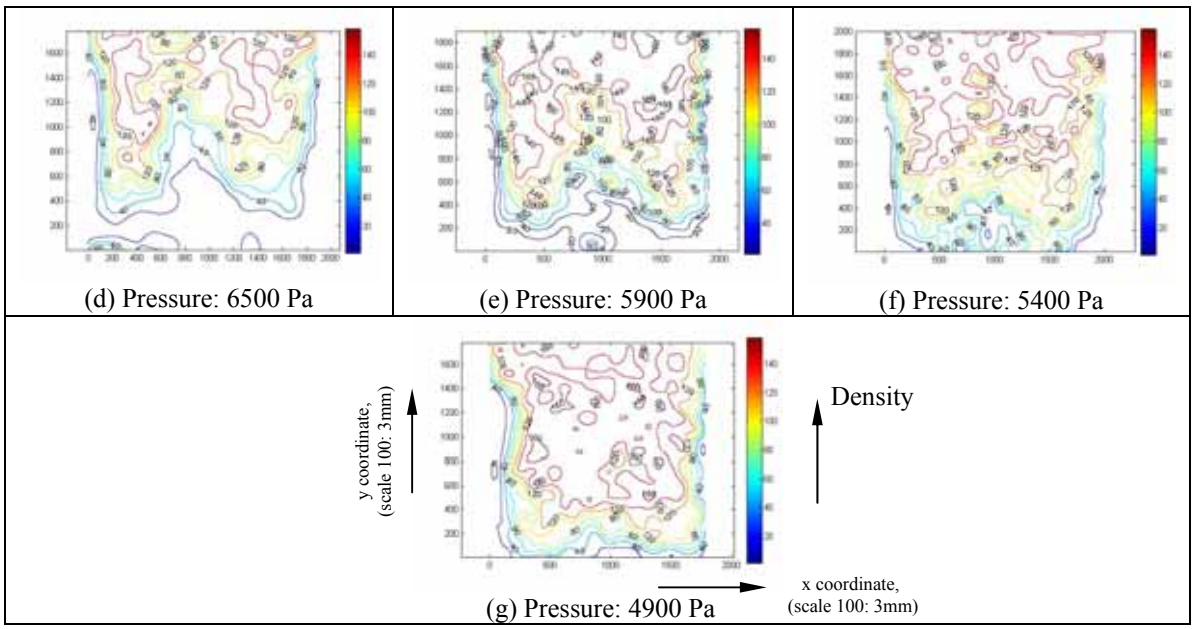

Figure 64: Foams sonicated at decreasing acoustic pressure amplitude from the probe radiating a frequency 20kHz soundwave

Performing the intersection between the topographic profile of the sample images and the plane of sonication, aligned with the horn tip (when h is 1000), graphs that allowed comparison of porosity gradient among different foams could be isolated.

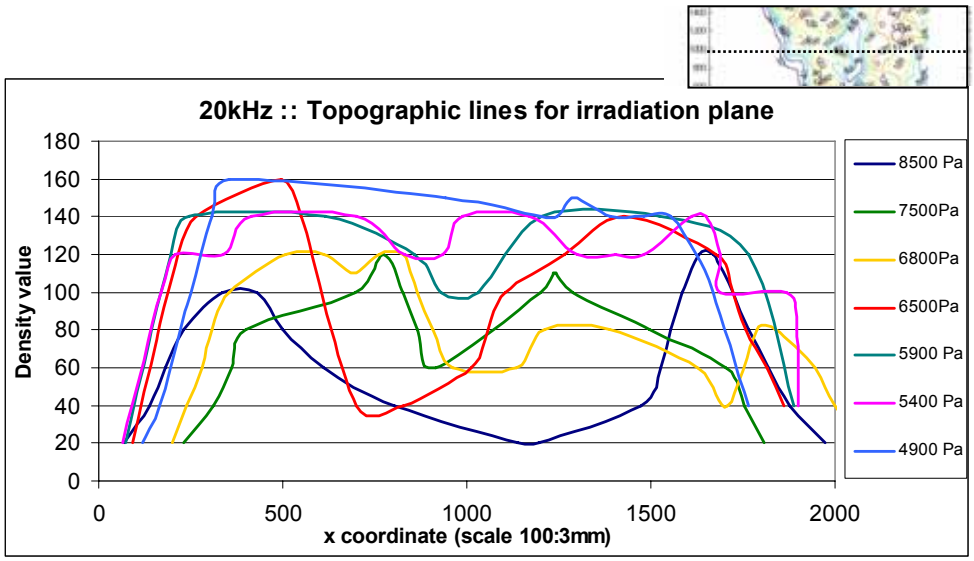

Figure 65: Topographic lines intersecting the irradiation plane for samples irradiated at 20kHz

These curves were analysed using the trapezoidal rule for numerical integrals and quantified the area bounded under the topographic lines.

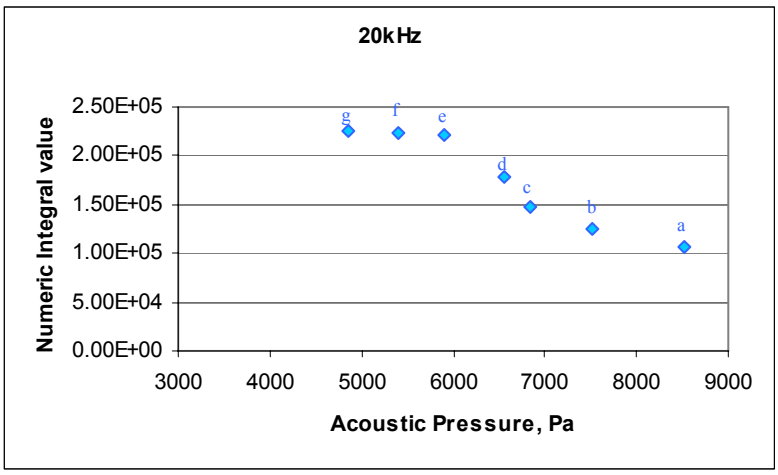

Figure 66: Quantification of heterogeneity in irradiated foams at 20kHz

5.5.1.2 *Foams irradiated at 25 kHz*

Procedure was followed in the same way for an irradiation frequency of 25 kHz.

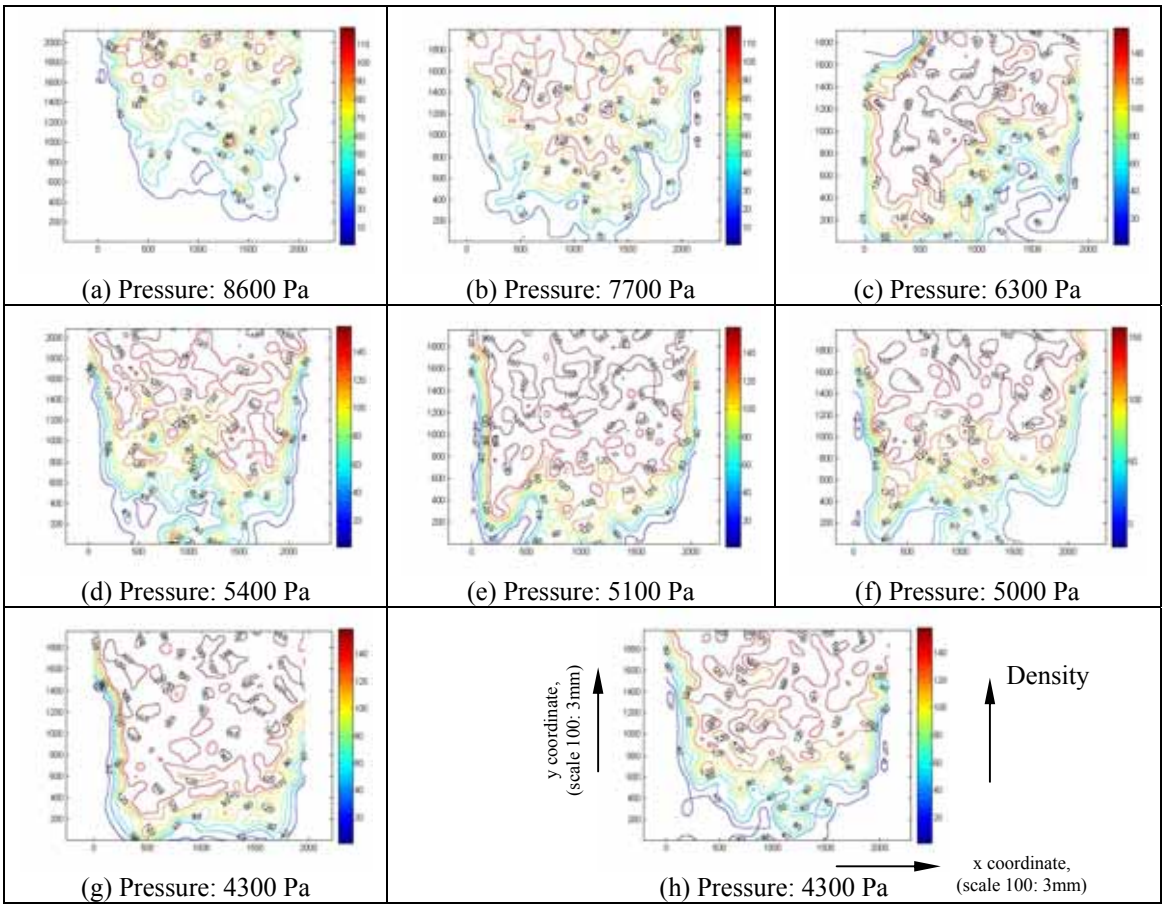

Figure 67: Foams sonicated at decreasing acoustic pressure magnitude and probe radiating at frequency 25kHz

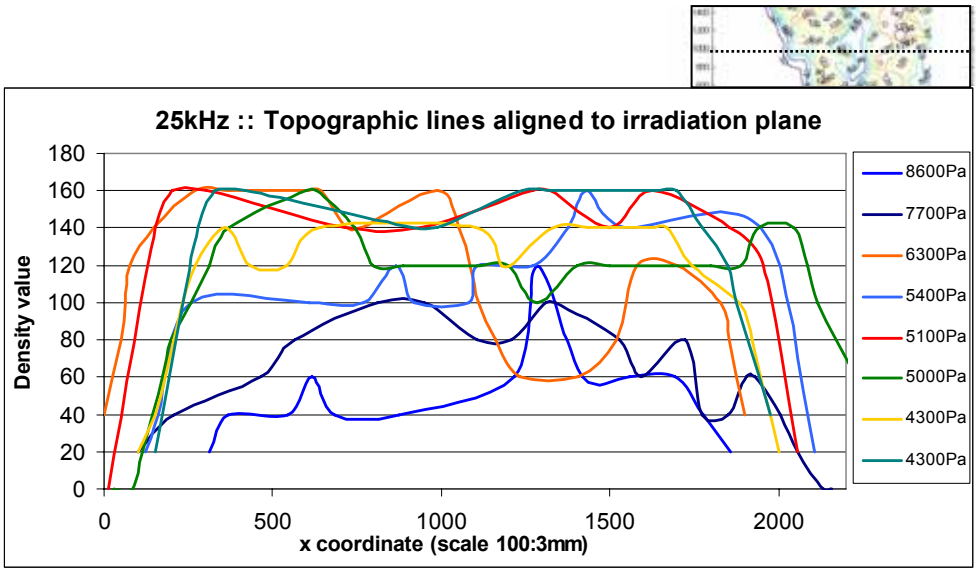

Figure 68: Topographic lines intersecting the irradiation plane for samples irradiated at 25kHz

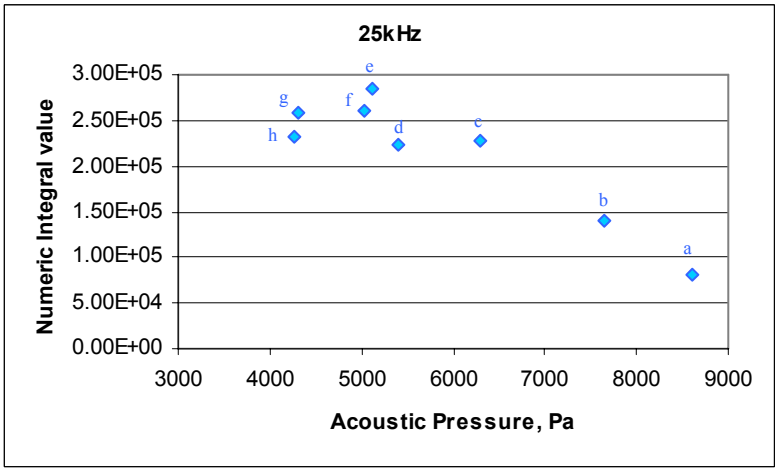

Figure 69: Quantification of heterogeneity in irradiated foams at 25kHz

5.5.1.3 *Foams irradiated at 30 kHz*

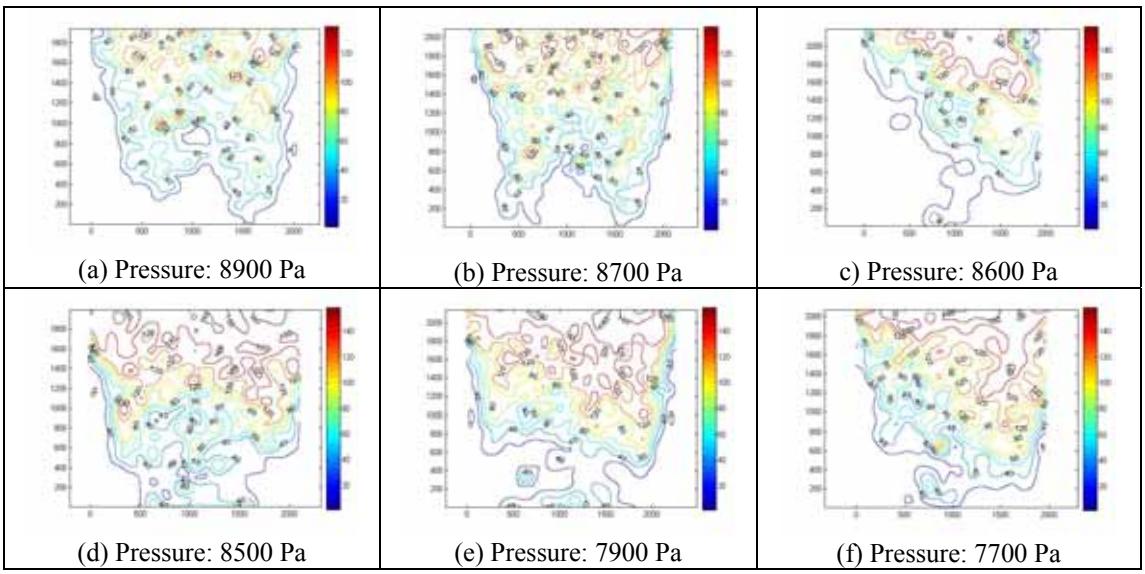

(a) Pressure: 8900 Pa | (b) Pressure: 8700 Pa | c) Pressure: 8600 Pa

(d) Pressure: 8500 Pa | (e) Pressure: 7900 Pa | (f) Pressure: 7700 Pa

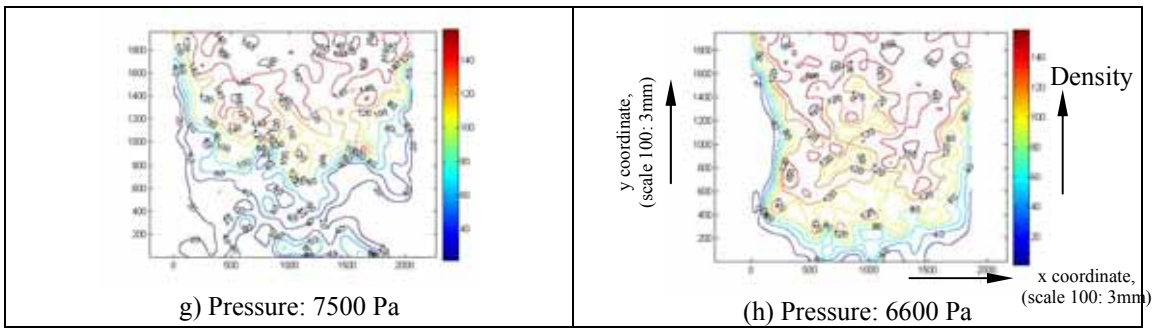

g) Pressure: 7500 Pa (h) Pressure: 6600 Pa

Figure 70: Foams sonicated at decreasing acoustic pressure amplitude and probe radiating at frequency 30kHz

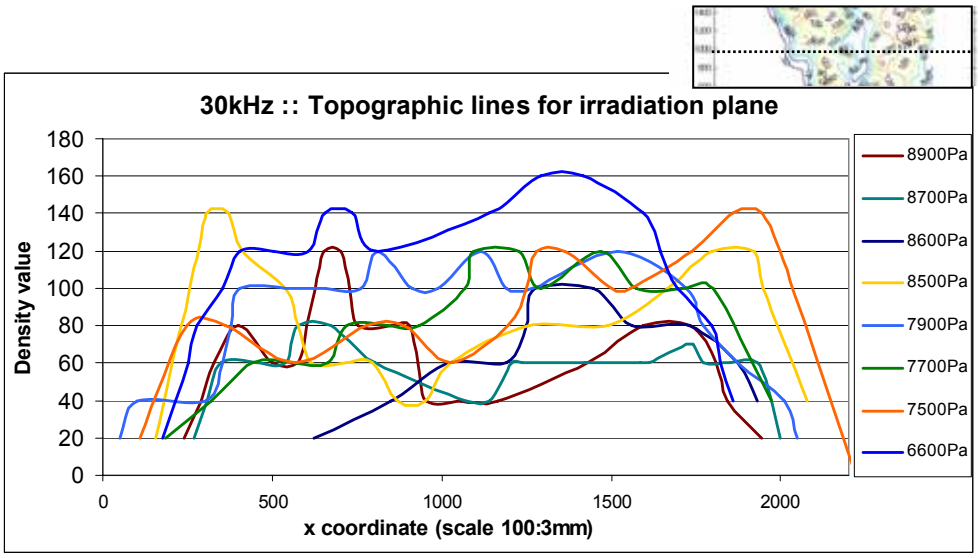

Figure 71: Topographic lines intersecting the irradiation plane for samples irradiated at 30kHz

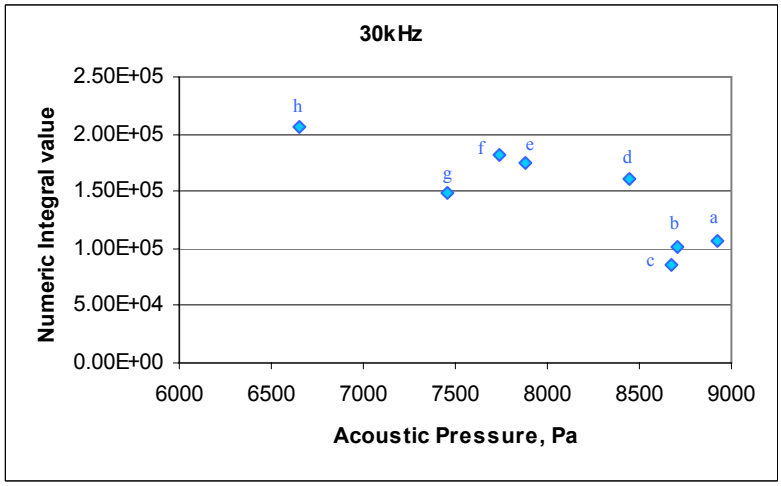

Figure 72: Quantification of heterogeneity in irradiated foams at 30kHz

Conclusion to section 5.5.1: For all frequencies tested, the diagrams show a minimum value of acoustic pressure below which a constant value of heterogeneity (or else, homogeneity in this case) was achieved. When the porosity gradation was not distinguishable for values below a certain acoustic pressure, that was considered to be the threshold for porosity engineering gradation (approx 6000Pa for 20 kHz and approx 5500Pa for 25 kHz). This

value was not as clear when samples were radiated at 30 kHz. It is believed that the threshold lies under the acoustic pressure tested, and this limitation was imposed by the experimental rig itself. In other words, the ultrasonic probe used in this work did not allow lower input powers required to investigate this area of the acoustic pressure range.

The results indicate that the porosity gradient increased directly with the acoustic pressure at which the samples were subjected to.

5.5.2 Tailoring porosity

The cross-sections shown in Figure 73 were obtained from foams irradiated when the ultrasonic probe was located on their left-hand side. The main difference between them lies in the distribution of the material: the porosity gradation. As mentioned in section 4.5.3.2, the irradiated foams' porosity distribution can be classified into three types: foams type 1, 2 and 3 (see Figure 41a). In type 1 foams (Figure 73a), the porosity gradient is negative because the pore size varies from large (left side) to small (right side). Type 2 foams (Figure 73b) present a positive porosity gradient, from small to big pore size. For type 3 foams (Figure 73c), the distribution seems to follow a symmetric distribution, with an outer perimeter of lower porosity density than the inner volume.

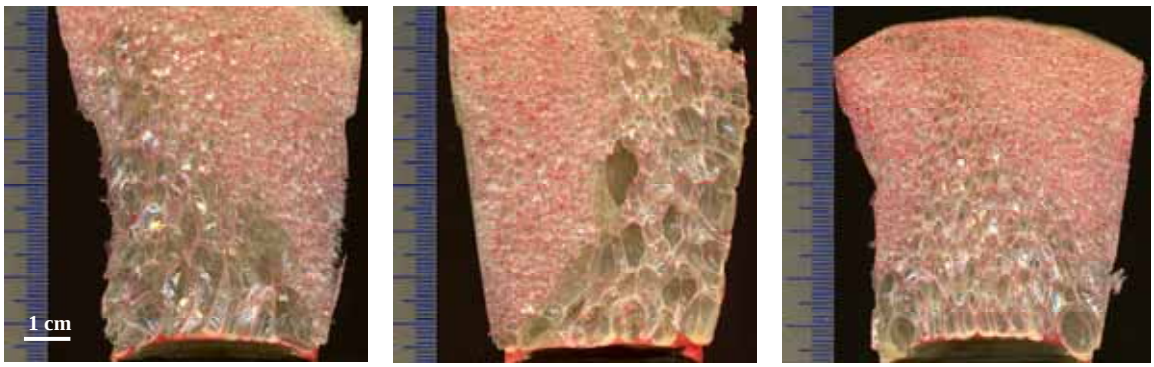

(a) (b) (c)

Figure 73: Cross-section of sonicated foams at different experimental conditions

A direct link is thought to exist between the soundwave topology (e.g. amplitude, wavelength, location of maxima, antinodes, minima of energy, nodes, etc) and the porosity distributions in the samples. In order to establish a correlation between the gradient in the sample's porosity distribution and their position within the acoustic field, a series of experiments were carried out. The vessel locations chosen for this experimental series were in the region near the probe where the decay of the acoustic signal (i.e. attenuation) could be neglected or was within a tolerance range (i.e. less than 15cm, Figure 29). Three series of experiments were performed, one for each of the working frequencies (20, 25 and 30 kHz).

As explained in section 4.5.3.2, a numeric integration was used to calculate the area under the curves obtained from the topography of the sample's cross-section. A degree of symmetry was estimated for the samples.

The results presented below are the topographic surfaces of the sonicated foams, the correspondent slices to the irradiation plane (2.5cm from the free surface) and the symmetry determination (i.e. porosity gradient) which have been calculated by the numeric integrals (i.e. area under the curves).

5.5.2.1 *Tailoring porosity for 20 kHz*

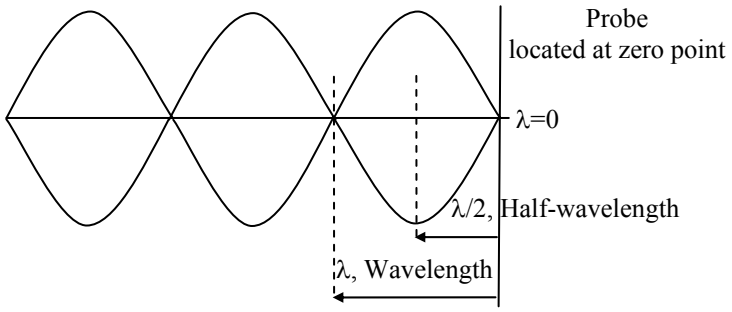

Figure 74: Sketch of standing wave in the bath from the irradiating probe at 20kHz

As already mentioned in section 4.3.2, the wavelength value for a soundwave of 20 kHz is 7.4cm. This means that half-wavelength (i.e. 3.70cm) and odd multiples will be antinodes (places of maximum energy, when amplitude is maximum), and the even multiples, nodes (places of zero value for the energy, amplitude equals to zero).

The foams were irradiated at the same power input applied to the transducer, 18000 Pa (with a 12% tolerance). The chosen distances for this experiment were: 3.7cm and 11.1cm (half-wavelength, antinode), 7.4 (wavelength, node) and at 8.6cm (to make the mid-plane of the foam coincide with the maximum of acoustic amplitude). It can be seen in the profiles that the foam sonicated at 11.1cm (Figure 75d) from the probe presented a more homogeneous porosity gradation in comparison with the foam sonicated at 3.7cm (Figure 75a), because the signal had attenuated at that distance.

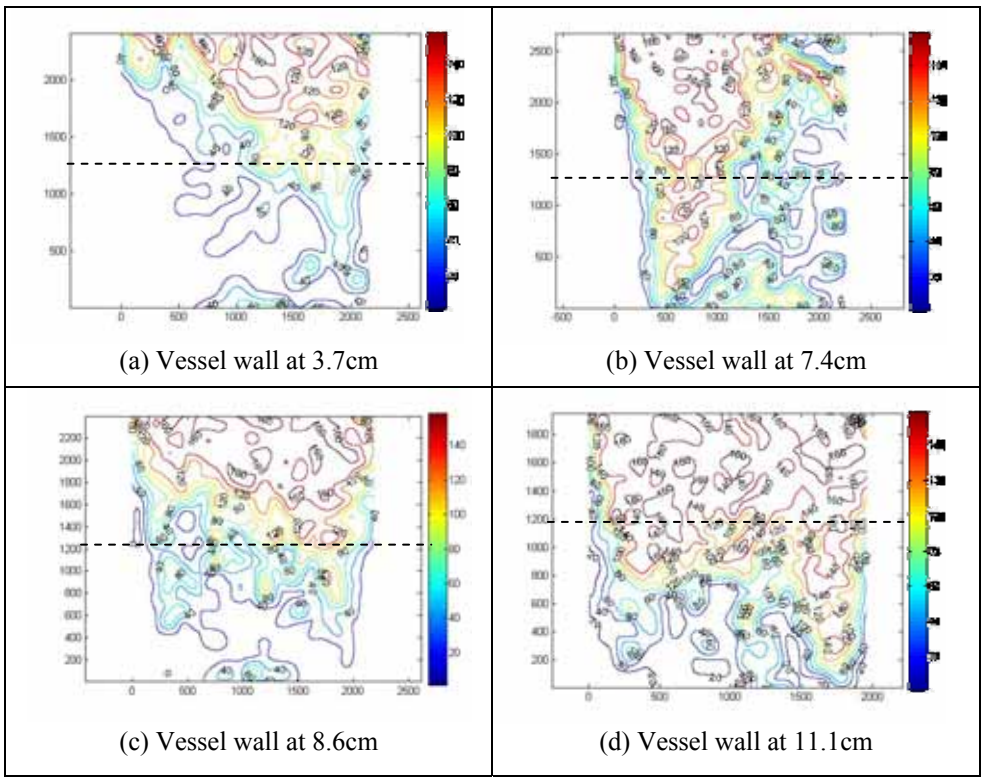

(a) Vessel wall at 3.7cm

(b) Vessel wall at 7.4cm

(c) Vessel wall at 8.6cm

(d) Vessel wall at 11.1cm

Figure 75: Foams irradiated at same frequency (20kHz) and variable distance from probe

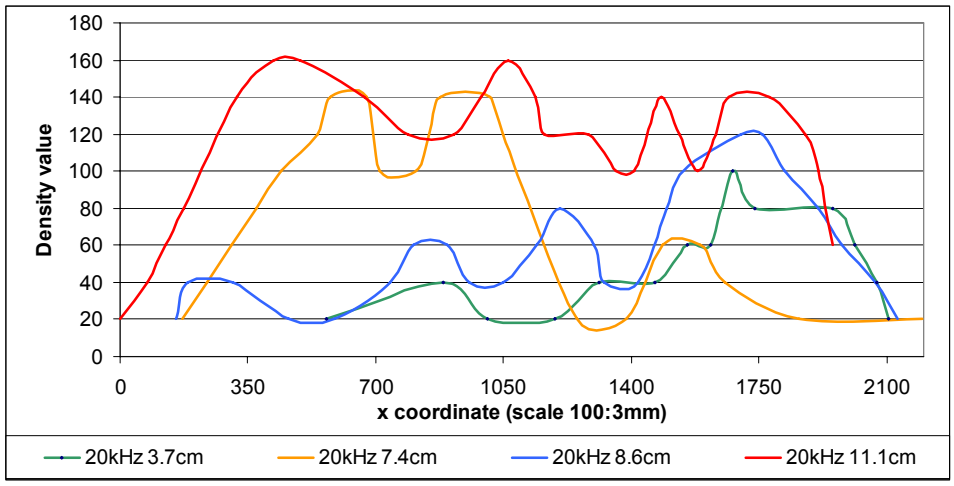

Figure 76: Cross-sections of foams irradiated at 20kHz

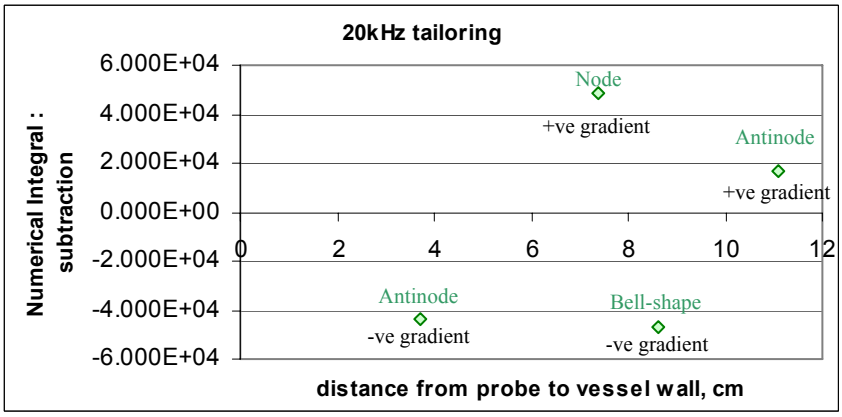

Figure 77: Porosity gradient for foams irradiated at 20kHz at variable distances

The positive values correspond to foams whose vessel's wall was placed at a node, and the negative values to those placed at an antinode.

Conclusion: 'negative gradient' are type 1 foams and 'positive gradient' are type 2 foams. Those foams placed at distant locations from the ultrasound source presented a more homogeneous structure due to the attenuation of the signal (i.e. secondary reflections, refractions, etc).

5.5.2.2 *Tailoring porosity for 25 kHz*

Likewise, when the foams were irradiated at 25kHz (where a wavelength equals to 5.90cm), the antinodes were at odd multiples of half-wavelengths, 2.95cm, (maximum amplitude) and the even multiples were the nodes (amplitude zero). The applied acoustic pressure was 12000Pa (9% tolerance).

The foams were irradiated at distances: 2.95cm and 8.85cm (antinodes), 5.90cm (node) and 6.35cm (in order to make the central axis of the container coincident with the maximum amplitude location).

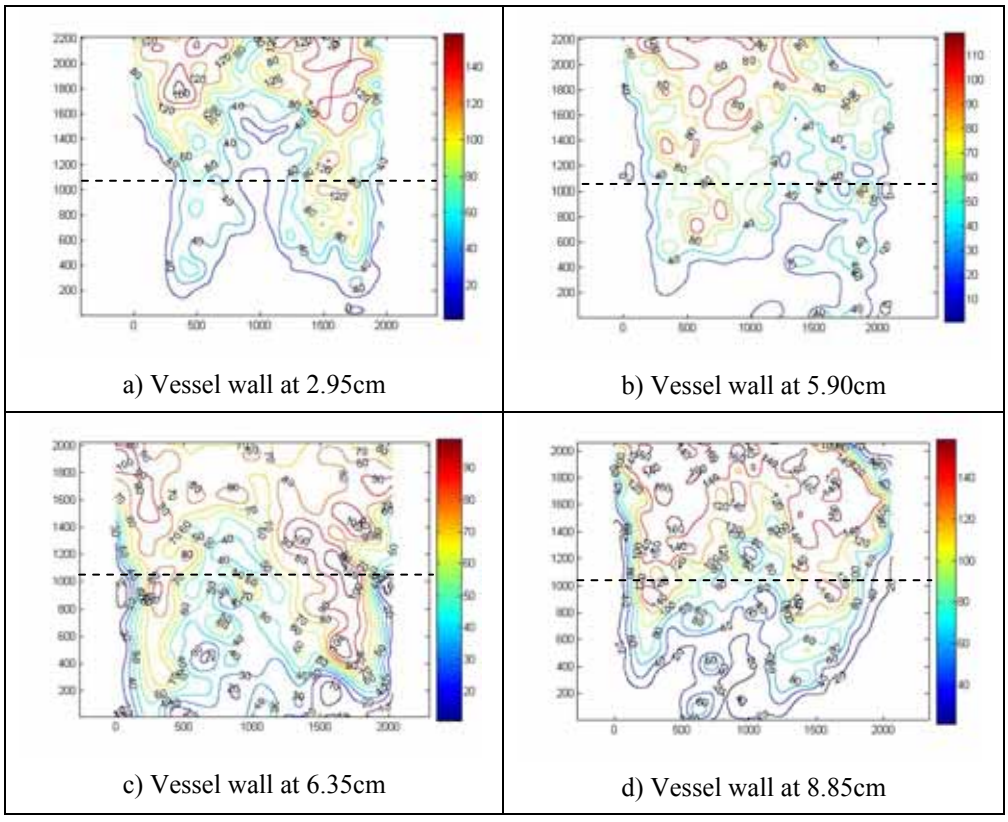

a) Vessel wall at 2.95cm

b) Vessel wall at 5.90cm

c) Vessel wall at 6.35cm

d) Vessel wall at 8.85cm

Figure 78: Foams irradiated at same frequency (25kHz) and variable distance from probe

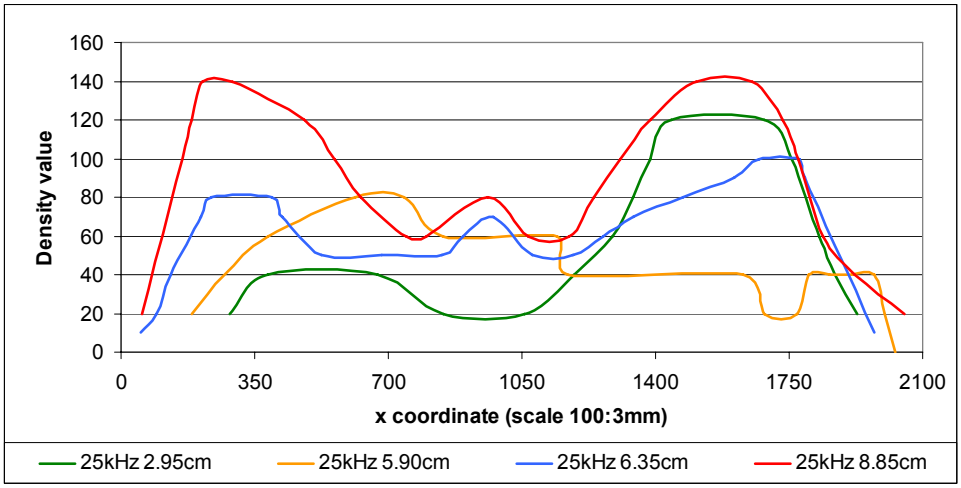

Figure 79: Cross-sections of foams irradiated at 25kHz

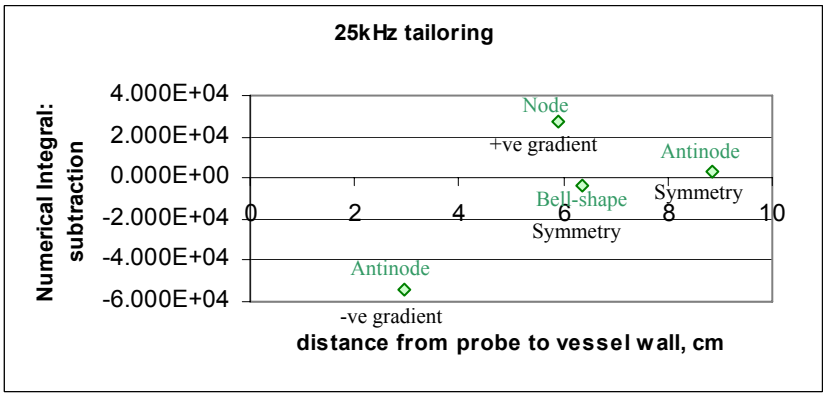

Figure 80: Porosity gradient for foams irradiated at 25kHz at variable distances

Conclusions: Heterogeneity in the porosity distribution can be seen in the two foams irradiated at closest distances: negative gradient for the foam irradiated at the antinode and positive for that irradiated at the node. For the other two foams, the symmetry in their distribution is obvious: an outer layer of high density material involving a core of higher porosity. In the foam irradiated further away, this distribution can also be seen, but it is less distinct. It is thought to be due to signal attenuation too.

5.5.2.3 *Tailoring porosity for 30 kHz*

Similarly, for the frequency 30 kHz, the distances were: 2.45cm (antinode), 4.9cm (node) and 7.35cm (antinode). The distance at which the container's central axis was aligned with the antinode (i.e. maximum acoustic pressure) was not tested because that value is only 4.85cm (0.05cm apart from the sample irradiated at the node). The acoustic pressure at which the foams were subject to was 8900Pa with a 4% tolerance in the readings.

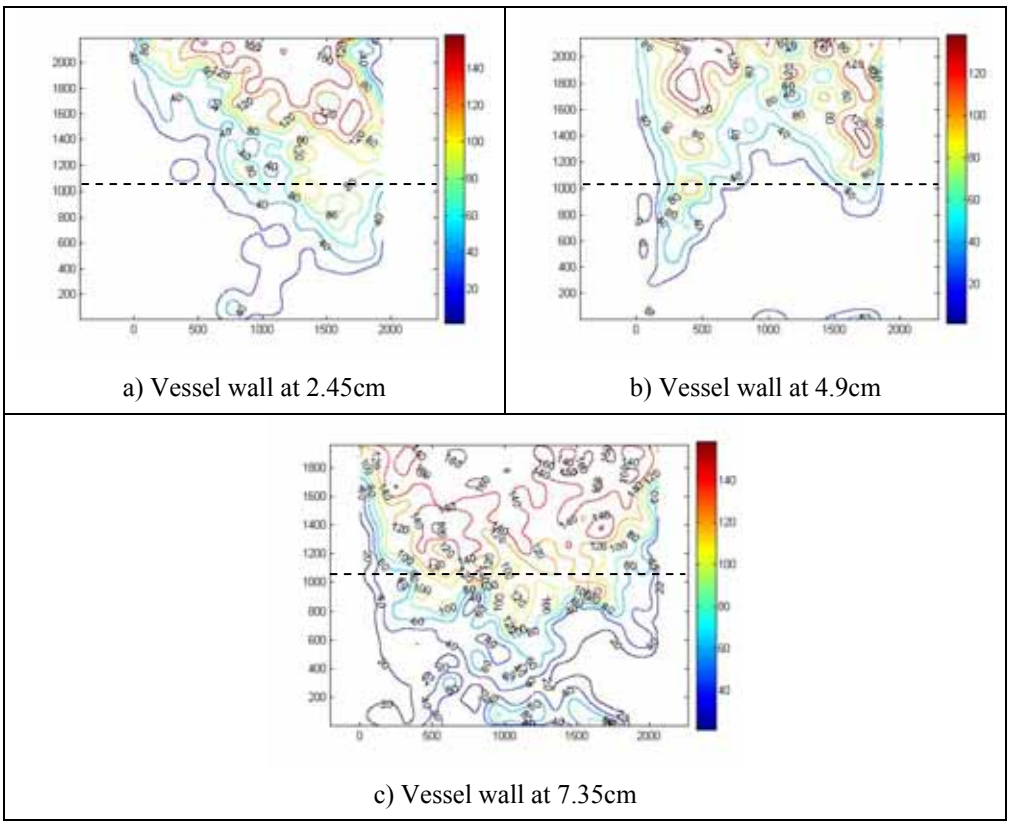

a) Vessel wall at 2.45cm

b) Vessel wall at 4.9cm

c) Vessel wall at 7.35cm

Figure 81: Foams irradiated at same frequency (30kHz) and variable distance from probe

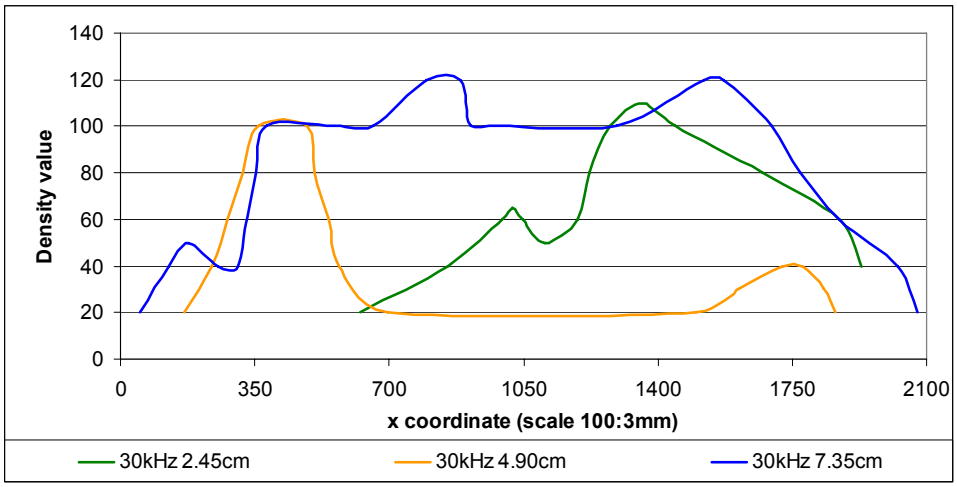

Figure 82: Cross-sections of foams irradiated at 30kHz

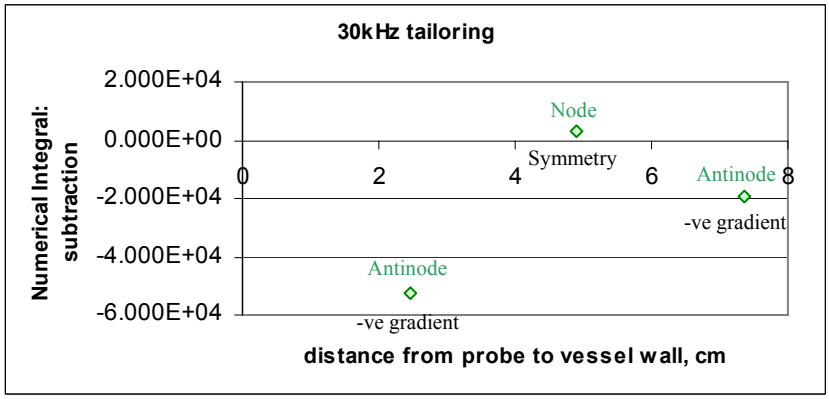

Figure 83: Porosity gradient for foams irradiated at 30kHz at variable distances

Conclusion: The two foams irradiated at the antinodes present a negative porosity gradient, more obvious in the foam irradiated at a closer distance to the probe. The foam irradiated at the antinode shows a symmetrical distribution, slightly towards a positive gradient. This is because the distance of the node is coincident at this frequency to the distance at which the central axis of the container, of 5cm diameter, is aligned to the maximum amplitude.

5.5.3 Correlation of experimental results with simulated model

Simulations were carried out in order to find out how the variation in the local pressure amplitude of the acoustic field inside of the bath affected the porosity distributions in the samples.

The simulation for a vessel immersed in the water bath is performed, as shown in Figure 84. The distance between the probe and the vessel wall is 11.1cm (three times the half-wavelength for the frequency 20kHz).

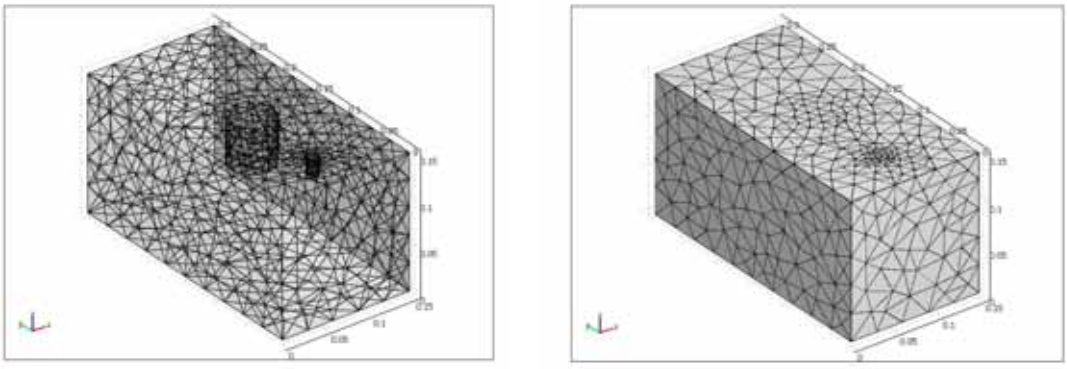

Figure 84: (a) Internal mesh on the modelled rig with immersed vessel; (b) Outer mesh on the modelled rig with immersed vessel

The mesh consisted of 7027 elements and the simulator solved for a model with 10043 degrees of freedom. Time stepping was set at 0:0.1:1s to reach its steady state for a tolerance of 0.01s. The averaged solution time was 78.328s.

The pattern of the acoustic field in the water bath was simulated in the presence of an immersed container and compared to the results obtained for an empty bath (Figure 85). The red area in the bath of the figures illustrated the position of the sonotrode.

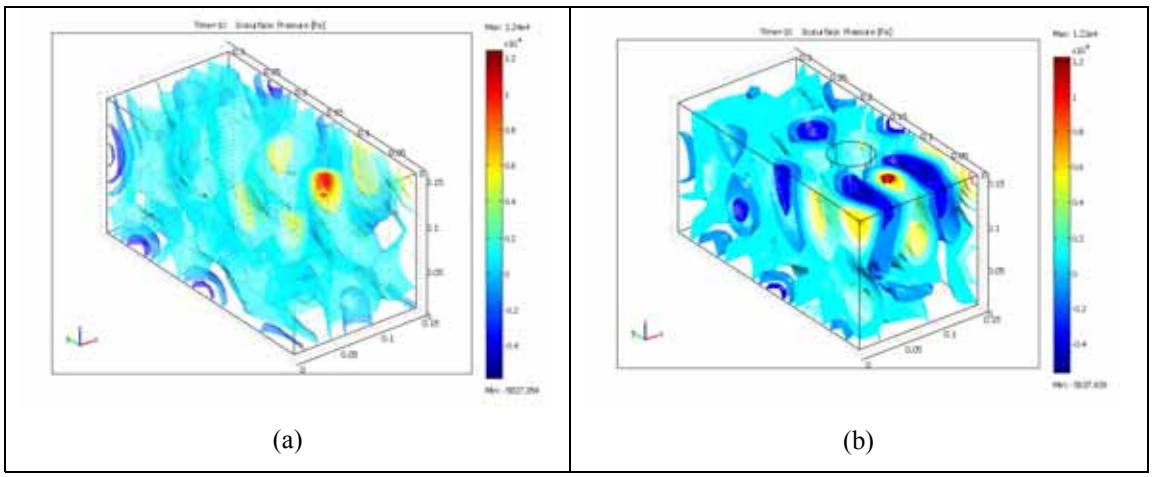

(a) (b)

Figure 85: Results of the simulated baths in 'isolines mode' representation: a) for an empty bath; b) for bath with an immersed vessel at 3.7cm distant from the probe

Vertical planes were extracted from the modelled representations in order to assess how the presence of the immersed vessel changed the pattern of the acoustic field inside of the water bath. Figure 86 shows a series of planes corresponding to the 3D pressure fields at different distances between the probe and the vessels containing the foaming reactants.

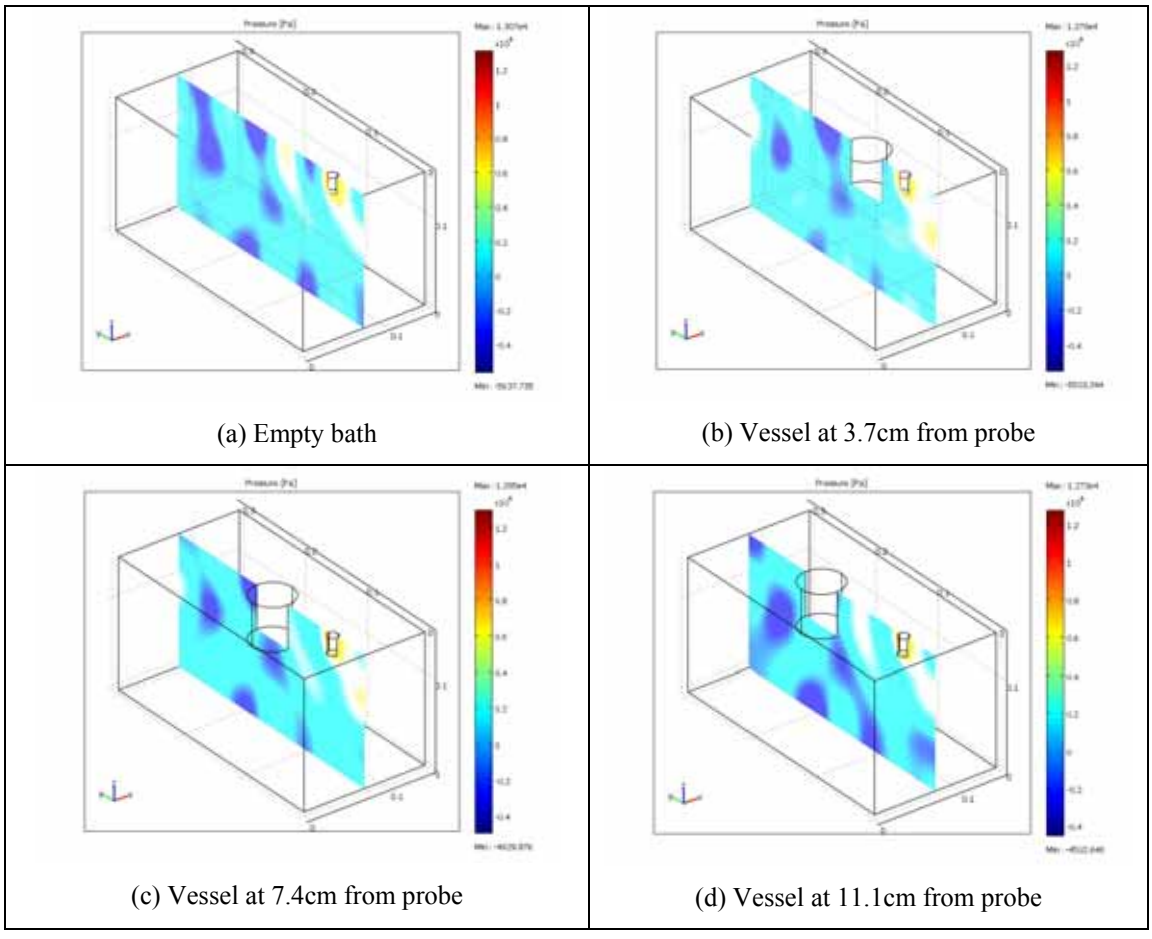

(a) Empty bath (b) Vessel at 3.7cm from probe

(c) Vessel at 7.4cm from probe (d) Vessel at 11.1cm from probe

Figure 86: Extracted vertical planes from modelled baths with immersed vessels at different distances from the probe

Comparing the acoustic field in the bath without (Figure 86a) and with the vessel (Figure 86b, c, d), a distinct difference in the acoustic pressure distribution can be observed between them. It should be noticed that, with an immersed vessel, the pressure pattern is distorted in the vicinity of the container. The formation of these patterns is thought to be attributed to the interference between secondary waves and the primary standing waves.

The acoustic pattern inside of each of the containers located at the different distances from the probe was extracted from the model (Figure 87). Corresponding figures to the other working frequencies can be found in Appendix II.

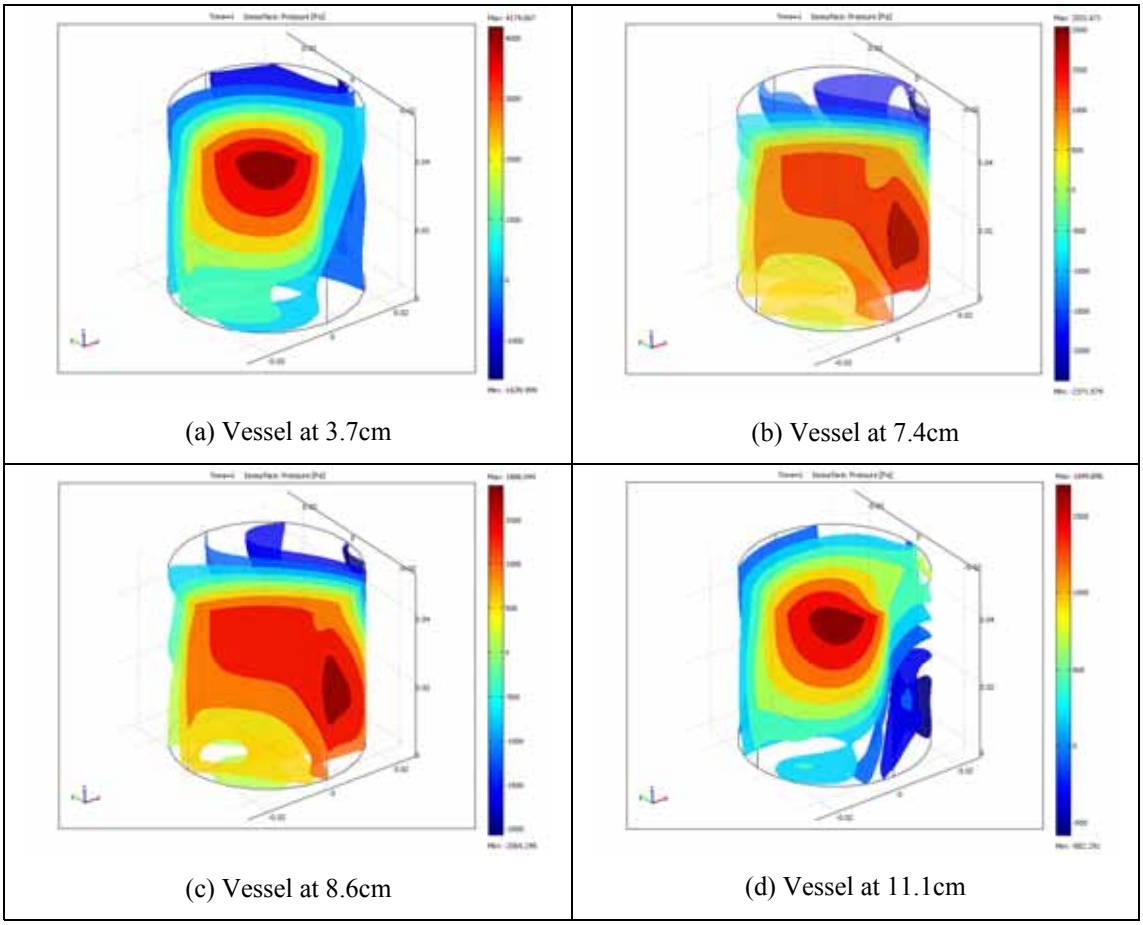

(a) Vessel at 3.7cm

(b) Vessel at 7.4cm

(c) Vessel at 8.6cm

(d) Vessel at 11.1cm

Figure 87: Acoustic fields inside vessels irradiated at 20kHz in 'isolines mode' representation

As before, vertical planes aligned to be parallel to the acoustic signal arriving from the sonotrode, were obtained to investigate how the acoustic pressure distribution inside of the vessels varied with the distance from the sonotrode's tip.

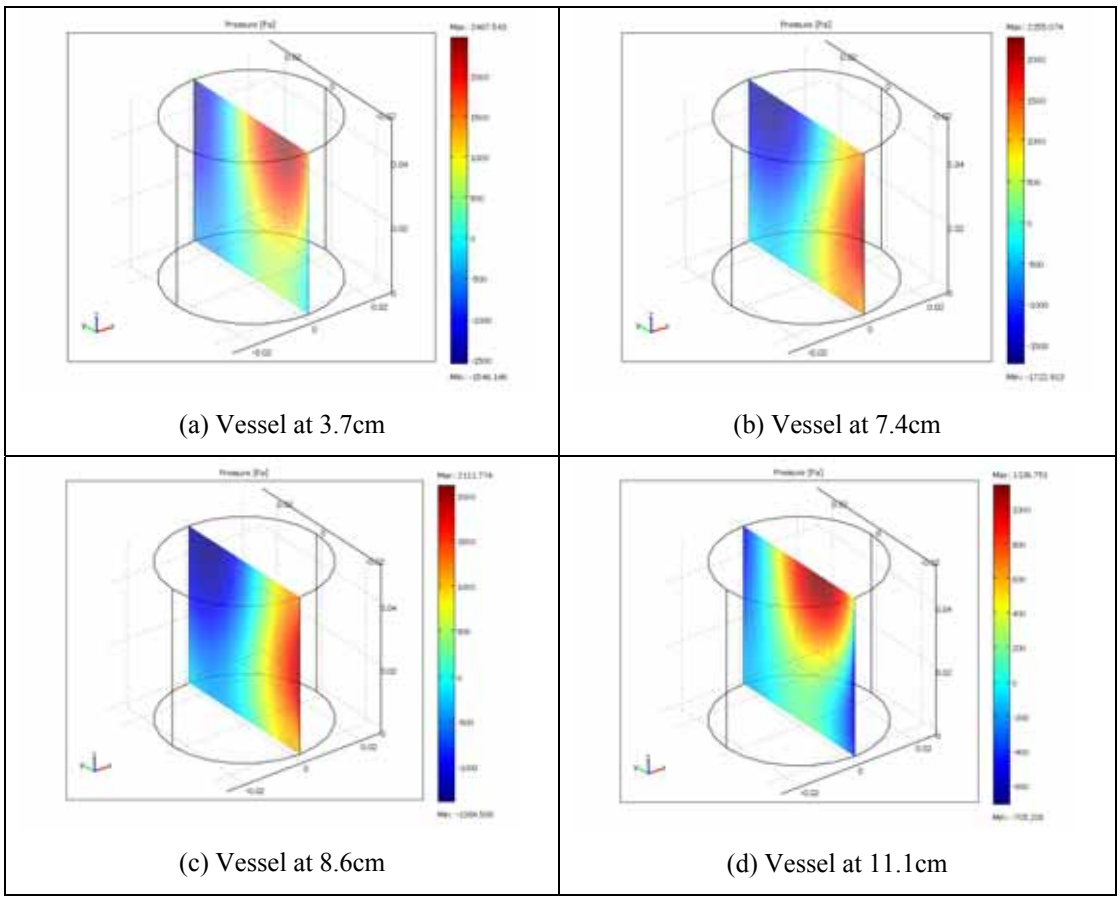

(a) Vessel at 3.7cm

(b) Vessel at 7.4cm

(c) Vessel at 8.6cm

(d) Vessel at 11.1cm

Figure 88: Extracted vertical planes from modelled containers irradiated with ultrasound

In order to establish a relationship between the porosity gradation of the polymeric foams and the acoustic field inside of the vessels, the sound pressure level distribution inside of the containers (as obtained by the simulated model) were plotted along with the cross-section values of the foams' porosity distributions. These porosity distributions were obtained from the inversed values of the density distributions (section 5.5.2) extracted by using the 'Topo-porosity' image processing program detailed in section 4.5.3.

Although the bulk density (defined as the ratio of mass to volume) or its inverse, bulk porosity, remained approximately the same from Stage C onwards until fully cross-linking of the polymer, the local porosity and, therefore, the acoustic impedance, varied continuously. The change in acoustic impedance for a given mixture is the underpinning principle for on-line monitoring of the viscosity and density variations of liquids in process engineering (e.g. food technologies). The acoustic impedance of a viscous fluid is a function of the density of the fluid, its viscosity and the circular frequency ($\omega = 2\pi f$) of the ultrasonic wave [172], in the same way that the acoustic impedance of a solid is the resultant value of the product of the solid density and the longitudinal sound velocity (section 3.3.1.3).

During foam cross-linking, the irradiated medium was a mixture of water, carbon dioxide and polyurethane foam. Therefore, the acoustic impedance was expected to change from an initial value similar to water (Z_{water}=1.48MRayl) at initial stages (B and C), through a resin acoustic impedance (Z_{resin}= 1.5-1.8MRayl) [156] when the viscosity was high, evolving finally towards a typical acoustic impedance value in the range of the porous materials (7.4-10MRayl) [155] or compact bone (9.3MRayl for a density of 1930kg/m^3) [173] when the foam is fully cured and dry. For the purpose of the irradiated foam in the simulated bath, the working acoustic impedances that were used corresponded to the water (Z=1.48MRayl; density 1000kg/m^3, longitudinal sound velocity c_S =1480m/s) and to typical cortical bone ($Z_{cort\ bone}$ = 2.6MRayl for a density of 1630kg/m^3, c_S =1550m/s) [174], which matched the expected density of the foam at those stages in the reaction.

Figure 89 illustrates the comparison made between experimental and simulated results. For each case (Figure 90, Figure 91 and Figure 92), the porosity distribution across the section of the foams (solid line) was plotted along with the acoustic pressure level in the bath as extracted from the simulator, modelling the material properties of the foam to water (dash and dot line) and to cortical bone (dashed line).

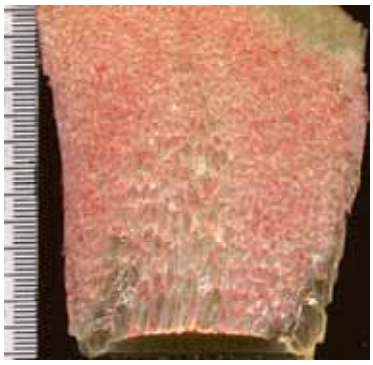

(a) Photograph of the sonicated foam

Image Analysis of the sample with 'Topo-porosity mapping'	**Simulation of the irradiated sample with COMSOL™**

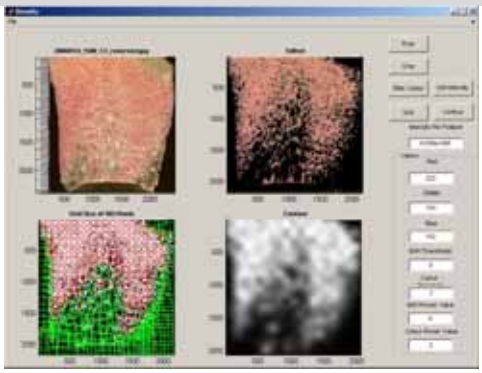

(b) Topo-porosity interface applied to the photograph

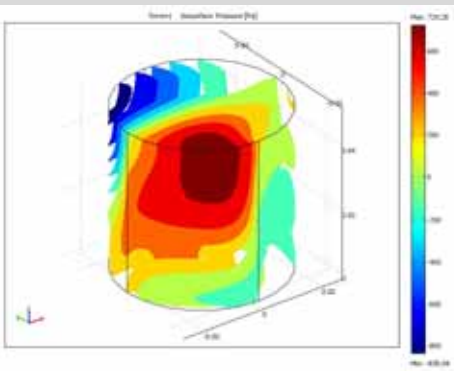

(c) Modelled immersed vessel irradiated in the water bath

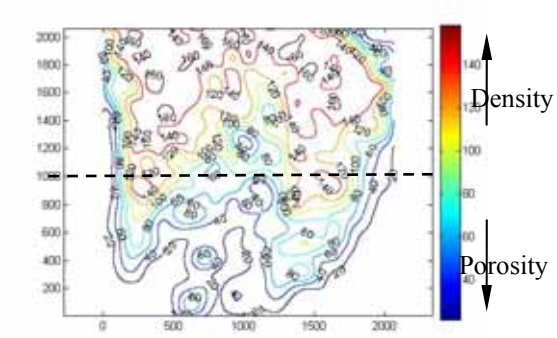

(d) Cross-section of the sample in 'contour lines' mode

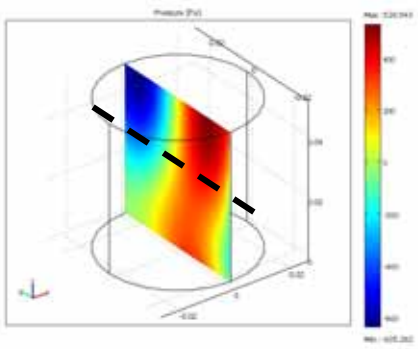

(e) Vertical plane from modelled vessel

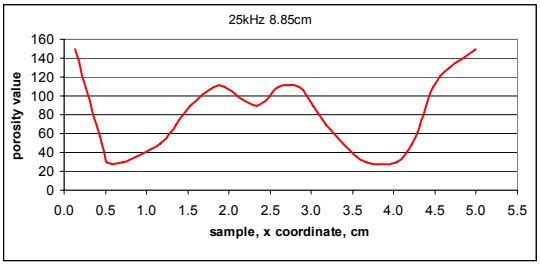

(f) Porosity line (inverse of density values) extracted at 'sonication plane' aligned with sonotrode

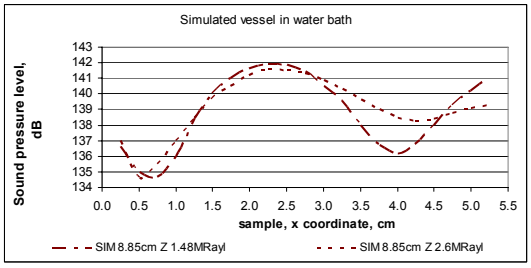

(g) Sound pressure levels extracted from modelled vessel at 'sonication plane' aligned with sonotrode for two acoustic impedances

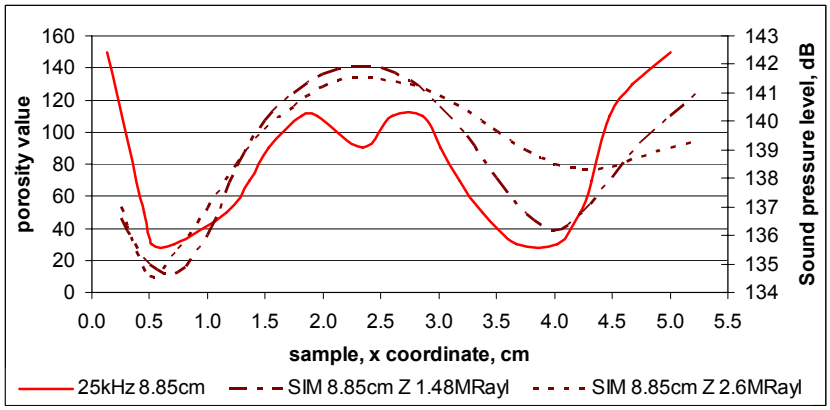

(h) Comparison porosity (experimental) vs sound pressure distributions (simulation) for irradiated foam

Figure 89: Procedure for analysis of foam irradiated at 25kHz and 8.85cm distant from the sonotrode while immersed in the water bath

For those foams irradiated at 20 kHz and 18000Pa, the comparison between the porosity distribution and the sound pressure level in both modelled cases (water and cortical bone) are presented in Figure 90.

Likewise, Figure 91 and Figure 92 present the resulting comparison for foams irradiated at 25 kHz and 12000 Pa and those irradiated at 30 kHz and 8900 Pa, respectively.

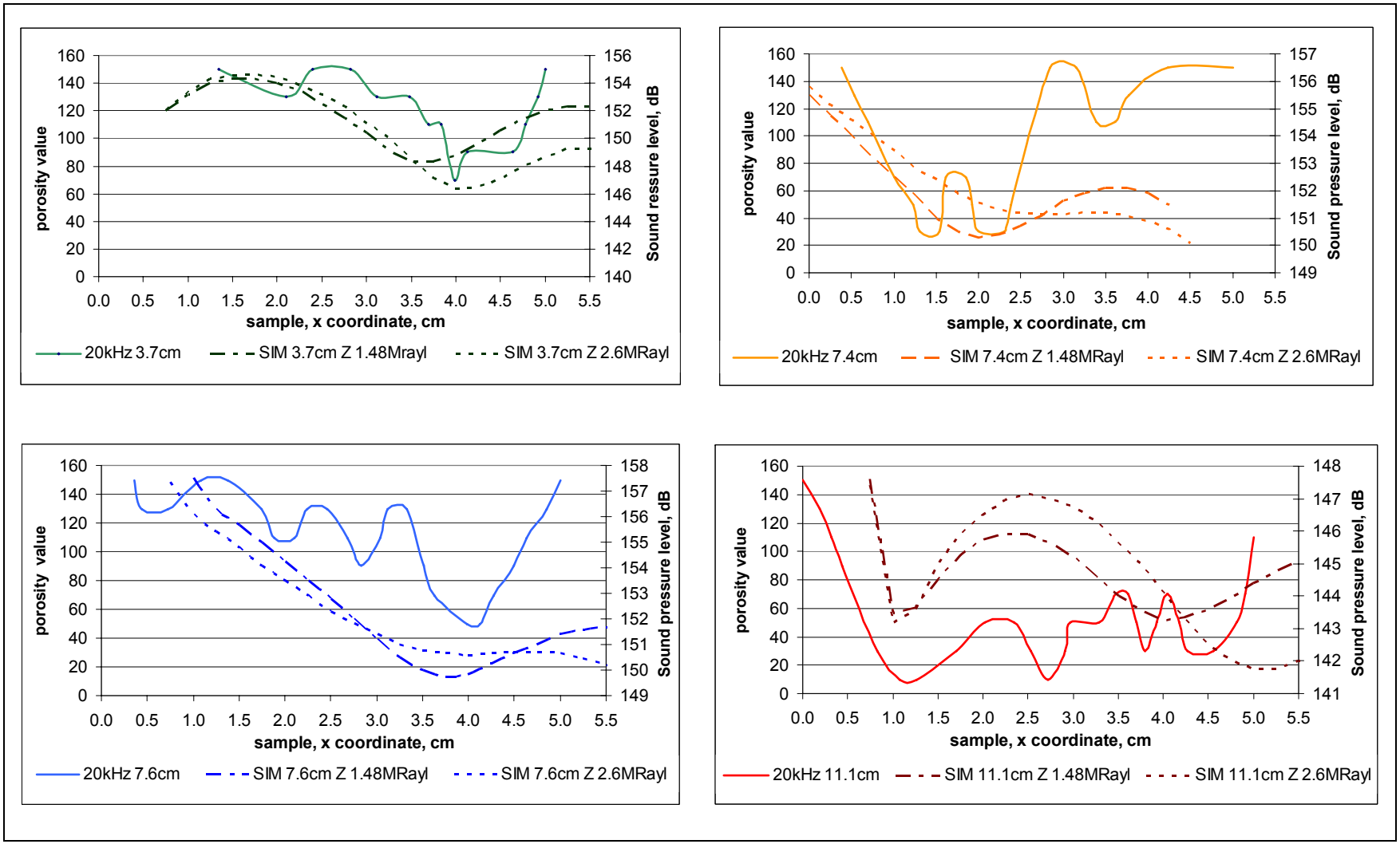

Figure 90: Comparison of porosity and sound pressure distributions for foams irradiated at 20kHz

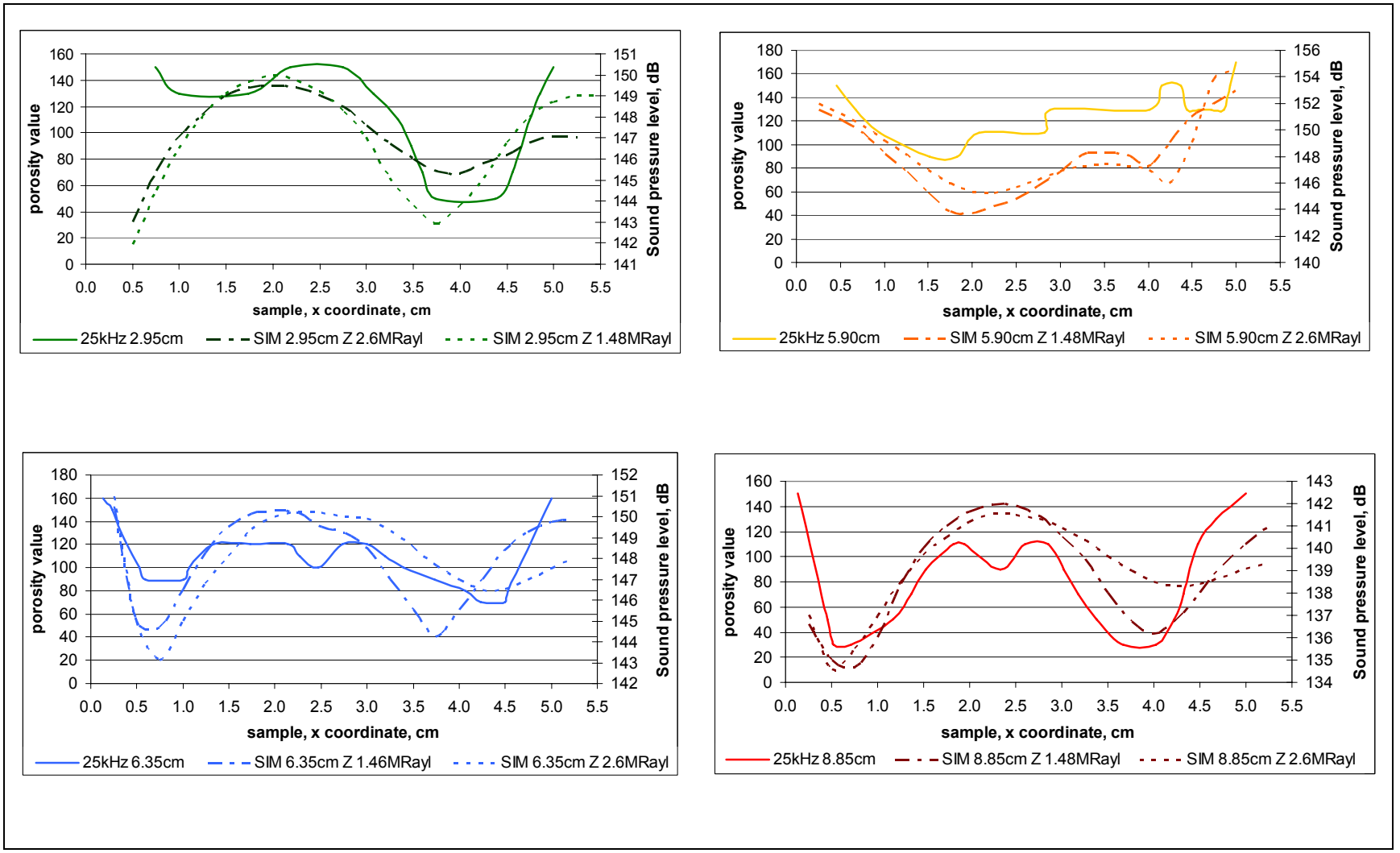

Figure 91: Comparison of porosity and sound pressure distributions for foams irradiated at 25kHz

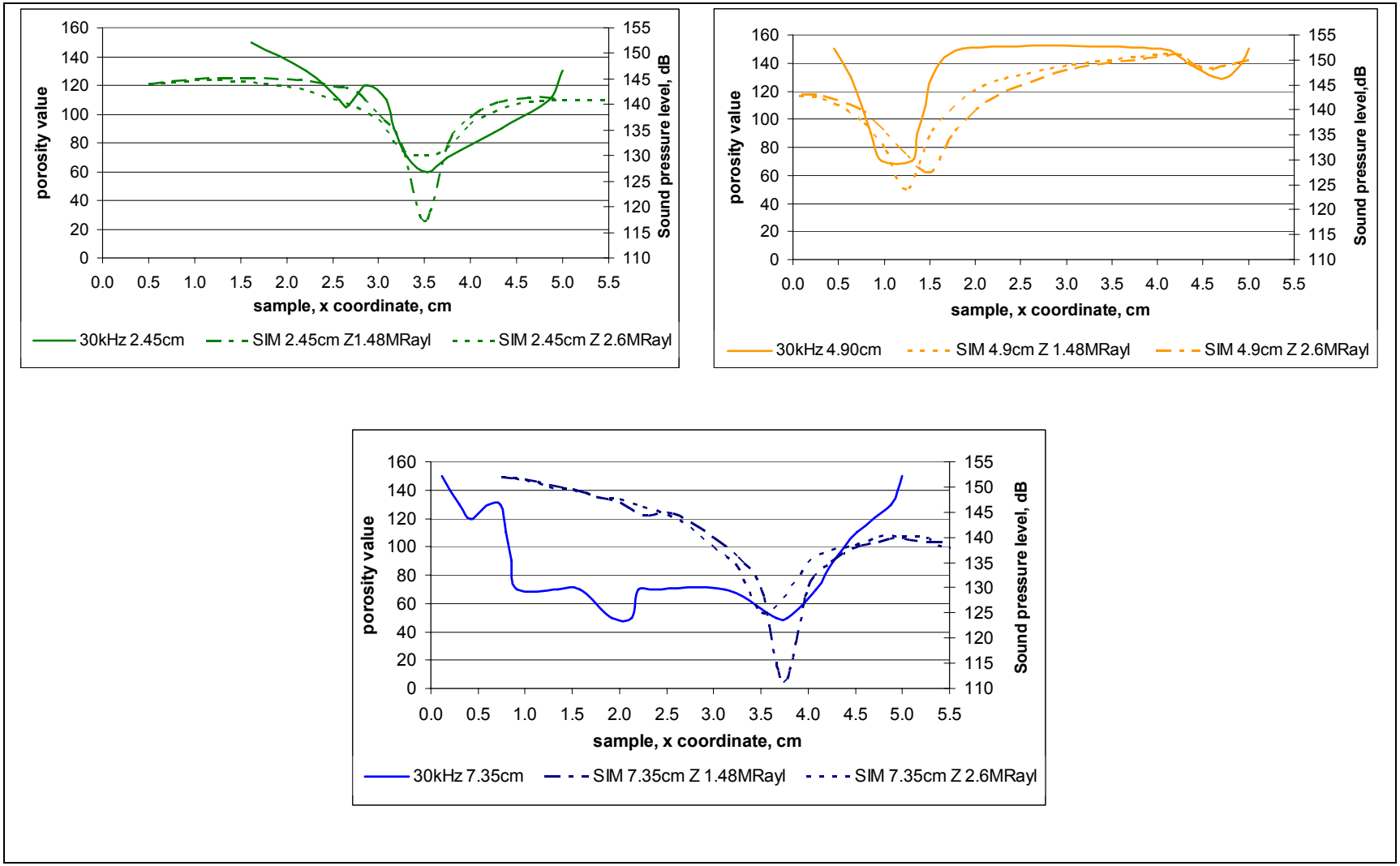

Figure 92: Comparison of porosity and sound pressure distributions for foams irradiated at 30kHz

Conclusion: The samples that were irradiated at higher acoustic pressures and/or shorter distance to the probe present a better correlation between the porosity distribution and the acoustic pressure level. However, those foams irradiated at lower acoustic energy and/or further from the sonotrode (e.g. foam irradiated at 11.1cm, 20 kHz and 6.35cm, 30 kHz) showed a weaker correlation with the simulated pressure distribution. In fact, it was also noted that this was the area of the water bath in which the simulation deviated most from the measured results (see Figure 29).

The approximation of the foam mixture to water for the modelled pressure distribution inside of the container when irradiated appears to produce a closer correlation with the experimental results than to porous bone. This is due possibly to the liquid nature of the mixture in stages B, C and the high percentage of water/acetone impregnating the cavities at stage D that has not evaporated/reacted yet.

The next chapter discusses the findings that have been reported in this chapter and links them to the theoretical principles that were exposed in Chapter 3. An assessment of the robustness of the methodology and the analysis of the weak constrains will also be discussed for the foam manufacture, the texture analysis of the foams and the simulated model. The resulting statements will be compared against the hypotheses listed in Chapter 3 and the aims and objectives of this research work mentioned in Chapter 1. Finally the relationship between the irradiating conditions and the porosity distribution will be established and discussed against the hypotheses of this research.

CHAPTER 6. DISCUSSION

This chapter contains a discussion of the results described in Chapter 5 with reference to the theory presented in Chapter 3 and the methodology explained in Chapter 4.

It is suggested in this work that when conditions of stable cavitation are established, ultrasound can create porosity gradation by producing bubbles of different sizes depending on the acoustic pressure to which they are subjected. This mechanism allows the engineering of standing waves to 'tailor' the porosity of the polymeric matrix that finally solidifies into a foam.

Aside from the clear effect of acoustic irradiation on porosity distribution, some other aspects of the work derived from observations and experimental procedures for the sonication of polymeric melts are also discussed. This chapter is divided into five parts.

First, the electrical resistivity tracking method is appraised with regard to its suitability to accurately identify the formation stages in the foam, as described by other authors. Secondly, some evidence of the sonochemistry in the reaction is reviewed. The third section summarises a number of findings that can be drawn from the analysis of the influence that acoustic pressure had on the cellular structure of a foamed material presented in Chapter 5 in conjunction with the hypothesis stated in Chapter 3, and other applications already found in industry and reported by other researchers (Chapter 2). The relationship between ultrasonic pressure, frequency and porosity is also examined. In this way, porosity is related to ultrasonic irradiation conditions to form a conclusion in the context of the hypotheses set out in Chapter 3. The following section assesses the prediction made in Chapter 4 regarding the acoustic pattern in the bath and compares the measured values of ultrasound magnitude with the observable effect on the foams. In the fourth section of this Chapter, the analysis produced by the image processing methodology developed for this work is revisited and discussed in the light of the results. Finally, the last section verifies the correlation between measured porosity distribution and simulated sound pressure in the samples and also points out benefits and limitations of the simulation tool.

6.1 Electrical resistivity measurements

The purpose of this section is to interpret, as far as possible, the raw data in terms of variation in the electrical resistivity, and to compare these with the published data, allowing

a comparison between the variations observed (Chapter 5) and the stages reported in the literature (Chapter 3). Although the electrical resistivity is weakly dependant on temperature [175] for the range of working temperatures and pressures (i.e. open vessel) used here, the changes must be caused by the polymerisation reaction.

A typical graph like the one presented in Figure 45b showed distinguishable events that took place during the foam formation. For example, at point 3, a minimum value for the electrical resistivity of the mixture was detected. This implied that the value for the electrical conductivity was at its maximum at that point. This statement makes sense when the individual conductivities are considered (distilled water (catalyst): 0.5-1 μS/cm, acetone (solvent): 0.02 μS/cm; melted PU (reactant, at 54°C): 1200 μS/cm) [176]. The major contribution to the overall conductivity value was by the melted polymer. At the opposite extreme, at point 9, the resistivity value reached an asymptotic maximum, therefore, minimum conductivity. At that stage, the foam was fully reacted PU (dry PU (product):10^{-12} μS/cm) [176]. The resistivity in the mixture increased from point 3 to 9 due to the formation of cavities that provoked conductivity depletion (i.e. air/gas bubbles in the volumetric specimen tested).

Studied in detail, the information provided by the Figure 45b aided the monitoring of the stages for the foaming process dynamics and allowed tracking for such reaction, thus giving support to the hypothesis in Chapter 3 that "*conductivity can be used to monitor the reaction phases*".

It can be seen from the electrical resistivity measurements that three main states of the foaming process can be distinguished (Figure 93): pre-gelation state, gelation and post-gelation state.

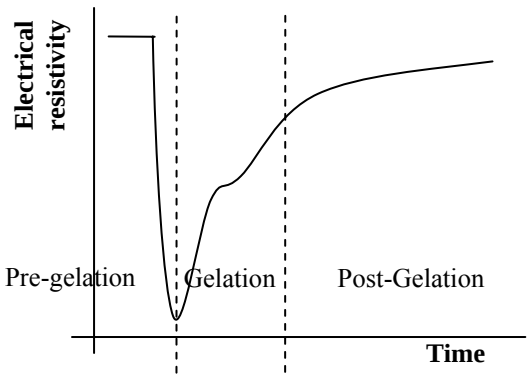

Figure 93: Main stages of formation for the polymeric foam

I. Pre-gelation: foam grew (from point 1 to 3 in Figure 45b) due to the reaction between reactants and blowing agent, and the wetted pens read the decline in resistivity. When the maximum foam height was reached the wetting stage finished.

II. Gelation: cavities formed and the reaction initiated the cross-linking in the monomers (points 3 to 7) that would close up cell walls permanently and lock the pores size.

III. Post-gelation: from points 7 to 9, the foam was fully reacted and, consequently dried out the extra water content.

Table 6 below summarises the information provided by the electrical resistivity measurements and assimilates each stage described in Chapter 3, to events that the foam suffers during formation at the macro and microscopic level.

At the macroscopic level, the observed phenomena are: growing (i.e. bulk diffusion of CO_2 gas both within the foam and to the atmosphere, as the vessel is open); heat transfer from the foam to the vessel, and from the vessel to the water bath; bulk diffusion of water vapour to the atmosphere (condensation on conductivity pens); and, once the reaction has finished, heat transfer from the foam to the bath (drying).

At the microscopic level, the predominant phenomenon at each stage is: nucleation of bubbles (i.e. tiny bubbles formed the nuclei into which the developing gas, CO_2, blowing agent, diffused as the reaction proceeds); the polyurethane reaction took place and produced CO_2. Remaining water evaporated and diffusion of the CO_2 and water vapour into the bubbles occurred producing the growth of the matrix (diffusion of CO_2 and water into the growing bubble maintains the differential pressure ΔP required for growing). It has been reported in [159] that the presence of water vapour molecules buffers any rapid increment in temperature and pressure and diminishes the creation of ‘hot’ or ‘unstable’ spots that could provoke implosion of bubbles within the melt or coalescence of the bubbles into larger cells. Occasional instabilities in the matrix and unbalances of production of gases with respect to the viscosity of the matrix might have originated temporary collapses, which was represented in Figure 45b as a “double-belly”. The next event involves the cellular structure being set as a consequence of the cross-linking stage of the reaction (first phase for the double diffusion mechanism, as reported by [165]) and the pores started to form. Finally, all solvent was washed away by the water and evaporated, as described in Chapter

4 (a ‘double diffusion’ phenomenon noted in section 4.1). Eventually, the foam dried and the reaction was then considered finished.

Macroscopic	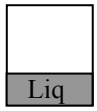	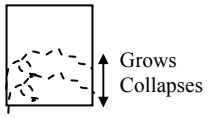	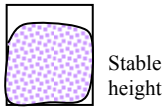	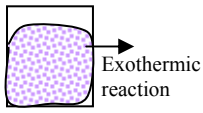	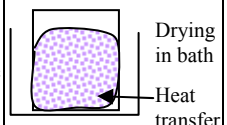
Microscopic	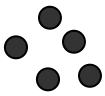 Nucleation	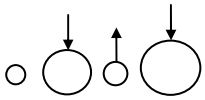 Diffusion of CO_2 into bubbles  If the cavitation is unstable, bubbles can implode: partial collapse	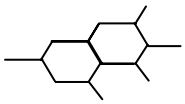 Cross-linking	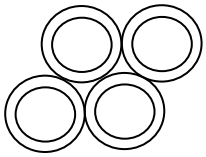 Gelation, locking size of cavities	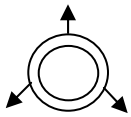 Diffusion, from foam bulk to the atmosphere
Stage *(as described in Chapter 3)*	Stage A 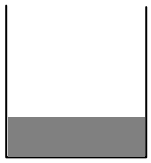	Stage B 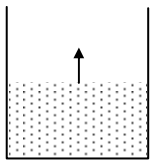	Stage C 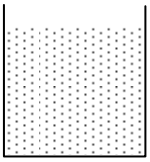	Stage D 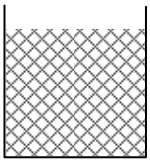	Stage E 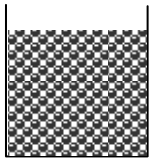
Resistance *(Figure 45b)*	1	1-3	3-6	6-8	8-9
States ***(Figure 93)***	**Pre-gelation**		**Gelation**	**Post-gelation**	

Table 6: Compilation of events during foam formation

The energy and mass balance of each Stage (Chapter 3) indicated that the foam formation was more sensitive to the application of ultrasound if it happened at Stages C and D. At these two stages, the aim is to pump in/out the dissolved vapour/gas into the bubbles for controlling their final size. Bubble growth occurred when the driving force for expansion was larger than the resisting force (i.e. gas flowed from liquid to bubble). On the contrary, when the resisting force was greater, the bubble tended to dissolve (i.e. gas flow is from the bubble to the liquid). When both forces are equal, the bubble remained in equilibrium and there was no gas flow [117].

Viscosity is a defining feature for the polymeric foams tested in this research work. The increment in the viscosity value for the PU mixtures implied a larger stress in the viscoelastic medium, retarding in this way bubble growth. For large viscosity values, bubble shrinkage would occur (to an extreme, collapse). At a smaller size, the bubble's stress in the viscoelastic medium declined, permitting a new cycle of expansion. The overall oscillatory behaviour finally stopped when the stress on the bubble walls was greater than the internal forces that stretched the bubble. It is believed that this process could be aided by ultrasound because it could sustain the flexibility of the walls for a longer time and so allow a greater intake of vapour/gas into the bubbles while that reaction was still active (i.e. CO_2 gas still being formed), hence delaying the rigidity stresses that could suppress the stretching motion at critical stages in porosity tailoring. Therefore, the mixture is believed to have a viscoelastic behaviour at stages C and D.

There seems to be a consensus in the literature that viscoelasticity enhances bubble growth [177-179] especially in low molecular weight polymers [163] and, as this research work intends, in early stages of high-molecular ones. However, more recent studies [180] [181] redirect the protagonism from viscoelasticity and supports the conclusion that its reduction has little effect on bubble growth, giving more importance to blowing agent concentration, pressure surrounding the bubble and diffusivity. This does not contradict the experimental results obtained here, since the nature of the effect of ultrasound on the foaming process is not well-known, and it can be related possibly to these at the same time: viscoelasticity (i.e. incremented shear rate due to mechanical stirring), enhancement of diffusivity, as well as pressure gradient provoked by stable cavitation (i.e. bubble bouncing steadily in increments).

This electrical resistivity measuring technique presents benefits for the tracking and identification of "sensitive to ultrasonic irradiation" stages of foam formation. However, it also has limitations. One of most obvious ones is the delayed response to any variation in the bulk of the polymer. Conductivity changes can be detected only once the event has happened. The accuracy and sensibility of the equipment is still not known. In addition to this, the pens have to be in intimate contact with the foam at early stages for satisfactory results and these pens have to be pre-tempered (i.e. at the same temperature as the reaction) in order to avoid instabilities when the pens are inserted. It is evident that this method evaluates electrical conductivity variations only for bulk volumes. Local changes of porosity cannot be detected, because only the bulk resistivity on the material is measured. A

different approach needs to be followed when aiming the measurement of anisotropy in the foaming polymer by conductivity variations.

6.2 Effect on the chemistry of the reaction

The evidence of a sonochemical effect of ultrasound in the reaction can be demonstrated by the results shown in section 5.2, where the acoustic pressure irradiated by the ultrasonic probe is shown to enhance the reaction rate. The gelation point was reached at shorter time with the application of ultrasound. This effect confirms the phenomenon already reported by other authors: for example, ultrasonic irradiation applied to sol-gel reactions resulted in sonogels with unique structural properties in terms of porosity. An obvious result was the shorter time to reach gelation point [110]. It was also shown (section 5.3) that the application of ultrasound aided a faster production of intermediate species to generate products. For a given acoustic pressure, ultrasound increased the efficiency of the reaction and provided a better ratio reactants/products (Figure 51).

It needs to be noted that Figure 51 only offers a qualitative measure of intermediate species production aided by ultrasound, and it is not a deep study on the ultrasonic effect on the reaction kinetics. A quantitative method is required to relate the efficiency of the sonochemical reaction to the energy of the ultrasonic irradiation used to produce the final foam. Confirmation of these interpretations has to be searched with the necessary, but technically difficult, analysis of the liquid/gas phases by techniques such as 'gel permeation chromatography (GPC)' and the employment of more sophisticated temperature scans (e.g. DSC and DTA). This would verify that the number of radicals and chemical species formed by ultrasonic irradiation depends on both acoustic magnitude and frequency.

6.3 Effects of ultrasonic irradiation on porosity

In this section, some of the results obtained in Chapter 5 will be discussed to show how acoustic effects can be applied to tailor the porosity in polymeric foams as well as the significance of the ultrasonic magnitude on the foaming process with regard to increase their efficiency and to improve product quality.

Other authors have exploited acoustic cavitation for the control of bubble size (normally one bubble in water) [115-119], defoaming of liquids [113] or homogeneisation of polymeric matrixes [107]. Rather than imploding the bubbles in the matrix via an unstable pulsation, the application of ultrasound used in this study was aimed towards a technique that could allow a low-intensity, continuous, linear ultrasonic vibration system in order to

produce stable cavitation for the water vapour/CO_2 gas filled bubbles and allow them to grow.

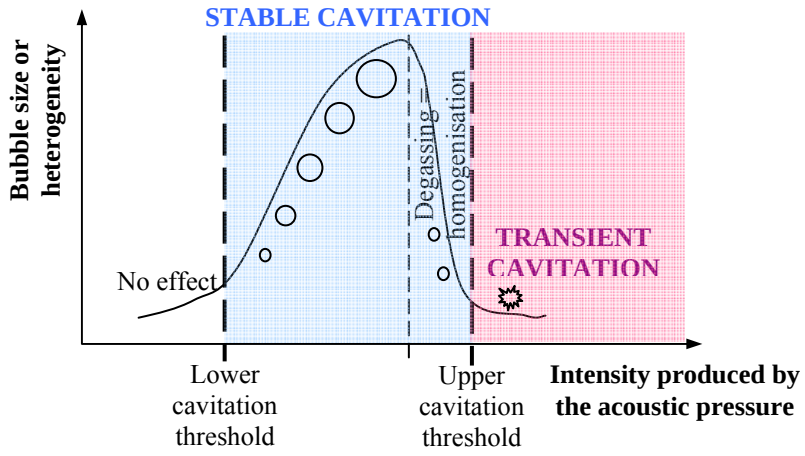

Figure 94: Stages of acoustic cavitation exploited for the tailoring of polymeric foams

Figure 94 presents a schematic of the different effects that acoustic cavitation has been shown to have on the porosity distribution of a polymeric foam. This sketch completes the description offered by [98] where gas bubbles submerged in liquid could only suffer enlargement (stable cavitation) or implosion (transient cavitation).

It is suggested here that the relationship between the intensity produced by the acoustic pressure and the heterogeneity is as follows:

- No effect was visible on the samples' cellular structure if the acoustic pressure irradiating the foams is lower than a given threshold of energy. The lower limit for the stable cavitation of this polymeric foam formation was explored by increasing the acoustic pressure until an effect was visible in the foam porosity. In this work, the lower threshold was explored in section 5.5.1 and established for insonicated samples irradiated at 20kHz, a lower threshold of approximately 6000Pa; approx 5000Pa for 25kHz and roughly 7000Pa for 30kHz, although the latter value is not immediately clear from Figure 72 due to the technical limitations that made it impossible to test samples at 30kHz and acoustic pressures lower than 6500Pa.

- When foams where irradiated at an acoustic pressure larger than the lower threshold, a direct relationship could be established between size of bubbles (or else, heterogeneity in the sample) and acoustic pressure level: bubble enlargement was proportional to the increment of acoustic pressure. Higher amplitude generated larger bubbles possibly by coalescence of smaller, or even invisible bubbles. As Leighton et al. refer [117], in a stable

cavitation scenario, it can be assumed that the energy stored during the positive half of each stress cycle is not dramatically different from the energy given up during the negative half, therefore experimental conditions of sonication were favourable to the diffusion of gas into the bubble that underwent an incremental but sustainable growth.

- For larger values of intensity, it has been demonstrated that the energy of the irradiating ultrasound was conveyed into a physical effect (i.e. stirring) which, under controlled circumstances, could provoke degassing of the matrix, and so homogenising the final cellular structure. Supported by the technical background already exploited for other industrial applications [107], this principle was re-scaled for the purposes of this study and the degassing effect was explored in section 5.4.3 and section I.6 of Appendix I. The phenomenon can be explained in terms of the enhanced diffusivity produced: acoustic conditions would be favourable to the nucleation of many bubbles that would be competing for the limited amount of gas available in the matrix during the chemical reaction. The presence of nearby bubbles prevented each one from growing any larger. Bubbles solidified producing an even cellular structure in the final foam. Pores had a smaller size on average (with smaller standard deviation in its distribution). This effect is considered by this author as a prior step before approaching transient cavitation conditions, an intermediate state between stable and transient cavitation, where bubbles were more excited than when set at stable cavitation but did not coalescence. Although the focus has been kept on polyurethane foams, other foams (i.e. poly-dimethyl siloxane foams) were also irradiated and tested in order to establish basic principles and re-assure the effect described in the hypothesis.

- Beyond the threshold stable-to-transient cavitation (upper cavitation threshold) the environmental conditions are not favourable to linear ultrasonic vibration. The bubbles were engaged in a non-stable swift cavitation which provoked their implosion and, finally, collapse of the foam. This mechanism has already been described in the literature but only for liquid foams, especially in food technologies [102] and waste water and soil treatment [84]. The polymeric foam final appearance was of a burnt piece of rubber due to the pyrolisis of the polymer. It is proposed that the underpinning mechanisms for this phenomenon are both physical (i.e. extended shear stresses and mechanical stirring that have a degassing effect) and sonochemical (i.e. ‘hot spots’ in the matrix that produce undesirable chemical reactions that burn the foam), section I.6 of Appendix I.

One of the difficulties when controlling the porosity distribution is the local environment created for volumes of bubbles in the matrix. Enhanced diffusivity provoked that many bubbles had to compete for the available gas in the matrix. Therefore, the growth of some

bubbles was limited by the presence of nearby bubbles that prevent each group from growing any larger. Further work is needed in order to establish the interaction between groups of bubbles and to predict with greater accuracy and quantify the behaviour of a neighbourhood of bubbles in a viscoelastic matrix. This is an essential step before any attempt to the scale up of the experimental rig.

6.3.1 Relationship between acoustic magnitude, frequency and porosity

In this section, the data were re-grouped into irradiation frequencies and acoustic powers in order to exploit a wider range of applications for the manufacture of tailorable porosity artefacts. When the frequency was fixed, the porosity of the samples was found to increase when the amplitude of the signal increased. Bubble enlargement was limited by a 'ceiling' of intensity, beyond which homogenisation of the matrix would occur. When considering foams subjected to equal value of sound pressure, the effect in the porosity was studied for different values of frequency. Despite the limited number of frequencies that could be tested, the results from 20, 25 and 30kHz identify a direct relationship between frequency and pore size. Unlike other authors, whose experimental results in sonoluminescence [182] or mathematical models for one single gas bubble cavitating in water have shown that an increase in the irradiation frequencies would produce *smaller* bubbles [119], results indicate here that an increment in the samples pore size could be observed with increased frequency. This statement is supported by some published work in the medical field [183], where the ultrasonic cavitation is exploited in viscoelastic matrices (e.g. muscle, fat) rather than bubble/water scenarios. The explanation offered in the context of this application is that, as the frequency increased, the bubbles pulsated at a faster rate, which resulted in more rectified mass transfer per ultrasonic cycle. This caused the bubbles to expand more but with less time to recover its initial size in each cycle. These short periods of expansion due to the shorter wavelength produced a larger final volume of bubbles which solidified into pores. Although there seems to exist competing factors as the frequency is increased (e.g. number of antinodes/nodes increase, higher signal attenuation, etc). Unfortunately no data on frequencies above 30kHz could be obtained or found in the literature. Therefore, a final conclusion cannot be defended here.

6.3.2 Verification of the sonication field in the water bath

The geometry of the water bath and relative positions of sonotrode-to-container had an important influence on the irradiated acoustic field in the bath, and hence the acoustic pressure that the samples were subjected to. The mapping of the acoustic pressure was relevant at the experimental design stage as it predicted the acoustic signal magnitude of the

sonicating field within the bath. However, the actual spatial distribution of acoustic pressure maxima and minima within the bath was complex due to the relatively small volume available for the sound to travel in the water bath.

The material used for the containers where the reactants were irradiated was polypropylene (PP), the lowest acoustic impedance that could be found and, at the same time, with an inert behaviour towards the reaction. This materials' acoustic impedance (2.40MRayl) is still far from the water impedance (1.48MRayl). Wave reflection takes place whenever waves in one medium try to enter another medium where acoustic impedances are not identical. The greater the difference between the acoustic impedances, the higher the reflectivity (i.e. reflected energy). Therefore, the energy received by the melt undergoing foaming was only a percentage of that travelling in the water bath.

Also, the partial pressure maxima and minima found in the water bath did not correspond directly to those in the vessels. The latter were slightly off-set. The reason for this displacement might lie on the change of transmitting medium (water-PP-foam) and also on the fact that sound travels at different longitudinal speeds depending on the nature of the coupling agent. Therefore, the speed of ultrasound in the water bath is not the same as inside the container, whose content is, at times, a mixture of melted polymer, acetone, water, carbon dioxide and water vapour.

6.4 Final remarks on the appraisal of the image analysis methods for porosity distribution measurement

Section 4.5 described the benefits and the limitations of the various imaging software used for the measurement of the porosity distribution in the samples. Among all the available techniques, computerised microtomography seemed to be the most appropriate application because it provided a non-destructive characterisation of the foam microstructure. However, the high running costs and the lack of a software that could measure internal dimensions of the pores made it impossible to use this technology for the purpose of this work.

Sections 5.4 and 5.5 of this thesis have explored the synergistic benefits of applying concurrently two 2D imaging methods to assess the impact of the ultrasonic irradiation on the cellular structure of the foam. The main drawback in the techniques adopted lies in the fact that an invasive and destructive method (i.e. slicing of the material) had to be used. In addition, the ultrasensitivity of the 'Topo-porosity' MatLab™ image processor for the porosity gradation might have offered misleading results when correlated to the simulated

values for the variation in the vessel's acoustic field. However, the selected imaging techniques, a4i_Docu and 'Topo-porosity mapping' image application, unlike other imaging methods (e.g. QWIN), offered the advantage of processing areas where pores did not have to be well-defined isolated cavities. This feature was sufficient to consider their use for the purpose of this work.

6.5 Assessment of the water bath simulation results

A simulation tool in COMSOL Multiphysics™ 3.3a was developed for assessing and controlling the energy irradiated into the foaming samples. It has proven to be a robust technique for the purpose of this study because the solving equations included the existing attenuation due to the physical boundaries for the acoustic field (i.e. the walls) and allowed simulation at different degrees of 'hardness' for the wall (i.e. intermediate scenarios between a fully absorbent 'soft' wall and an ideal 'hard' reflective wall). Unlike other simulations recently referenced in the literature [184], the absorption of ultrasound due to the progression of the sound wave in the medium was not omitted in this case. Consequently, the sonication environment in the bath could be successfully modelled and produce simulated results which correlated well with those obtained experimentally (Table 7). The correlation factor used here is the 'Pearson correlation coefficient' [185], which measures the strength of the relationship between two series of data, in other words, whether or not they are statistically significant. The range of values is (0,1), 0 suggesting a random relationship and 1, a perfect relationship. Most of the series of data present a strong correlation. Unfortunately, some of them (e.g. the porosity distribution of 20kHz, 11.10cm and 25kHz, 6.35cm, which are type 3 foams, as indicated in section 4.5.3.2) appeared to be weak.

Pearson correlation coefficient for the water bath				
Experimental results obtained by hydrophone vs simulated data with COMSOL Multiphysics™ 0.804				
Pearson correlation coefficient for the irradiated vessels containing reaction				
Frequency of irradiation	distance vessel wall to probe	Experimental-Simulation Z 1.48MRayl (water)	Experimental-Simulation Z 2.60MRayl (bone)	Simulation Z 1.48MRayl (water) – Z 2.60MRayl (bone)
20kHz	3.70cm	0.862	0.747	0.854
	7.40cm	0.644	0.351	0.943
	7.60cm	0.503	0.636	0.948
	11.10cm	0.316	0.294	0.587
25kHz	2.95cm	0.952	0.831	0.908
	5.90cm	0.846	0.731	0.898
	6.35cm	0.233	0.450	0.661
	8.85cm	0.874	0.632	0.901
30kHz	2.45cm	0.819	0.889	0.789
	4.90cm	0.490	0.519	0.907
	7.35cm	0.436	0.457	0.900

Table 7: Pearson correlation coefficient for the simulated and measured values in the bath and the irradiated foams

The simulation was also performed for the acoustic field created inside of the vessels when these held a hypothetical content (i.e. water and bone, representing the extreme scenarios for the acoustic impedance of the foaming reactant). Table 7, last column, presents the Pearson correlation coefficient for both simulations. Each number could be interpreted as the difference in attenuation that each acoustic condition offers (e.g. for irradiation conditions 20 kHz 7.60cm, the simulation performed with water and with porous bone do not differ as much as the simulation performed at 20 kHz 11.10cm, where the low coefficient indicates a high attenuation of the signal provoked by the bone medium). Unfortunately, it was not possible for the system studied here to measure the sound pressure

inside of the actual foaming polymer during its reaction. These values are necessary for the determination of the actual acoustic impedance for accurate modelling conditions, and consequently, assessing the accuracy of the modelled system.

Despite the good correlation obtained for the sound pressure distribution inside the irradiated vessel studied in conjunction with the porosity distribution, this simulation tool showed its main weakness in the impossibility of processing two active domains (i.e. water in the bath and foaming material in the vessel) at the same time. Therefore, the vessels had to be modelled separately by feeding the peripheral conditions and boundary settings extracted from the acoustic field in the water bath for every experimental series (e.g. sonotrode power, frequency, acoustic values, position within the bath) maintaining three dimensional arrays of information.

6.6 Summary

This chapter has discussed a number of conclusions that can be drawn from an analysis of the results. It has been done by revisiting the research hypotheses presented in Chapter 3, assessing their consistency and pointing out limitations and weaknesses that the research procedure, measuring equipment and simulation tools intrinsically had.

In fact, the conductivity can be used to monitor the reaction phases (i.e. progression through pre-gelation, gelation and post-gelation stages); ultrasound has proven a sonochemical effect in the polymerisation reaction as well as a physical effect by altering the dynamics of the foaming process, the mass and heat transfer. And, as the final objective for this research work, it has been shown that the sound field pattern can be used to tailor porosity within the bulk of the foam by subjecting the bubbles to stable cavitation and pulsations that allows bubble size adjustment before solidification.

CHAPTER 7. CONCLUSIONS

Motivated by the desire to manufacture materials with a controlled cellular structure, this work describes the investigation of the precisely controlled application of ultrasonic irradiation on polymeric melts undergoing foaming. Having established the theoretical mechanism, experiments were carried out to evaluate the influence of the irradiation on the cellular structure of the foamed material, and whether this can be done in a predictable manner.

Polyurethane foams have been irradiated with ultrasound aiming to produce a gradation of porosity. Initially a wide range of powers were applied to the transducer and several working frequencies explored to determine the impact of ultrasonic irradiation on the polymeric melts undergoing foaming. These experiments have shown that ultrasound can be used to affect local physical and chemical processes in the foaming medium. These effects can be observed directly in cross-sections of foam that have been sonicated using an immersion technique during their formation. The images from the sonicated foams (Figure 5 and Figure 73) showed a thinning effect of cell wall, which enhanced gas transport and increased permeability during the initial stages of foam formation.

It was found that the bubble growth rate depended on the ultrasonic specifications (i.e. sound pressure, frequency and exposure time) and therefore, the final porosity distribution of the foamed material also depended on these sonication conditions. Results showed that bubble enlargement was proportional to the sound pressure when this was larger than a lower threshold value (below which there was no effect on the cellular structure), and lower than an upper threshold value, that provoked homogenisation and, at an extreme, collapsing of the polymeric cellular structure through breaking the polymer chains and implosion of bubbles.

The lower limit for stable cavitation (i.e. lower threshold) was explored by decreasing the acoustic power until no noticeable effect was visible in the foam porosity. At the other extreme, when the acoustic intensity applied to the foams reached greater values, but still within the boundaries of stable cavitation, a homogenisation effect on the matrix could be observed. This can be explained in terms of the enhanced diffusivity produced: acoustic conditions would be favourable to the nucleation of many bubbles that would be competing for the limited amount of gas available in the matrix during the chemical reaction. The

presence of nearby bubbles prevented each one from growing any larger. In consequence, the bubbles solidified producing an even cellular structure in the final foam. It was observed that pores had a smaller size on average (with smaller standard deviation in its distribution). This effect is considered by the author as a precursor to 'transient cavitation' conditions.

Changes in the pore size with frequency were also measured. The average amount of gas contained in the bubble during the reaction increased proportionally to the frequency of the ultrasonic signal applied: a higher pulsation rate resulted in more rectified mass transfer per ultrasonic cycle. As the frequency increased, the bubbles expanded more and had less time to recover its initial size. These short periods of expansion produced larger final bubble volume.

The geometry of the water bath and relative positions of the sonotrode to container had an important influence on the acoustic field irradiated in the bath, and hence the acoustic pressure to which the samples were subject. The mapping of the acoustic pressure was relevant at the experiment design stage as it predicted the acoustic signal magnitude of the sonicating field within the bath. The position of the container holding the foaming material in a standing wave is tightly connected with the distribution of resulting pore sizes. Variations in the container position within the bath led to variations of the sound intensity within the container and corresponding change of the bubble growth rate and final size.

Areas of higher porosity in foams were caused by the formation of larger pores when the mixture was still of a viscoelastic nature (i.e. liquid to solid transition). The author believes that for a given frequency, a specific range of values for the signal magnitude in the acoustic field (applied during the 'pre-gelation' (stage C), 'gelation' and 'post-gelation' (stage D) of the foam formation) produced stable cavitation (i.e. rectified diffusion of gas content from the polymer matrix into the cavities) for the water vapour/CO_2 gas filled bubbles in the polymeric mass. Consequently, the timing for the ultrasound irradiation needs to be closely controlled, as its application might cause the opposite effect on the foams (e.g. degassing or outsized bubbles intrinsically unstable in the matrix).

Porosity evaluation in the specimens was carried out with the aid of image analysis software that provided comparable data in order to establish the cause-effect relationship of sonication conditions for porosity distribution. A multi-physics simulation tool (COMSOL™) was used for verification of the experimental results.

Aside from the clear effect of acoustic irradiation on the porosity gradation of the solidified polymeric foams, a variation in the reaction rate was also detected. The reaction would reach the 'gelation point' and therefore, finalise the polymeric cross-linking, at shorter time frames under sonicating conditions due to the enhancement of convective and diffusive events that would speed up the reaction. In addition, the thermal conduction rate was seen to increase, which, along with the improved convection, produced a decrement on the temperature gradient. This implied a thinner, if non-existent, skin on the outer perimeter of the foam.

The work described in this thesis has also shown that it is feasible to use an indirect method such as electrical resistivity to monitor and track the different stages of the reaction. This is ultimately useful for the detection of those 'sensitive' stages to ultrasound during the foaming of the melt that allow the design of an effective strategy for irradiation for porosity tailoring of polymeric foams.

To summarise, the author concludes that the suitable manipulation of the position of a foaming polymeric melt within a sonication field (with a known acoustic pressure amplitude and frequency), permits the tailoring of the bubbles, then pores, to a desired size. These findings essentially form part of the strategy for developing a multi-source equipment optimised for the fine control of an acoustic pressure field that could exploit this phenomenon for the manufacturing of tailorable porosity graded materials that can be used in specific applications where engineered cellular structures are required '*ad-hoc*' (e.g. bio-mimetics and orthopaedics; structural components, etc). The proposed programme is suggested in the next chapter.

CHAPTER 8. FUTURE WORK

This chapter highlights the opportunity for future work aimed to lead to the development of a manufacturing process for foams with tailorable porosity. It also describes the key research challenges associated with the sonication of polymeric foams for porosity tailoring purposes.

The most obvious extension of the research work described in this thesis is to study and identify 'sensitive' stages of formation (during which stable cavitation conditions can be tuned) for other polymeric foams, especially those which can be used in bio-medical and high-tech applications. Porous biomaterials with controlled amount of both open and closed pores as well as graded porosity are needed for some implant applications [186].

It is also essential to carry out a more extensive study of the stable cavitation conditions for polyurethane (and similar) foams, as well as quantifying the degree of disturbance that ultrasound causes form the physical point of view, such as diffusion, convection, conduction event, etc, and chemical approach (i.e. establish a relationship between the efficiency of the sonochemical reaction and the energy of ultrasonic irradiation used to produce a chemical effect). Perfecting the current technology reported in this thesis will lead to further refinement in the process. The compilation of a database or library of porosity features as a function of ultrasonic irradiation and soundwave pattern will permit the design and manufacture of more complicated porosity distributions (Figure 95).

It is recommended that future work should aim to develop a sonication chamber where the acoustic field could be accurately controlled and so the irradiation magnitude on a foam is precisely predictable. There are two specific suggestions:

8.1 Modification to the rig

8.1.1 Commission of a multi-source rig

The study of a sonication field created by more than one ultrasonic probe (Figure 96b) might form a tightly controlled wave pattern within the bath, and thus allow the magnitude and features of the irradiation received by the foaming melt to be optimised. This issue requires further study in order to identify and evaluate the interaction of the directional ultrasound with the foaming melt.

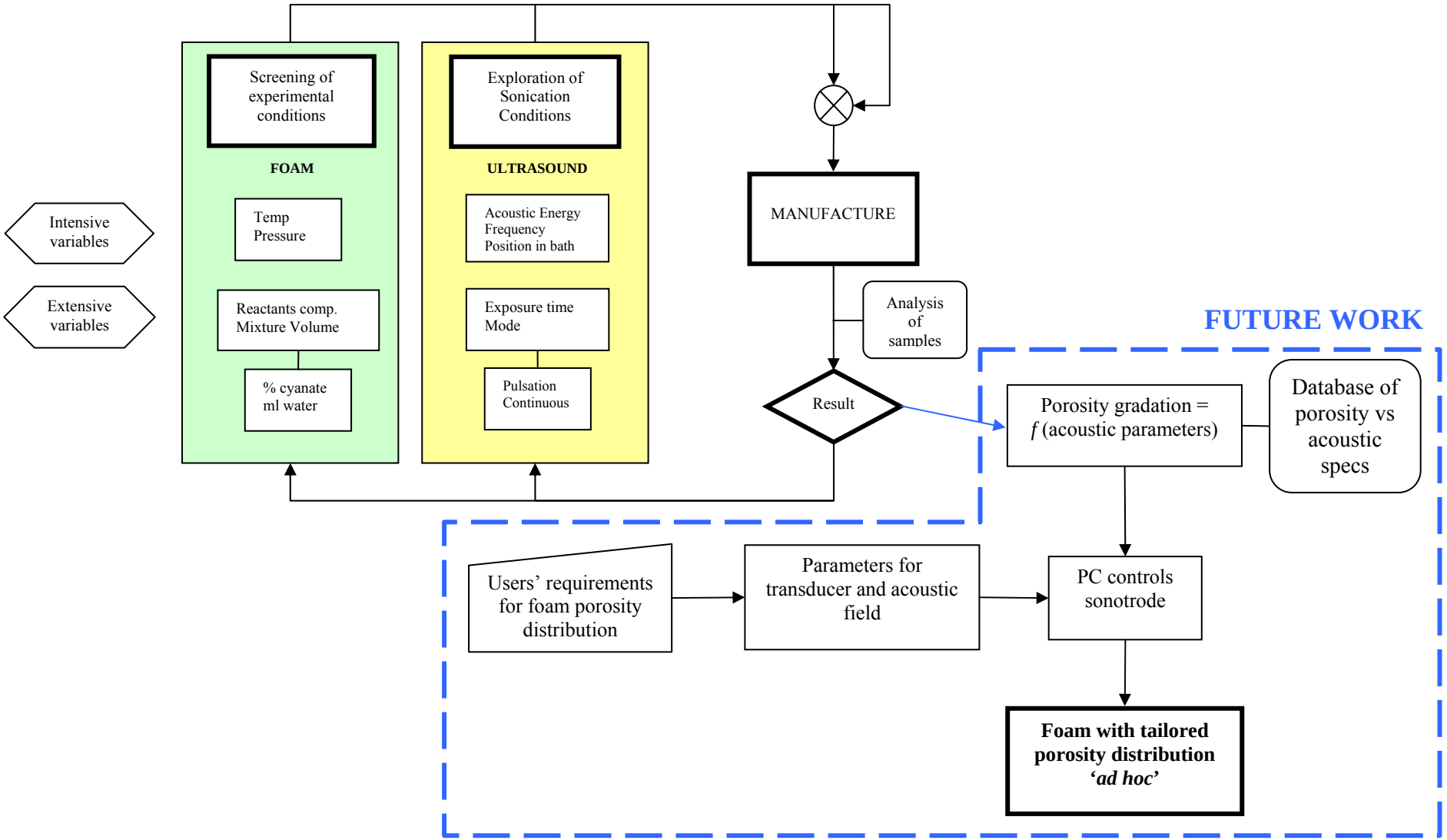

Figure 95: Flow chart for the design and automated manufacturing process

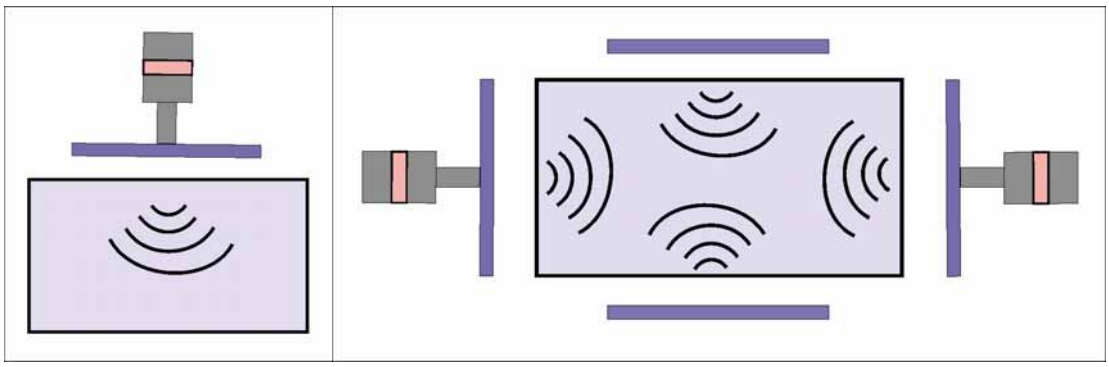

Figure 96: (a) Single probe; (b) Multi-probe arrangement

The acoustic field created in the water bath that has been used for this study in the simulations (i.e. stainless steel walls, 20kHz, 150W applied to the sonotrode) presents a strongly regular pattern when two identical probes are immersed in the water in comparison to the single arrangement (Figure 85a)

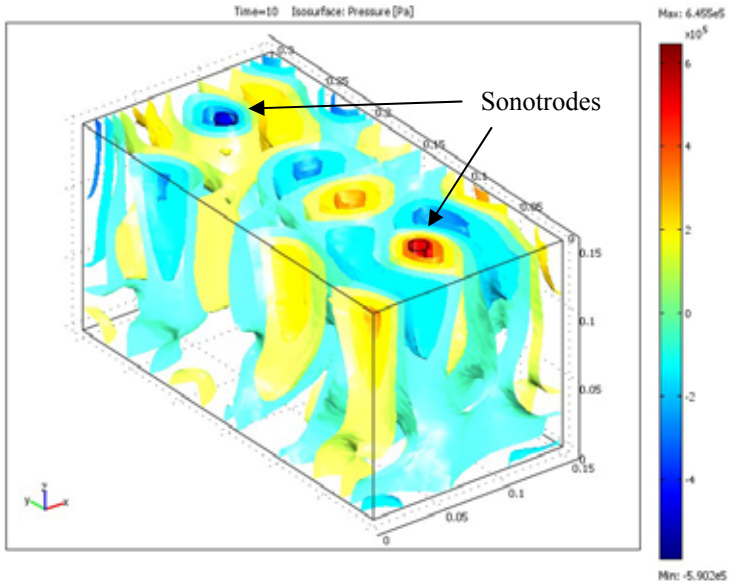

Figure 97: Multi-probe rig with modelled acoustic field

8.1.2 Re-design of the experimental rig.

The exploitation of the vertical propagation of sound is also a possibility for improving the acoustic field. This involves the relocation of the ultrasonic probes so that the longitudinal axis of the transducer is perpendicular to the axis of both containers and not parallel. In this way the energy transferred to the containers would be higher as some attenuation effects (e.g. refraction, reflection on the walls, etc) would be diminished.

8.2 Optimisation of the coupling agent for confocal acoustics

In this work, water was used as the coupling agent for the propagation of the ultrasonic waves. The coupling fluid needs to be used to avoid the formation of air gaps which would have caused a very high attenuation of the imposed ultrasonic waves. It was also used to buffer possible changes in temperature within the foam due to the exothermic reaction of the polyurethane. As the longitudinal speed of sound in a medium depends on its density and acoustic impedance, a more advantageous coupling agent could be used that allow a better channelling to focus and direct the acoustic beam as necessary, decreasing its divergence as it propagates in the medium.

Another concern is how the desirable cavitational activity exhibited in the water bath could be guided and managed in order to complete an efficient design and scale-up of the reaction chamber. One of the drawbacks in the control and instrumentation for this ultrasonic tailoring technology is that foaming cannot be turned off at specific moments.

Therefore, in order to overcome this problem and develop efficient industrial equipment, further research needs to be done to identify key factors that affect the interaction ultrasound-foaming reaction. The development of a simulation tool that could model the bubble growth mechanism would allow the scrutiny of possible strategies to perfect the actual technology. In this way, using sonication for polymers undergoing foaming could be considered a plausible route for the fabrication of heterogeneous materials with a geometric complexity that could include a myriad of features and differing dimensional scales and would allow local composition control where polymers, metals and/or ceramics can be blended into composites with a fine control of the porosity.

APPENDIX I DESIGN OF EXPERIMENTS

This section details the rationale underlying the design of the experimental rig reported in this thesis and describes how the range of experimental parameters (i.e. frequency, power, time, reactants' concentration, etc) was determined.

I.1 Ultrasonic bath versus ultrasonic horn

Various foam irradiation methods were investigated in the early stages of the research work. Having determined that an ultrasonic field might affect the foaming process, an ultrasonic cleaning bath (Figure 98) was used to establish whether any sonochemical phenomenon could be observed on a foaming material. The bath dimensions were 150mm depth x 315mm length x 290mm width, and it provided with a convenient but unstructured ultrasonic field. The irradiation power could be adjusted from 200 to 400W. The frequency sweep range offered by the ultrasonic bath transducer was 35-45kHz. Different exposures (1h, 1.2h, 1.4h, and 1.6h) at various stages of the polyurethane foaming process (i.e. minutes after reaction has started: 0, 15min, 30min, 45min, 45min and 60min) were tested. The location of the samples in the bath was not fixed, therefore the location of the sample in relation to the local acoustic wave (i.e. maximum, minimum) was not known. An irradiation effect was only observed in some samples.

The results of this study were very variable, ranging from no visible effect to a complete collapse of the foam. The conclusion was that some effect was clearly taking place but only under certain experimental conditions. At the time, it was unclear why this happened; with hind sight, it appears likely that there were large variations in the acoustic field within the bath, major reflections and refractions that produced signal attenuation.

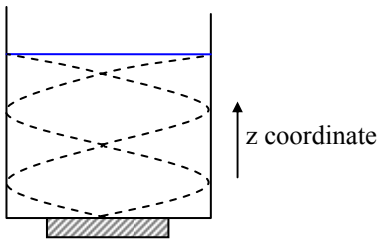

Figure 98: Sonochemical reactor with ultrasonic transducer attached to the bottom (ultrasonic bath) with representation of a standing-wave

The antinodes are points of maximum acoustic energy (i.e. pressure) and the nodes, minimum acoustic energy. It is believed that the position of the samples in the bath that presented signs of irradiation were the ones located at antinodes (or nearby). Moreover, the

frequency was not fixed. Pore size was not predictable, nor could it be correlated to other experimental values due to the swept range of frequencies that foams where exposed to. As Iida et al. refer [168], the ultrasonic bath gathers bubbles at antinodes due to Bjerness forces, mentioned in Chapter 3.

To try and establish the range of experimental parameters that produced an effect, an ultrasonic horn of a single frequency irradiating in a water tank was used, so the location of the samples could be related to the mapped wave amplitudes and correlated to any changes in the resulting porosity.

I.2 Determining the amount of catalyst (i.e. water)

A fixed amount of diisocyanate had to be used throughout this research in order to obtain comparable results. In order to identify what would be an appropriate quantity of diisocyanate, the nature of the reaction was studied along with the interaction between the diisocyanate, limitant reactant, water, catalyst for the reaction, and acetone. Several proportions of acetone:monomeric mixture and water:monomeric mixture were tested and the following proportions judged optimum for use in all the experiments, due to the reasons described below: 40% diisocyanate, 50:50 Acetone:mixture and 20%vol of distilled water to ml of diisocyanate solution.

This formulation minimised the following side-effects, illustrated in Figure 99:

1. Too large proportion of water created an excess of CO_2 gas, which provoked foam collapsing as too many bubbles were formed at a non-sustainable rate.

2. White dust: Once solid, some foams presented a layer of white dust at the bottom of the container. This dust was a residual polyurethane emulsion produced by the phase inversion of the acetone:polyurethane solution with water. It was formed during the stirring phase because of an excess of water [187].

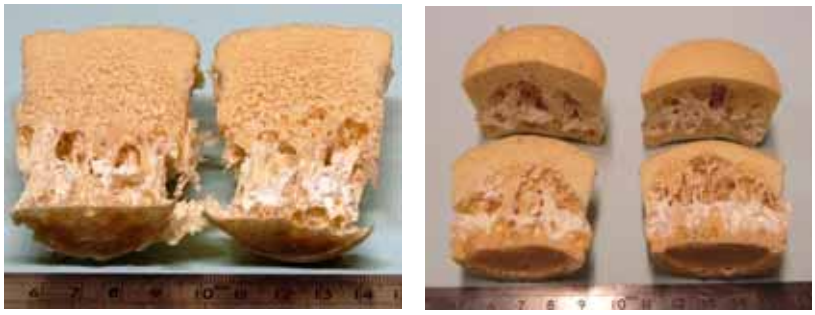

Figure 99: Polymeric foams with an excess of water and acetone (too many bubbles and white dust at the bottom)

I.3 Working temperature

It was determined that the peak temperature of the reaction fell in the range 54-56°C. Consequently, the working temperature chosen for the water bath was 50°C (i.e. 323K). An extreme temperature gradient was undesirable because it could have promoted the formation of a large skin thickness in the outer layer of the foam due to reasons covered in Chapter 3 (i.e. high rate of condensation for gases and vapours)

Also, temperatures greater than 50°C caused the acetone to evaporate too fast and caused excessive generation of bubbles. This created instabilities due to the change in the equilibrium vapour pressure (i.e. evaporated solvent, catalysis and/or steam from the water bath would migrate into the bubbles). Furthermore, if the reaction was enhanced by temperature, bubbles would appear over-filled by the evaporated species (condensable gases). This would interfere with the quantification of the influence of ultrasound as a porosity gradation generator because a bubble full of gas (i.e. non-condensable phase, e.g. $CO_{2\ gas}$) is preferable for cavitation at low temperatures [168].

I.4 Stirring procedure

Once the acetone was added (to degas the reactants from the blowing agents present in the commercial mixture), the amount of air was kept fixed and any additional entrance of air was avoided to ensure consistent experimental conditions. After preparation, the mixture was considered to have dissolved gas in equilibrium (following Henry's Law, see Chapter 3). The mixture was kept in a sealed bottle and stirred at low rate until its use. The addition of the distilled water (i.e catalyst for the reaction) and stirring was done at a speed of 2 cycles per second for a total of 70 seconds. The air content in the liquid mixture played an important role at the initial stages of the reaction as potential nucleation sites for bubbles. Pre-existing microbubbles in the mixture play an important role as seeds for those future 'adult' bubbles when temperature and pressure conditions are favourable to the reaction [69, 163]. In essence, the role played by the initial dissolved air can be summarised as follows: the presence of gas in equilibrium in the liquid mixture aided the nucleation of bubbles that would cavitate in resonance with the acoustic field (i.e. stable cavitation, enhanced diffusion). If the liquid mixture could not generate any bubbles, or those were of a very small size, transient cavitation would collapse the polymeric foam and burn it [69].

Figure 100: Foam with no initial gas dissolved in the monomeric mixture

There is a direct correlation between the initial concentration of dissolved air in the mixture and the average mass of the gas contained in the bubble [119]. If this bubble is too small, it will dissolve [117] therefore, no stable cavitation effect occurs but transient cavitation (Figure 100).

I.5 Reaction vessel

The suitability of polypropylene (PP) as a material for the reaction vessels (used to hold the foam inside the water bath) was studied. From the point of view of the reaction, polypropylene was inert to reactants and products, chemical reaction and allowed an easy de-moulding of the foams as polyurethane does not stick to PP [62].

The acoustic behaviour of the polypropylene containers was also studied. When sound propagates from one medium into another, materials with very different acoustic impedance will reflect sound waves. The intensity reflection coefficient is given by the expression [154-156]:

$$R_a = \frac{(Z_1 - Z_2)^2}{(Z_1 + Z_2)^2} \tag{31}$$

Where Z_1 represents the acoustic impedance of the medium from which sound goes (water, Z_1=1.48x10^6 kg/sm^2), and Z_2, the medium to which sound goes (PP, Z_2=2.40x10^6 kg/sm^2).

When the values for both medium impedances are very similar, the reflection coefficient tends to zero. For the water-PP interface, R is 0.0562. When the values for media are very different, the reflection coefficient is approximately 1. For the air|water interface (air, Z=429 kg/sm^2), R is 0.9994.

Likewise, the intensity transmission coefficient is given by [154-156]:

$$T_a = 1 - R_a = \frac{4 \cdot Z_1 \cdot Z_2}{(Z_1 + Z_2)^2} \quad (30)$$

For the water-PP interface, the corresponding value is T=0.9438. When the value for both medium impedances is very similar, the reflection coefficient tends to one. When this is very different, the reflection coefficient tends to zero.

Because both impedances are so similar, the material was judged to be appropriate for this application. In addition, walls of the bath (impedance of steel is 45.6×10^6 kg/sm^2) were covered by absorbent material to minimise reflections from the walls. To enable investigation of the effects of "direct" sonication (i.e. not secondary reflections) the cups were shielded around 180 degrees of the circumference on the opposite side from the probe with an air chamber and corrugated aluminium sheet (7μm).

I.6 Acoustic field adjustment

As the experimental hypotheses suggested that acoustic pressure was one of the most important properties of ultrasound that could influence bubble formation, the levels of acoustic signal strength were kept between a minimum value, high enough to produce local bubble growth in the foam; and a maximum, above which bubbles implode due to the effects of the transient cavitation.

While the low acoustic pressure threshold is explored in Chapter 5 (see section 5.5.1), the upper limit had to be established by experimental observation. It was detected that when sonication pressure was above 40000Pa, conditions favoured the creation of a large number of nucleation events, which led in many cases to partial coalescence in some areas (Figure 101). For acoustic pressures between 35000-40000Pa, ultrasound provoked a degassing effect in the samples as the dissolved gas was expelled by the action of the ultrasonic agitation producing a more homogeneous matrix of polymer with more, but smaller, pores. Therefore, the maximum acoustic pressure applied to the foams was established at 35000Pa (this value is the acoustic pressure value measured at the first measurable wavelength maximum when the input to the transducer was 150W).

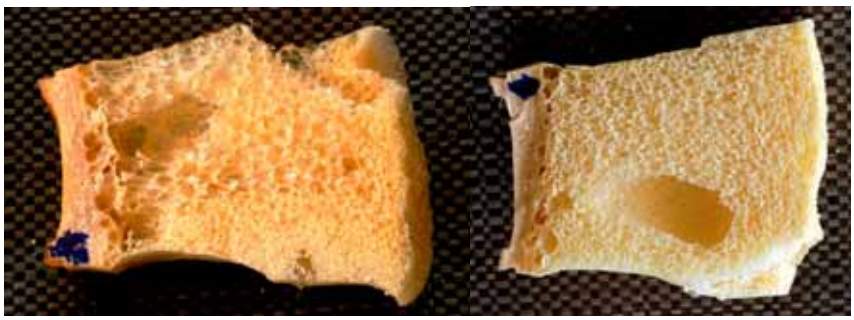

Figure 101: Local collapse of bubbles in the polymeric matrix

Due to the complexity of interaction among neighbouring bubbles, there is not a full explanation of the 'partial collapse' phenomenon and so the following is based on informed speculation. The author believes that the acoustic field experienced by an individual bubble was affected by the interference of other bubbles forming and resonating around it. When one bubble imploded, the energy released from that implosion affected the bubbles in its close vicinity. So, the closest bubble would also implode, due to the shockwave, but that wave would also be attenuated within the matrix (every cell acted as an individual scatterer, where the wavefront was reflected and/or refracted producing a heating effect and final reduction of the signal strength). It is believed that this attenuation prevents a chain reaction occurring leading to other distant bubbles collapsing.

The complete understanding of the progress of an energy wave through a complex matrix of growing bubbles is extremely challenging and is beyond the scope of this research work. The difficulty lies in the changing of elasticity of the bubbles' shell with time. Bubbles must be elastic enough to take the amount of energy released, otherwise, they will collapse. Likewise, if the foam matrix is not elastic enough, the whole body will collapse. If the collapsing event takes place at an early stage of the reaction due to shear forces (i.e. low viscosity in the mixture assisted by ultrasound), the matrix could recover and evolve into a final well formed foam. If not, it might result into an extended coalescence of bubbles and total collapse of the foam.

I.7 Cyclic irradiation

The irradiation pattern was 2 minutes on/1 minute off for a time frame of 20 minutes. The main reason for this irradiation strategy lies in the nature of the polyurethane cross-linking reaction. In early stages of the chemical reaction and growth, the polymeric foam was a *meta-stable* system and shear stress caused by ultrasound, along with the convective process within the foam, could provoke "sonic saturation" in the sample, accelerating coalescence and increasing probabilities for its collapse. The application of ultrasound to these samples had to happen during critical parts of the process, and these were the cream time and the

rise period (Stage B) and around the ‘gelation point’ (Stage C), periods that underwent study.

Early experimentation showed that continuous ultrasonic exposure throughout the foaming process could lead to complete collapse. The 2 minute exposure was sufficient to modify foaming process without leading to collapse.

APPENDIX II SIMULATION OF THE ACOUSTIC PRESSURE DISTRIBUTION

This appendix compiles further details of the simulations performed for the characterisation of the acoustic field inside of the water bath (section 3.2.1, in Chapter 4) and the modelling of the sound pressure levels at which the polymeric mass in the containers were subjected to (section 5.3, in Chapter 5). The software package used for the simulations was COMSOL Multiphysics version 3.3a.

II.1 Time-harmonic analysis

For calculation of the acoustic pressure distribution, the wave equation is solved. In this case, as the coupling agent is water, the shear stress is neglected, and the wave propagation is linear. Therefore, the wave equation is expressed in terms of pressure (p), density of the fluid (ρ_0) and speed of sound (c) as:

$$\frac{1}{\rho_0 \cdot c^2} \cdot \frac{\partial^2 p}{\partial t^2} + \nabla\left(\frac{-1}{\rho_0} \cdot \nabla p\right) = 0 \tag{48}$$

Equation 48: General wave equation

The solving option for the pressure was set to time harmonic and, as the pressure variation in time is $p=p_0.e^{(i\omega t)}$, the wave equation for acoustic waves reduces to the Helmholtz equation, where the angular frequency ($\omega=2\pi f$) is introduced as another variable:

$$\nabla\left(\frac{-1}{\rho_0} \cdot \nabla p\right) - \frac{\omega^2 \cdot p}{\rho_0 \cdot c^2} = 0 \tag{49}$$

Equation 49: Helmholtz equation

II.2 Boundary conditions

Following the sensitivity of the modelled rig analysis in Chapter 4, section 4.3.2.1, the decisions adopted for the bath simulation in Chapter 5, section 5.5.3, are as follows: the water bath walls were set at an impedance corresponding to that of the steel (Z=45.6 MRayl) and the water|air interface was simulated as a 'hard' wall (i.e. 100% reflective boundary). The radiation condition for the ultrasonic probe was set to cylindrical at each of the values required for each individual simulation.

II.3 Scalar variables

The pressure reference for the model was set at $20x10^{-6}$Pa for all the simulations and the excitation frequency was 20, 25 or 30 kHz, depending on the simulation series.

II.4 Mesh generation

In order to perform the finite element analysis, the domain (i.e. water bath) had to be decomposed into tetrahedrons (Figure 102). This decomposition was automatically achieved by using the available grid generation tools, which discretised the domain using the quadratic Lagrange elements.

For the model presented in Figure 102, the number of tetrahedral elements was set to 6030, which left 1284 mesh points and 8960 degrees of freedom to solve.

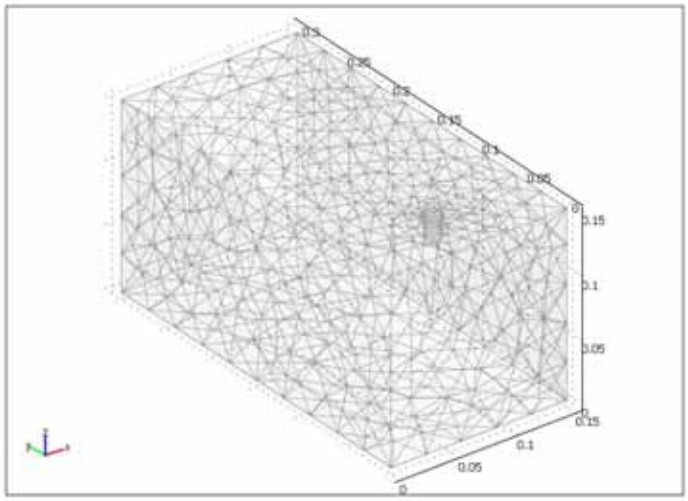

Figure 102: Scheme of the mesh used for the simulations

II.5 Solver settings: time stepping

The model was tested in order to identify the necessary time frame to reach steady state in the simulated conditions. For the water bath simulation model, it was set to 10s. The time stepping for the solving protocol was set to 0.5s and the relative tolerance (i.e. error for the time stepping) was 0.01s. For solving the containers simulation model, the method was set to 1s for the steady state, with a 0.1s stepping and a tolerance of 0.01s.

The solving method processed the model, whose solution was represented in 3D isolines of acoustic pressure (Figure 103)

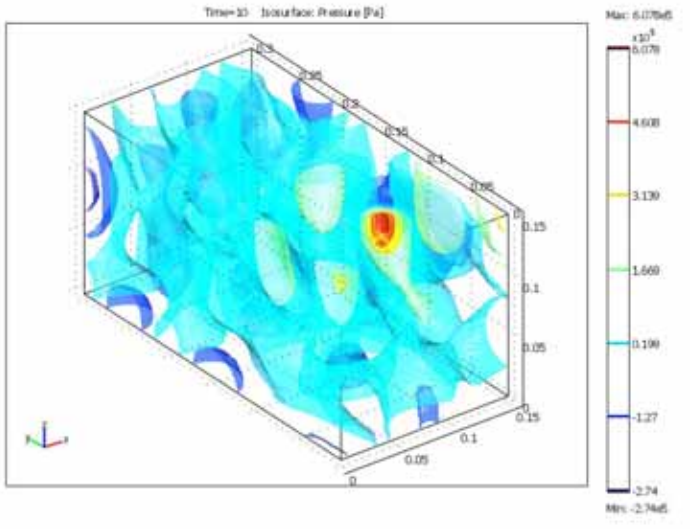

Figure 103: Resultant water bath after processing the simulated conditions

II.6 Post-processing of results

The study on the sensitivity of the modelled rig has been presented in Chapter 4, section 4.3.2.1. The following section offers the possibility to present more defining planes and cross-sections for both the water bath and the vessels containing the foaming polymeric mixture that was subject to irradiation.

By using the pressure reference as 20×10^{-6}Pa, the acoustic profiles were, in some cases, post-processed in order to obtain the sound pressure value, defined as in equation (44):

$$L_p(dB) = 20 \cdot \log_{10}\left(\frac{P_{RMS}}{P_0}\right) \tag{44}$$

Equation (44): Sound level pressure, in dB

II.6.1 Subdomain: empty water bath

Acoustic pressure distributions could be extracted from the solved model (Figure 103). Figure 104 (a and b) presents two examples of views, plan and lateral view, respectively.

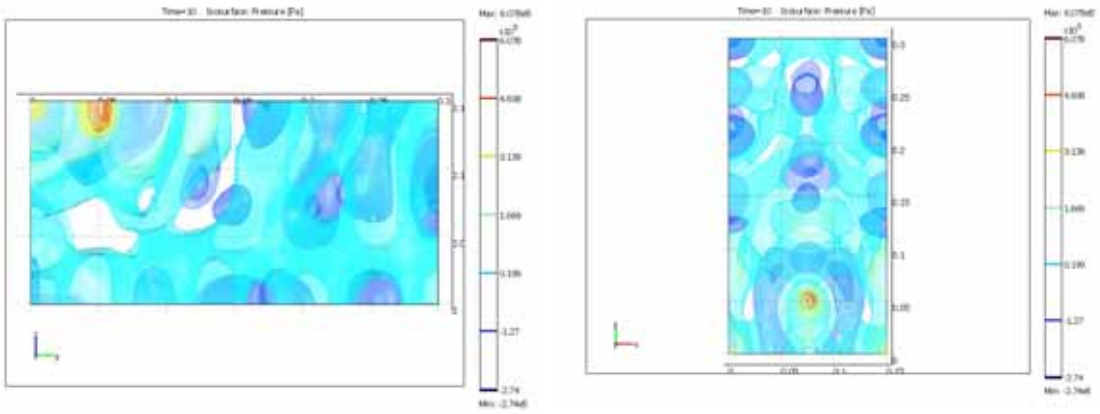

(a) Plan view (b) Lateral view

Figure 104: Different views of the simulated acoustic environment in the water bath

Planes were extracted across the bath in the x and y directions, using the same z coordinate (i.e. aligned to the sonotrode's tip plane).

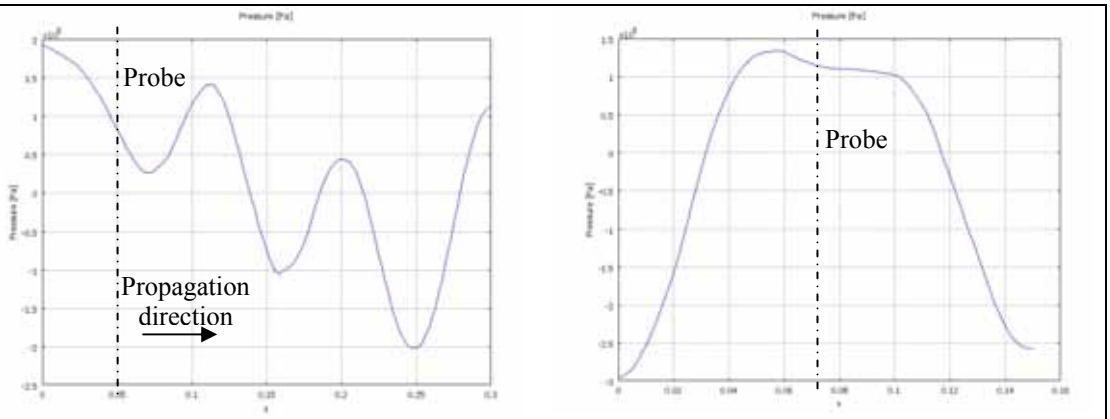

(a) Plot of acoustic pressure across the bath, y=[0, 30cm] (b) Plot of acoustic pressure across the bath, x=[0, 15cm]

Figure 105: Plots of acoustic pressure inside the water bath

II.6.2 Subdomain: water bath with immersed vessels

The following figures (Figure 106) present a series of water baths that have a vessel immersed at different distances from the probe. The sonotrode irradiated at 20 kHz and 18000Pa in a 'cylindrical' soundwave shape.

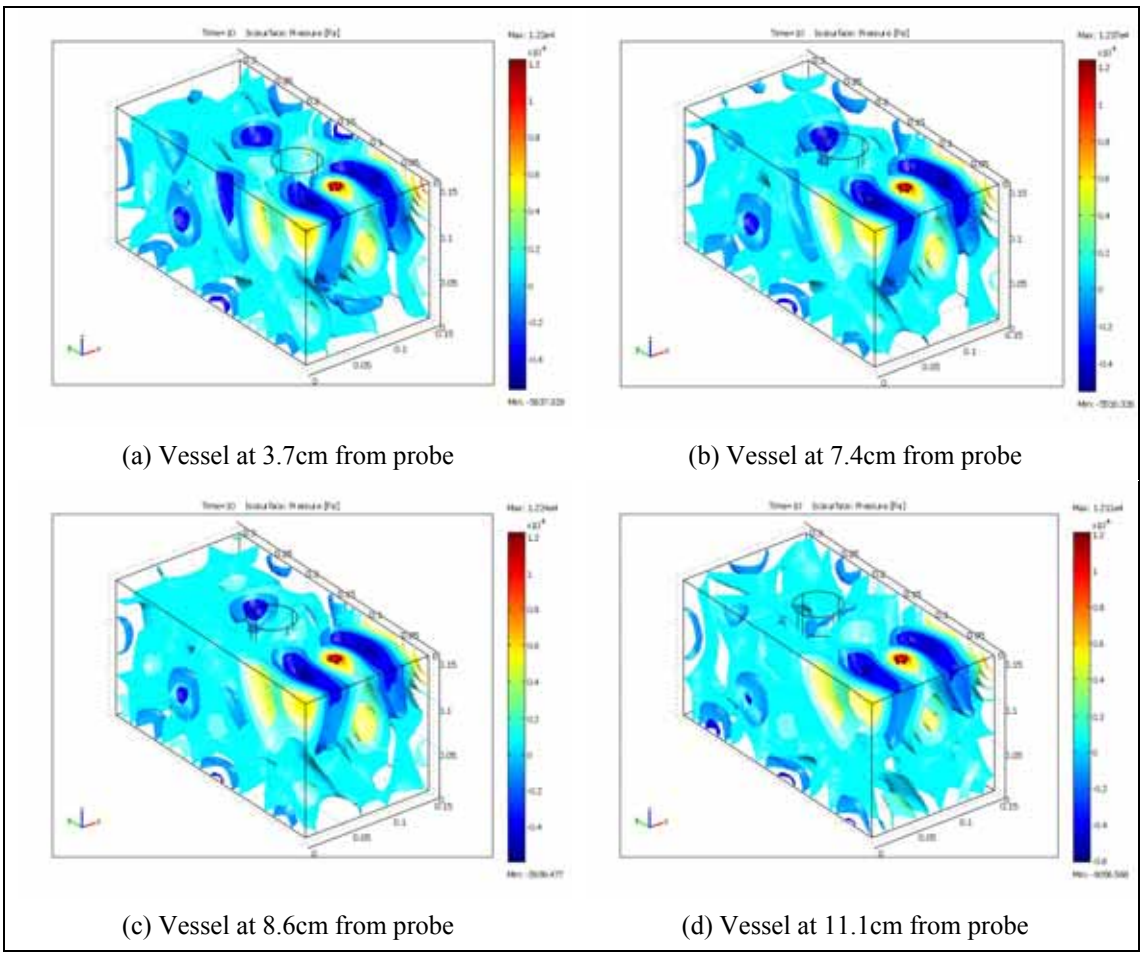

(a) Vessel at 3.7cm from probe

(b) Vessel at 7.4cm from probe

(c) Vessel at 8.6cm from probe

(d) Vessel at 11.1cm from probe

Figure 106: Simulated water baths with immersed vessels at different distances

The mid-plane cross-sections can be found in Figure 86.

Plots for the acoustic distribution in the water bath when the vessel is immersed at different distances from the probe are presented in Figure 107.

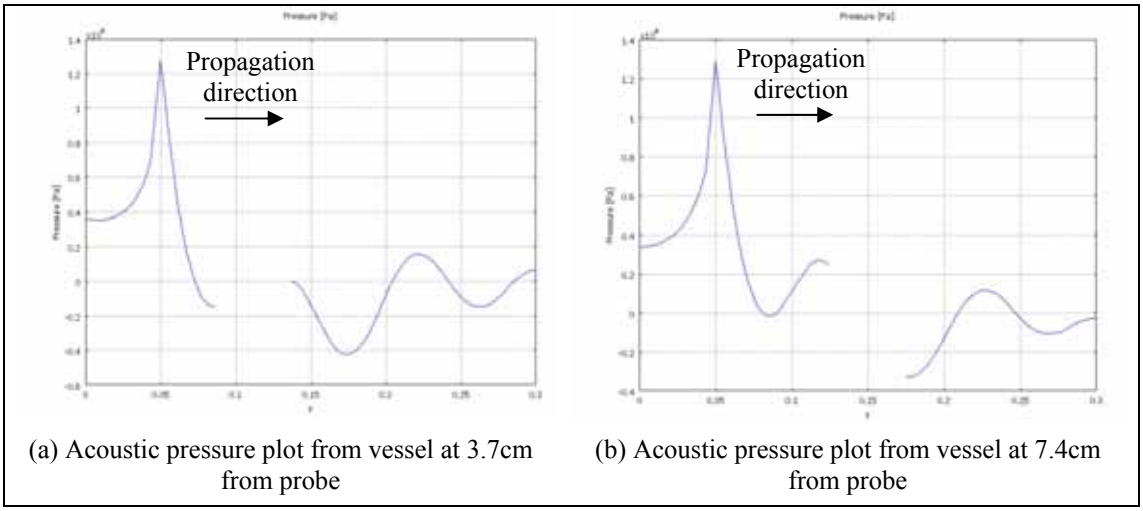

(a) Acoustic pressure plot from vessel at 3.7cm from probe

(b) Acoustic pressure plot from vessel at 7.4cm from probe

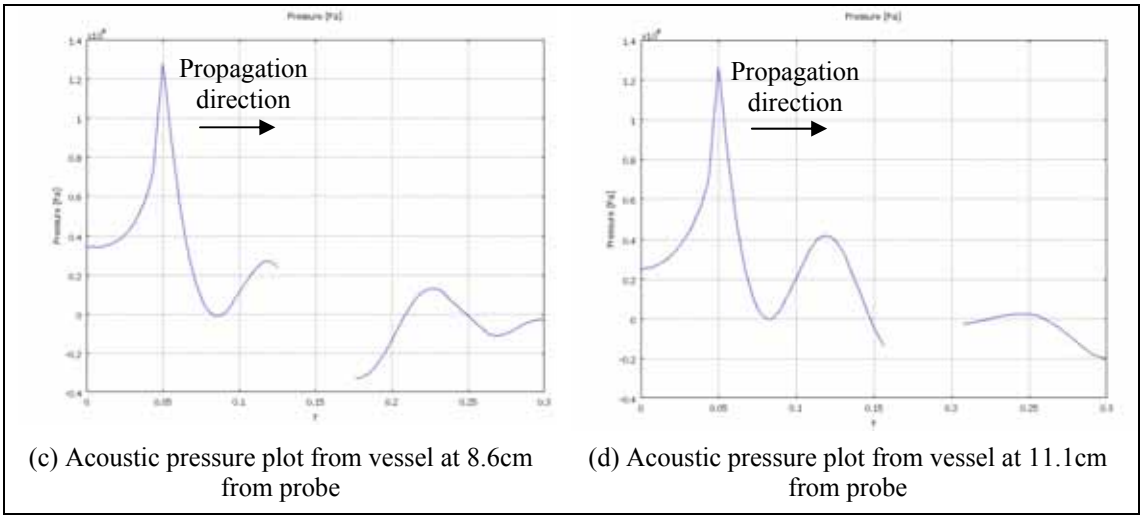

(c) Acoustic pressure plot from vessel at 8.6cm from probe

(d) Acoustic pressure plot from vessel at 11.1cm from probe

Figure 107: Acoustic pressure plots from simulated water baths with immersed vessels at different distances

II.6.3 Subdomain: irradiated vessel

In order to couple the acoustic field in the water bath to that 'seen' by the polymeric foams inside of the containers, the boundary conditions for the vessels must be set (i.e. the acoustic impedance of the polypropylene container). On the outer perimeter of the container, an incident cylindrical wave was specified to represent an incoming sound wave with the same characteristics than that travelling across the water bath for a given distance from the probe.

The acoustic pressure distribution for the vessels irradiated at 20kHz were presented in Chapter 5, section 5.5.3. In the following, figures of the vessels irradiated at 25kHz (Figure 108) and 30kHz (Figure 111) are presented.

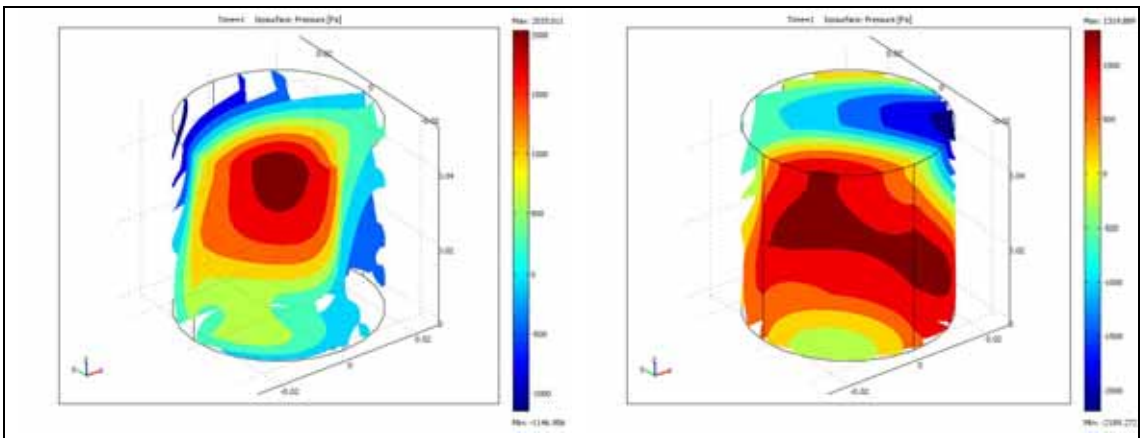

(a) Vessel at 2.95cm from probe

(b) Vessel at 5.90cm from probe

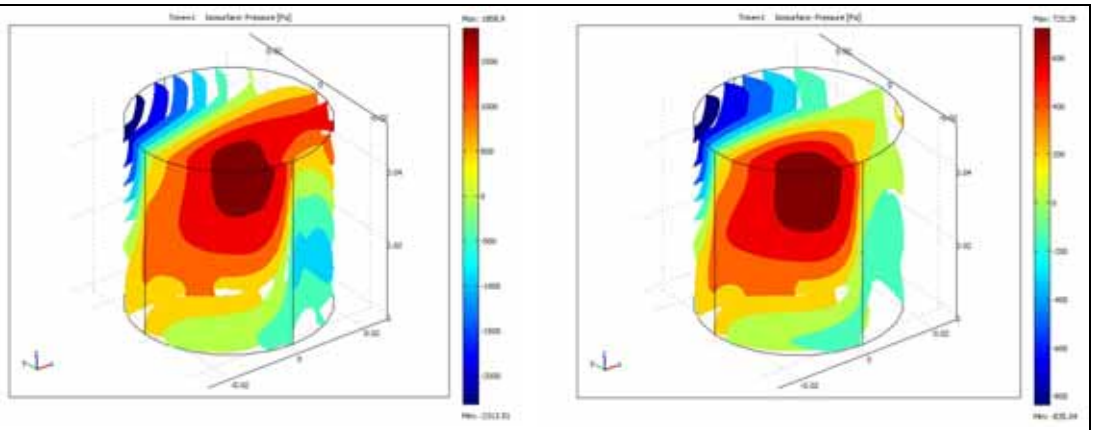

(c) Vessel at 6.35cm from probe (d) Vessel at 8.85cm from probe

Figure 108: Vessels irradiated in the bath at 25kHz and 12000Pa

For the model presented in Figure 108, the number of tetrahedral elements in the mesh was set to 13571. The method solved for 19928 degrees of freedom in 495.75s (in average).

The sections presented in Figure 109 were extracted from the vessels in Figure 108 using a vertical plane aligned to the acoustic wave that is received by the containers immersed in the acoustic field.

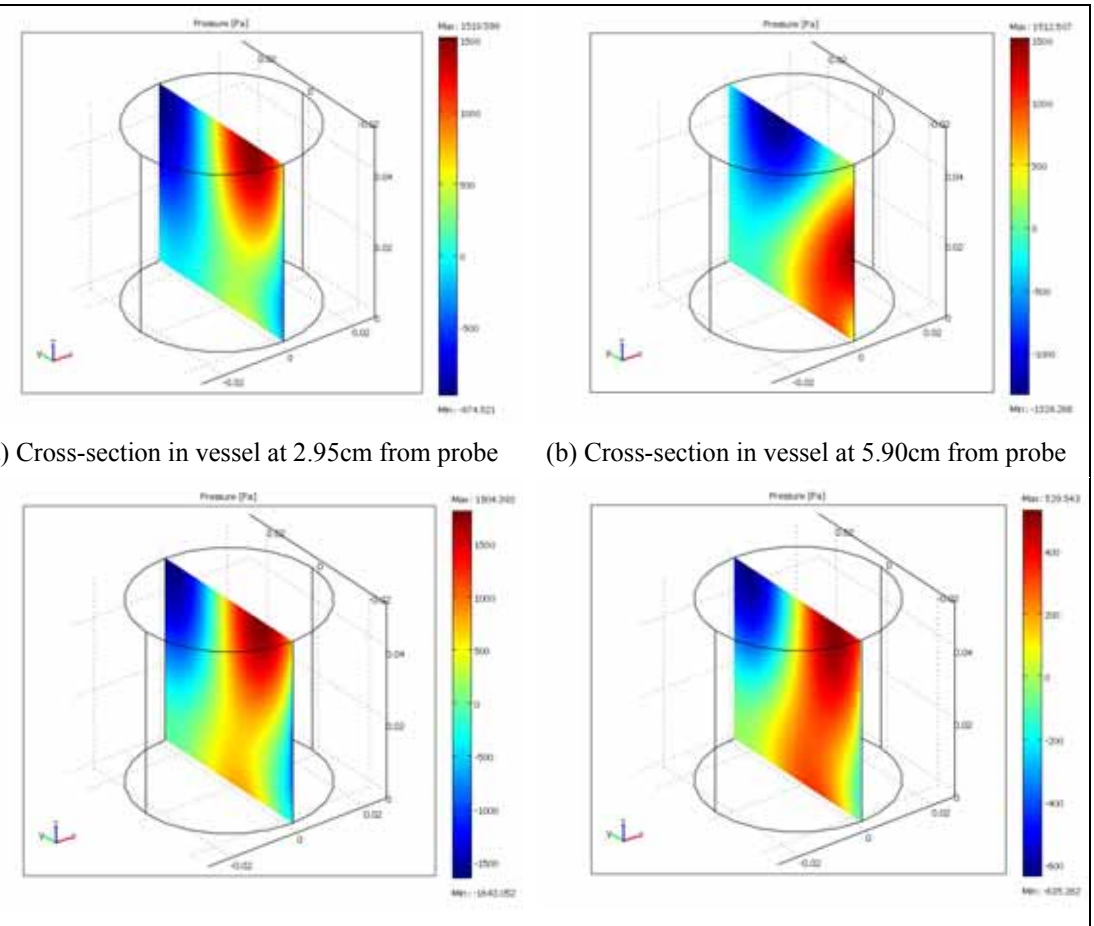

(a) Cross-section in vessel at 2.95cm from probe (b) Cross-section in vessel at 5.90cm from probe

(c) Cross-section in vessel at 6.35cm from probe (d) Cross-section in vessel at 8.85cm from probe

Figure 109: Cross-sections from vessels irradiated at 25kHz and 12000Pa

The sound pressure level at a plane aligned with the ultrasonic probe was extracted. This data was used in Chapter 5, section 5.5.3 to establish a comparison between final porosity in the sample and the acoustic magnitude that the foam had been subjected to during its formation in the water bath. Some examples extracted from vessels that were irradiated at 25 kHz in the simulation, are presented below.

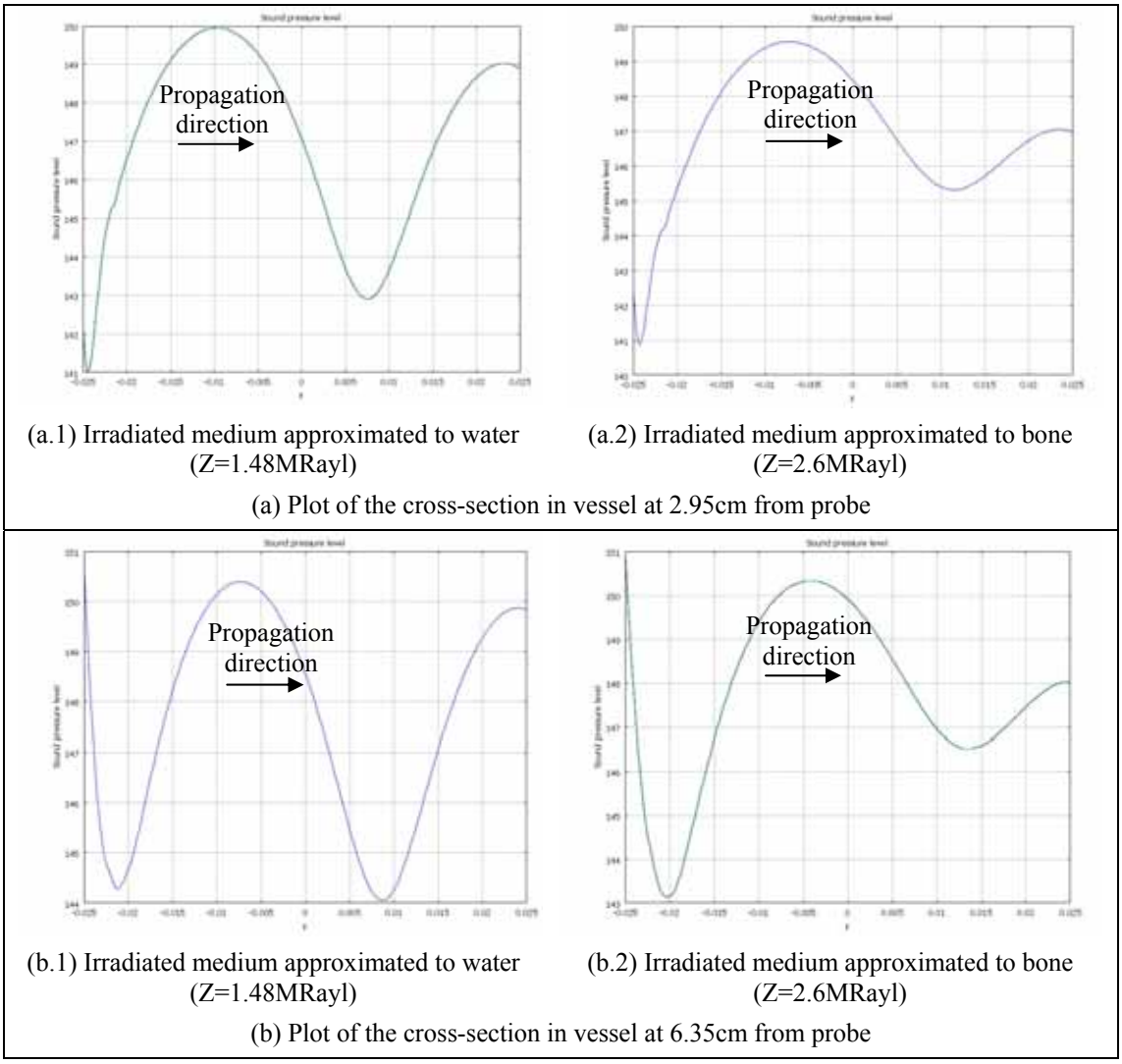

(a.1) Irradiated medium approximated to water (Z=1.48MRayl)

(a.2) Irradiated medium approximated to bone (Z=2.6MRayl)

(a) Plot of the cross-section in vessel at 2.95cm from probe

(b.1) Irradiated medium approximated to water (Z=1.48MRayl)

(b.2) Irradiated medium approximated to bone (Z=2.6MRayl)

(b) Plot of the cross-section in vessel at 6.35cm from probe

Figure 110: Sound pressure level plots from vessels irradiated at 25kHz and 12000Pa

In the same way, vessels irradiated at 30 kHz and 8900Pa placed at different locations in the bath were analysed. The acoustic pressure distribution in each of the vessels is presented below (Figure 111). For solving the model, the simulator generated a grid with 13571 elements. The method solved for 19928 degrees of freedom in an averaged solution time of 509.453s.

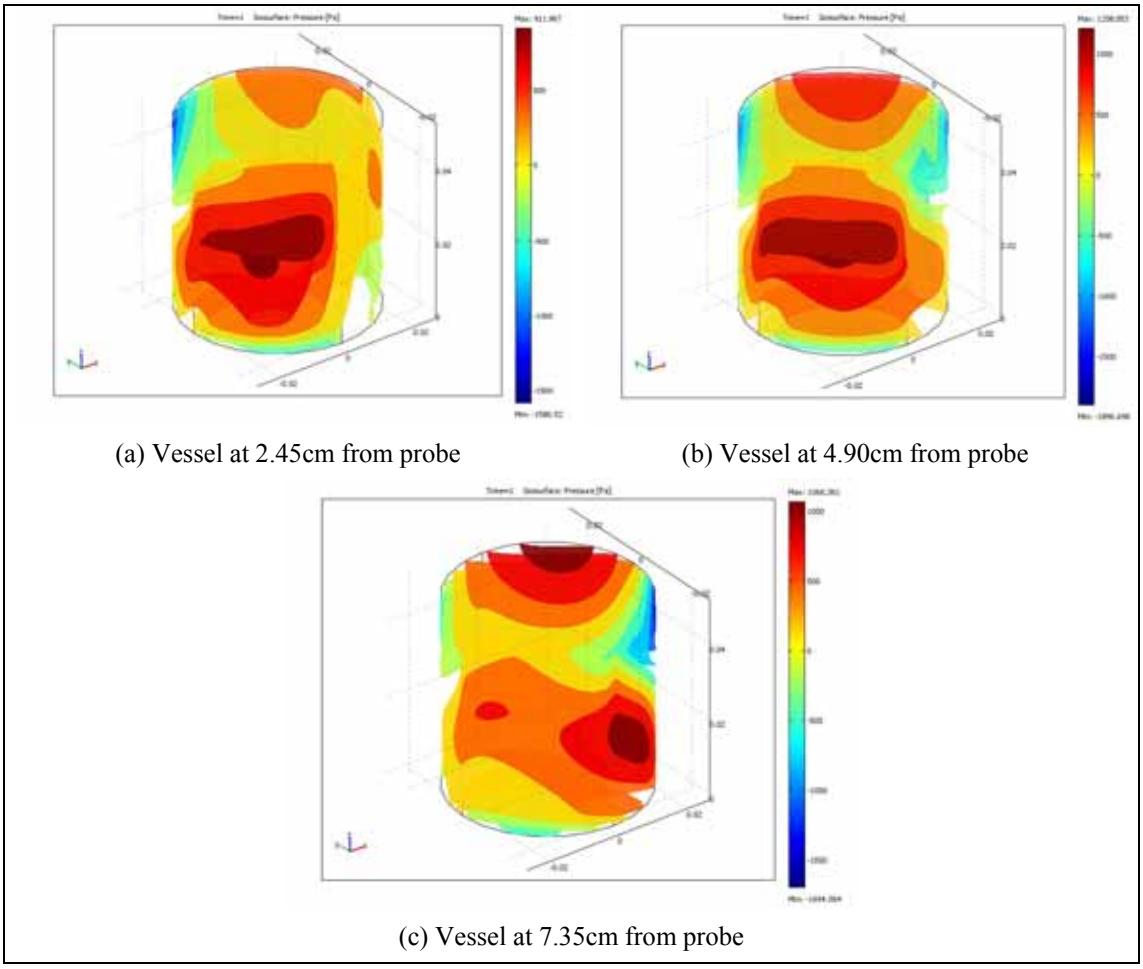

(a) Vessel at 2.45cm from probe

(b) Vessel at 4.90cm from probe

(c) Vessel at 7.35cm from probe

Figure 111: Vessels irradiated in the bath at 30kHz and 8900Pa

The correspondent cross-sections on a vertical plane aligned to the irradiated soundwave from the sonotrode are presented below Figure 112.

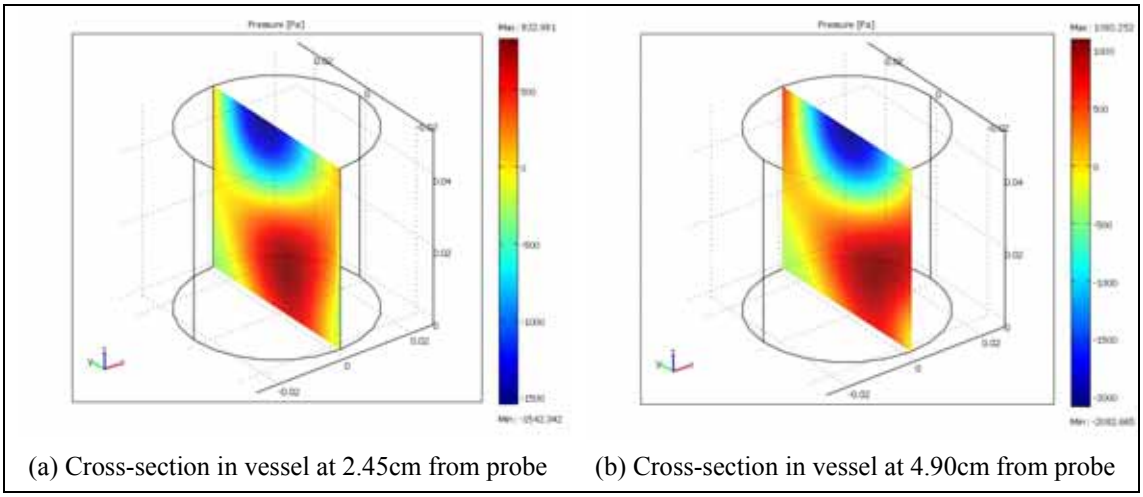

(a) Cross-section in vessel at 2.45cm from probe

(b) Cross-section in vessel at 4.90cm from probe

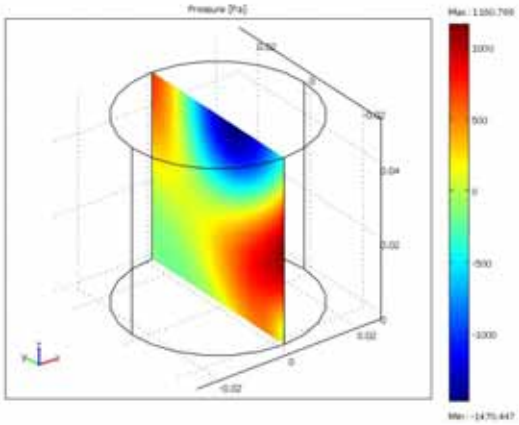

(c) Cross-section in vessel at 7.35cm from probe

Figure 112: Cross-sections from vessels irradiated at 30kHz and 8900Pa

The sound pressure level at a plane aligned with the ultrasonic probe was extracted from each one of Figure 112. The plots are presented below in Figure 113.

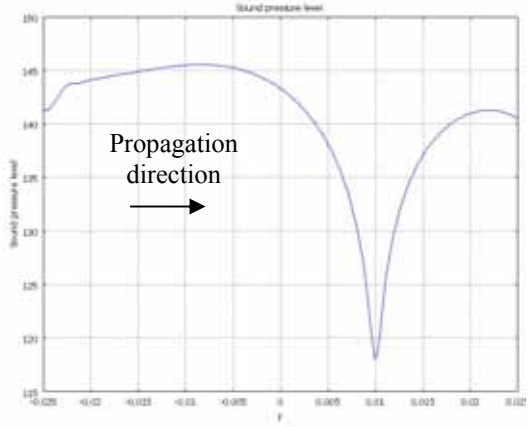

(a.1) Irradiated medium approximated to water (Z=1.48MRayl)

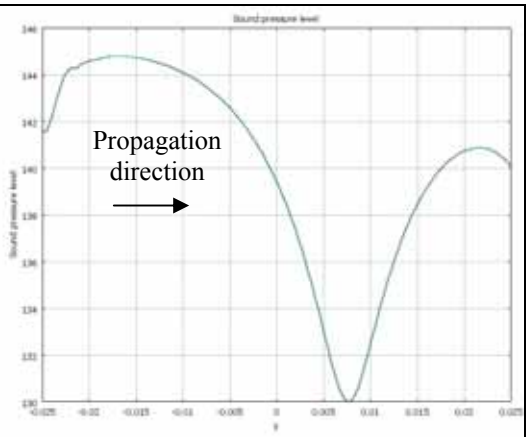

(a.2) Irradiated medium approximated to bone (Z=2.6MRayl)

(a) Plot of the cross-section in vessel at 2.45cm from probe

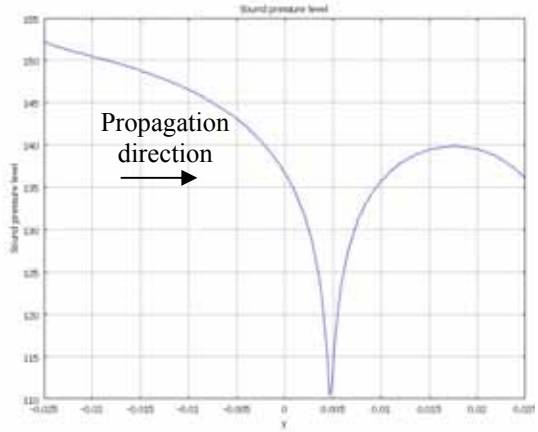

(b.1) Irradiated medium approximated to water (Z=1.48MRayl)

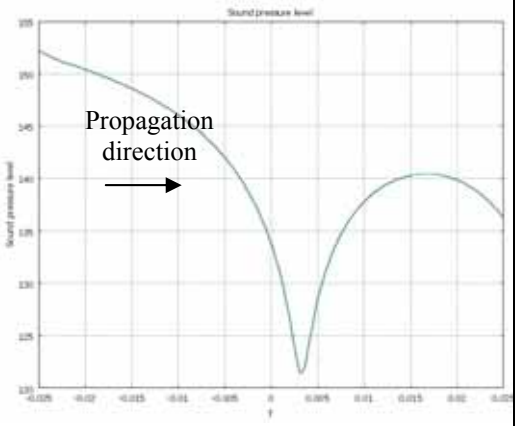

(b.2) Irradiated medium approximated to bone (Z=2.6MRayl)

(b) Plot of the cross-section in vessel at 7.35cm from probe

Figure 113: Sound pressure level plots from vessels irradiated at 30kHz and 8900Pa

APPENDIX III MICROTOMOGRAPHY SCAN

This appendix shows the detailed parameters for the set-up for the micro computer tomography scanning carried out on some of the sonicated and non-sonicated foam samples.

1. Acquisition Geometry:

Distance from source to detector = 635.900024mm.
Distance from source to rotation axis = 159.490997mm.
Pixel width = 0.200000mm.
Pixel height = 0.200000mm.
First pixel is at (-199.900003, 0.000000) mm.
Number of pixels is 2000 by 1780.
Number of projection images = 2661.
Angular increment = -0.135290 degrees.
Initial angle = 0.000000 degrees.

2. Filter:

A ramp filter was used.
Cut-off frequency = 100.000001 percent of maximum.

3. Reconstructed Volume:

Number of voxels = 942 by 942 by 838.
Voxel size = 0.106573mm by 0.106573mm by 0.106573mm.
X-range = -50.195883mm to 50.195883mm.
Y-range = 50.195883mm to -50.195883mm.
Z-range = -44.654087mm to 44.654087mm.
Centre of rotation offsets: top = 0.000000 pixels, bottom = 0.000000 pixels.

4. Others

Fast viewing enabled.

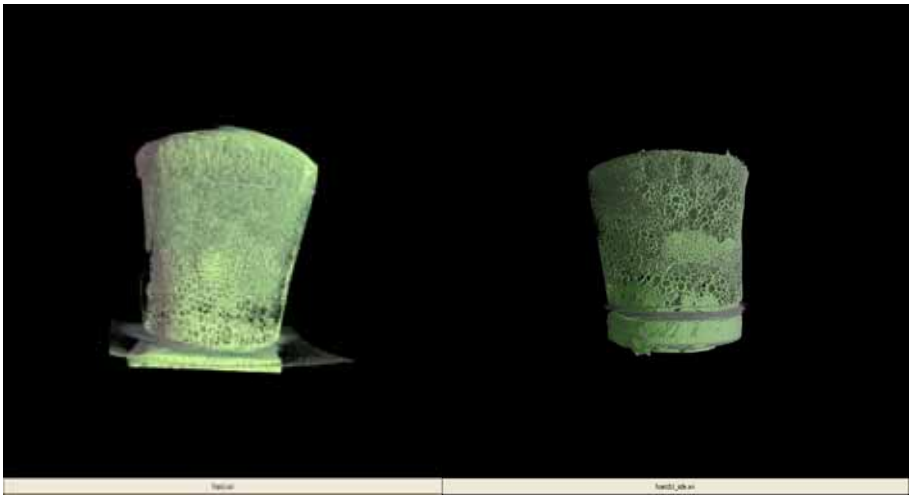

Figure 114: μ-CT image of two sonicated foams

REFERENCES

1. Mano, J.F. and R.L. Reis, *Some trends on how one can learn from and mimic nature in order to design better biomaterials.* Materials Science and Engineering: C, 2005. **25**(2): p. 93-95.

2. Lanzetta, M. and E. Sachs, *Improved surface finish in 3D printing using bimodal powder distribution.* Rapid Prototyping Journal, 2003. **9**(3): p. 157-166.

3. Smay, J.E., J. Cesarano, and J.A. Lewis, *Colloidal inks for directed assembly of 3-D periodic structures.* Langmuir, 2002. **18**(14): p. 5429-5437.

4. Head, P.R., *Construction materials and technology: a look at the future.* Proceedings of the Institution of Civil Engineers-Civil Engineering, 2001. **144**(3): p. 113-118.

5. Chu, T.M.G., et al., *Mechanical and in vivo performance of hydroxyapatite implants with controlled architectures.* Biomaterials, 2002. **23**(5): p. 1283-1293.

6. Morvan, S., *MMA-Rep, A representation for multi-material solids. PhD thesis*. 2001, The Graduate School of Clemson University.

7. Yang, T.H.J., *Structure property relationships in biological tissues. PhD thesis*. 2007, Heriot-Watt University: Edinburgh.

8. Gibson, L.J. and M.F. Ashby, *Cellular solids: structure and properties*. 2nd ed. 1997: Cambridge University Press.

9. Atalla, N., et al., *Acoustic absorption of macro-perforated porous materials.* Journal of Sound and Vibration, 2002. **256**(2): p. 389-389.

10. Bergstrom, J.S. and M.C. Boyce, *Mechanical behavior of particle filled elastomers.* Rubber Chemistry and Technology, 1999. **72**(4): p. 633-656.

11. Kalita, S.J., et al., *Development of controlled porosity polymer-ceramic composite scaffolds via fused deposition modeling.* Materials Science and Engineering: C, 2003. **23**(5): p. 611-620.

12. Beruto, D.T., M. Baiardo, and S.A. Mezzasalma, *Foaming power, bubble nature, and sample density related to the expansion regime in polyurethane foams.* Journal of Materials Synthesis and Processing, 1999. **7**(4): p. 229-237.

13. Barbero, E.J., *Introduction to composite materials design*. 1999, Ann Arbor, Michigan: Taylor & Francis Inc.

14. Shin, K.H., et al., *A method for the design and fabrication of heterogeneous objects.* Materials and Design, 2003. **24**(5): p. 339-353.

15. Markworth, A.J. and J.H. Saunders, *A Model of Structure Optimization for a Functionally Graded Material.* Materials Letters, 1995. **22**(1-2): p. 103-107.

16. Hassani, B. and E. Hinton, *A review of homogenization and topology optimization I - homogenization theory for media with periodic structure.* Computers & Structures, 1998. **69**(6): p. 707-717.

17. Dutta, D., et al., *Layered Manufacturing: Current status and future trends.* Journal of Computing and Information Science in Engineering, 2001. **1**(1): p. 60-71.

18. Yan, X. and P. Gu, *A review of rapid prototyping technologies and systems.* Computer-Aided Design, 1996. **28**(4): p. 307-318.

19. Steidle, C., et al. *Automated fabrication of custom bone implants using rapid prototyping* in *Proceedings of the 44th International SAMPE Symposium and Exhibition*. 1999. Long Beach, CA; USA.

20. Kumar, P., et al., *Direct-write deposition of fine powders through miniature hopper-nozzles for multi-material solid freeform fabrication.* Rapid Prototyping Journal, 2004. **10**(1): p. 14-23.

21. Tolochko, N., et al., *Selective laser sintering of single- and two-component metal powders.* Rapid Prototyping Journal, 2003. **9**(2): p. 68-78.

22. Envisiontec Ltd, *http://www.envisiontec.de/ [last accessed 25 May 2007]*. Stoke-on-Trent, UK.

23. Woesz, A., et al., *Towards bone replacement materials from calcium phosphates via rapid prototyping and ceramic gelcasting.* Materials Science and Engineering: C, 2005. **25**(2): p. 181-186.

24. Pompe, W., et al., *Functionally graded materials for biomedical applications.* Materials Science and Engineering A, 2003. **362**(1-2): p. 40-60.

25. SolidScape Inc, *http://www.solid-scape.com*. [last accessed 25 May 2007], NH, USA.

26. Atwood, C., et al. *Laser engineered net shaping (LENS): a tool for direct fabrication of metal parts* in *Proceedings of the ICALEO '98: Laser Materials Processing Conference*. 1998. Orlando, FL, USA.

27. Fessler, J., et al. *Functional gradient metallic prototypes through shape deposition manufacturing*. in *Proceedings of the Solid Freeform Fabrication Symposium*. 1997. The University of Texas at Austin, USA.

28. Fessler, J., Merz, R., Nickel, A., Prinz, F., and Weiss, L. *Laser deposition of metals for Shape Deposition Manufacturing*. in *Proceedings of the Solid Freeform Fabrication Symposium*. 1996. The University of Texas at Austin, USA.

29. Chen, Z.Z., et al., *Fabrication of artificial bioactive bone using rapid prototyping.* Rapid Prototyping Journal, 2004. **10**(5): p. 327-333.

30. Yan, Y., et al., *Layered manufacturing of tissue engineering scaffolds via multi-nozzle deposition.* Materials Letters, 2003. **57**(18): p. 2623-2628.

31. Rodriguez, J.F., J.P. Thomas, and J.E. Renaud, *Design of fused-deposition ABS components for stiffness and strength.* Journal of Mechanical Design, Transactions of the ASME, 2003. **125**(3): p. 545-551.

32. Fang, Z., B. Starly, and W. Sun, *Computer-aided characterization for effective mechanical properties of porous tissue scaffolds.* Computer-Aided Design, 2005. **37**(1): p. 65-72.

33. Jackson, T.R., et al., *Modeling and designing functionally graded material components for fabrication with local composition control.* Materials & Design, 1999. **20**(2-3): p. 63-75.

34. Jackson, T.R., *Analysis of Functionally Graded Material object representation models. PhD Thesis*. 2000, Massachusetts Institute of Technology.

35. Wu, H., et al. *Distributed design and fabrication of parts with Local Composition Control*. in *Procedings of the 2000 NSF Design and Manufacturing Grantees Conference*. 2000. Vancouver, Canada.

36. Siu, Y.K. and S.T. Tan, *Modeling the material grading and structures of heterogeneous objects for layered manufacturing.* Computer-Aided Design, 2002. **34**(10): p. 705-716.

37. Lam, C.X.F., et al., *Scaffold development using 3D printing with a starch-based polymer.* Materials Science & Engineering C, 2002. **20**(1-2): p. 49-56.

38. Singh, P. and D. Dutta, *A process planning framework for multi-direction layered deposition*, in *Geometric and Algorithmic Aspects of Computer-Aided Design and Manufacturing*, R. Janardan, M. Smid, and D. Dutta, Editors. 2005. p. 221-244.

39. Pandey, P.M., N. Venkata Reddy, and S.G. Dhande, *Part deposition orientation studies in layered manufacturing.* Journal of Materials Processing Technology, 2007. **185**(1-3): p. 125-131.

40. Gervasi, V.R., A. Schneider, and J. Rocholl, *Geometry and procedure for benchmarking SFF and hybrid fabrication process resolution.* Rapid Prototyping Journal, 2005. **11**(1): p. 4-8.

41. Taboas, J.M., et al., *Indirect solid free form fabrication of local and global porous, biomimetic and composite 3D polymer-ceramic scaffolds.* Biomaterials, 2003. **24**(1): p. 181-194.

42. Zeltinger, J., et al., *Effect of pore size and void fraction on cellular adhesion, proliferation, and matrix deposition.* Tissue Engineering, 2001. **7**(5): p. 557-572.

43. Knitter, R., W. Bauer, and D. Gohring, *Manufacturing of ceramic microcomponents by a rapid prototyping process chain.* Advanced Engineering Materials, 2001. **3**(1-2): p. 49-54.

44. v. Lacroix, F., J. Loos, and K. Schulte, *Morphological investigations of polyethylene fibre reinforced polyethylene.* Polymer, 1999. **40**(4): p. 843-847.

45. Widmer, M.S., et al., *Manufacture of porous biodegradable polymer conduits by an extrusion process for guided tissue regeneration.* Biomaterials, 1998. **19**(21): p. 1945-1955.

46. Thomson, R.C., et al., *Hydroxyapatite fiber reinforced poly([alpha]-hydroxy ester) foams for bone regeneration.* Biomaterials, 1998. **19**(21): p. 1935-1943.

47. Kasuga, T., et al., *Preparation and mechanical properties of polylactic acid composites containing hydroxyapatite fibers.* Biomaterials, 2001. **22**(1): p. 19-23.

48. Kikuchi, M., et al., *Preparation and mechanical properties of calcium phosphate copoly-L-lactide composites.* Journal of Materials Science-Materials in Medicine, 1997. **8**(6): p. 361-364.

49. Zettl, B., et al., *Fatigue properties of aluminium foams at high numbers of cycles.* Materials Science and Engineering A, 2000. **292**(1): p. 1-7.

50. Sepulveda, P. and J.G.P. Binner, *Processing of cellular ceramics by foaming and in situ polymerisation of organic monomers.* Journal of the European Ceramic Society, 1999. **19**(12): p. 2059-2066.

51. Schwarzwalder, K. and A.V. Somers, *Method of making a porous shape of sintered refractory ceramic articles*. 1963, US3090094: United States Patent Office.

52. Nangrejo, M.R. and M.J. Edirisinghe, *Porosity and strength of silicon carbide foams prepared using preceramic polymers.* Journal of Porous Materials, 2002. **9**(2): p. 131-140.

53. Haugen, H., et al., *Ceramic TiO2-foams: characterisation of a potential scaffold.* Journal of the European Ceramic Society, 2004. **24**(4): p. 661-668.

54. van Tienen, T.G., et al., *Tissue ingrowth and degradation of two biodegradable porous polymers with different porosities and pore sizes.* Biomaterials, 2002. **23**(8): p. 1731-1738.

55. Peng, H.X., et al., *Microstructure of ceramic foams.* Journal of the European Ceramic Society, 2000. **20**(7): p. 807-813.

56. Garrn, I., et al., *Clot-forming: the use of proteins as binders for producing ceramic foams.* Journal of the European Ceramic Society, 2004. **24**(3): p. 579-587.

57. Dunand, D.C., *Processing of titanium foams.* Advanced Engineering Materials, 2004. **6**(6): p. 369-376.

58. Brothers, A.H. and D.C. Dunand, *Density-graded cellular aluminum.* Advanced Engineering Materials, 2006. **8**(9): p. 805-809.

59. Brothers, A.H. and D.C. Dunand, *Plasticity and damage in cellular amorphous metals.* Acta Materialia, 2005. **53**(16): p. 4427-4440.

60. Spoerke, E.D., et al., *A bioactive titanium foam scaffold for bone repair.* Acta Biomaterialia, 2005. **1**(5): p. 523-533.

61. Zhang, X.D., et al., *Role of silicone surfactant in flexible polyurethane foam.* Journal of Colloid and Interface Science, 1999. **215**(2): p. 270-279.

62. *Handbook of polymeric science and technology*. Performance properties of plastics and elastomers, ed. M.P. Cheremisinoff. Vol. 2. 1989: CRC Press: Taylor & Francis.

63. Lee, S.-T., C.B. Park, and N.S. Ramesh, *Polymeric Foams: Science and Technology*. 1st ed. 2006: CRC Press: Taylor & Francis. 220 pages.

64. Richards, W.T. and A.L. Loomis, *The chemical effects of high frequency sound waves. I. A preliminary survey.* J. Am. Chem. Soc., 1927. **49**(12): p. 3086-3100.

65. Apfel, R.E., *Acoustic cavitation prediction.* Journal of the Acoustical Society of America, 1981. **69**(6): p. 1624-1633.

66. Crum, L.A., *Acoustic cavitation.* IEEE Ultrasonics Symposium, 1982: p. 1-11.

67. Suslick, K.S., *Sonochemistry.* Science, 1990. **247**(4949): p. 1439-1445.

68. Suslick, K.S. and G.J. Price, *Applications of ultrasound to materials chemistry.* Annual Review of Materials Science, 1999. **29**: p. 295-326.

69. Kruus, P., M. O'Neill, and D. Robertson, *Ultrasonic initiation of polymerization.* Ultrasonics, 1990. **28**(5): p. 304-309.

70. Price, G.J., *Recent developments in sonochemical polymerisation.* Ultrasonics Sonochemistry, 2003. **10**(4-5): p. 277-283.

71. Kuijpers, M.W.A., et al., *Influence of CO2 on ultrasound-induced polymerizations in high-pressure fluids.* Aiche Journal, 2005. **51**(6): p. 1726-1732.

72. Price, G.J. and P.F. Smith, *Ultrasonic degradation of polymer solutions: 2. The effect of temperature, ultrasound intensity and dissolved gases on polystyrene in toluene.* Polymer, 1993. **34**(19): p. 4111-4117.

73. Diao, B., A.I. Isayev, and V.Y. Levin, *Basic study of continuous ultrasonic devulcanization of unfilled silicone.* Rubber Chemistry and Technology, 1999. **72**(1): p. 152-164.

74. Shim, S.E., S. Ghose, and A.I. Isayev, *Formation of bubbles during ultrasonic treatment of cured poly(dimethyl siloxane).* Polymer, 2002. **43**(20): p. 5535-5543.

75. Masselin, I., et al., *Effect of sonication on polymeric membranes.* Journal of Membrane Science, 2001. **181**(2): p. 213-220.

76. Madras, G., S. Kumar, and S. Chattopadhyay, *Continuous distribution kinetics for ultrasonic degradation of polymers.* Polymer Degradation and Stability, 2000. **69**(1): p. 73-78.

77. Ghose, S., A.I. Isayev, and E. von Meerwall, *Effect of ultrasound on thermoset polyurethane: NMR relaxation and diffusion measurements.* Polymer, 2004. **45**(11): p. 3709-3720.

78. Gaitan, D.F., et al., *Sonoluminescence and bubble dynamics for a single, stable, cavitation bubble.* Journal of the Acoustical Society of America, 1992. **91**(6): p. 3166-3183.

79. Crum, L.A., *Sonoluminescence.* Physics Today, 1994. **47**(9): p. 22-29.

80. Yasui, K., *Alternative model of single-bubble sonoluminescence.* Physical Review E - Statistical Physics, Plasmas, Fluids, and Related Interdisciplinary Topics, 1997. **56**(6): p. 6750-6760.

81. Yasui, K., *Mechanism of single-bubble sonoluminescence.* Physical Review E - Statistical Physics, Plasmas, Fluids, and Related Interdisciplinary Topics, 1999. **60**(2 B): p. 1754-1758.

82. Weninger, K.R., C.G. Camara, and S.J. Putterman, *Observation of bubble dynamics within luminescent cavitation clouds: Sonoluminescence at the nano-scale.* Physical Review E, 2001. **6302**(1).

83. Lorimer, J.P. and T.J. Mason, *Sonochemistry .1. the Physical Aspects.* Chemical Society Reviews, 1987. **16**(2): p. 239-274.

84. Mason, T.J., A. Collings, and A. Sumel, *Sonic and ultrasonic removal of chemical contaminants from soil in the laboratory and on a large scale.* Ultrasonics Sonochemistry, 2004. **11**(3-4): p. 205-210.

85. Manousaki, E., et al., *Degradation of sodium dodecylbenzene sulfonate in water by ultrasonic irradiation.* Water Research, 2004. **38**(17): p. 3751-3759.

86. Mason, T.J., *Developments in ultrasound--Non-medical.* Progress in Biophysics and Molecular Biology, 2007. **93**(1-3): p. 166-175.

87. Gallego-Juarez, J.A., et al., *Process and device for continuous ultrasonic washing of textiles*, in *Spanish Intellectual Property Office*, CSIC, Editor. 1994, Patent: Spain.

88. Suslick, K.S., M.M. Mdleleni, and J.T. Ries, *Chemistry induced by hydrodynamic cavitation.* Journal of the American Chemical Society, 1997. **119**(39): p. 9303-9304.

89. Moussatov, A., C. Granger, and B. Dubus, *Ultrasonic cavitation in thin liquid layers.* Ultrasonics Sonochemistry, 2005. **12**(6): p. 415-422.

90. Haydock, D. and J.M. Yeomans, *Acoustic enhancement of diffusion in a porous material.* Ultrasonics, 2003. **41**(7): p. 531-538.

91. Husseini, G.A., et al., *The role of cavitation in acoustically activated drug delivery.* Journal of Controlled Release, 2005. **107**(2): p. 253-261.

92. Mulet, A., et al., *New food drying technologies - Use of ultrasound.* Food Science and Technology International, 2003. **9**(3): p. 215-221.

93. Pitt, W.G., *Defining the role of ultrasound in drug delivery.* Am J Drug Delivery, 2003. **1**(1): p. 27-42.

94. Price, G.J., A.J. White, and A.A. Clifton, *The effect of high-intensity ultrasound on solid polymers.* Polymer, 1995. **36**(26): p. 4919-4925.

95. Swain, S.K. and A.I. Isayev, *Effect of ultrasound on HDPE/clay nanocomposites: Rheology, structure and properties.* Polymer, 2007. **48**(1): p. 281-289.

96. Hamdaoui, O. and E. Naffrechoux, *An investigation of the mechanisms of ultrasonically enhanced desorption.* AIChE Journal, 2007. **53**(2): p. 363-373.

97. Bund, R.K. and A.B. Pandit, *Sonocrystallization: Effect on lactose recovery and crystal habit.* Ultrasonics Sonochemistry, 2007. **14**(2): p. 143-152.

98. Zheng, L. and D.W. Sun, *Innovative applications of power ultrasound during food freezing processes - a review.* Trends in Food Science & Technology, 2006. **17**(1): p. 16-23.

99. Eskin, G.I. and D.G. Eskin, *Effects of ultrasonic (cavitation) melt processing on the structure refinement and property improvement of cast and worked aluminum alloys*, in *Aluminum Alloys 2002: Their Physical and Mechanical Properties Pts 1-3*. 2002. p. 77-82.

100. Chow, R., et al., *A study on the primary and secondary nucleation of ice by power ultrasound.* Ultrasonics, 2005. **43**(4): p. 227-230.

101. Gallego-Juarez, J.A., et al., *Application of acoustic agglomeration to reduce fine particle emissions from coal combustion plants.* Environmental Science & Technology, 1999. **33**(21): p. 3843-3849.

102. Gallego-Juarez, J.A., et al., *Macrosonic system for industrial processing.* Ultrasonics, 2000. **38**(1): p. 331-336.

103. Chen, G.S., S.Y. Guo, and H.L. Li, *Ultrasonic improvement of the compatibility and rheological behavior of high-density polyethylene/polystyrene blends.* Journal of Applied Polymer Science, 2002. **86**(1): p. 23-32.

104. Chen, Y.Z. and H.L. Li, *Effect of ultrasound on the morphology and properties of polypropylene/inorganic filler composites.* Journal of Applied Polymer Science, 2005. **97**(4): p. 1553-1560.

105. Isayev, A.I. and S. Mandelbaum, *Effect of Ultrasonic-Waves on Foam Extrusion.* Polymer Engineering and Science, 1991. **31**(14): p. 1051-1056.

106. Park, H. and J.R. Youn, *Processing of Cellular Polyurethane by Ultrasonic Excitation.* Journal of Engineering for Industry-Transactions of the Asme, 1992. **114**(3): p. 323-328.

107. Youn, J.R. and H. Park, *Bubble growth in reaction injection molded parts foamed by ultrasonic excitation.* Polymer Engineering and Science, 1999. **39**(3): p. 457-468.

108. Xu, H., et al., *Degassing of molten aluminum A356 alloy using ultrasonic vibration.* Materials Letters, 2004. **58**(29): p. 3669-3673.

109. Stathopulos, P.B., et al., *Sonication of proteins causes formation of aggregates that resemble amyloid.* Protein Sci, 2004. **13**(11): p. 3017-3027.

110. Tonanon, N., et al., *Improvement of mesoporosity of carbon cryogels by ultrasonic irradiation.* Carbon, 2005. **43**(3): p. 525-531.

111. Balabushevich, N.G. and N.I. Larionova, *Fabrication and Characterization of Polyelectrolyte Microparticles with Protein.* Biochemistry (Moscow), 2004. **69**(7): p. 757-762.

112. Dedhia, A.C., P.V. Ambulgekar, and A.B. Pandit, *Static foam destruction: role of ultrasound.* Ultrasonics Sonochemistry, 2004. **11**(2): p. 67-75.

113. Gallego-Juarez, J.A., et al. *Development of industrial models of high-power stepped-plate sonic and ultrasonic transducers for use in fluids*. in *Proceedings of the IEEE Ultrasonics Symposium*. 2001.

114. Cho, W.J., H. Park, and J.R. Youn, *Ultrasonic bubble nucleation in reaction injection moulding of polyurethane.* Proceedings of the Institution of Mechanical Engineers, Part B: Journal of Engineering Manufacture, 1994. **208**(B2): p. 121-128.

115. Crum, L.A., *Measurements of the growth of air bubbles by rectified diffusion.* Journal of the Acoustical Society of America, 1980. **68**(1): p. 203-211.

116. Watanabe, T. and Y. Kukita, *Translational and radial motions of a bubble in an acoustic standing wave field.* Physics of Fluids, A, 1993. **5**(11): p. 2682-2688.

117. Leighton, T.G., *The Acoustic Bubble*. 1st ed. 1994, San Diego, CA: Academic Press Inc.

118. Abe, Y., M. Kawaji, and T. Watanabe, *Study on the bubble motion control by ultrasonic wave.* Experimental Thermal and Fluid Science, 2002. **26**(6-7): p. 817-826.

119. Naji Meidani, A.R. and M. Hasan, *Mathematical and physical modelling of bubble growth due to ultrasound.* Applied Mathematical Modelling, 2004. **28**(4): p. 333-351.

120. Hoff, L., P.C. Sontum, and J.M. Hovem, *Oscillations of polymeric microbubbles: Effect of the encapsulating shell.* Journal of the Acoustical Society of America, 2000. **107**(4): p. 2272-2280.

121. Jimenez-Fernandez, J. and A. Crespo, *Bubble oscillation and inertial cavitation in viscoelastic fluids.* Ultrasonics, 2005. **43**(8): p. 643-651.

122. Yang, X.M. and C.C. Church, *Nonlinear dynamics of gas bubbles in viscoelastic media.* Acoustics Research Letters Online-Arlo, 2005. **6**(3): p. 151-156.

123. Postema, M. and G. Schmitz, *Ultrasonic bubbles in medicine: Influence of the shell.* Ultrasonics Sonochemistry, 2007. **14**(4): p. 438-444.

124. Church, C.C., *The effects of an elastic solid-surface layer on the radial pulsations of gas-bubbles.* Journal of the Acoustical Society of America, 1995. **97**(3): p. 1510-1521.

125. Floros, J.D. and H. Liang, *Acoustically assisted diffusion through membranes and biomaterials.* Food Technology, 1994. **48**(12): p. 79-84.

126. Chen, Y. and H. Li, *Effect of ultrasound on the viscoelasticity and rheology of polystyrene extruded through a slit die.* Journal of Applied Polymer Science, 2006. **100**(4): p. 2907-2911.

127. Hu, A., J. Zheng, and T. Qiu, *Industrial experiments for the application of ultrasound on scale control in the Chinese sugar industry.* Ultrasonics Sonochemistry, 2006. **13**(4): p. 329-333.

128. Cannillo, V. and W.C. Carter, *Computation and simulation of reliability parameters and their variations in heterogeneous materials.* Acta Materialia, 2000. **48**(13): p. 3593-3605.

129. Langer, S.A., E. Fuller, and W.C. Carter, *OOF: An image-based finite-element analysis of material microstructures.* Computing in Science & Engineering, 2001. **3**(3): p. 15-23.

130. Adachi, H., T. Hasegawa, and T. Asano, *Cell distributions in and sound absorption characteristics of flexible polyurethane foams.* Journal of Applied Polymer Science, 1997. **65**(7): p. 1395-1402.

131. Goto, A., et al., *Modeling of cell structure in polyurethane foam.* Journal of Cellular Plastics, 2004. **40**(6): p. 481-488.

132. Langton, C.M., et al., *Prediction of mechanical properties of the human calcaneus by broadband ultrasonic attenuation.* Bone, 1996. **18**(6): p. 495-503.

133. Tuan, H.S. and D.W. Hutmacher, *Application of micro CT and computation modeling in bone tissue engineering.* Computer-Aided Design, 2005. **37**(11): p. 1151-1161.

134. Thompson, J.L. and B. Illerhaus, *A new reconstruction of the Le Moustier 1 skull and investigation of internal structures using 3-D-[mu]CT data.* Journal of Human Evolution, 1998. **35**(6): p. 647-665.

135. Hollister, S.J., R.D. Maddox, and J.M. Taboas, *Optimal design and fabrication of scaffolds to mimic tissue properties and satisfy biological constraints.* Biomaterials, 2002. **23**(20): p. 4095-4103.

136. Montminy, M.D., A.R. Tannenbaum, and C.W. Macosko, *The 3D structure of real polymer foams.* Journal of Colloid and Interface Science, 2004. **280**(1): p. 202-211.

137. Schroeder, C., et al., *Computer-aided design of porous artifacts.* Computer-Aided Design, 2005. **37**(3): p. 339-353.

138. Farben, I.G., *Verfahren zur Herstellung von Polyurethanen bzw. Polyharnstoffen*, in *Espacenet, EU Intellectual Property Office*, P. Deutsches Reich Reichspatentamt, Editor. 1942: Germany.

139. Lipshitz, S.D. and C.W. Macosko, *Kinetics and energetics of a fast polyurethane cure.* Journal of Applied Polymer Science, 1977. **21**(8): p. 2029-2039.

140. Rojas, A.J., J.H. Marciano, and R.J. Williams, *Rigid polyurethane foams: A model of the foaming process.* Polymer Engineering & Science, 1982. **22**(13): p. 840-844.

141. Navarchian, A.H., F. Picchioni, and L. Janssen, *Rheokinetics and effect of shear rate on the kinetics of linear polyurethane formation.* Polymer Engineering & Science, 2005. **45**(3): p. 279-287.

142. Marciano, J.H., et al., *Integral-skin polyurethane foams.* Polymer Engineering and Science, 1986. **26**(11): p. 717-724.

143. Gupta, V.K. and D.V. Khakhar, *Formation of integral skin polyurethane foams.* Polymer Engineering and Science, 1999. **39**(1): p. 164-176.

144. Modesti, M., V. Adriani, and F. Simioni, *Chemical and physical blowing agents in structural polyurethane foams: Simulation and characterization.* Polymer Engineering and Science, 2000. **40**(9): p. 2046-2057.

145. Niyogi, D. and R.K. Gandhi, *Modeling of bubble-size distribution in free rise polyurethane foams.* AIChE Journal, 1992. **38**(8): p. 1170-1184.

146. Baser, S.A. and D.V. Khakhar, *Modeling of the dynamics of R-11 blown polyurethane foam formation.* Polymer Engineering & Science, 1994. **34**(8): p. 632-641.

147. Incropera, F.P. and D.P. de Witt, *Fundamentals of heat and mass transfer*. 3rd ed. 1990, West Lafayette, IN, USA: John Wiley & Sons, Inc. editors.

148. Bejan, A., *Convection heat transfer*. 2nd ed. 1995, Durham, NC, USA: John Wiley & Sons, Inc. editors.

149. Seo, D. and J.R. Youn, *Numerical analysis on reaction injection molding of polyurethane foam by using a finite volume method.* Polymer, 2005. **46**(17): p. 6482-6493.

150. Amon, M. and C.D. Denson, *A Study of the Dynamics of Foam Growth - Simplified Analysis and Experimental Results for Bulk-Density in Structural Foam Molding.* Polymer Engineering and Science, 1986. **26**(3): p. 255-267.

151. Phianmongkhol, A. and J. Varley, *A multi point conductivity measurement system for characterisation of protein foams.* Colloids and Surfaces B: Biointerfaces, 1999. **12**(3-6): p. 247-259.

152. Lemlich, R., *A theory for the limiting conductivity of polyhedral foam at low density.* Journal of Colloid and Interface Science, 1978. **64**(1): p. 107-110.

153. Kim, A., et al., *Evaluation of compressive mechanical properties of Al-foams using electrical conductivity.* Composite Structures, 2005. **71**(2): p. 191-198.

154. Blitz, J., *Fundamentals of ultrasonics*. 2nd ed. 1967, London: Butterworths & Co. Ltd publishers. 214 pages.

155. Cheeke, J.D.N., *Fundamentals and applications of ultrasonic waves*. 1st ed. 2002: CRC publisher. 480 pages.

156. Albers, V.M., *Underwater Acoustics. Handbook II*. 1st ed. 1965: The Pennsylvania State University Press.

157. Leighton, T.G., *Bubble population phenomena in acoustic cavitation.* Ultrasonics Sonochemistry, 1995. **2**(2): p. S123-S136.

158. Kanthale, P.M., et al., *Mapping of an ultrasonic horn: Link primary and secondary effects of ultrasound.* Ultrasonics Sonochemistry, 2003. **10**(6): p. 331-335.

159. Yasui, K., T. Tuziuti, and Y. Iida, *Dependence of the characteristics of bubbles on types of sonochemical reactors.* Ultrasonics Sonochemistry, 2005. **12**(1-2): p. 43-51.

160. Crum, L.A. and Y. Mao, *Acoustically enhanced bubble growth at low frequencies and its implications for human diver and marine mammal safety.* Journal of the Acoustical Society of America, 1996. **99**(5): p. 2898-2907.

161. Yasui, K., *Influence of ultrasonic frequency on multibubble sonoluminescence.* Journal of the Acoustical Society of America, 2002. **112**(4): p. 1405-1413.

162. Crum, L.A. and G.M. Hansen, *Generalized equations for rectified diffusion.* Journal of the Acoustical Society of America, 1982. **72**(5): p. 1586-1592.

163. Feng, J.J. and C.A. Bertelo, *Prediction of bubble growth and size distribution in polymer foaming based on a new heterogeneous nucleation model.* Journal of Rheology, 2004. **48**(2): p. 439-462.

164. Bikard, J., et al., *Numerical prediction of the foam structure of polymeric materials by direct 3D simulation of their expansion by chemical reaction based on a multidomain method.* Journal of Materials Science, 2005. **40**(22): p. 5875-5881.

165. Font, R., M.C. Sabater, and M.A. Martínez, *The leaching kinetics of acetone in an acetone-polyurethane adhesive waste.* Journal of Applied Polymer Science, 2002. **85**(9): p. 1945-1955.

166. Cui, Z., et al., *Bubble modulation using acoustic standing waves in a bubbling system.* Chemical Engineering Science, 2005. **60**(22): p. 5971-5981.

167. Birkin, P.R., et al., *Experimental and theoretical characterization of sonochemical cells. Part 1. Cylindrical reactors and their use to calculate the speed of sound in aqueous solutions.* Journal of Physical Chemistry A, 2003. **107**(2): p. 306-320.

168. Iida, Y., et al., *Sonochemistry and its dosimetry.* Microchemical Journal, 2005. **80**(2): p. 159-164.

169. Reid, C.A., *Texture analysis of bone mineralisation surfaces. PhD thesis*. 1995, University of Glasgow.

170. Maxwell, C., *Digital assessment of porosity distribution - foam samples. BEng final project*. 2006, Heriot-Watt University Edinburgh.

171. Torres-Sánchez, C., J. Corney, and J.A. Steel, *Sonication of Polyurethane and Poly-dimethyl Siloxane foams*, in *AWE/HWU Collaborative Foam Sonication Project CDK0314*. 2006, AWE plc.

172. Balasubramaniam, K. and S. Sethuraman, *Ultrasonic interferometric sensor for rheological changes of fluids.* Review of Scientific Instruments, 2006. **77**(8).

173. Raum, K., et al., *Derivation of elastic stiffness from site-matched mineral density and acoustic impedance maps.* Physics in Medicine and Biology, 2006. **51**(3): p. 747-758.

174. Yoshizawa, M., H. Ushioda, and T. Moriya. *Development of a bone-mimicking phantom and measurement of its acoustic impedance by the interference method*. in *Ultrasonics Symposium, 2004 IEEE*. 2004.

175. Lipshitz, S.H. and C.W. Macosko, *Rheological changes during a urethane network polymerization.* Polymer Engineering & Science, 1976. **16**(12): p. 803-810.

176. Kaye, G.W.C. and T.H. Laby, *Tables of Physical and Chemical constants and some Mathematical functions*. 14th ed. 1973: Longman Publishers. 386.

177. Yoo, H.J. and C.D. Han, *Oscillatory Behavior of a Gas Bubble Growing (or Collapsing) in Viscoelastic Liquids.* Aiche Journal, 1982. **28**(6): p. 1002-1009.

178. Arefmanesh, A. and S.G. Advani, *Diffusion-induced growth of a gas bubble in a viscoelastic fluid.* Rheologica Acta, 1991. **30**(3): p. 274-283.

179. Sagui, C., et al., *Elastic effects in the foaming of thermoplastics.* Physical Review E, 1998. **58**(4): p. 4654.

180. Otsuki Y. and T. Kanai, *Numerical simulation of bubble growth in viscoelastic fluid with diffusion of dissolved foaming agent.* Polymer Engineering & Science, 2005. **45**(9): p. 1277-1287.

181. Chen, X., J.J. Feng, and C.A. Bertelo, *Plasticization effects on bubble growth during polymer foaming.* Polymer Engineering and Science, 2006. **46**(1): p. 97-107.

182. Beckett, M.A. and I. Hua, *Impact of ultrasonic frequency on aqueous sonoluminescence and sonochemistry.* Journal of Physical Chemistry A, 2001. **105**(15): p. 3796-3802.

183. Luo, H., et al., *Effect of external ultrasound frequency on thrombus disruption in vitro.* Journal of Thrombosis and Thrombolysis, 1996. **3**(1): p. 63-66.

184. Klima, J., et al., *Optimisation of 20 kHz sonoreactor geometry on the basis of numerical simulation of local ultrasonic intensity and qualitative comparison with experimental results.* Ultrasonics Sonochemistry, 2007. **14**(1): p. 19-28.

185. Bolboaca, S. and L. Jantschi, *Pearson versus Spearman, Kendall's tau correlation analysis on structure-activity relationships of biologic active compounds.* Leonardo Journal of Sciences, 2006. **9**: p. 179-200.

186. Boccaccini, A.R., *Fabrication, microstructural characterisation and mechanical properties of glass compacts containing controlled porosity of spheroidal shape.* Journal of Porous Materials, 1999. **6**(4): p. 369-379.

187. Chinwanitcharoen, C., et al., *Preparation of aqueous dispersible polyurethane: Effect of acetone on the particle size and storage stability of polyurethane emulsion.* Journal of Applied Polymer Science, 2004. **91**(6): p. 3455-3461.